

AFWAL-TR-87-4009

DTIC FILE COPY

DEVELOPMENT OF IRON ALUMINIDES



Dr. R. G. Bordeaux
United Technologies Corporation
Pratt & Whitney
Government Products Division
P.O. Box 109600
West Palm Beach, Florida 33410-9600

May 1987

Final Report for Period September 1981 - January 1986

~~Approved for public release; distribution is unlimited.~~

This document has been approved
for public release and sale; its
distribution is unlimited.

Materials Laboratory
Air Force Wright Aeronautical Laboratories
Air Force Systems Command
Wright-Patterson Air Force Base, Ohio 45433-6533

DTIC
COLLECTOR
AUG 10 1987
R

AD-A185 190

UNCLASSIFIED

SECURITY CLASSIFICATION OF THIS PAGE

ADA185190

This document has been approved
for public release and sale; its
distribution is unlimited.

REPORT DOCUMENTATION PAGE

1a. REPORT SECURITY CLASSIFICATION UNCLASSIFIED		1b. RESTRICTIVE MARKINGS None									
2a. SECURITY CLASSIFICATION AUTHORITY N/A		3. DISTRIBUTION/AVAILABILITY OF REPORT Approved for public release; distribution is unlimited.									
2b. DECLASSIFICATION/DOWNGRADING SCHEDULE N/A											
4. PERFORMING ORGANIZATION REPORT NUMBER(S) P&W FR-18807		5. MONITORING ORGANIZATION REPORT NUMBER(S) AFWAL-TR-87-4009									
6a. NAME OF PERFORMING ORGANIZATION United Technologies Corporation Pratt & Whitney Government Products Division		7a. NAME OF MONITORING ORGANIZATION Materials Laboratory (AFWAL/MLLM) Air Force Wright Aeronautical Laboratories									
6b. OFFICE SYMBOL (If applicable)		7b. ADDRESS (City, State and ZIP Code) Wright-Patterson Air Force Base Ohio 45433-6533									
6c. ADDRESS (City, State and ZIP Code) P.O. Box 109600 West Palm Beach, FL 33410-9600		9. PROCUREMENT INSTRUMENT IDENTIFICATION NUMBER F33615-81-C-5110									
8a. NAME OF FUNDING/SPONSORING ORGANIZATION Air Force Materials Lab		8b. OFFICE SYMBOL (If applicable) AFWAL/MLLM									
8c. ADDRESS (City, State and ZIP Code) AFWAL/MLLM WPAFB, OH 45433-6533		10. SOURCE OF FUNDING NOS. <table border="1"><thead><tr><th>PROGRAM ELEMENT NO.</th><th>PROJECT NO.</th><th>TASK NO.</th><th>WORK UNIT NO.</th></tr></thead><tbody><tr><td>62102F</td><td>2417</td><td>04</td><td>18</td></tr></tbody></table>		PROGRAM ELEMENT NO.	PROJECT NO.	TASK NO.	WORK UNIT NO.	62102F	2417	04	18
PROGRAM ELEMENT NO.	PROJECT NO.	TASK NO.	WORK UNIT NO.								
62102F	2417	04	18								
11. TITLE (Include Security Classification) Development of Iron Aluminides											
12. PERSONAL AUTHOR(S)											
13a. TYPE OF REPORT Final		13b. TIME COVERED FROM Sept 1981 TO Jan 1986									
14. DATE OF REPORT (Yr., Mo., Day) 5/5/87		15. PAGE COUNT 265									
16. SUPPLEMENTARY NOTATION R. G. Bourdeau, C. M. Adam, M. J. Blackburn, C. V. Law, E. R. Slaughter											
17. COSATI CODES <table border="1"><thead><tr><th>FIELD</th><th>GROUP</th><th>SUB GR.</th></tr></thead><tbody><tr><td>11</td><td>06</td><td></td></tr></tbody></table>		FIELD	GROUP	SUB GR.	11	06		18. SUBJECT TERMS (Continue on reverse if necessary and identify by block number) Powder Metallurgy, Rapid Solidification, Iron Aluminides, Dispersions, Ferritic and Austenitic Manganese Steels, Consolidation, and Post Working.			
FIELD	GROUP	SUB GR.									
11	06										
19. ABSTRACT (Continue on reverse if necessary and identify by block number) <p>This program addresses the development of iron aluminide base alloys by rapid solidification and the determination of their potential for use in aircraft turbine engines as alternatives to high chromium steels and nickel-base alloys. The program was divided into three tasks. A process and model development task to define thermo-mechanical processing requirements for Fe₃Al base alloys, a task to produce and deliver to the Air Force Materials Laboratory a number of alloys produced by the P&W rapidly solidified powder process and a task for the development of austenitic Fe-Mn-Al alloys with improved elevated temperature properties.</p>											
20. DISTRIBUTION/AVAILABILITY OF ABSTRACT UNCLASSIFIED/UNLIMITED <input checked="" type="checkbox"/> SAME AS RPT. <input type="checkbox"/> DTIC USERS <input type="checkbox"/>		21. ABSTRACT SECURITY CLASSIFICATION UNCLASSIFIED									
22a. NAME OF RESPONSIBLE INDIVIDUAL W. R. Kerr		22b. TELEPHONE NUMBER (Include Area Code) 513-255-4769									
		22c. OFFICE SYMBOL AFWAL/MLLM									

Variations in consolidation and working conditions for the processing of $\text{Fe}_3\text{Al}+\text{TiB}_2$ and the use of fine vs coarse powder caused variations in microstructure which were found to be the major reason for variation in strength and ductility. In general, the finer and more continuous grain structures, derived from a fine TiB_2 dispersion, produced the best combination of mechanical properties.

The Fe_3Al alloy produced as rolled plate from a rectangular extrusion was found to have a tensile strength of 140 ksi (965 MPa) and an elongation of 15% to 16%. The alloy rolled at 1150F (621C) recrystallized at about 1200F (650C) and transformed from an aligned to an equiaxed grain structure with an elongation reduced to about 8%. In contrast, the $\text{Fe}_3\text{Al}+\text{TiB}_2$ alloy produced in rolled plate had a tensile strength of 180 ksi (1241 MPa) and an elongation of 11% to 15%. The alloy rolled at 1500F (815C) resisted recrystallation (abnormal grain growth in this case) to about 1800F (982C) and this temperature was raised to over 2000F (1093C) by alloying or by working under conditions which limited residual stresses. Abnormal grain growth significantly reduced the ductility of the alloy.

Investigation of alloys containing aluminum concentrations beyond that in Fe_3Al , to effect an increase in elastic modulus, produced a material with a relatively high specific elastic modulus. An Fe-18.3Al-8Cr-2Mo-1.9TiB₂ (wt%) alloy, in the as-extruded condition, was found to have a tensile strength of 163 ksi (1124 MPa), an elongation of 6% and a specific modulus of 145 (10)⁶ in. (based on a density of 0.228 lb/in.³ (6.26 gm/cm³)).

Three types of alloys based on Fe-Mn-Al were prepared and evaluated in the austenitic alloys development program. The first type relied on the precipitation of an ordered perovskite carbide for strength. A second series was modeled after the austenitic iron-based superalloys from the FeNi(Cr)Al system. The final alloy was taken from development work performed in the 1950's designated BA36-1. Significant strength and creep resistance were achieved in the austenite:perovskite alloys. It was found that modulated structures could be produced by a variety of thermal treatments. Slow continuous cooling from high temperatures resulted in the most stable structures with the best balance of properties. In certain alloys, the formation of ferrite:perovskite phase mixtures by a cellular reaction reduced the creep capability. The use of a more stable austenite to suppress this transformation coupled with the addition of small amounts of refractory elements yielded alloys with excellent creep properties. However, workability and ductility of such alloys were found to be limited and future efforts for enhancing these properties by processing and alloying changes were needed. For alloys in the second series, stabilization of the L1₂ phase in an austenitic matrix was proved difficult and poor creep resistance was observed due to the formation of an ordered bcc phase. The use of higher titanium levels for stabilization of the L1₂ structure, instead of the bcc phase, was also investigated. The excellent creep resistance of Alloy BA36-1 was verified. However, it was also observed that exposure of this alloy for long periods of time (over 200 hours at 650°C) or at higher temperatures would reduce the creep resistance drastically which could be correlated with dissolution of a coherent precipitate and formation of a plate-like phase in this alloy.

FOREWORD

This final technical report describes the work performed by Pratt & Whitney/Engineering Division (P&W/ED) of the United Technologies Corporation (UTC) for the Air Force, Wright-Patterson Air Force Base, Ohio under Contract F33615-81-C-5110. This report covers the period 1 September 1981 to 31 January 1986. It was assigned internal report number FR-18807. The contract was administered under the technical direction of Mr. W. R. Kerr of the AFWAL Materials Laboratory.

Task I and II efforts were performed at P&W/ED -- South with Dr. C. M. Adam and Mr. E. R. Slaughter acting as principal investigators, and Mr. V. R. Thompson responsible for the production of rapidly solidified (RSR) powder. Task III was performed at P&W/Engineering Division -- North under the direction of Dr. M. J. Blackburn with Dr. C. C. Law as principal investigator. The program was administered at P&W/ED-S by Dr. R. G. Bourdeau.

This report does not have military application. Distribution Statement A is correct.
Per Mr. W. R. Kerr, AFWAL/MLLM

Change Rate
DTIC HAS
28 AUG 87
ETZ

Distribution	
Availability Codes	
Initial and/or	
Dist	Special
A-1	

Letter on file
10/28/87



TABLE OF CONTENTS (Continued)

Section	Page
I INTRODUCTION	1
II PROGRAM PLAN AND SCHEDULE	3
Process and Model Development — Task I	3
Powder for Alloy Development — Task II	5
Austenitic Iron Aluminides — Task III	6
III RESULTS AND DISCUSSION	13
Process and Model Development — Task I	13
Powder Processing and Evaluation	13
Consolidation and Working of Fe_3Al	34
Laboratory Scale Processing	34
Consolidation and Working of $\text{Fe}_3\text{Al} + \text{TiB}_2$	42
Laboratory Scale Processing	42
Large Scale Processing of Fe_3Al and $\text{Fe}_3\text{Al} + \text{TiB}_2$	59
Heat Treatment	63
Microstructural Analysis	67
Microstructure of Material Processed in Small Lots	67
Microstructure of Large Scale Extruded and Worked Material ..	79
Fe_3Al	79
Deformation Process Modeling	90
Texture of Material Processed in Small Lots	100
Texture of Material Processed in Large Lots	103
Property Evaluation	109
Tensile Properties of Swaged Fe_3Al and $\text{Fe}_3\text{Al} + \text{TiB}_2$	109
Properties as a Function of Powder Size	115
Tensile Properties of Alloys Produced in Large Lots	124
Stress Rupture Properties of Alloys Produced in Large Lots	128
Fracture Toughness Properties of Alloys Produced in Large	
Lots	133
Evaluation of Dispersoids — Task I Extension	139
IV CONCLUSIONS — Task I	147
Powder for Alloy Development — Task II	148
Powder Processing	148
V TASK III	149
Introduction	149
Alloy Screening	149
Alloy Formulation	149
Experimental	154
Results and Discussions	157
Detailed Evaluations of Selected Alloys	236
Experimental	236
Results and Discussion	241
CONCLUSIONS — Task III	263
REFERENCES	264

LIST OF ILLUSTRATIONS

<i>Figure</i>		<i>Page</i>
1	Program Schedule for Tasks I, II, and III	4
2	Extended Program Schedule for Tasks I and II	5
3	The P&W AGT 400000 Rapid Solidification Rate Powder Rig	6
4	Predicted Mean Cooling Rates Versus Particle Size for the P&W Rapid Solidification Powder Rig	7
5	Fe-Mn-Al Ternary Diagram at 1400°F	7
6	One-Hundred-Hour Specific Creep Strength of Fe-Al Alloys and Commercial Alloys	8
7	Detailed Plan for Task III	10
8	Particle Size Distribution of the Fe ₃ Al and Fe ₃ Al + TiB ₂ Alloys Produced for Task 1	14
9	SEM of the Surface of -15 μ Fe ₃ Al + TiB ₂ Powder (Alloy 724)	15
10	SEM of the Surface of -30 + μm Fe ₃ Al + TiB ₂ Powder (Alloy 724) ..	16
11	SEM of the Surface of -65 +60 μm Fe ₃ Al + TiB ₂ Powder (Alloy 724)	17
12	SEM of the Surface of -150 +125 μm Fe ₃ Al + TiB ₂ Powder (Alloy 724)	18
13	SEM of the Surface of -15 μm Fe ₃ Al Powder (Alloy 729)	19
14	SEM of the Surface of -30 +20μ Fe ₃ Al Powder (Alloy 729)	20
15	SEM of the Surface of -65 +60μ Fe ₃ Al Powder (Alloy 729)	21
16	SEM of the Surface of -150 +5μm Fe ₃ Al Powder (Alloy 729)	22
17	Microstructure of Fe ₃ Al + TiB ₂ (724) Powder Particles — As-Produced	25
18	Microstructure of Fe ₃ Al (729) Powder Particles As-Produced	26
19	SEM of Fine (-270 Mesh) and Coarse (-80 + 100 Mesh) Fe ₃ Al + TiB ₂ Alloy Powder	28
20	SEM of Fine (-270 Mesh) and Coarse (-80 + 100 Mesh) Fe ₃ Al + TiB ₂ Alloy Powder	29
21	Solidification Structure and Particle Entrapment/Porosity in Fe ₃ Al + TiB ₂ Powder	30

LIST OF ILLUSTRATIONS (Continued)

Figure		Page
22	Microstructure of Fine (-270 Mesh) and Coarse (-80 + 100 Mesh) Fe ₃ Al + TiB ₂ Powder	31
23	Microstructure of Fine (-270 Mesh) and Coarse (-80 +100 Mesh) Fe ₃ Al + TiB ₂ Powder	32
24	Microstructure of Fine and Coarse Fe ₃ Al + TiB ₂ Powder Particles Randomly Selected	33
25	Alloy 729 (Fe ₃ Al) — HVC 1700°F/30 ksi -140 +200 Mesh Powder	36
26	Alloy 729 (Fe ₃ Al) — HIP 2000°F (1093°C) — Roll 2100°F (1149°C) Kalling's Etch	37
27	Development of Fiber Structure in Fe ₃ Al HIP at 2000°F and Rolled at 2100°F	38
28	Alloy 729 (Fe ₃ Al) — HIP at 2000°F -140 +200 Mesh Powder	39
29	Alloy 729 (Fe ₃ Al) — HIP 2000°F (1093°C) — Roll 2100°F (1149°C) Kalling's Etch	40
30	Alloy 729 (Fe ₃ Al) — HIP 2000°F (1093°C) — Roll 2100°F (1149°C) to 50% — Roll 1150°F (621°C) to 95% Total	41
31	Bend Samples Employed to Evaluate the Effect of Heat Treatment on Ductility of Fe ₃ Al Rolled Strip	44
32	Fracture Surface of Rolled FE ₃ Al (729) Alloy Bend Samples	45
33	TEM of Fe ₃ Al (729) Alloy Consolidated, Post Worked and Annealed at 1200°F (649°C) — Polygonized Area, Partially Recrystallized	46
34	TEM of Fe ₃ Al (729) Alloy Consolidated, Post Worked, and Annealed at 1200°F (649°C) — Recrystallized and Polygonized Area Showing Abnormal Grain Growth	47
35	Microstructure of Extruded and Swaged Fe ₃ Al+1 9% TiB ₂ (723) Alloy	48
36	Microstructure of Extruded and Swaged Fe ₃ Al+1 9% TiB ₂ (545) Alloy	50
37	Microstructure of Extruded and Swaged Fe ₃ Al+3 82TiB ₂ (549) Alloy	51
38	Alloy 723 (Fe ₃ Al + TiB ₂) — HVC 1700°F/30 ksi — Ion/Mill 5 deg -140 +200 Mesh Powder	52

LIST OF ILLUSTRATIONS (Continued)

Figure		Page
39	Alloy 723 (Fe_3Al - TiB_2) — HVC 2000°F (1093°C)/30 ksi — Ion Beam Mill -140 +200 Mesh Powder	53
40	Microstructure of Extruded Fe_3Al + TiB_2 Powder Extruded 4 to 1 at 1700°F (927°C)	54
41	Alloy 545 (Fe_3Al + TiB_2) Extruded and Swaged Microstructures	55
42	Fe_3Al + TiB_2 Extruded 10 to 1 at 1700°F (927°C) and Rolled 90% at 1700°F (927°C)	56
43	Bend Samples Employed to Evaluate the Effect on Heat Treatment on Ductility of Fe_3Al + TiB_2 (Alloy 545) Rolled Strip	57
44	Alloy 545 — Extruded 8 to 1 at 1700°F (927°C) — Rolled 90% at 1700°F (927°C) and Heat Treated	58
45	Extrusion Can	61
46	Schematic of Hot Dynamic Outgasser	62
47	Fe_3Al + TiB_2 Alloy Rolled 66% in Light Passes at 1500°F Showing Abnormal Grain Growth After 2-Hour Heat Treatment at 1800°F	65
48	Fe_3Al + TiB_2 Alloy Rolled 66% in Heavy Passes at 1750°F Showing Resistance to Abnormal Grain Growth After 2-Hour Heat Treatment at 2200°F	66
49	TEM of Sample R-82 (Fe_3Al + TiB_2) Extruded 8 to 1 at 1650°F and Swaged 75% at 1300°F Fine (-270 Mesh) Powder	68
50	TEM of Sample R-80 (Fe_3Al + TiB_2) Extruded 8 to 1 at 1650°F and Swaged 75% at 1600°F Fine (-270 Mesh) Powder	69
51	TEM of Sample R79 (Fe_3Al + TiB_2) Extruded 8 to 1 at 1650°F and Swaged 75% at 1600°F Coarse (-80 +100 Mesh) Powder	70
52	TEM of Sample R69 (Fe_3Al + TiB_2) Extruded 8 to 1 at 1700°F and Swaged 75% at 2000°F Coarse (-80 Mesh Powder)	71
53	TEM of Fe_3Al + TiB_2 Extruded 8 to 1 at 1650°F -80 + 100 Mesh Powder — Three General Areas A, B, and C	73
54	TEM of Fe_3Al + TiB_2 Extruded 8 to 1 at 1650°F and Swaged 75% at 1300°F (-270 Mesh Powder) — Four General Areas A, B, C, and D ..	74
55	TEM of Fe_3Al + TiB_2 Extruded 8 to 1 at 1650°F and Swaged 75% at Two Different Temperatures (-80 + 100 Mesh Powder)	75

LIST OF ILLUSTRATIONS (Continued)

Figure		Page
56	TEM of Sample R069 ($\text{Fe}_3\text{Al} + \text{TiB}_2$) Extruded 8 to 1 at 1700°F and Swaged 75% at 2000°F (-80 Mesh) Powder	77
57	TEM of Sample R079 ($\text{Fe}_3\text{Al} + \text{TiB}_2$) Extruded 8 to 1 at 1650°F and Swaged 75% at 1600°F (-80 +100 Mesh) Powder	78
58	TEM of Sample R081 ($\text{Fe}_3\text{Al} + \text{TiB}_2$) Extruded 8 to 1 at 1650°F and Swaged 75% at 1300°F (-80 +100 Mesh) Powder	80
59	TEM of Sample R080 ($\text{Fe}_3\text{Al} + \text{TiB}_2$) Extruded 8 to 1 at 1650°F and Swaged 75% at 1600°F (-270 Mesh) Powder	81
60	TEM of Sample R082 ($\text{Fe}_3\text{Al} + \text{TiB}_2$) Extruded 8 to 1 at 1650°F and Swaged 75% at 1300°F (-80 +100 Mesh) Powder	82
61	TEM of Sample R082 ($\text{Fe}_3\text{Al} + \text{TiB}_2$) Extruded 8 to 1 at 1650°F and Swaged 75% at 1300°F (-80 +100 Mesh) Powder	83
62	Microstructure of Fe_3Al (A- as Extruded 7.4 to 1 at 1700°F; B- as Rolled 68% at 1150°F)	84
63	Fe_3Al from (-80 Mesh) Powder (A- as Extruded 8 to 1; B- as Rolled 73% at 1150°F)	85
64	$\text{Fe}_3\text{Al} + \text{TiB}_2$ from Fine (-270 Mesh) Powder, A- as Extruded 8 to 1 at 1700°F and B- as Rolled 73% at 1500°F	87
65	$\text{Fe}_3\text{Al} + \text{TiB}_2$ from Fine (-270 Mesh) Powder a. Extruded 8:1 at 1700°F b. Rolled 65% at 1500°F	88
66	$\text{Fe}_3\text{Al} + \text{TiB}_2$ from Coarse (-80 40 Mesh) Powder, A- as Extruded 8 to 1 at 1700°F and B- as Rolled 69% at 1500°F	89
67	TEM of $\text{Fe}_3\text{Al} + \text{TiB}_2$ (Alloy 545) Extruded 8 to 1 at 1700°F (927°C) Showing Elongated Grains and the Distribution of TiB_2 Inherited from the Original Solidification Structure	91
68	TEM of $\text{Fe}_3\text{Al} + \text{TiB}_2$ (Alloy 545) Extruded 8 to 1 at 1700°F (927°C) Showing the Distribution of TiB_2 in Prior Dendrite Arms	92
69	(110) and (200) Pole Figures of Extruded Alloy $\text{Fe}_3\text{Al} + \text{TiB}_2$ (RSR 545) Showing Strong <110> Fiber Textures	93
70	(110) Pole Figures for Different Thermomechanical Processing Sequences for Alloy 729 (Fe_3Al)	95
71	(110) Pole Figures from Different Thermomechanical Processing Sequences for $\text{Fe}_3\text{Al} + \text{TiB}_2$ (Alloy 723)	96

LIST OF ILLUSTRATIONS (Continued)

Figure		Page
72	(110) Pole Figure of $\text{Fe}_3\text{Al} + \text{TiB}_2$ (Alloy 545) Rolled at 1700°F (927°C) Showing Ductile at Bend Test Behavior	97
73	Bright Field TEM of Alloy 729 (Fe_3Al) Rolled and Annealed at 1150°F (621°C) for 1 Hour, Showing Extensive Polygonization Networks	98
74	Bright Field TEM of Alloy 729 (Fe_3Al) Rolled and Annealed at 1150°F (621°C) for 1 Hour, Showing Nucleation of New Strain Free Grains Within the Deformed Matrix	99
75	Dark Field TEM of Rolled and Annealed 545 Alloy ($\text{Fe}_3\text{Al} + \text{TiB}_2$) Showing the General Grain Elongation and Subgrain Polygonization Within the Grain	101
76	TEM Alloy 545 ($\text{Fe}_3\text{Al} + \text{TiB}_2$) Showing the Distribution of $\sim 200\text{\AA}$ Diameter TiB_2 and Their Relationship to Polygonized Subgrain Boundaries	102
77	(110) Pole Figures of Extruded and Swaged $\text{Fe}_3\text{Al} + \text{TiB}_2$	104
78	(110) Pole Figures of Extruded, Swaged, and Annealed $\text{Fe}_3\text{Al} + \text{TiB}_2$..	105
79	<110> Pole Figure Resulting from the Extrusion of Fe_3Al to a Rectangular Cross Section	106
80	<110> Pole Figure Resulting from the Warm Rolling of Fe_3Al Which Had Been Extruded to a Rectangular Cross Section	107
81	<110> Pole Figure of As-Extruded $\text{Fe}_3\text{Al} + \text{TiB}_2$ Produced from Fine (-270 Mesh) Powder	107
82	<110> Pole Figure of As-Extruded $\text{Fe}_3\text{Al} + \text{TiB}_2$ Produced from Coarse (-80 +140 Mesh) Powder	108
83	<110> Pole Figure of Rolled $\text{Fe}_3\text{Al} + \text{TiB}_2$ Produced from Fine (-270 Mesh) Powder	108
84	<110> Pole Figure of Rolled $\text{Fe}_3\text{Al} + \text{TiB}_2$ Produced from Coarse (-80 +140 Mesh) Powder	109
85	Microstructure of Fe_3Al (729) Alloy Extruded and Swaged	111
86	Tensile Properties of Alloy 729 (Fe_3Al) HIP at 2200°F (1093°C)	112
87	Tensile Properties of Alloy 729 (Fe_3Al) Extruded 4 to 1 at 1700°F (927°C)	113
88	Tensile Properties of Alloy 723 ($\text{Fe}_3\text{Al} + \text{TiB}_2$) Extruded 4 to 1 at 1700°F (927°C)	114

LIST OF ILLUSTRATIONS (Continued)

Figure		Page
89	Effect of Particle Size and Working Temperature on the 1800°F Tensile Strength of $\text{Fe}_3\text{Al} + \text{TiB}_2$	119
90	Effect of Particle Size on Yield Strength of $\text{Fe}_3\text{Al} + \text{TiB}_2$ at Different Test Temperatures	119
91	Effect of Swaging Temperature on 1800°F Stress Rupture Strength of $\text{Fe}_3\text{Al} + \text{TiB}_2$	121
92	Stress Rupture Samples Tested at 1800°F (982°C)	122
93	Stress Rupture Samples Tested at 1800°F (982°C)	123
94	Yield Strength Versus Temperature for Extruded and Rolled Fe_3Al With and Without TiB_2	127
95	Tensile Strength Versus Temperature for Extruded and Rolled Fe_3Al With and Without TiB_2	128
96	Elongation Versus Temperature for Extruded and Rolled Fe_3Al With and Without TiB_2	129
97	Reduction of Area Versus Temperature for Extruded and Rolled Fe_3Al With and Without TiB_2	130
98	Stress Rupture Samples of $\text{Fe}_3\text{Al} + \text{TiB}_2$ Produced from Fine (A) and Coarse (B) Powder and Tested at 1800°F	134
99	Stress Rupture in 100 Hours for Fe_3Al and $\text{Fe}_3\text{Al} + \text{TiB}_2$ Provided from a Large Rolled Extrusion	135
100	Typical Fracture Surface of the Fe_3Al and $\text{Fe}_3\text{Al} + \text{TiB}_2$ Alloys	136
101	Cross Sections of Fracture Toughness Samples Produced from Extruded and Rolled Material Longitudinal Fractures	137
102	Fracture Surface of Fe_3Al Alloy	138
103	Fracture Surface of $\text{Fe}_3\text{Al} + \text{TiB}_2$ Alloy	139
104	Dynamic Modulus vs. Temperature	142
105	(110) Pole Figure for Extruded Fe-Al-TiB ₂ Alloy	143
106	(110) Pole Figure for Extruded Fe-Al-Cr-Mo-TiB ₂ Alloy	144
107	(110) Pole Figure for Extruded and Swaged Fe-Al-Mo-TiB ₂ Alloy	145

LIST OF ILLUSTRATIONS (Continued)

Figure		Page
108	Fe-Mn-Al Ternary Diagram at 760°C. (Schmatz, 1959). The Approximate Position of the Base Alloy (Alloy 103) Is Indicated by the Filled Circle in the Austenite Phase Field	150
109	Compositional Dependence of As-Quenched Structure of Fe-Mn-Al-2.0C Alloys Formed by Rapid Quenching (Melt Spinning) Technique. After Inoue et al, 1981 (Ref. 3)	153
110	Fe-Ni-Al Ternary System at 950°C. After Bradley, 1949*. Positions of Alloys in the Present Studies Are Shaded, Assuming Interchangeability of Ni and Mn in These Types of Alloys. γ -fcc, γ -Ni ₃ Al β -bcc, β -FeAl, NiAl	154
111	Isothermal Section of the Fe-Ni-Ti System at 700°C. After Speich, 1963**. The Positions of Some of the Alloys Selected for the Present Studies Are Indicated by Dots	155
112	Hardness of Alloys 103 Through 106 vs Aging Temperature. Specimens Aged for 16 Hours at the Indicated Temperatures. a. Alloys Rolled at 593°C, b. Alloys Rolled at 1150°C	159
113	Hardness of Alloys 107 Through 111 vs Aging Temperature. Specimens Aged for 16 Hours at the Indicated Temperatures. (a) — Alloys Rolled at 593°C, (b) — Alloys Rolled at 1050°C	160
114	Microstructure of Alloy 106 (a) After Rolling at 593°C and After Aging for 16 Hours at (b) 593°C (c) 649°C (d) 704°C	162
115	Microstructure of Alloy 110 (a) After Rolling at 593°C and After Aging for 16 Hours at (b) 593°C (c) 649°C (d) 704°C	163
116	Microstructure of Alloy 104 After Rolling at 593°C and Aging for 16 Hours at 704°C (a) Optical Micrograph Showing No Evidence of Recrystallization, (b) Secondary Electron Micrograph Illustrating the Morphology and Distribution of the Precipitates, (c) Transmission Electron Micrograph Showing High Dislocation Density in the Warm-Rolled Alloy	164
117	Microstructure of Alloy 110 (a) After Rolling at 1150°C. After Solution Heat Treatment at 1120°C for 1 Hour Followed by an Oil Quench and Aged for 16 Hours at (b) 593°C (c) 649°C (d) 704°C	165
118	Secondary Electron Micrographs Illustrating the Relative Quantity of Precipitates Formed in Alloy 111. (a) After 593°C Rolling (b) After 1150°C Rolling. The Alloy Was Aged at 649°C for 16 Hours After Rolling in Both Cases	166

LIST OF ILLUSTRATIONS (Continued)

Figure		Page
119	Microstructure of Alloy 106 (a) After Rolling at 1150°C. After Solution Heat Treatment at 1120°C for 1 Hour Followed by an Oil Quench and Aged for 16 Hours at (b) 593°C (c) 649°C (d) 704°C	167
120	Transmission Electron Micrographs Illustrating the Major Precipitates in Alloy 111 After Warm Rolling and Aging Treatment at 650°C for 16 hours. (a) Bright Field (b) Dark Field	168
121	Part of 1000°C Ternary Isothermal Section of Mn-Fe-Al System (Chakrabarti, 1977). Within the bcc Phase Field, Alloys Showing CsCl-Type Superlattice Lines Are Indicated By Filled Circles (•), and Disordered Alloys by Open Circles (O). The Approximate Position of the Base Alloy (103) Is Indicated by the (X) in the Austenite Phase Field	172
122	Fe-Ni-Al Ternary System at 950°C (Bradley, 1949). The Approximate Compositions of Alloys 107 Through 111, Assuming Mn Behaves Like Ni, Is Indicated by the Filled Circle in the (γ + β) Phase Field. β = bcc, γ = fcc, γ' = Ni ₃ Al, β' = FeAl, NiAl	173
123	Creep Behavior of Alloys 103 Through 106 in Warm-Rolled, 650°C/16 Hours Aged Condition at 650°C and 293 MPa	174
124	Creep Behavior of Alloys 107 Through 111 in Warm-Rolled, 650°C/16 Hours Aged Condition at 650°C and 293 MPa	174
125	Creep Behavior of Alloys 107 Through 111 in Hot-Rolled, Solution Heat Treated (1038°C/1hr/OQ) and Aged (650°C/16 Hours) Condition at 650°C and 293 MPa	175
126	Duplex Phase Microstructures of Powder Compacts of (A) Alloy 67, and (B) Alloy 68 Consolidated by Vacuum Hot Pressing at 1040°C, 3 ksi for 0.5 Hour	176
127	Microstructure of Alloy 140 After Heat Treatments of 1040°C/1h/OQ and 650°C/16h/AC. Note the Inhomogeneous Grain Structure in This Material	178
128	Detailed Microstructures of Alloy 140 With Heat Treatments Described in the Preceding Illustrating (a) Densely Populated Fine Coherent Precipitate in Recrystallized Grains (b) Coarser Particles in Grains Undergoing Recovery and Recrystallization	179
129	Microstructure of Alloy 140 After Aging at 705°C for 75 Hours Illustrating the Presence of a New Phase, A. With a Plate Morphology and Equiaxed Particles, B. The Latter Are Present Also at a Lower Aging Temperature. The Fine Coherent Precipitate Which Forms at a Lower Aging Temperature Can No Longer be Observed (See 128)	180

LIST OF ILLUSTRATIONS (Continued)

Figure		Page
130	Creep Behavior of Alloy 140 at 650°C and 293 MPa After Various Aging Heat Treatments Indicated. Solution Heat Treatment 1040°C/1h/OQ	181
131	Grain Structure in Alloy 97 Ingot	182
132	Transmission Electron Micrograph of Alloy 97 Ingot Showing the Ordered γ Phase. The White Rectangular Pattern Was Believed To Be the Boundaries of Ordered Domains (Ref. 3)	183
133	Selected Area Diffraction Patterns of Alloy 97 Ingot With Zone Axes (a) [001], (b) [011], (c) [112], and (d) [013]	184
134	Unit Cell of T_3BC	185
135	Phase Fields of Some Ternary T_3AlC_x Compounds	185
136	Isothermal Section Through the Fe-Al-C Phase Diagram at 1000°C. After Morral, 1934***. The Positions of Alloys Which Have the Same Al and C Contents as Alloys 97 and 103 Are Indicated by the Filled Circles 1 and 2, Respectively. α Ferrite, γ Austenite, ϵ = Perovskite ...	186
137	Microstructure of Alloy 97 RSR Powder (a) Optical Micrograph Showing the Usual Dendritic Structure, (b) Transmission Electron Micrograph Illustrating That the RSR Powder Particle Is Essentially a Single Phase Solid Solution	187
138	Microstructures of (a) Alloy 97 (b) Alloy 101 and (c) Alloy 102 After Hot Isostatic Consolidation at 1040°C and 100 MPa. Cracks Are Present in All the Powder Compacts in the As-Consolidated Condition	188
139	Transmission Electron Micrographs of Consolidated Powder Alloy 97 (a) Elongated $L1_2$ -Type Ordered Precipitates in a Matrix With Modulating Contrast, (b) Modulating Structure Shown in a High Magnification, (c) Modulating Structure Imaged Using a Superlattice Reflection	189
140	Creep Behavior of Alloy 97 in As-Cast Condition at 650°C and 290 MPa	191
141	Electron Micrographs of Alloys 97 After a Solution Treatment at 1150°C (2100°F) for 5 Minutes Followed by Quenching in Oil. (a) Bright Field (b) Dark Field Using a Superlattice Reflection (c) Selected Area Diffraction Pattern, $\langle 001 \rangle$ Zone Axis	194

LIST OF ILLUSTRATIONS (Continued)

Figure		Page
142	Optical Micrographs of Alloy 97 After a Solution Treatment at 1150°C (2100°F) for 5 Minutes Followed by Quenching in Oil and Aging at (a) 650°C for 24 Hours (b) 760°C for 8 Hours (c) Illustrates the Grain Boundary Microstructure Resulting from Heat Treatments in (a) and (b)	195
143	Electron Micrograph of the Lamellar Structure at Grain Boundary Regions in Alloy 97. The Dark and Light Phases Were Identified, Using Microelectron Diffraction Techniques, as Perovskite Carbide and Ferrite, Respectively	196
144	Secondary Electron Micrographs of Alloy 97 Illustrating the Modulated Phase Structures Resulting from Isothermal Aging Treatments at (a) 650°C for 24 Hours (b) 760°C for 8 Hours	197
145	Micrographs of Alloy 97 After the 650°C/24 Hour Aging Treatment Illustrating the Modulated Phase Structure in Greater Detail (a) Secondary Electron Image Showing Square and Rectangular Cross Sections of the Perovskite Particles (b) Dark Field Transmission Electron Micrography Imaged With a Superlattice Reflection. The Perovskite Carbide Particles Are Aligned Along <001> Directions	198
146	Optical Micrograph of Alloy 97 After a Furnace-Cool Heat Treatment from 1040°C to 815°C at an Average Rate of 2.5°C per Minute	200
147	Optical Micrographs of Alloy 97 After the Furnace-Cool Treatment Described in the Preceding Figure with Additional Exposure at 650°C for 50 Hours. Note the Presence of Lamellar Colonies at Grain Boundary Regions Which Were Produced During the 650°C Exposure .	201
148	Microstructures of Alloy 154 After Solution Treatment of 1040°C/1h/OQ (a), Reheated to 1040°C and Furnace Cooled to 815°C at an Average Rate of 2.5°C per Minute (b) (c) Detailed Microstructure Resulting from Heat Treatment (b) Illustrating the Blocky Perovskite Carbide at Grain Boundary Regions and Coarsening of the Modulated Structure in Certain Regions Within the Grains	202
149	Transmission Electron Micrographs of Alloy 154 After the Furnace Cool-Heat Treatment Described in the Preceding Figure Illustrating (a) the Very Fine Modulated Structure Produced in the Grains (b) Coarsened Modulated Structure in Certain Regions of the Grains Shown in the Preceding Figure	203
150	Microstructure of the Furnace-Cooled Alloy 154 After Additional Exposure at 650°C for 100 Hours. The Apparent Discontinuous Precipitation at Grain Boundary Regions Shown in (a) and (b) Is in Fact Coarsening of Perovskite Carbide Particles. (c) Illustrates the Blocky Perovskite Carbide at Grain Boundaries and Extensive Coarsening of the Modulated Structure	204

LIST OF ILLUSTRATIONS (Continued)

<i>Figure</i>		<i>Page</i>
151	Microstructures of Alloy 155 After (a) "Solution" Treatment of 1040°C/1h/OQ (b) Solution Treatment of 1095°C/1h/OQ	205
152	Microstructure of Alloy 155 After Heat Treatment at 1095°C for 1 Hour Followed by Cooling to 815°C at an Average Rate of About 2.5°C Per Minute. Note the Rapid Coarsening of the Modulated Structure During the Slow Cooling from 1095°C	206
153	Transmission Electron Micrograph Illustrating the Modulated Structure in Alloy 155 After the Slow-Cool Heat Treatment Described in the Preceding Figure	207
154	Microduplex Structure Consisting of Perovskite Particles and Austenite Grains Observed in Alloy 142 After Heat Treatment at 1040°C for 10 Minutes Followed by Cooling to 815°C at an Average Rate of 2.5°C Per Minute	210
155	Creep Behavior of Alloy 97 at 650°C and 293 MPa After Various Aging Heat Treatments Indicated. Solution Heat Treatment 1150°C/5 min/OQ	211
156	Creep Behavior of Alloy 141 at 650°C and 293 MPa After Various Aging Heat Treatments Indicated. Solution Heat Treatment 1040°C/1h/OQ	211
157	Creep Curves of Alloys 97, 142, 145, 146 and 154 at 650°C and 293 MPa Illustrating the Effect of Mn on Creep Resistance	212
158	Creep Curves of Alloys 97 and 144 at 650°C and 293 MPa Illustrating the Effect of Two Different Combinations of Al and C Contents on Creep Resistance	212
159	Creep Curves of Alloys 141, 144, 154 and 155 at 650°C and 293 MPa Illustrating the Affects of Co and Refractory Metals Additions on Creep Resistance	213
160	Hardness and Room Temperature Bend Ductility of Alloy 97 After Various Heat Treatments	213
161	Fracture Features of Alloy 97 in a Room Temperature Bend Test. Heat Treatment: 1150°C/5 min/OQ+ 650°C/24h/AC	214
162	Fracture Features of Alloy 154 in a Room Temperature Bend Test. Heat Treatment: (a) 1040°C/10 min/Cooled to 815°C at a Rate of 2.5°C/min Followed by Cooling to Room Temperature in Air (b) Heat Treatment as in (a) Plus Isothermal Aging at 650°C for 100 Hours	215

LIST OF ILLUSTRATIONS (Continued)

Figure		Page
163	Fracture Surface Features of Alloy 142 in a Room Temperature Bend Test. Heat Treatment: 1040 C/10 min/Cooled to 815°C at a Rate of 2.5°C/min Followed by Cooling to Room Temperature in Air	216
164	0.2% Yield Strengths of Alloys 142, 154, and 155 and the Iron-Base Superalloy A286	216
165(a)	Optical Micrographs of Alloys in the Third Series After a Solution Treatment of 1095°C for 30 min Followed by Furnace Cooling to 815°C a. Base Composition (Alloy 168)	218
165(b)	Optical Micrographs of Alloys in the Third Series After a Solution Treatment of 1095°C for 30 min Followed by Furnace Cooling to 815°C, b. Base + 0.5 wt% Ti (Alloy 156) c. Base + 0.5 wt% Zr (Alloy 157) d. Base + 0.5 wt% Hf (Alloy 158) e. Base + 0.5 wt% V (Alloy 159)	219
165(c)	Optical Micrographs of Alloys in the First Series After a Solution Treatment of 1095°C for 30 min Followed by Furnace Cooling to 815°C f. Base + 0.5 wt% Cr (Alloy 160) g. Base + 0.5 wt% Mo (Alloy 161) h. Base + 0.5 wt% W (Alloy 162) i. Base + 1.5 wt% Co (Alloy 163)	220
165(d)	Optical Micrographs of Alloys in the First Series After a Solution Treatment of 1095°C for 30 min Followed by Furnace Cooling to 815°C j. Base + 1.5 wt% Ni (Alloy 164) k. Base + 1.5 wt% Cu (Alloy 165) l. Base + 0.5 wt% Si (Alloy 166) m. Base + 0.5 wt% Mo + 0.02 wt% β (Alloy 167)	221
166	Transmission Electron Micrograph of Alloy 159 After the Furnace Cool Heat Treatment Described in the Preceding Figure Illustrating the Precipitation of Very Fine Perovskite Carbide Particles in the Matrix (a), the Equiaxed Shaped Primary Perovskite Carbide Particles (b), and the Vanadium-Rich Particles (c)	222
167	Creep Curves of Alloys 155 (1 wt% Mo + 0.5 wt% W), 161 (0.5 wt% Mo), 162 (0.5 wt% W), 167 (0.5 wt% + 0.2 wt% β) and 168 (Base) at 650°C and 293 MPa	224
168	Creep Curves of Alloys 156 (1.5 wt% Co), 164 (1.5 wt% Ni) 165 (1.5 wt% Cu) and 168 (Base) at 650°C and 293 MPa	224
169	Creep Curves of Alloys 156 (0.5 wt% Ti), 157 (0.5 wt% Zr), 158 (0.5 wt% Hf), 159 (0.5 wt% V), 160 (0.5 wt% Cr), 161 (0.5 wt% Mo), and 166 (0.5 wt% Si and 168 (Base)) at 650°C and 293 MPa	225

LIST OF ILLUSTRATIONS (Continued)

Figure		Page
170	Optical Micrographs of Selected Alloys in the Fe-Ni/Mn-Ti Alloy Series Illustrating Microstructure Changes When an Increasing Amount of Ni Was Replaced With Mn Alloys Were a Solution Heat Treated at 1040°C for 1 hr Followed by Quenching in Oil and Then Aging at 650°C for 16 hr. a. Alloy 243 (30 a/o Ni) b. Alloy 244 (18.5 a/o Mn+11.5 a/o Ni) c. Alloy 245 (22.5 a/o Mn + 7.5 a/o	227
171	Transmission Electron Micrographs of Alloy 243 After the Heat Treatment Described in the Preceding Figure. These Figures Illustrate the Precipitation of Very Fine L ₁₂ -Type Particles (A) Bright Field ² (B) Dark Field Illuminated by a Superlattice Reflection	228
172	Electron Micrograph of Alloy 245 Illustrating the Absence of L ₁₂ Type Particles in the Matrix and the Formation of More Massive Ti-Rich Particles Distributed Throughout the Alloy	229
173	Micro-micro Electron Diffraction Patterns from the Ti-rich Particles Shown in the Preceding Figure. These and Other Diffraction Patterns Could be Indexed as hcp With Lattice Parameters of a = 4.56Å, c = 7.40Å, (a)(100), (b)(231)	230
174	Creep Curves of Alloys 147, 151, 152, and 153 at 650°C and 293 MPa	231
175	Creep Curves of Alloys 169 (2 a/o Ti) and 170 (4 a/o Ni), at 650°C and 293 MPa	232
176	Creep Curves of Alloys 243 (30 a/o Ni), 246 (45 a/o Ni), and 170 (23 a/o Ni + 37 a/o Mn) at 650°C and 293 MPa	233
177	Creep Curves of Alloys 243 (30 a/o Ni), 244 (11.5 a/o Ni + 18.5 a/o Mn) and 245 (7.5 a/o Ni + 22.5 a/o Mn) at 650°C and 293 MPa	233
178	Creep Curves of Alloys 246 (45 a/o Ni), 247 (17.3 a/o Ni + 27.7 a/o Mn) and 248 (11.25 a/o Ni + 33.75 a/o Mn) at 650°C and 293 MPa .	234
179	Creep Curves of Alloys 244 (0 Cu) and 250 (2 Cu) at 650°C and 293 MPa	234
180	(A) Weight Change Versus Exposure Time in Cyclic Oxidation Between 20 and 760°C in 2-Hour Cycle. (B) Appearance of the Specimens After 250 Hours	235
181	(A) Weight Change Versus Exposure Time in 650°C Sulfidation Tests With a Mixture of 50 Wt% Na ₂ SO ₄ and 50 Wt% NaCl. (B) Appearance of the Specimens After 250 Hours	237
182	(A) Weight Change Versus Exposure Time in 650°C Sulfidation Tests With a Mixture of 75 Wt% Na ₂ SO ₄ and 25 Wt% NaCl. (B) Appearance of the Specimens After 250 Hours	238

LIST OF ILLUSTRATIONS (Continued)

<i>Figure</i>		<i>Page</i>
183	(A) Weight Change Versus Exposure Time in 650°C Sulfidation Tests With a Mixture of 50 Wt% Na ₂ SO ₄ 50 Wt% NaCl. Specimens Protected With Aluminized Coatings. (B) Appearance of the Specimens After 250 Hours	239
184	(A) Weight Change Versus Exposure Time in 650°C Sulfidation Tests With a Mixture of 50 Wt% Na ₂ SO ₄ and 50 Wt% NaCl. Specimens Protected With Chromized Coatings. (B) Appearance of the Specimens After 250 Hours	240
185	Standard Specimen Configurations	242
186	Specimen Configuration for Dynamic Modulus Determinations by the Longitudinal Vibration Method	243
187	Schematic of the Dynamic Modulus Apparatus	243
188	The Relative Dimensions and Appearance of the Extrusion Preform and the Extruded Bar of Alloy 252	244
189	Microstructure of Alloy 252 in the As-extruded Condition	245
190	Microstructure of Alloy 253 in the As-extruded Condition	246
191	Yield Strength and Ultimate Tensile Strength of Alloy 252 and A286 .	248
192	Tensile Fracture of Alloy 252 at 400°F (204°C)	249
193	Tensile Fracture of Alloy 252 at 1300°F (704°C)	250
194	Dislocation Structure in Alloy 252 Resulting from Tensile Deformation at Temperatures Below the Brittle-Ductile Transition	251
195	Dislocation Structure in Alloy 252 Resulting from Tensile Deformation at Temperatures Above the Brittle-Ductile Transition (a) Bright Field Micrograph (b) Dark Field Showing Microtwins in the Same Area as (a)	252
196	(a) General Microstructure of Alloy 252 After Creep Testing at 1200°F (650°C) for 110 hours $g = [020]$. (b) Detailed Appearance of the Fine Perovskite Carbide Particles Showing Presence of Interfacial Dislocations, $g = [020]$	255
197	Dislocations in the Large Perovskite Carbide Particles of Alloy 252 After Creep Testing at 1200°F (650°C) for 110 hours. Arrow Indicates Paired Dislocations, $g = [200]$	256

LIST OF ILLUSTRATIONS (Continued)

<i>Figure</i>		<i>Page</i>
188	Stress vs Number of Cycles to Failure for Alloys 252 and 253 Fatigue Tested at Room Temperature, R=0.1 and 1 Hz. Corresponding Data for an Austenitic Stainless Steel Type 301 Are Also Included for Comparison	257
199	Fatigue Fracture of Alloy 252 of 70F (20C). (a) Sectional View Showing Formation of Cracks in Large Perovskite Carbide Particles at Grain Boundary (b) Appearance of Fracture Surface	258
200	Fatigue Fracture of Alloy 253 at 70F (20C) (a) Sectional View Showing Intergranular Fracture (b) Appearance of Fracture Surface	259
201	Fatigue Crack Growth Rates of Alloys 252 and 253 at Room Temperature, Stress Ratio of 0.1 and Frequency of 1 Hz. Corresponding Data for A286 Are Also Shown for Comparison	260
202	Thermal Expansion Characteristics of Alloys 252 and 253. Corresponding Data for Austenitic Stainless Steels and A286 Are Included for Comparison	262

LIST OF TABLES

<i>Table</i>	<i>Page</i>
1 Occurrence of Phases in Binary and Ternary Transition Elements Systems (Reference 9)	9
2 Lattice Parameter of Iron Aluminide Powders as a Function of Particle Size	27
3 Composition of the $\text{Fe}_3\text{Al} + \text{TiB}_2$ Alloy Produced During This Reporting Period — in Weight Percent	34
4 Consolidation and Working of Fe_3Al Alloys	34
5 Composition of Alloys	49
6 Thermomechanical Processing of $\text{Fe}_3\text{Al} + \text{TiB}_2$	60
7 Large Scale Extrusion at AMAX	63
8 Rolling Conditions Employed for the Large Extrusions of $\text{Fe}_3\text{Al} + \text{TiB}_2$ Alloy	63
9 Temperatures for Abnormal Grain Growth in $\text{Fe}_3\text{Al} + \text{TiB}_2$ Alloys	64
10 $\text{Fe}_3\text{Al} + \text{TiB}_2$ Alloy Samples Examined in TEM With Thinned Foils ..	67
11 Grain Aspect Ratio and TiB_2 Dispersion Size for $\text{Fe}_3\text{Al} + \text{TiB}_2$ Produced With Fine and Coarse Powders	76
12 Grain Size in Fe_3Al and $\text{Fe}_3\text{Al} + \text{TiB}_2$ After Extrusion and Rolling	90
13 Texture Analysis	94
14 Strength of $\langle 110 \rangle$ Fiber Texture (Times Random) Versus Swaging Temperature	103
15 Texture Results	109
16 Tensile Properties of Fe_3Al (729) Alloy	110
17 Tensile Properties of $\text{Fe}_3\text{Al} + \text{TiB}_2$ at Ambient Temperature	116
18 Tensile Properties of $\text{Fe}_3\text{Al} + \text{TiB}_2$ at 500°F (260°C)	116
19 Tensile Properties of $\text{Fe}_3\text{Al} + \text{TiB}_2$ at 1000°F (538°C)	117
20 Tensile Properties of $\text{Fe}_3\text{Al} + \text{TiB}_2$ at 1200°F (649°C)	117
21 Tensile Properties of $\text{Fe}_3\text{Al} + \text{TiB}_2$ at 1800°F (982°C)	118
22 Tensile Properties at Elevated Temperatures	118

LIST OF TABLES (Continued)

Table		Page
23	Stress Rupture Properties of $\text{Fe}_3\text{Al} + \text{TiB}_2$ at 1800°F (932°C) (-270°F Mesh Fine Powder)	120
24	Longitudinal and Transverse Tensile Properties of Fe_3Al Alloy as Rolled at 1150°F (621°C) and Recrystallized at 1350°F (732°C)	125
25	Longitudinal and Transverse Tensile Properties of $\text{Fe}_3\text{Al} + \text{TiB}_2$ Alloy as Rolled at 1500°F (815°C)	126
26	Stress Rupture Properties of Fe_3Al in the Longitudinal (Rolling Direction)	131
27	Stress Rupture Properties of Fe_3Al Produced From Fine and Coarse Powder Tested in the Longitudinal/Rolling Direction	131
28	Stress Rupture Properties of Fe_3Al Produced From Fine and Coarse Powder Tested in the Transverse Direction	132
29	Fracture Toughness Properties of Rolled Fe_3Al	136
30	Fracture Toughness Properties of Rolled $\text{Fe}_3\text{Al} + \text{TiB}_2$ Alloy Produced With Fine and Coarse Powder	136
31	Processing Parameters for Alloy (1)	140
32	Processing Parameters for Alloys (2) and (3)	140
33	Room Temperature Tensile Properties	141
34	Dynamic Elastic Modulus	142
35	Texture Strength (X random)	145
36	Aluminide Powders Produced for AFML	148
37	Alloys For Basic Studies, At.%, (Wt%)	150
38	Promising Alloys of the 1950's and Present Modifications, Wt%	151
39	Nominal Compositions of Alloys (Wt%) Studied in Cyclic Oxidation and Sulfidation Tests	152
40	Compositions of Fe-Mn-Al-C Alloys, At. (Wt%)	152
41	Fe-Mn-Ni-Al Alloys At.% (Wt%)	155
42	Nominal Compositions of Fe-Mn/Ni-Ti/Al Alloys, At.% (Wt%)	156
43	Purity of Raw Materials Used For Melting	156

LIST OF TABLES (Continued)

Table		Page
44	Analyzed Compositions of Cast + Wrought Alloys, Wt%	158
45	Compositions of Matrix and Precipitates by Energy Dispersive Spectroscopy 593C Rolled + 650C/16h Aged	169
46	Structures of Extracted Precipitates From 593C Rolled + 650°C/16h Aged Alloys	170
47	Phases and Structures in Annealed Filings of Hot-Rolled Alloys 103-111*	171
48	Analyzed Compositions of Powder Alloys	171
49	Analyzed Compositions, Wt%	175
50	Analyzed Phase Compositions of Alloy 67, Wt %	177
51	Results of Phase Identification By X-Ray From Filings of Alloy 140 CrK α Radiation	177
52	Analyzed Compositions of Powder Alloys	181
53	X-Ray Diffraction Data of Alloy 97 Ingot Sample Annealed at 1040°C For 4 Hours	184
54	Structural Data of Alloys 101 and 102 Obtained by X-Ray Diffraction Analysis	190
55	Austenite — Perovskite Alloys Nominal Composition (Wt%)	192
56	Analyzed Compositions of Alloys Wt% Austenite-Perovskite Series	192
57	Nominal Compositions of Fe-Mn-Al-C Alloys, Wt%	217
58	Analyzed Compositions of Fe-Mn-Al-C Alloys, Wt%	217
59	X-Ray Analysis From Filings	222
60	Effect of Alloying on Austenite and Perovskite Carbide Latticed Parameters	223
61	Analyzed Compositions of Fe-Ni/Mn-Al Alloys, Wt%	225
62	Analyzed Compositions of Fe-Ni/Mn-Ti Alloys, Wt%	225
63	Results of Phase Identification By X-Ray From Filings of Alloys 147-153, CrK α Radiation	226
64	Analyzed Compositions of Phase III Alloys, Wt%	244

LIST OF TABLES (Continued)

<i>Table</i>		<i>Page</i>
65	Tensile Properties of Phase III Alloys	247
66	Creep Rupture Properties of Phase III Alloys	254
67	One-Hundred-Hour Rupture Strength k_{ai} (MPa)	254
68	Fracture Toughness of Austenite-Perovskite Alloys at Room Temperature	256
69	Physical Data For Calculation of Densities and Elastic Moduli of Alloys 252 and 253	260
70	Dynamic Modulus Data at Room and Elevated Temperatures For Alloys 252 and 253	261
71	Mean Coefficient of Thermal Expansion (70° to temp.) $\times 10^{-6}/^{\circ}\text{F}$	261

SECTION I

INTRODUCTION

This program addressed the development of iron aluminide base alloys by rapid solidification rate (RSR) and the determination of their potential for use in aircraft turbine engines as alternatives to high chromium steels and nickel-base alloys. The program was an initial 36-month effort followed by a 12-month extension divided into three concurrent tasks performed at Pratt & Whitney/Engineering Division-South (P&W/ED-S) and Pratt & Whitney/Engineering Division-North (P&W/ED-N). A fourth task performed at TRW on the development of Fe_3Al alloys was part of a total program aimed at the development of this unique class of alloys.

The potential of these iron aluminides rests on (1) a lower density than iron and nickel-base alloys, (2) excellent oxidation/sulfidation resistance, (3) no critical element requirements, and (4) a lower base cost than currently employed elevated temperature alloys. The overall goals of the program were to investigate and define thermomechanical processing requirements for optimum mechanical properties, and to modify a base composition for improved elevated temperature properties while enhancing or retaining base alloy ductility and processability.

Task I was a 24-month initial effort and a 12-month extension performed at the P&W/ED-S. It was a process and model development task employing Fe_3Al with and without TiB_2 . Under a prior DARPA/AFWAL program (F33615-77-C-5114), TiB_2 had been found to be effective in retaining a fine grain size for improved thermomechanical processing characteristics and mechanical properties. The information generated during this task was to provide a basis for the thermomechanical processing of alloy modifications investigated in Task III and IV of the total program. The extension to Task I evaluated the effects of titanium diboride dispersions on the tensile properties, and especially, the specific modulus of two alloys having aluminum contents significantly greater than that in Fe_3Al .

Task II was a 36-month effort and a 12-month extension performed at P&W/ED-S for the production of Rapid Solidified Iron Base Powders which were delivered to the AFWAL Materials Laboratory.

Task III was a 36-month effort conducted at P&W/ED-N for the development of austenitic iron aluminides for use at temperatures up to about 1200°F (650°C). Alloy compositions based on the Fe-Mn-Al ternary phase diagram were chosen for this study. Although Fe-Mn-Al alloys were investigated about 20 years ago (References 1 and 2), the physical metallurgy of the alloys and the strengthening mechanisms were not studied in any detail. Renewed interest for developing the Fe-Mn-Al as a low-cost alloy to replace 12 wt% Cr steels was inspired by a recent discovery of a nonequilibrium ordered phase with L1_2 -type structure when the alloy is rapidly quenched from the melt (Reference 3). The ordered alloys have high strength and good ductility. Such structures could also be anticipated to give superior creep resistance. Thus, another one of the goals was to gain insight into the effect of alloying additions on precipitation processes in Fe-Mn-Al alloys, and to study the development of ordered phases in the Fe-Mn-Al alloys. Two types of processing were also evaluated during the studies. The physical metallurgy and strengthening mechanisms were investigated using cast and wrought alloys. The formation of ordered phases was studied using powder alloys.

Cast and wrought alloys can be designed to form carbides as the particle dispersion strengthener; some background information was available for this approach. Other potentially useful phases for strengthening include intermetallics and borides; however, basic information of such compounds in the Fe-Mn-Al system was lacking. Therefore, a preliminary microstructural

study was conducted to search for suitable intermetallic phases based on the recent Japanese work. Older German studies also provided additional guidance. To gain basic familiarity with the system, promising alloys studied in the past, which could also serve as useful alloy bases, were examined. Two alloys were formulated from the programs of the 1950's, and are described in Section III of this report.

As stated previously, the major objective of Task III was to identify useful alloys for use at intermediated temperatures. Any alloys must also exhibit adequate corrosion resistance in a gas turbine environment if they are to replace existing alloys. A second goal of this program was to study the oxidation and sulfidation resistance of the Fe-Mn-Al alloys.

This is the final technical report on contract F33616-81-C-5110. It summarizes the work performed during the period 1 September 1981 to 1 February 1986.

SECTION II

PROGRAM PLAN AND SCHEDULE

PROCESS AND MODEL DEVELOPMENT — TASK I

Interest in iron-aluminum alloys was stimulated by the finding that a fine and stable titanium diboride dispersion could be produced by rapid solidification rate (RSR). The TiB_2 dispersion in an Fe_3Al alloy stabilized a fine grain size for increased high temperature strength while it enhanced the ductility of the alloy. As a result, iron aluminides which possess very good oxidation resistance, contain no strategic elements, and are 15% to over 25% lighter than nickel or iron base alloys, may be considered for gas turbine engine applications.

Rapidly solidified powders of iron-aluminum alloys containing titanium and boron consist of dendrites of ferrite with TiB_2 dispersed in interdendritic regions. The diboride particles are very fine (100 to 300 angstroms), but they are segregated to some extent. In comparison, the consolidated and worked powder product contains slightly coarser diboride particles, but the particles appear to be more uniformly distributed (Reference 4). It was proposed that deformation during metalworking tends to randomize the distribution, since deformation occurs by shear, and shear implies mixing. Observations of the TiB_2 dispersion in iron-aluminum alloys suggested that two possible conditions that may be related to the amount of mixing (deformation) are required to randomize the distribution. One is the magnitude of the distance between centers of similar regions, the interdendritic regions. The second is the ratio of the distance between particles in a uniform distribution to the corresponding distance in the original segregated regions. Comparison of powder and consolidated materials produced on the program aimed at verifying these assumptions.

Task I was divided into two subtasks. The first entailed definition of processing variables from the characterization of rapidly solidified powder structures through consolidation and post working to material characterization. The second was concerned with process model development and model verification for achieving optimum microstructure and mechanical properties in mill product forms produced from rapidly solidified iron aluminide powders.

As shown in Figure 1, Task I was completed during CY 1983, and Tasks II and III during CY 1984. An extension to the program covering Tasks I and II was awarded, and the schedule starting 1 February 1985 is shown in Figure 2.

Task I was extended to evaluate the effects of TiB_2 on the microstructure and mechanical properties, especially specific modulus, of two solid solution alloys with aluminum concentrations greater than that in Fe_3Al . Results obtained on this program and on P&W programs revealed that the specific modulus of Fe-Al alloys could be increased from 112 (10)⁶ in. to 129 (10)⁶ in. by increasing the aluminum concentration from 25 at.% to about 32 at.% (13.8 wt% to over 18 wt%). However, the ductility of the alloy decreased with increasing aluminum concentration to about 4 or 5% elongation. Since there is considerable interest in high specific modulus alloys for the shafts of high speed turbine engines, a goal was established to develop an alloy with a specific modulus of at least 140(10)⁶ in. and an elongation of 10%.



Figure 1. Program Schedule for Tasks I, II, and III

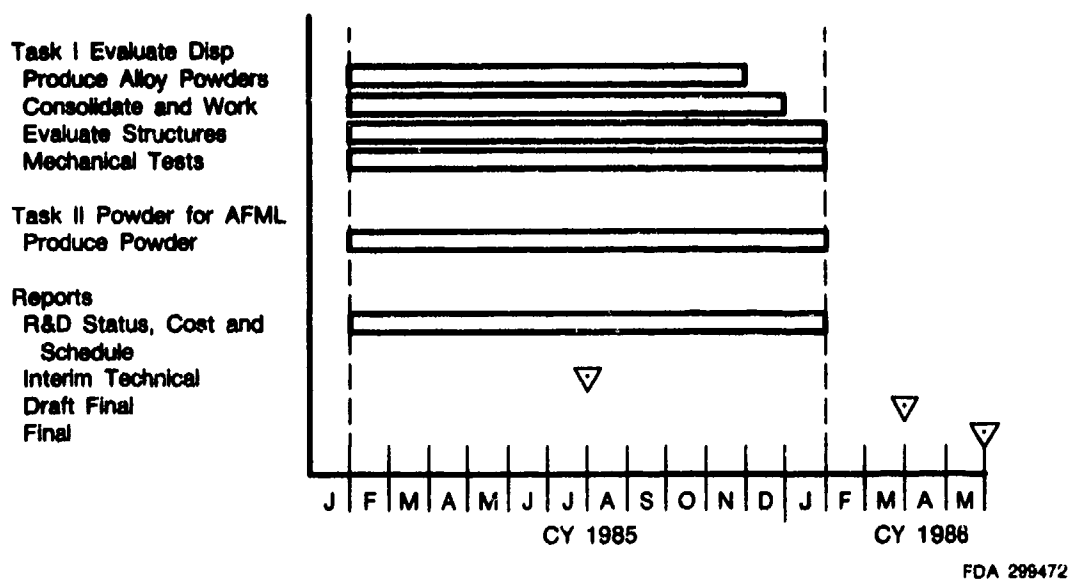


Figure 2. Extended Program Schedule for Tasks I and II

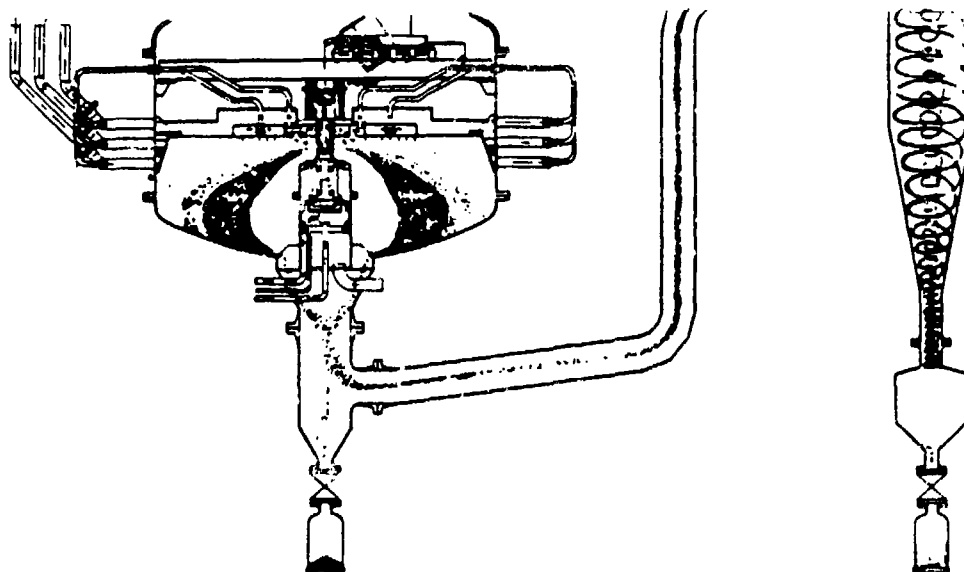
POWDER FOR ALLOY DEVELOPMENT — TASK II

The basic concept of a rapid solidification process to achieve a rapid quench rate in pilot scale quantities of material was conceived at P&W in 1974. The device shown schematically in Figure 3 became operational in early 1976. The process has since been used to investigate a number of alloy systems in several IR&D, DARPA, and AFWAL/ML sponsored programs, and is thoroughly discussed in the interim final report, AFWAL-TR-80-4051, to contract F33615-76-C-5136.

The technique uses rotary atomization to convert an induction melted alloy into high velocity droplets which are quenched to the solid state by cross flowing gas of high thermal conductivity, typically helium. The exact quench rate achieved depends on a number of factors including: (1) gas type, (2) temperature and pressure, (3) thermal properties and temperature of the droplets, (4) and droplet size and velocity. Theoretical mean quench rates calculated for typical processing conditions and for several alloys are shown in Figure 4. Depending on the particle size, range produced, and the quantity needed for study, variations of up to two orders of magnitude in quench rate may be obtained (from about 10^4 to about 10^6 C/sec mean quench rate).

P&W was to produce by its RSR powder process a specified number of alloyed powders for delivery to AFWAL/ML. Individual powder lots were to be screened to -80 mesh size and packaged in a vacuum. The requirements were:

- 25 kg/55 lb minimum of Fe_3Al
- 25 kg/55 lb minimum of FeAl
- 8 kg/18 lb minimum of 12 alloys specified by AFML.



FD 218660

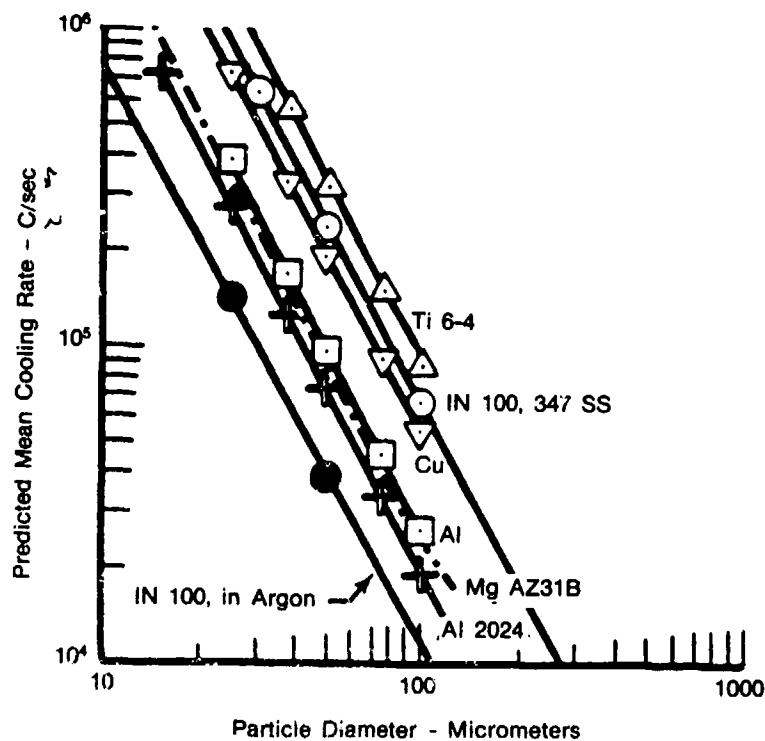
Figure 3. The P&W AGT 400000 Rapid Solidification Rate Powder Rig

An additional six alloys were added for processing during the follow-on 12-month extension.

AUSTENITIC IRON ALUMINIDES — TASK III

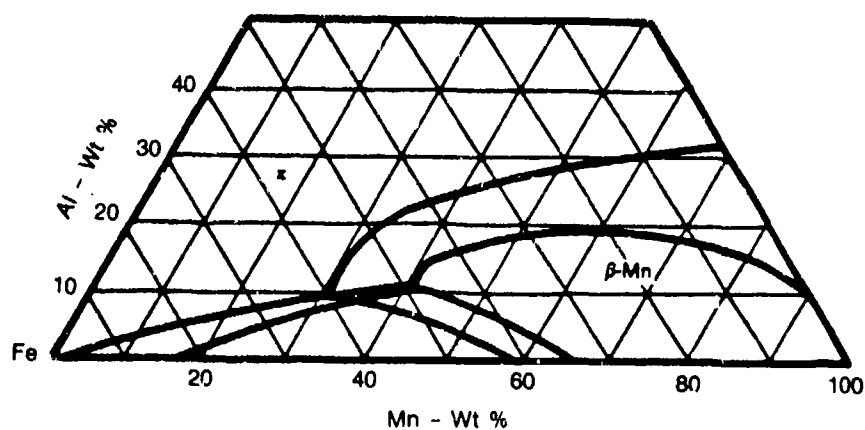
Extensive work (References 1 and 2) in the 1950's and the early 1960's showed that Fe_3Al based alloys had the potential to replace titanium alloys and some stainless steels. However, reservations over the ductility of these ferritic materials at lower temperatures prompted the development of a second alloy series with an austenitic structure. It was shown that the best, and lowest cost system for such a development, was Fe-Mn-Al. For reasons discussed below, the optimum aluminum content was about 7%.

The earlier studies showed that alloys of the basic type Fe-30Mn-7Al had excellent tensile ductility and intermediate strength. It would seem desirable to add more aluminum to the system to improve strength and more importantly creep rupture capability. As shown in Figure 5, this was restricted by the extent of the austenitic phase field in the Fe-Mn-Al system. It seems apparent that it would be advantageous to expand the austenite stability region, and to find alloying additions that produce more desirable bonding phases to those that occur in the ternary system. Alloying additions were evaluated in earlier development programs which improved the creep properties considerably, but as the alloys became more complex, they tended to be more difficult to process. The creep rupture properties of the best alloys, circa 1960, are compared with other materials used in gas turbine engines in Figure 6. It can be seen that creep capability is intermediate between the best 12% Cr steels, for example, H46, and the iron-based superalloy, A286.



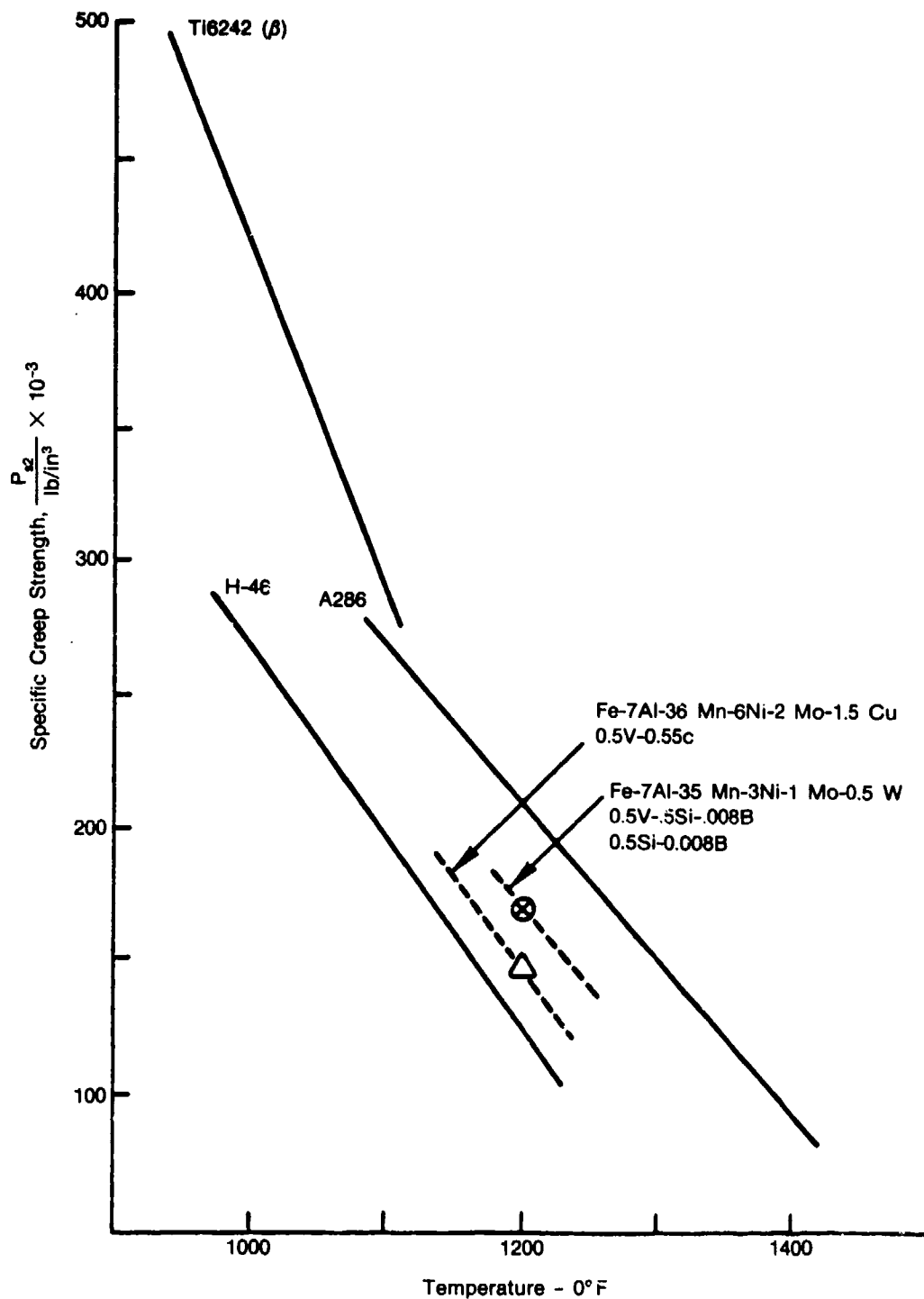
FD 219450

Figure 4. Predicted Mean Cooling Rates Versus Particle Size for the P&W Rapid Solidification Powder Rig



FD 22908

Figure 5. Fe-Mn-Al Ternary Diagram at 1400°F



FD 22909

Figure 6. One-Hundred-Hour Specific Creep Strength of Fe-Al Alloys and Commercial Alloys

Strength and creep capability of the alloys can be improved by several methods; one of which is by increasing the aluminum content which, as mentioned before, can only be tolerated if the extent of the austenite phase field is expanded. One way to accomplish this is by the addition of austenite stabilizing elements. However, Ni, Co, and Cu, which extend the austenite field in the Fe-Cr-C system, surprisingly had little effect on the ferrite/austenite relationship when added to Fe-Mn-Al-C alloys in amounts as high as 10% (References 5 and 6). In view of this result, it appears that a different approach would be more fruitful. Schmatz and Chakrabarti (References 6 and 7) have shown that the austenite field extends slowly to higher Al with increasing temperatures. Thus, it may be possible to obtain a higher Al austenite by rapid solidification techniques. Indeed, a nonequilibrium Ni_3Al type compound has been produced from Fe-Mn-Al-C systems by splat quenching (Reference 8), and such compounds have been produced in compositions of present interest, for example, Fe-35Mn-11Al-2C. These nonequilibrium compounds were found to have high strength and good ductility. The ordered structure should also be beneficial for creep resistance by analog with A286 and other superalloys. Therefore, it appears that rapid solidification, per se, offers the potential of achieving novel microstructures in Fe-Mn-Al alloys with accompanying property benefits.

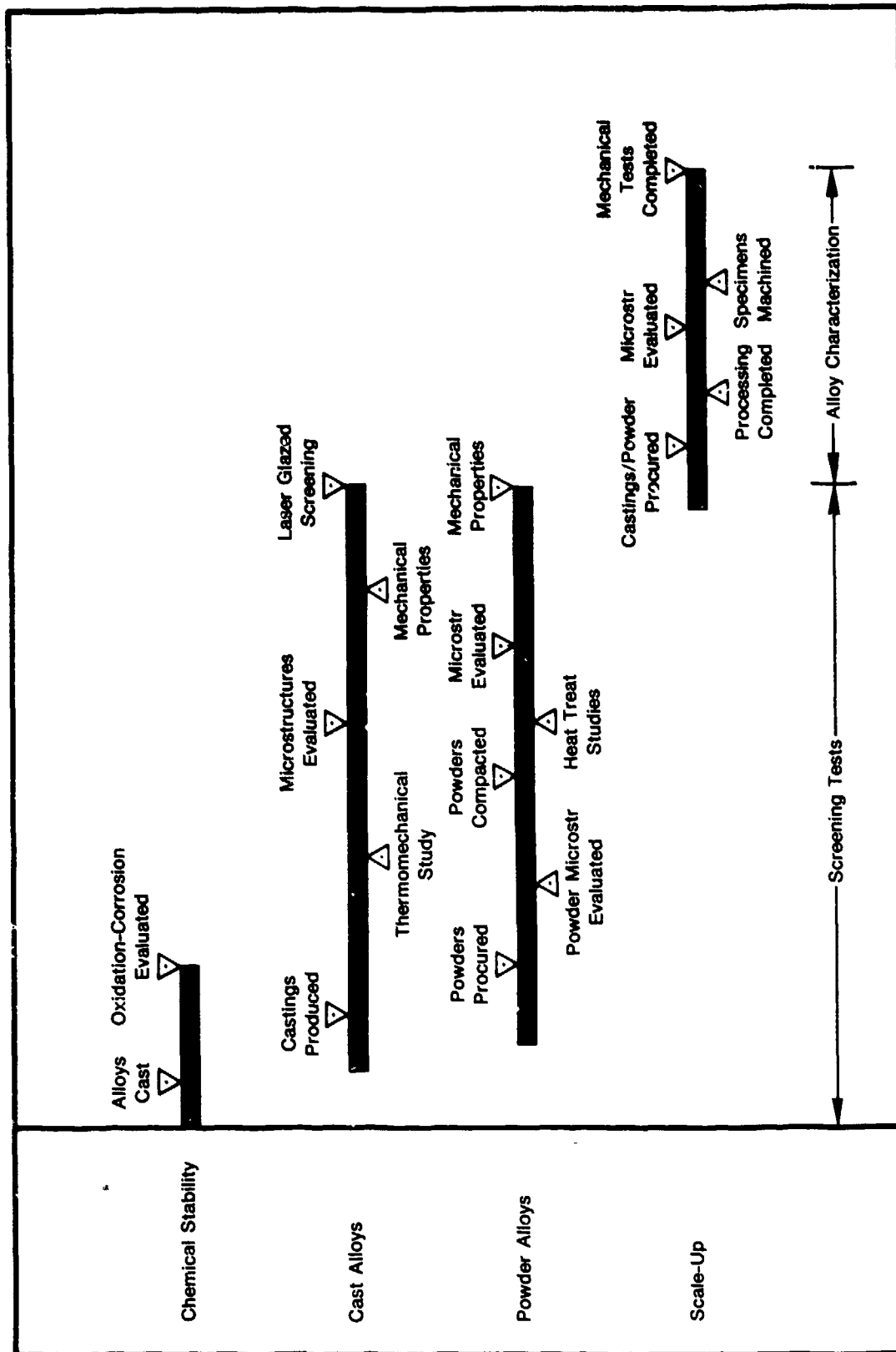
Fe-Mn-Al alloys can also be strengthened, and can be made more creep resistant by precipitation of fine, thermally stable particles. Two types of particles can be considered for the Fe-Mn-Al systems: intermetallics and nonintermetallics, such as carbides, borides, and sulfides. The B_3A compounds with Ll_2 type structures are the most useful intermetallics for strengthening austenitic iron alloys due to the equiaxed morphology, small interparticle spacing, coherency with the lattice and the high ductility of these phases compared with those containing other precipitates (Reference 9). However, no phase of the B_3A type has been found in which the B element is Mn or Fe, Table 1, under equilibrium conditions. The most likely phase to occur in Fe-Mn austenite with a third transition element, such as titanium, is the B_2A Laves phase which has a strong tendency to form continuous precipitates along grain boundaries resulting in embrittlement and little strengthening at high temperatures (Reference 8). It is not known to what extent the presence of 7 to 10 wt% Al changes the type of intermetallics. However, it has been demonstrated that intergranular precipitation of the $\text{Fe}_2(\text{TiMn})$ Laves phase can be avoided by mechanical working prior to aging, to introduce a dense distribution of heterogeneous nucleation sites, and also provide a defect structure to accelerate the diffusion process. The resulting microstructure is a uniform dispersion of fine $\text{Fe}_2(\text{TiMn})$ particles which resisted coarsening at 1500°F (816°C). A rather large enhancement of the mechanical properties was obtained from the thermomechanically processed Fe-Mn austenite (Reference 1). Therefore, additions of transition elements to the Fe-Mn-Al system, together with thermomechanical treatment, is another potential method for improving the strength and creep resistance of Fe-Mn-Al alloys.

TABLE 1. OCCURRENCE OF PHASES IN BINARY AND TERNARY TRANSITION ELEMENTS SYSTEMS (REFERENCE 9)

B Transition Element	A Element							
	Group IV			Group V			Group VI	
	Ti	Zr	Hf	V	Nb	Ta	Cr	Mo
Mn	B_2A	B_2A	B_2A		B_2A	B_2A		
Fe	B_2A BA	B_2A	B_2A	BA	B_2A	B_2A		B_2A

2711C

As shown in Figure 7, this task was divided into four parts. Three subtasks were performed concurrently in the first 24 months of the program, and the results were used to formulate alloys for the scale-up effort conducted in the final year.



FD 229014

Figure 7. Detailed Plan for Task III

Attempts to change the corrosion characteristics of Fe-Mn-Al alloys were based on the additions of limited amounts of chromium to the alloys. Corrosion resistance in saline environments and resistance to low melting salts were evaluated using standard methods. Alloys were produced as castings for this segment of the program.

To form a uniform dispersion of fine carbide particles, a strong carbide former was required. In ferritic steels, the carbide forming tendencies in the order of increasing intensities are Mn, Cr, Mo, W, Ta, V, Nb, Zr, and Ti. The stability of carbide particles with respect to coarsening depends on, among other factors, the surface energy between the matrix and the carbide phase which, in austenitic steels has been correlated directly with the lattice misfit between the carbide and the matrix. The smaller the misfit the smaller the carbide size and the slower rate of coarsening, resulting in higher creep strength (Reference 2). Single or combined additions of small quantities (0.01 to 0.1%) of N, B, and P are also effective in producing a uniform dispersion of fine carbide particles in austenitic steels (Reference 3). Other types of nonmetallic precipitates, such as borides and sulfides, can also enhance strength and creep resistance if a uniform dispersion of very fine, dimensionally stable particles can be produced. It is considered that rapid solidification, mechanical working, and judicious alloying additions are essential for achieving such a particle dispersion.

The major screening effort to define useful alloy additions was performed on castings. The choice of alloy compositions were based on the principles outlined above and included alloys strengthened by intermetallic particles, nonmetallic particles, and substitutional solutes.

Rapidly solidified powder was used for the third part of the initial evaluation. Alloys were to be chosen to: (1) check the occurrence and stability of metastable LI_2 phases; and (2) evaluate the processability and properties of the best alloys identified in programs conducted in the 1950's and 1960's.

The program schedule for Tasks 1, 2, and 3 was shown in Figure 1.

SECTION III

RESULTS AND DISCUSSION

PROCESS AND MODEL DEVELOPMENT — TASK I

Powder Processing and Evaluation

The $\text{Fe}_3\text{Al}+1.93\% \text{TiB}_2$ and Fe_3Al billet stock obtained in approximately 350 pound lots from Certified Alloys was processed to powder in the P&W 50 to 250 pound capacity atomization apparatus (AGT 400000).

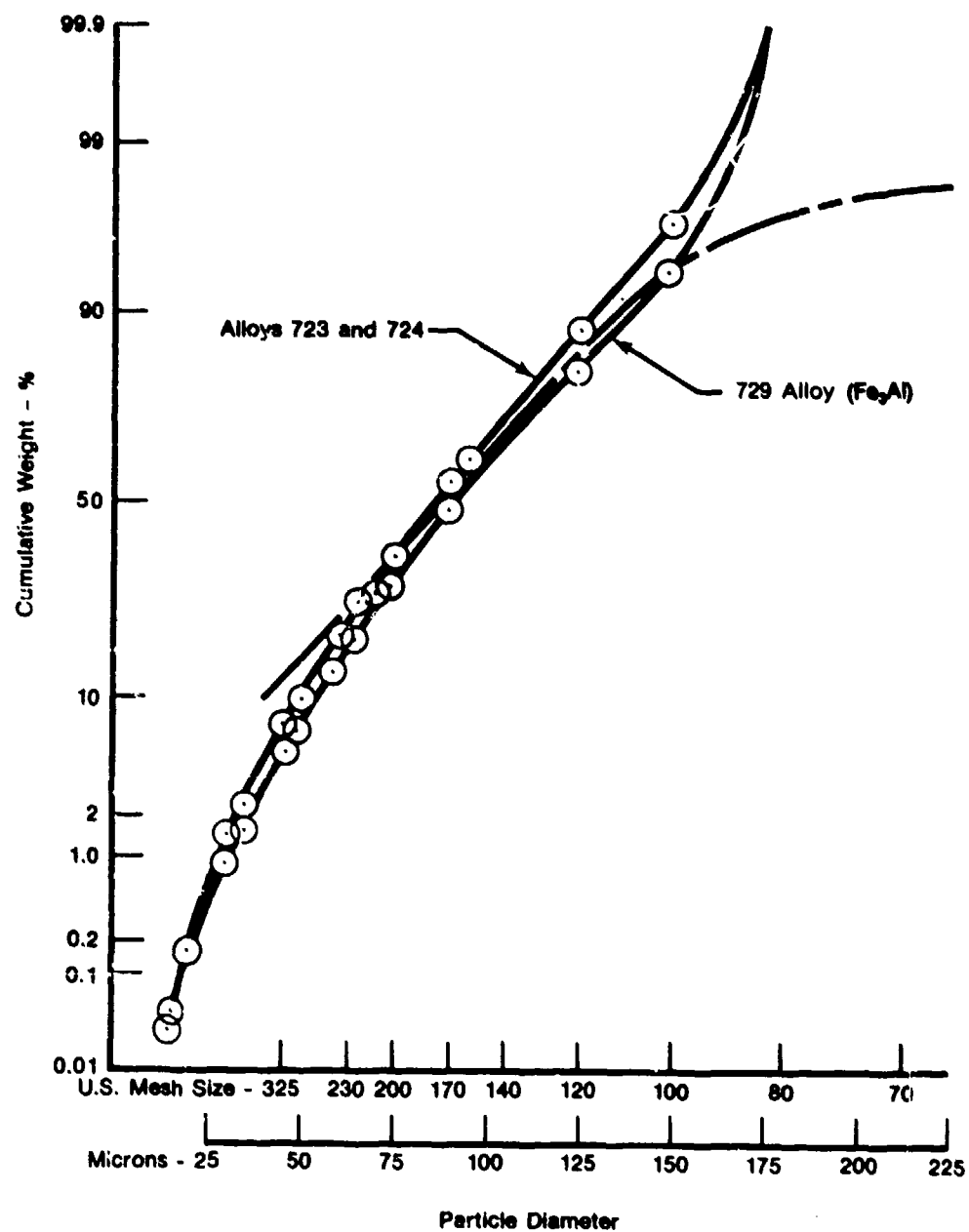
The following quantities of powder were produced for Task I process development studies.

<u>Run No.</u>	<u>Alloy</u>	<u>-80 Mesh, lb</u>
722	$\text{Fe}_3\text{Al} + 1.93$ TiB_2	30
723	$\text{Fe}_3\text{Al} + 1.93$ TiB_2	92.6
724	$\text{Fe}_3\text{Al} + 1.93$ TiB_2	139.8
727	Fe_3Al	15
729	Fe_3Al	70

The +80 mesh powder fraction which contained coarse material produced during start up transients and which amounted to less than 6 pounds per run was discarded. The first powder run (722) was saturated with water by a water line break subsequent to atomization. But the powder was used to determine the effects of exposure to water and of post outgassing heat treatments.

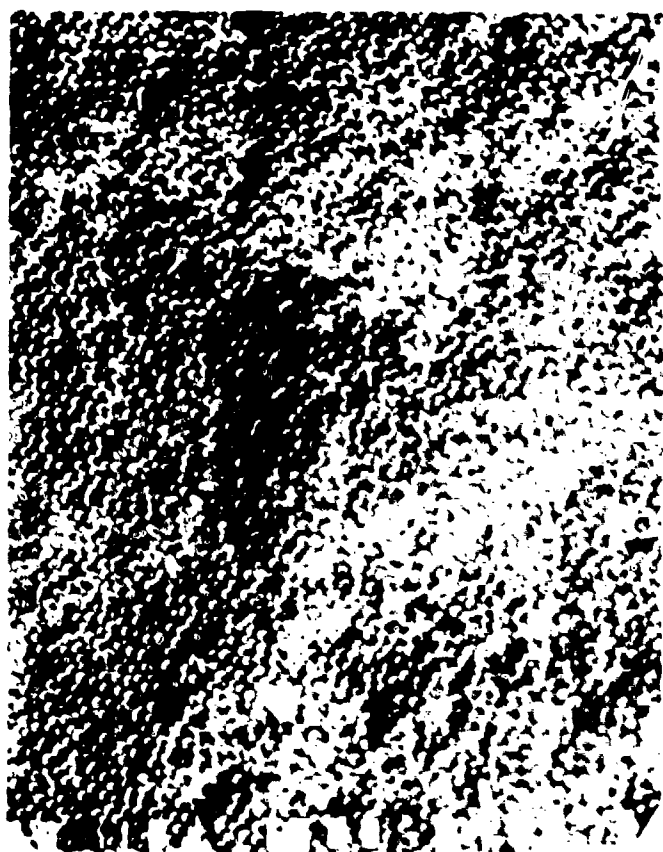
On a poured weight basis, the yield of -80 mesh (-177 μm) powder was high as 84%. The powders were screened with precision sieves, and the results are shown in Figure 8. The powder size distribution of Fe_3Al with TiB_2 (alloys 723 and 724) was similar to that of Fe_3Al (alloy 729) and the apparent difference with the size distribution for nickel-base alloys was more a result of the use of precision and finer sieves than because of alloy composition. The powder was also separated into three size fractions with about 60 wt% of the powder from -120 to +230 mesh for the bulk of the studies on consolidation and post working and the remainder split between a fine and a coarse size fraction to determine the effects of solidification rate on microstructure and mechanical properties.

In scanning electron microscope (SEM) analysis, the powders were seen to be spherical with some elongated cylindrical particles and fragments of broken particles especially in the larger size fractions. As shown in Figures 9 through 12, the surface of the $\text{Fe}_3\text{Al} + \text{TiB}_2$ powder particles are featureless to 5400 \times in particles less than 35 microns in diameter. A very faint cellular type structure appears in some of the 60- to 65 micron particles and in the 125- to 150-micron range a few particles reveal a dendritic substructure. In comparison, the surfaces of the Fe_3Al powder particles shown in Figures 13 through 16, are strongly cellular or microcrystalline in the fine 15-micron size and dendritic in the larger particle sizes.



FD 241837

Figure 8. Particle Size Distribution of the Fe₃Al and Fe₃Al + TiB₂ Alloys Produced for Task 1



100 μm



10 μm



10 μm



1 μm

Figure 9. SEM of the Surface of $\sim 15 \mu\text{ Fe}_3\text{Al} + \text{TiB}_2$ Powder (Alloy 724)

FD 241838

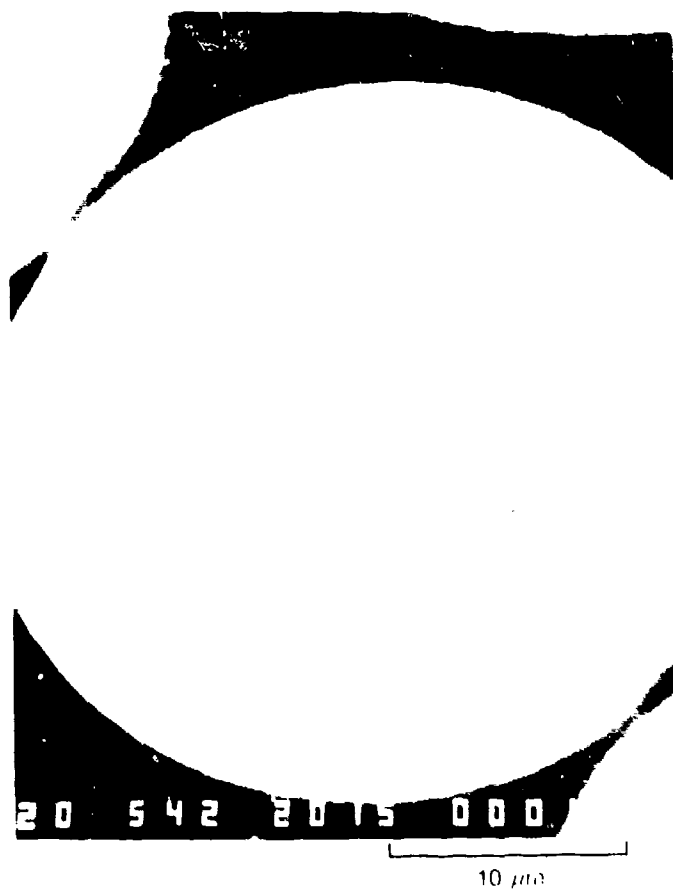
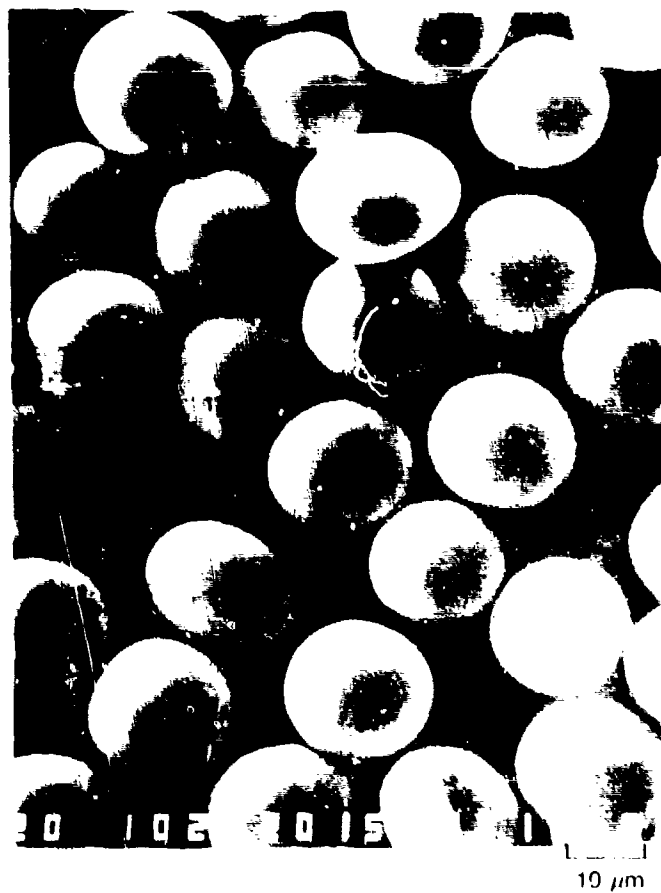
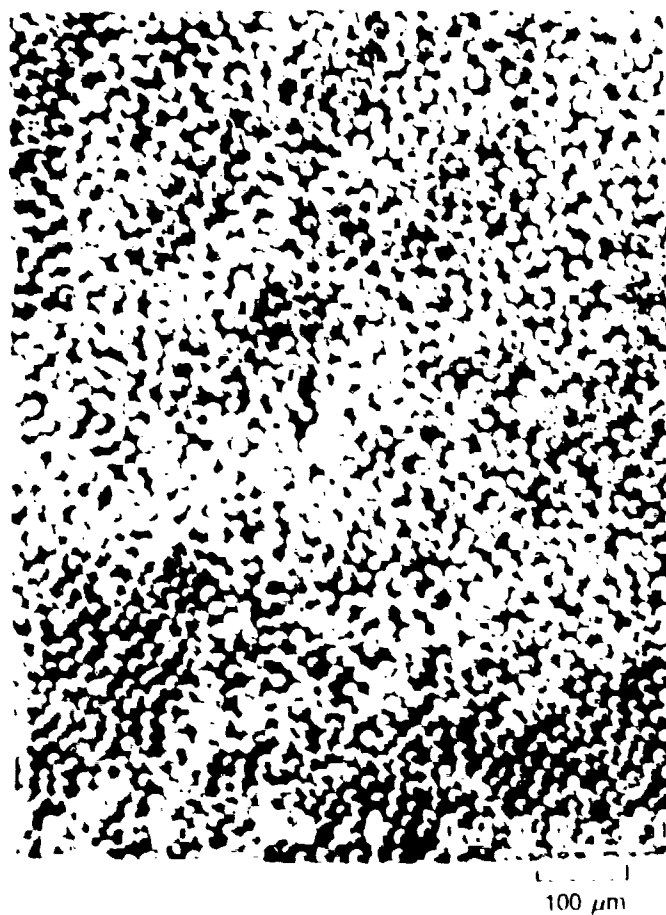
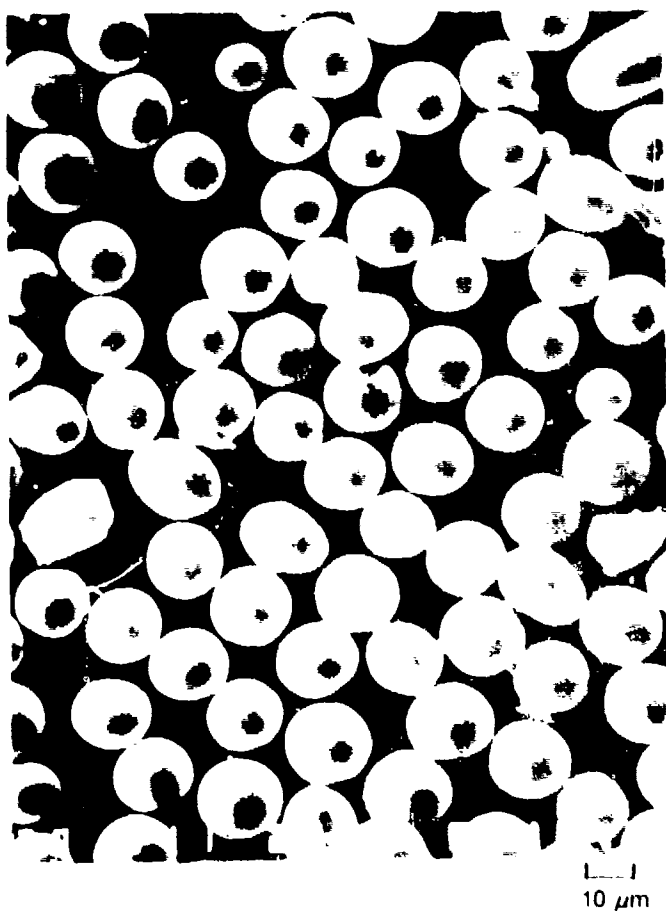


Figure 10. SEM of the Surface of $\sim 30 + \mu\text{m}$ $\text{Fe}_3\text{Al} + \text{TiB}_2$ Powder (Alloy 724)

FD 241839

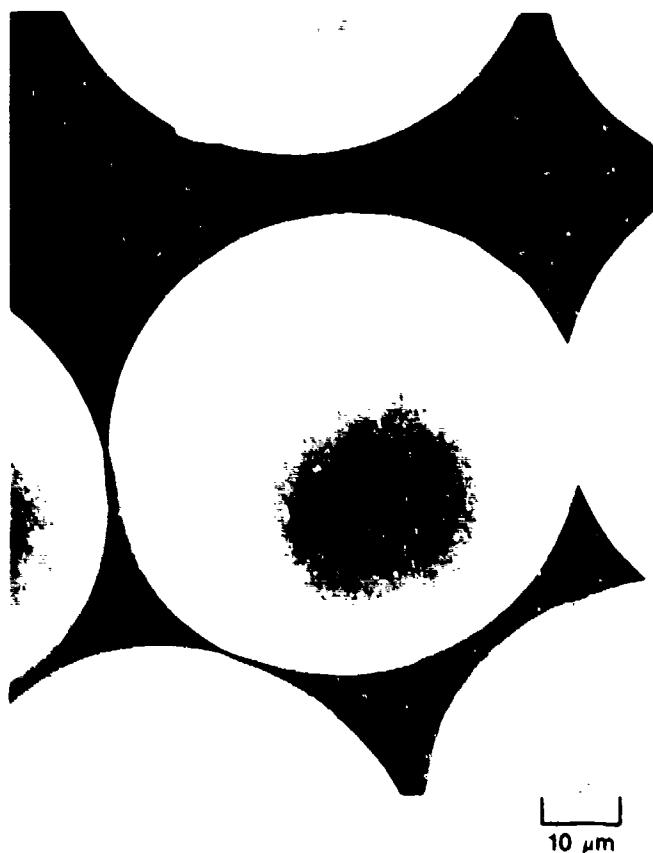
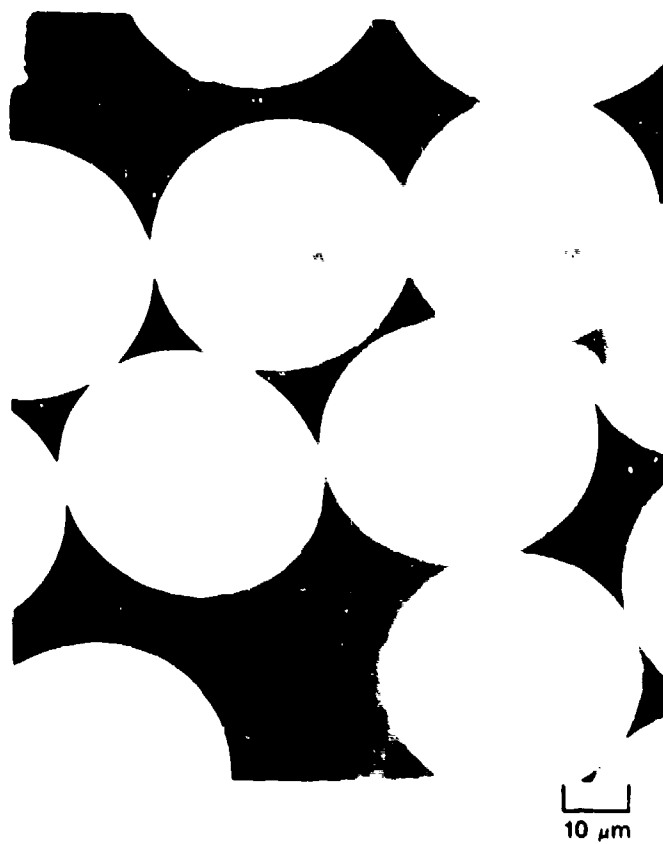
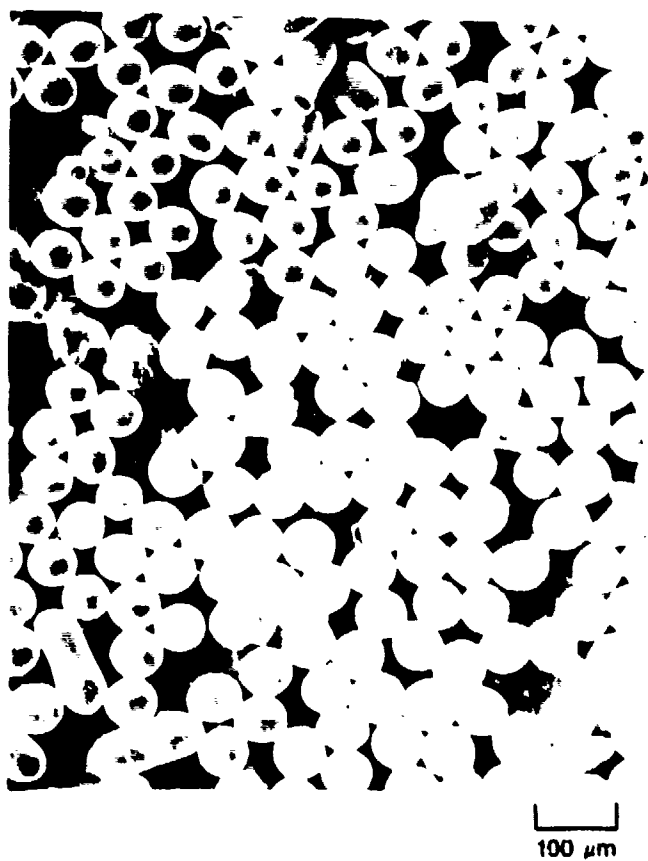


Figure 11. SEM of the Surface of $-65 +60 \mu\text{m}$ $\text{Fe}_3\text{Al} + \text{TiB}_2$ Powder (Alloy 724)

FD 241840

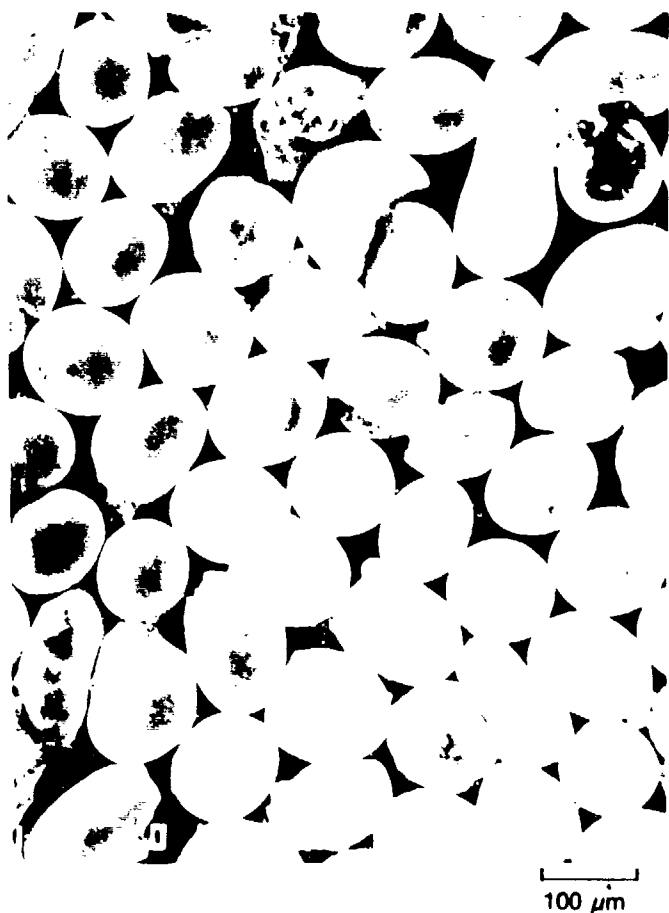
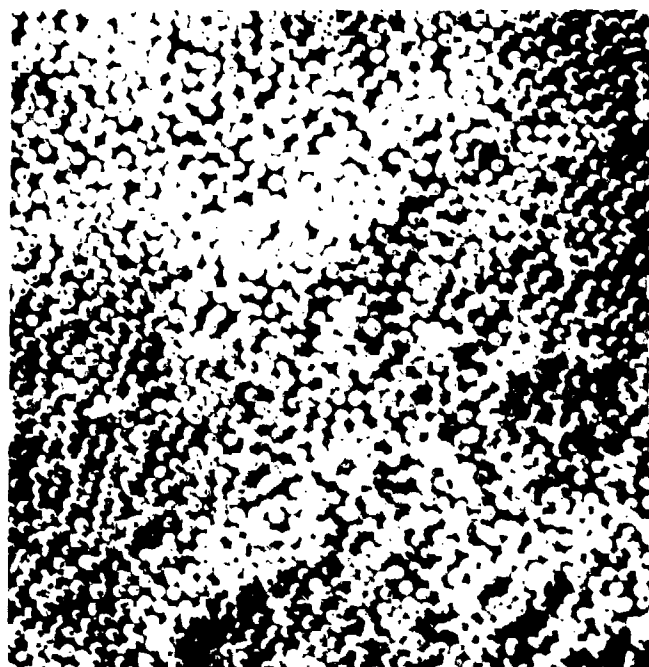
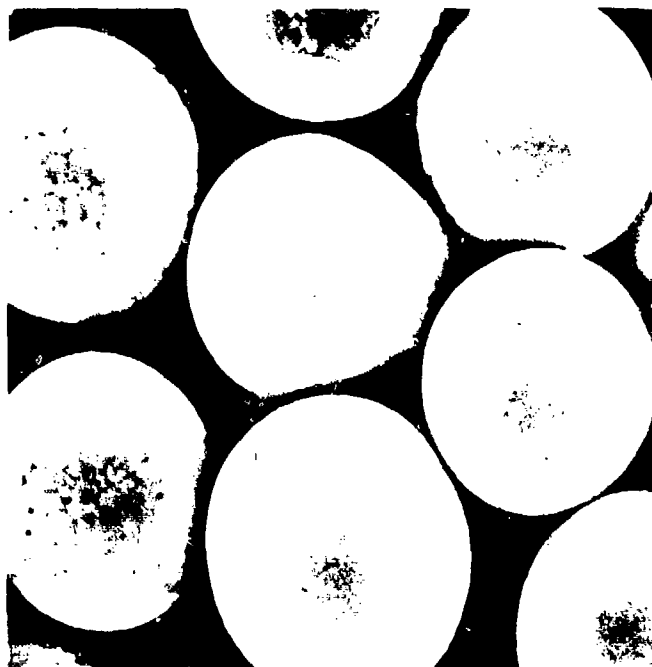


Figure 12. SEM of the Surface of $-150 +125 \mu\text{m}$ $\text{Fe}_3\text{Al} + \text{TiB}_2$ Powder (Alloy 724)

FD 241841



10 μm



5 μm



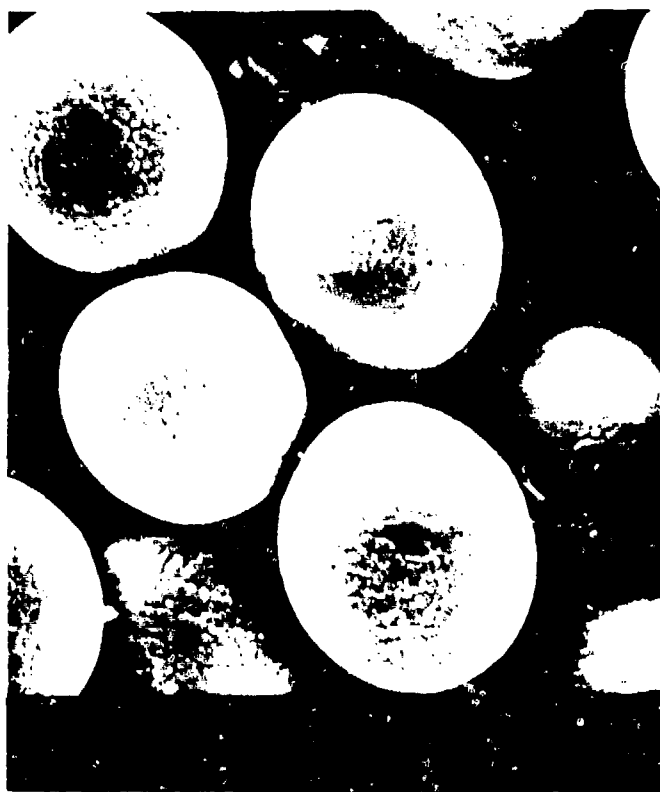
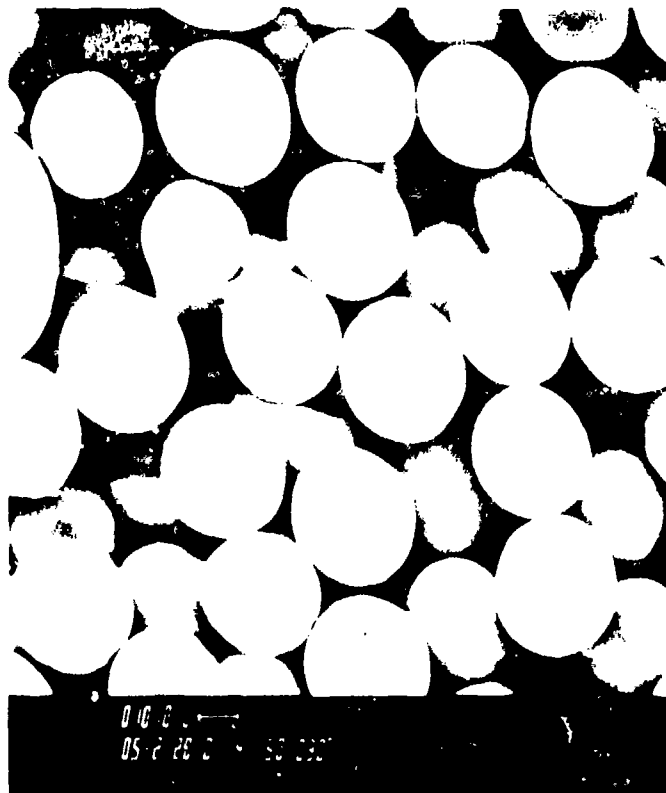
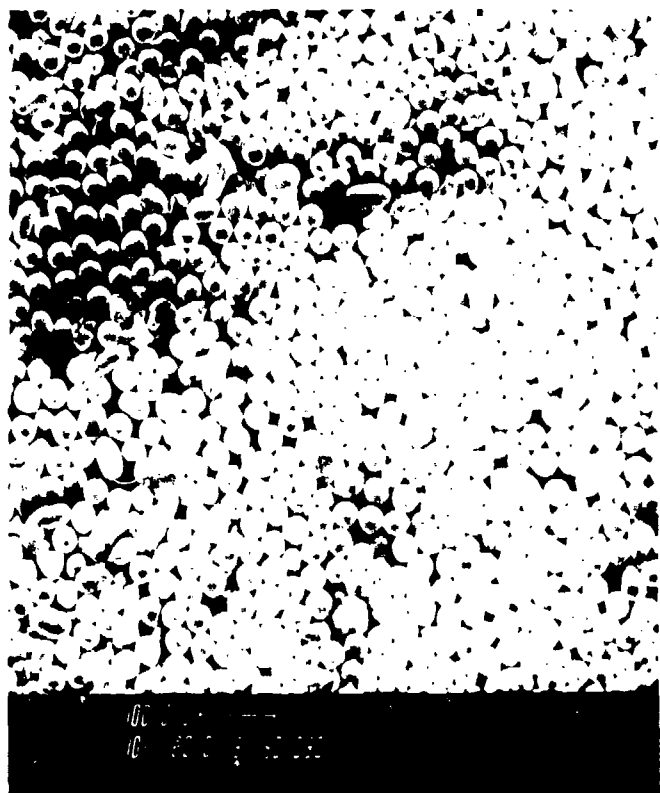
1 μm



1 μm

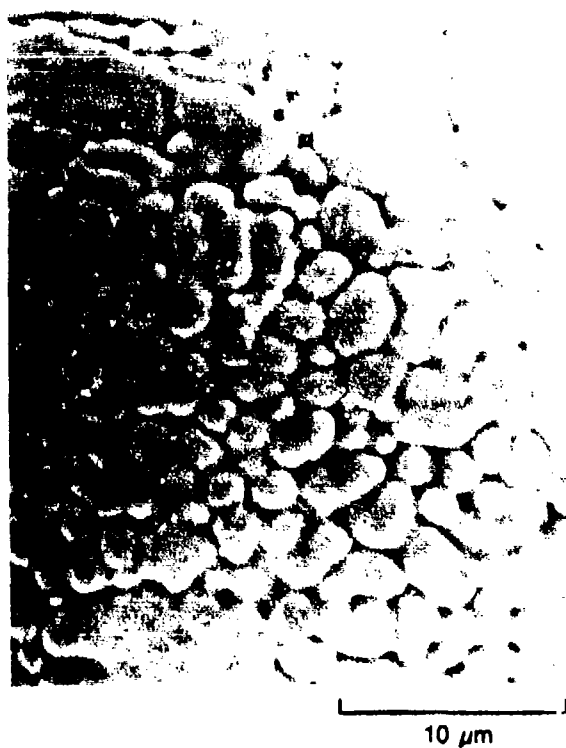
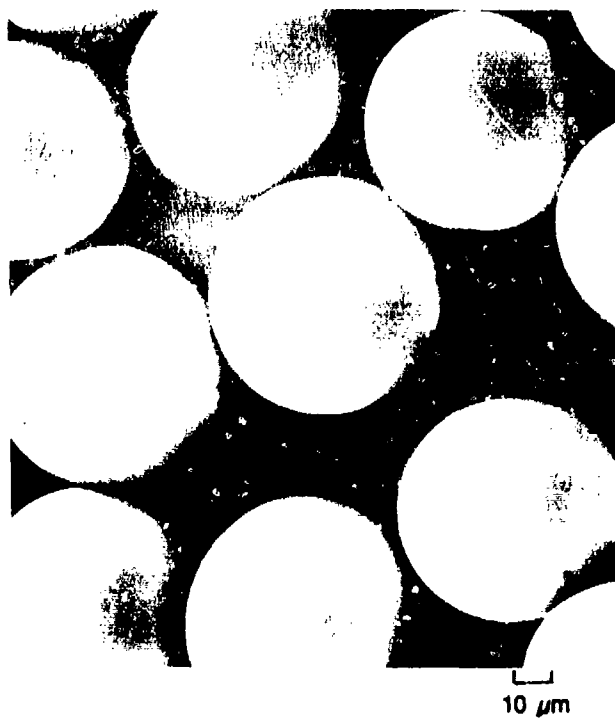
FD 241842

Figure 13. SEM of the Surface of $-15\ \mu\text{m}$ Fe_3Al Powder (Alloy 729)



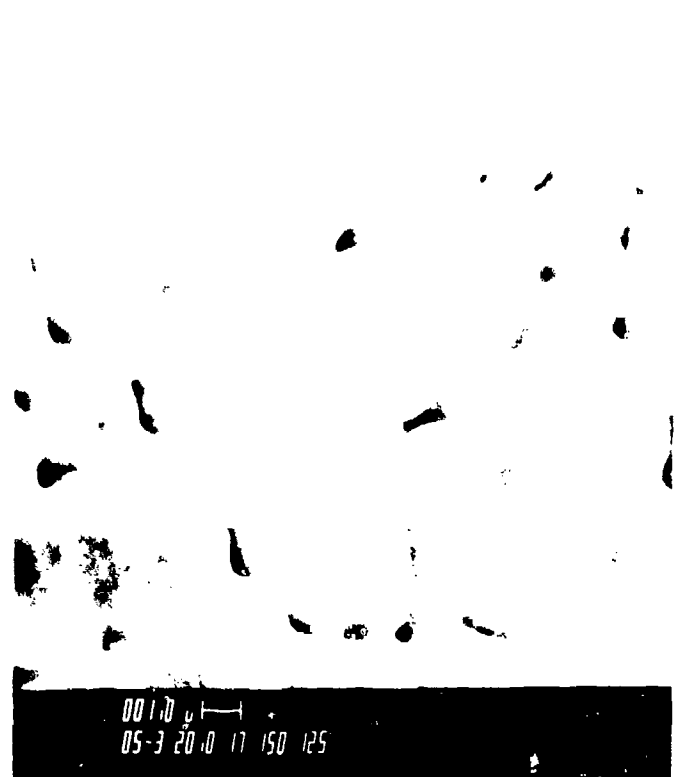
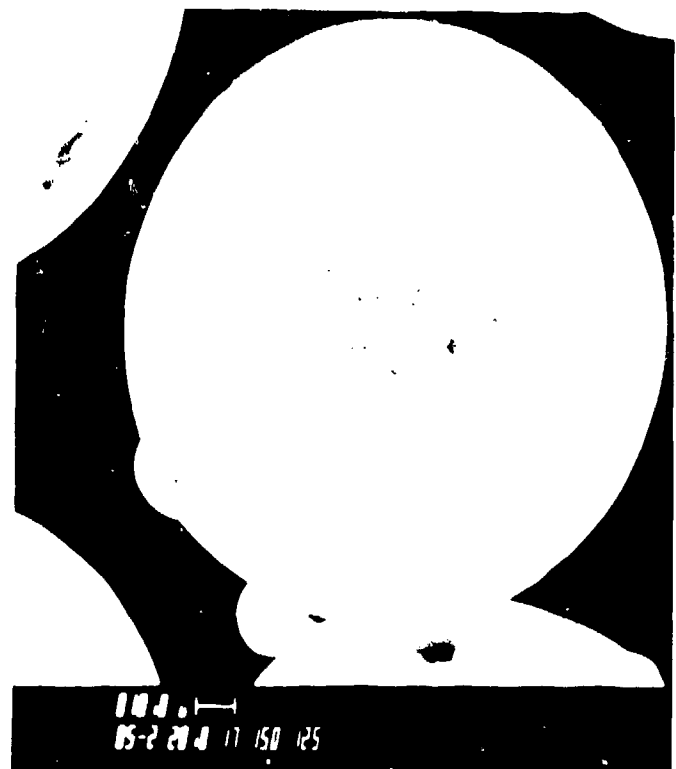
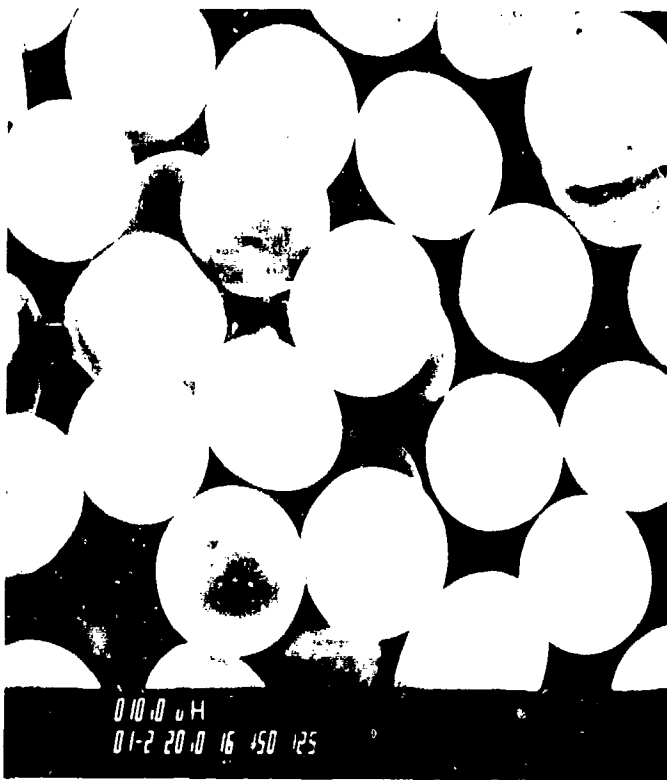
FD 241843

Figure 14. SEM of the Surface of $-30 + 20\mu$ Fe_3Al Powder (Alloy 729)



FD 241864

Figure 15. SEM of the Surface of $-65 +60\mu$ Fe_3Al Powder (Alloy 729)



FD 241845

Figure 16. SEM of the Surface of $-150 +125\mu\text{m}$ Fe_3Al Powder (Alloy 729)

The internal microstructure of the $\text{Fe}_3\text{Al} + \text{TiB}_2$ powder was found to be dendritic with an optically unresolved interdendritic phase in all particle sizes but with possibly a mixed dendritic cellular structure in the finer particle sizes as shown in Figure 17. The microstructures of the Fe_3Al particles were very difficult to etch because of lack of coring or change in composition during solidification. The cross sections, shown in Figure 18, revealed a multigrain structure except for the finer particles which consisted of many single-grain particles.

The major structural difference between the two alloys was a finer dendrite or cell size spacing in the alloy with TiB_2 . The secondary dendrite arm spacing for Fe_3Al (alloy 729) varied from approximately 1 micron to 3 microns for 15- to 150 micron diameter particles, while the spacing for $\text{Fe}_3\text{Al} + \text{TiB}_2$ (alloy 724) was about half that size varying from 0.5 to 1.5 microns for the same particle size range. As in other alloy systems, including nickel- and iron-base alloys, dendrite size was related to alloy composition. In the iron aluminide, the addition of titanium and boron produced a finer microstructure.

Transmission electron microscopy (TEM) on prepared thin sections of powder samples was carried out. This work showed that the $\text{Fe}_3\text{Al} + \text{TiB}_2$ powder ordered as the B2 phase on solidification. The Fe_3Al (alloy 729) powder was analyzed for lattice parameter variation as a function of powder particle size by conventional X-ray powder diffractometry. These lattice parameters, shown in Table 2, indicate that the rapidly solidified powder has a disordered B2 structure. There was evidence of a very weak (100) diffraction peak in all powder size fractions indicating that some attempt at structural ordering had commenced during the period of time taken for the powder to cool from the B2 phase field to room temperature. There was no change in lattice parameter as a function of particle size over the range of diameters from 15 to 150 microns. In alloys containing TiB_2 (alloy 724), some evidence of supersaturation in the B2 lattice was apparent in powders of the finest size examined (-45 to +35 micron size fraction), presumably due to increased solidification velocity in these fine powders and the associated solute trapping of titanium and boron.

For the production of larger quantities of powder required for the processing of wrought material in larger cross sections for transverse and fracture toughness property measurements, a newer and larger 12-foot diameter atomization device (AGT 5000000) was employed. With this system, over 300 pounds of $\text{Fe}_3\text{Al} + \text{TiB}_2$ powder were produced. The powders produced in both atomization systems were similar except for the minor differences noted as follows.

Initially, it was planned to use a -140 +230 mesh powder size fraction for the bulk of the processing study with the finer (-230 mesh) and coarser (-80 +140) mesh powder for a cursory evaluation of particle size or cooling rate on microstructure and mechanical properties. With the larger quantities of $\text{Fe}_3\text{Al} + \text{TiB}_2$ powder available, it was possible to carry out a more extensive study of cooling rate effects while providing sufficient material for large extrusions from fine (-270 mesh) and coarser (-80 +140 mesh) powder size fractions. Approximately 50-pound quantities of each size fraction were consolidated by extrusion in 7-inch diameter cans to provide the cross sections of required fracture toughness and other property measurements.

The surface characteristics and appearance of coarse (-80 +100 mesh) and fine (-270 mesh) powder size fractions produced in the larger 12-ft diameter device are shown in Figures 19 and 20. The powder is spherical with some broken fragments of larger particles in the finer powder. However, the greater difference between the two size fractions is in their surface structure. The coarser (-80 +100 mesh) powder has a well defined cellular/dendritic structure with a cell size in the range of 1 to 3 microns while the finer (-270 mesh) powder structure is too fine to resolve at the same magnifications. Comparing the structure of this powder with the structure of powder produced in the smaller atomization device, it appears that a coarser microstructure was produced in the larger atomization device. The $\text{Fe}_3\text{Al} + \text{TiB}_2$ alloy produced

in the smaller system had a carbon content about 10 times that in the larger system while the solidification rate, which is known to be related to the velocity of atomized droplets through a helium atmosphere, should be the same for both atomization systems. Therefore, it is believed that the difference in structure, which was observed, is probably due to the difference in the composition of the alloy.

The microstructure of the fine (-270 mesh) and coarse (-80 +100 mesh) $\text{Fe}_3\text{Al} + \text{TiB}_2$ powder produced are shown in Figures 21 to 23. The solidification microstructure, which was correlated to powder particle diameter, was determined by the solidification rate. The extremes in structure for $\text{Fe}_3\text{Al} + \text{TiB}_2$ are seen in Figure 21 with a small 20-micron diameter particle attached to a large particle some 150 microns in diameter. Also shown in Figure 21 is an example of porosity and/or particle entrapment which has been observed in RSR powder. Some gas (helium) porosity can be expected as a result of entrapment during spheroidization especially in non-filament degradation mode (for example, the film degradation mode). However, particle entrapment also takes place and to a greater extent than might be expected. It was not uncommon to observe fine solidified droplets embedded in larger powder particles but often these droplets were removed during metallographic preparation. Nevertheless, porosity resulting from helium gas entrapment can occur especially in coarse powder, and eliminating such porosity may be accomplished most readily by use of the finer powder size fractions.

The differences in structure between fine (-270 mesh) and coarse (-80 +100 mesh) powders are shown in Figure 22. The two coarse (-80 +100 mesh) particles in the figure have different structures but on closer examination it is seen that, except for the presence of large primary dendrites in one of the particles, the secondary dendrite arm spacing is reasonably uniform. The dendrite arm spacing of the finer 50 microns (-270 mesh) particle in Figure 22 was enlarged in Figure 23 and compared to the larger particles. The difference in secondary dendrite arm spacing was found to be about three to one. However, as shown in Figure 24 for two different randomly selected particle sizes, the dendrite spacing may not appear to be that different and as a result a number of particles must be examined to obtain a true correlation between particle size and dendrite arm spacing. For the powders produced, the typical structures shown in Figure 23 gave a value of 1 micron for the finer 50 microns (-270 mesh) particles and 3 microns for the coarser 160 microns (-80 +100 mesh) particle. In subsequent consolidation and working studies, an attempt was made to correlate powder particle size and structure with final wrought structure and mechanical properties.

The lattice parameter of the $\text{Fe}_3\text{Al} + \text{TiB}_2$ alloy produced in the larger atomization system was essentially constant for powder sizes from -270 mesh to -80 +100 mesh. The $\text{Fe}_3\text{Al} + \text{TiB}_2$ alloy produced in the smaller system (alloy 724) gave some evidence of supersaturation in the B2 lattice in -270 mesh powder. However, this was found only in very fine 35- to 45-micron particles. The lattice parameter of 2.899 angstroms (\AA), measured for the powder produced in the larger system, was essentially the same as that of the -270 mesh powder size fraction produced in the smaller system.

The composition of the $\text{Fe}_3\text{Al} + \text{TiB}_2$ produced and employed for thermomechanical processing during this period has the aim and measured compositions listed in Table 3. The composition of each batch of powder was measured by atomic absorption, and in a few cases, by an inductively coupled plasma emission method. The measurements by the two techniques are in good agreement and measured compositions are on the average close to the aim composition.



10 μm

-65 +60 μm Powder

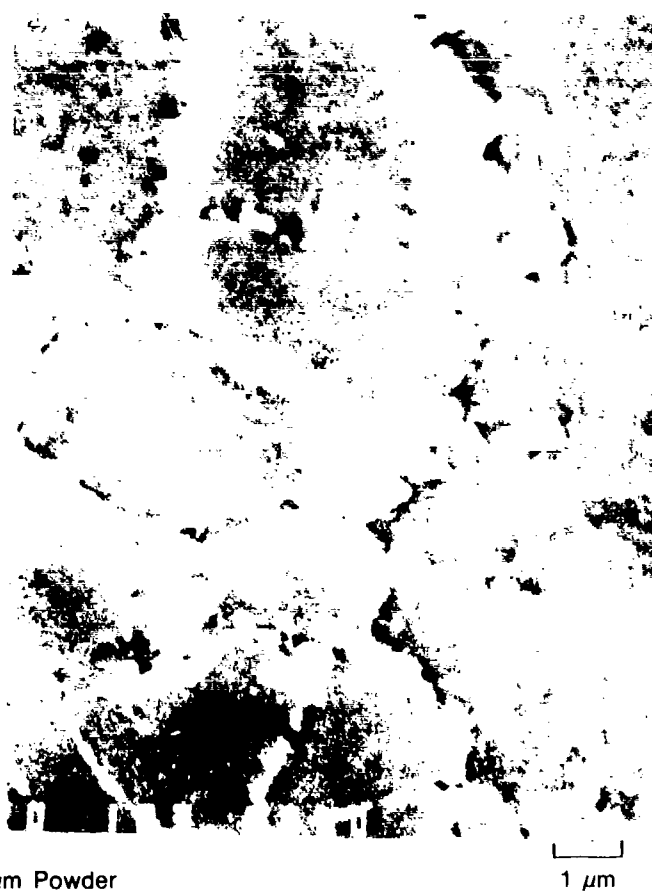


1 μm



10 μm

-150 +125 μm Powder



1 μm

Figure 17. Microstructure of $\text{Fe}_3\text{Al} + \text{TiB}_2$ (724) Powder Particles — As-Produced

FD 241846



-65 +60 μm

10 μm



-35 +30 μm

10 μm

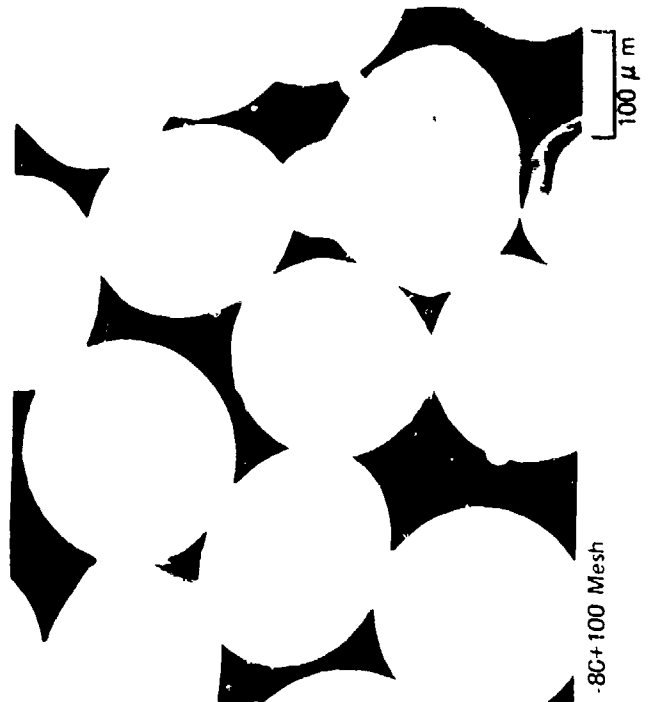
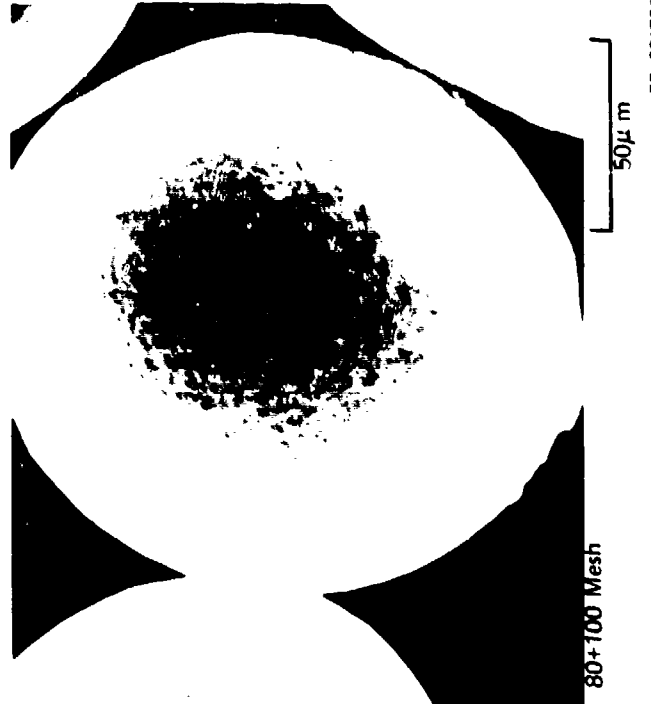
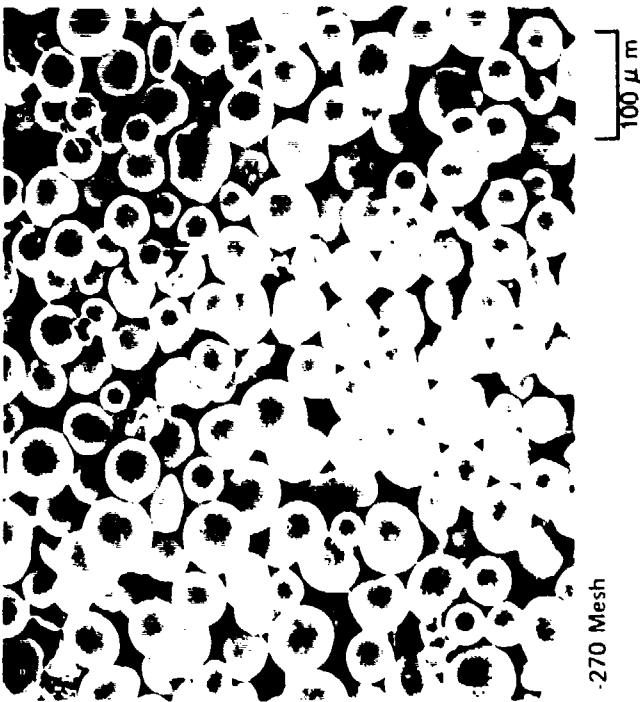
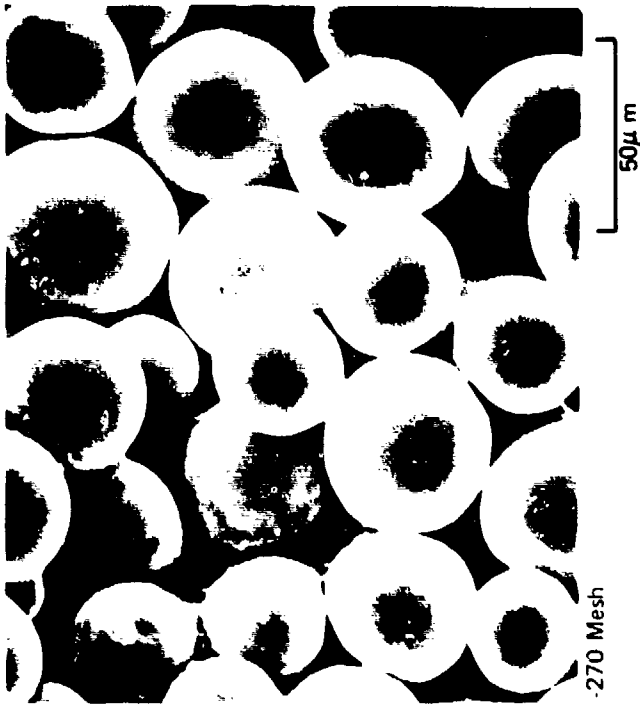
FD 241847

Figure 18. Microstructure of Fe_3Al (729) Powder Particles As-Produced

TABLE 2. LATTICE PARAMETER OF IRON ALUMINIDE POWDERS AS A
FUNCTION OF PARTICLE SIZE

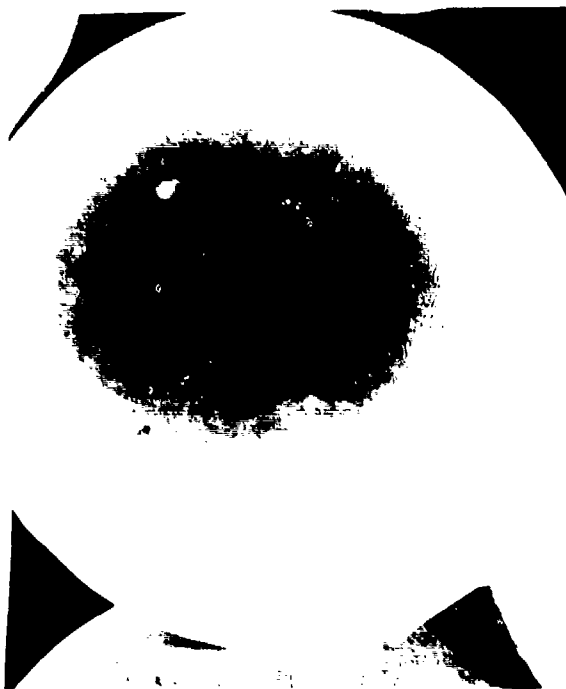
Size Fraction, μm	<i>Fe₃Al</i> , Alloy 429	<i>Fe₃Al</i> + <i>TiB₂</i> , Alloy 724
	Lattice Parameter (\AA)	
-150 +125	0.2897 \pm 0.0001	0.2896 \pm 0.0001
-75 +70	0.2896 \pm 0.0001	0.2897 \pm 0.0001
-65 +60	0.2898 \pm 0.0001	
-50 +45	0.2895 \pm 0.0001	0.2898 \pm 0.0001
-45 +35	0.2896 \pm 0.0001	0.2896 \pm 0.0001
-35 +30	0.2897 \pm 0.0001	
-30 +20	0.2897 \pm 0.0001	
-20 +15	0.2897 \pm 0.0001	
-15	0.2897 \pm 0.0001	

2711C



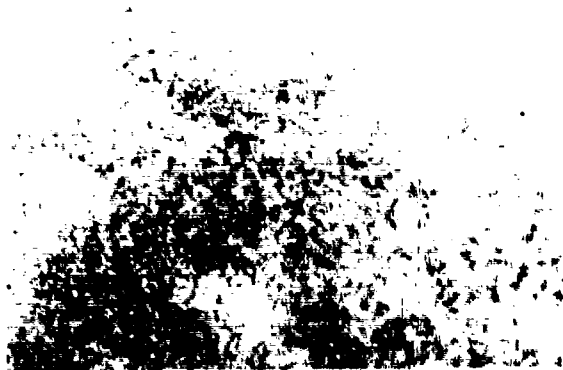
FD 261795

Figure 19. SEM of Fine (-270 Mesh) and Coarse (-80 + 100 Mesh) $\text{Fe}_3\text{Al} + \text{TiB}_2$ Alloy Powder



-270 Mesh

10 μm



-80+100 Mesh

2 μm



-80+100 Mesh

10 μm



-80+100 Mesh

2 μm

Figure 20. SEM of Fine (-270 Mesh) and Coarse (-80 + 100 Mesh) $\text{Fe}_3\text{Al} + \text{TiB}_2$ Alloy Powder

FD 261795

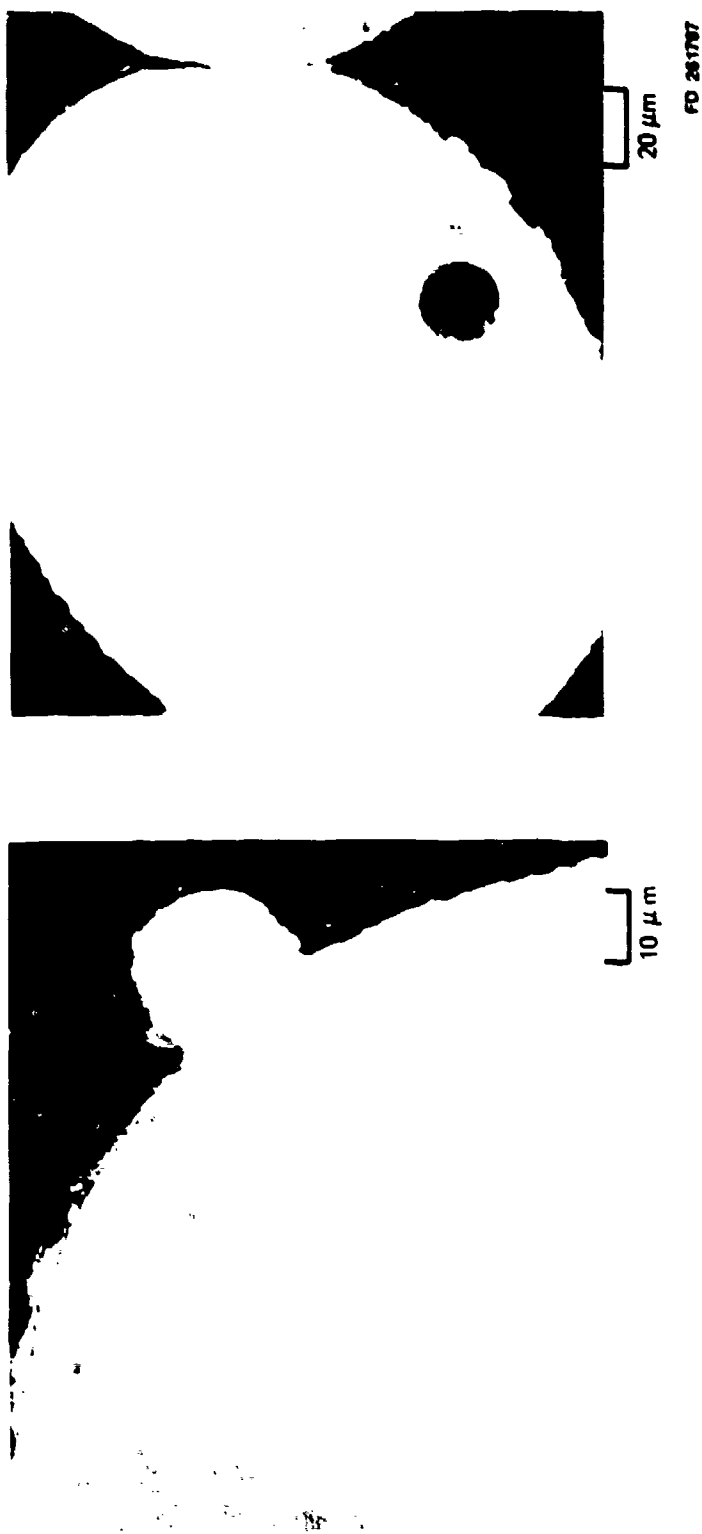
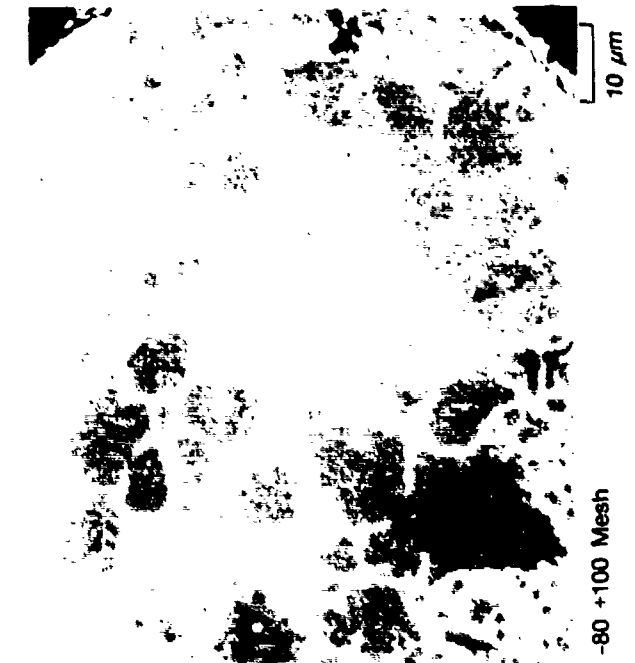
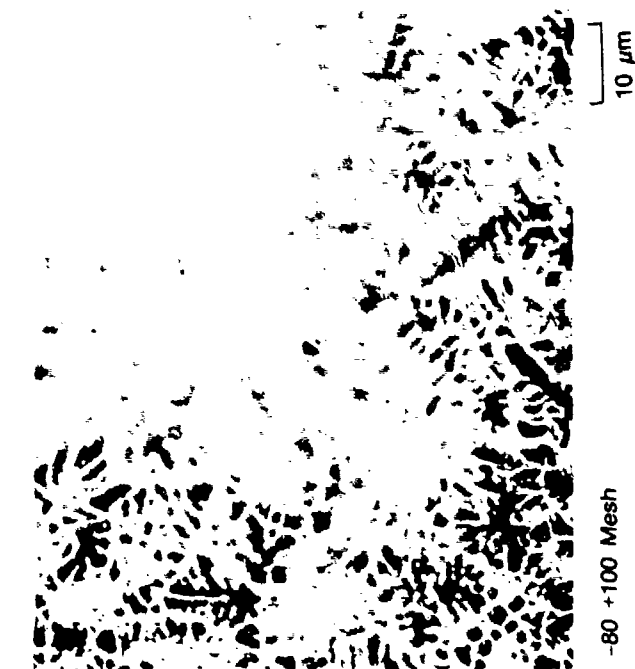
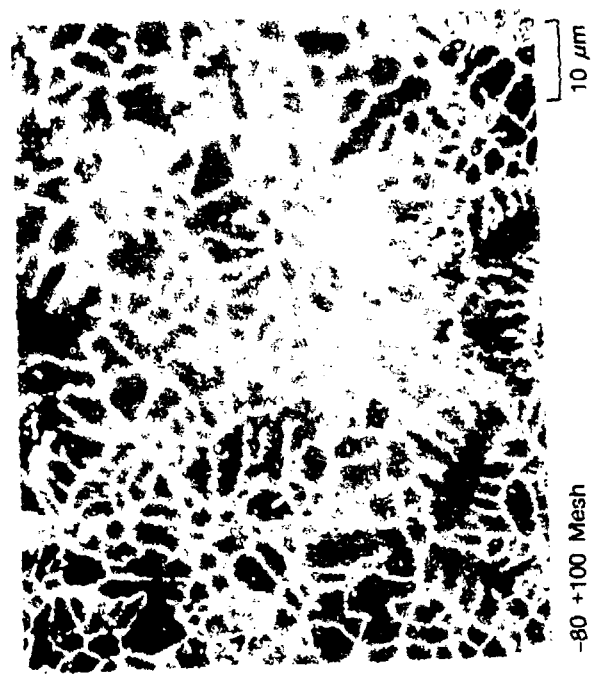
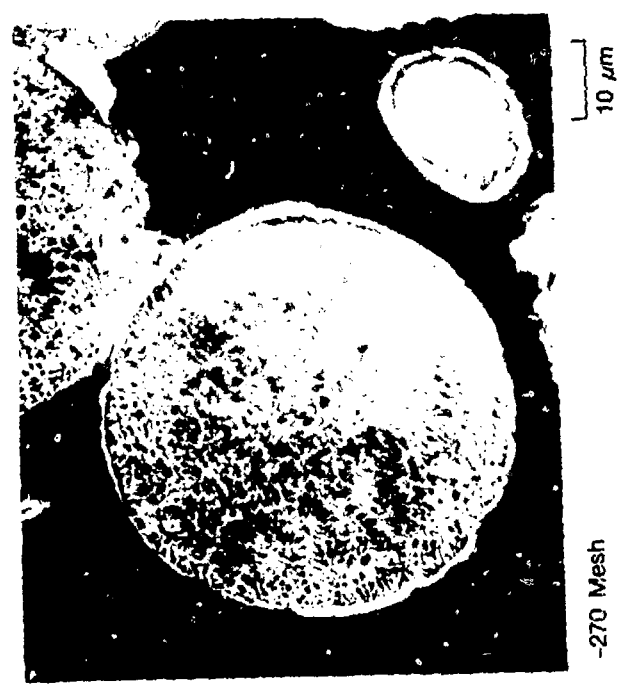
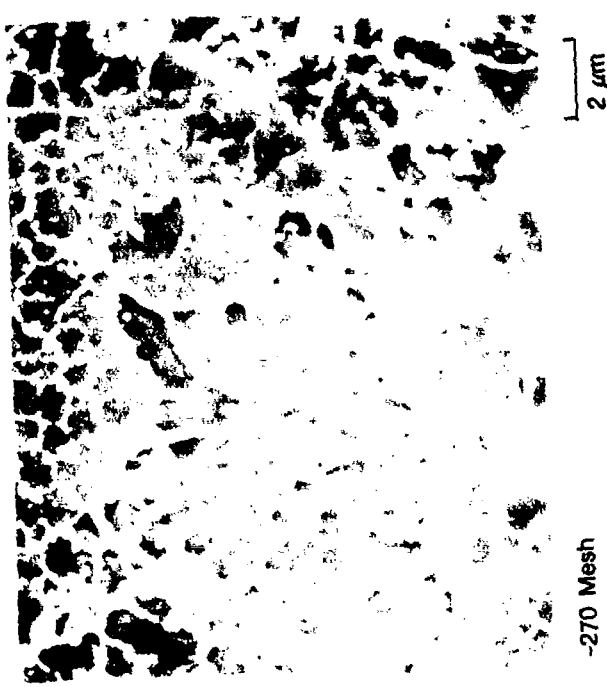


Figure 21. Solidification Structure and Particle Entrapment/Porosity in $\text{Fe}_3\text{Al} + \text{TiB}_2$ Powder



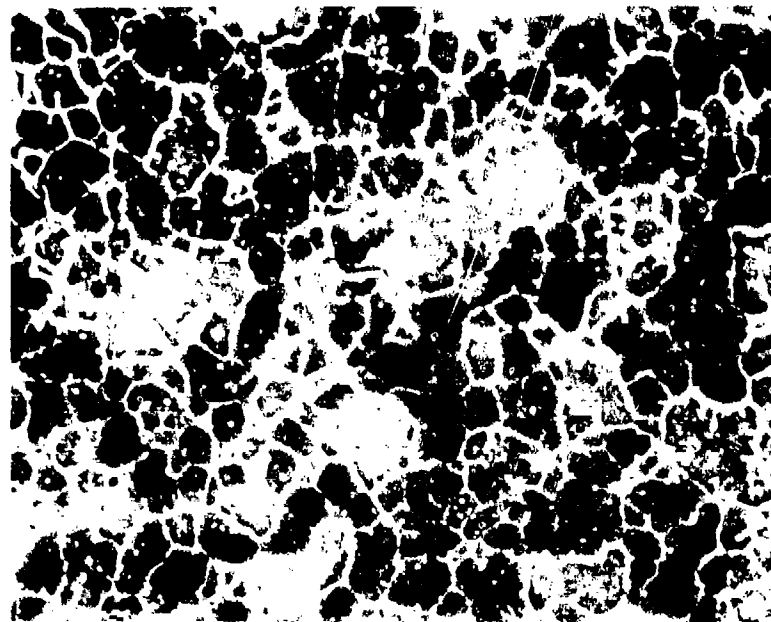
FD 261798

Figure 22. Microstructure of Fine (-270 Mesh) and Coarse (-80 + 100 Mesh) $\text{Fe}_3\text{Al} + \text{TiB}_2$ Powder

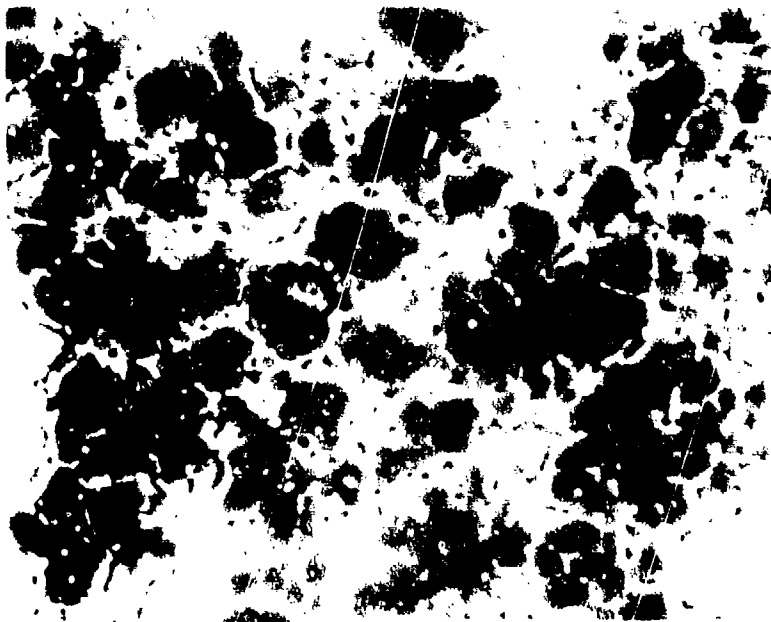


FD 261759

Figure 23. Microstructure of Fine (-270 Mesh) and Coarse (-80 +100 Mesh) $\text{Fe}_3\text{Al} + \text{TiB}_2$ Powder



60-65 μ m particle



125-150 μ m particle

AV252713

Figure 24. Microstructure of Fine and Coarse $\text{Fe}_3\text{Al} + \text{TiB}_2$ Powder particles Randomly Selected

TABLE 3. COMPOSITION OF THE $\text{Fe}_3\text{Al} + \text{TiB}_2$ ALLOY PRODUCED DURING THIS REPORTING PERIOD — IN WEIGHT PERCENT

Run No.	Fe	Al	Ti	B
II3*	85.6	12.3	1.55	0.55
II3	84.87	13.0	1.55	0.58
II6	84.51	13.49	1.45	0.55
II7	84.2	13.99	1.35	0.46
II8	84.03	13.99	1.45	0.53
II9	83.49	14.49	1.45	0.57
II10*	83.90	14.00	1.55	0.49
II10	84.13	13.99	1.40	0.48
AIM	84.39	13.6	1.41	0.6

*Inductively coupled plasma — others by atomic absorption.

2711C

CONSOLIDATION AND WORKING OF Fe_3Al

Laboratory Scale Processing

The consolidation and working of Fe_3Al was carried out under the conditions specified in Table 4. The table was arranged to show the consolidation by HVC and extrusion and of working by swaging, rolling, and forging. Included in the table are conditions used for the processing of $\text{Fe}_3\text{Al} + \text{TiB}_2$ produced from two lots of powder.

TABLE 4. CONSOLIDATION AND WORKING OF Fe_3Al ALLOYS

	Fe_3Al (729)	$\text{Fe}_3\text{Al} + \text{TiB}_2$ (723)	$\text{Fe}_3\text{Al} + \text{TiB}_2$ (545)
HVC	<ul style="list-style-type: none"> • 1700°F (927°C) — 15 ksi — 2 hr • 2000°F (1093°C) — 15 ksi — 2 hr 	<ul style="list-style-type: none"> • 1700°F (927°C) — 30 ksi — 2 hr • 2000°F (1093°C) — 30 ksi — 2 hr 	
HIP	<ul style="list-style-type: none"> • 2000°F (1093°C) — 15 ksi 		
Extrude	<ul style="list-style-type: none"> • 1700°F (927°C) — 4/1 • 1750°F (945°C) — 10/1 • 1950°F — 10/1 	<ul style="list-style-type: none"> • 1700°F (927°C) — 4/1 • 1750°F (945°C) — 10/1 • 1950°F — 10/1 	<ul style="list-style-type: none"> • 1700°F (927°C) — 8/1
Extrude + Swage	<ul style="list-style-type: none"> • 1750°F (945°C) — 10/1 + 1250°F to 1150°F — 6/1 and 3.7/1 • 1950°F — 10/1 + 1250°F to 1150°F — 6/1 and 3.7/1 	<ul style="list-style-type: none"> • 1750°F (945°C) — 10/1 + 1700°F (927°C) — 3.5/1 • 1950°F — 10/1 + 1700°F — 3.5/1 	<ul style="list-style-type: none"> • 1700°F (927°C) — 8/1 + 1550°F — 4.5/1
HIP + Roll	<ul style="list-style-type: none"> • 2000°F + 1350°F to 2000°F — NG • 2000°F + 2100°F — 80% • 2000°F + 2100°F — 50% + 1350°F + 1150°F — 90% 		
Extrude + Roll	<ul style="list-style-type: none"> • 1750°F (945°C) — 4/1 + 1350°F to 1150°F — 90% 	<ul style="list-style-type: none"> • 1750°F (945°C) — 10/1 + 1700°F (927°C) — 90% 	<ul style="list-style-type: none"> • 1700°F (927°C) — 8/1 + 1700°F (927°C) — 90%
Forge			

2711C

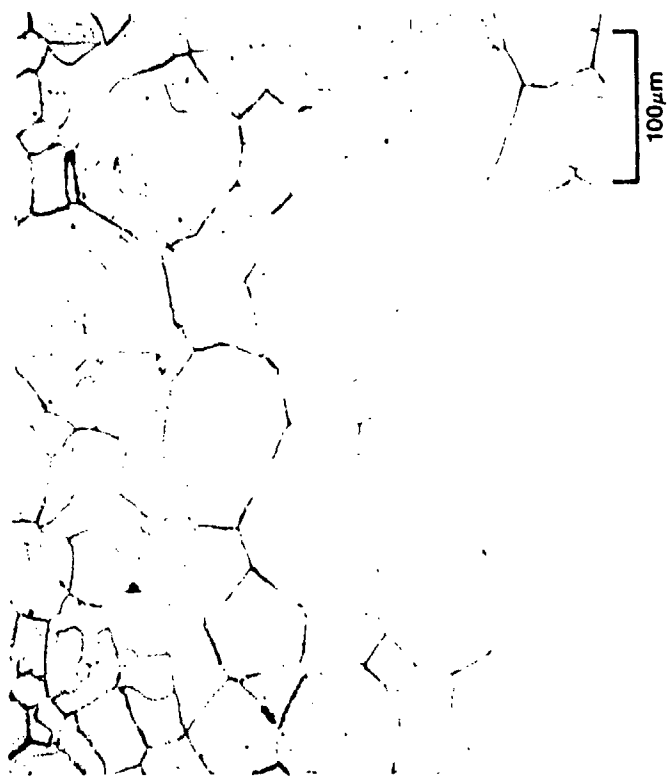
The Fe_3Al (alloy 729) powder with a $-140 +200$ mesh size, which had been stored in vacuum subsequent to its atomization, was consolidated by HVC and by hot isostatic pressing (HIP). For HVC, the Fe_3Al powder was exposed to the atmosphere prior to loading in a cylindrical die while for HIP the powder was transferred under a vacuum of 10^{-6} torr to stainless containers. After filling, the containers were sealed by forging of the filler tube.

The Fe_3Al (729) alloy was HVC'ed at 15 ksi (103 MPa) for two hours at 1700°F (927°C) and 2000°F (1093°C). The compacts were fully dense at both temperatures. However, the lower temperature compact contained numerous cracks, which followed powder particle boundaries almost exclusively. The 2000°F (1093°C) compact was free of cracks. Figure 25 shows the microstructure of Fe_3Al HVC'ed at 1700°F (927°C) after chemical etching with two reagents to reveal the grain structure. The prior particle boundaries were clearly delineated, and at both temperatures, the particle boundaries were found to be effective barriers to grain boundary motion. At the lower temperature, there were typically multigrains per particle, while at the higher 2000°F (1093°C) temperature, the powder particles were single grain.

The Fe_3Al (729) alloy was HIP'ed at 2000°F (1093°C) and 15 ksi (103 MPa) pressure for two hours. Consolidation was performed only at the higher temperature to produce stronger material as shown in Figure 26, however, the material still cracked along prior particle boundaries. Exposure of the powder to the atmosphere, at least for relatively short times prior to consolidation, did not appear to affect interparticle bond strength. However, even by processing under all inert or vacuum conditions the strength of Fe_3Al consolidated by both HIP and HVC methods remained relatively poor for subsequent working operations.

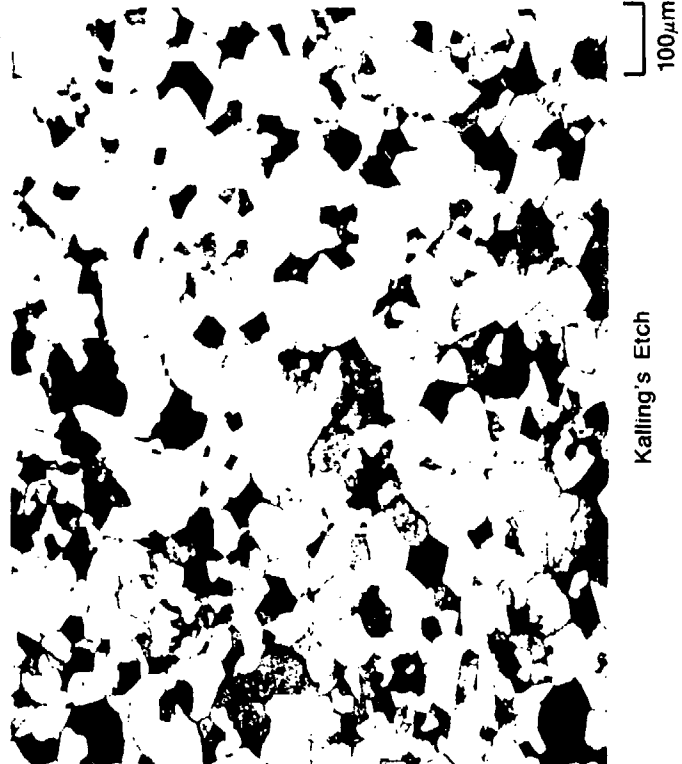
The Fe_3Al alloy extruded at 4 to 1 was warm rolled without difficulty at 1350°F to 1150°F (732°C to 621°C) to a true strain of 2.6. In comparison, rolling of HIP Fe_3Al led to early cracking of the material along prior particle boundaries. Additional rolling trials failed until the rolling temperature was increased to 2100°F (1149°C), initial reduction passes reduced to 5%, and the bulk of the rolling carried out in approximately 15% reduction steps to 90% total reduction. Figure 27 shows the microstructures with a modified glyceric etch which attacked prior particle boundaries. Between 55% and 65% reduction, the prior particle boundaries appeared to become discontinuous. As shown in Figure 28, with a Kalling's etch, abnormal grain coarsening had taken place in material rolled to and above 65% reduction in thickness. Figure 29 shows the same microstructures at a lower magnification. The resistance of the material to abnormal grain growth appears to be due to interparticle boundaries, which behave as a second phase in inhibiting grain growth. However, Fe_3Al , with the grain sizes shown in the latter figures, is inherently brittle with tensile elongations generally less than 2%.

The development of a fine microstructure with a maximum grain size related to the original powder particle size and to the degree of working was obtained by rolling HIP'ed Fe_3Al according to the following schedule. The material was first rolled at 2100°F (1149°C) to 50% reduction in thickness to increase interparticle bond strength. It was subsequently rolled at 1140°F (621°C) in approximately 15% reduction steps to a total reduction in thickness of 95%. As shown in Figure 30, the as-rolled structure annealed for 1 hour at 1150°F ($\sim 621^\circ\text{C}$) was produced by fiberization of the original powder particles. The average fiber diameter, shown in Figure 30, agrees with calculated values derived from simply transforming individual powder particles to fibers. An unexpected finding was that Fe_3Al powder handled entirely in a high-purity inert atmosphere produced relatively stable interparticle bonds, which were retained through extensive deformation.



Glyceregia Etch

100 μm



Kalling's Etch

100 μm

Figure 25. Alloy 729 (Fe_3Al) — HVC 1700°F/30 ksi — 140 +200 Mesh Powder

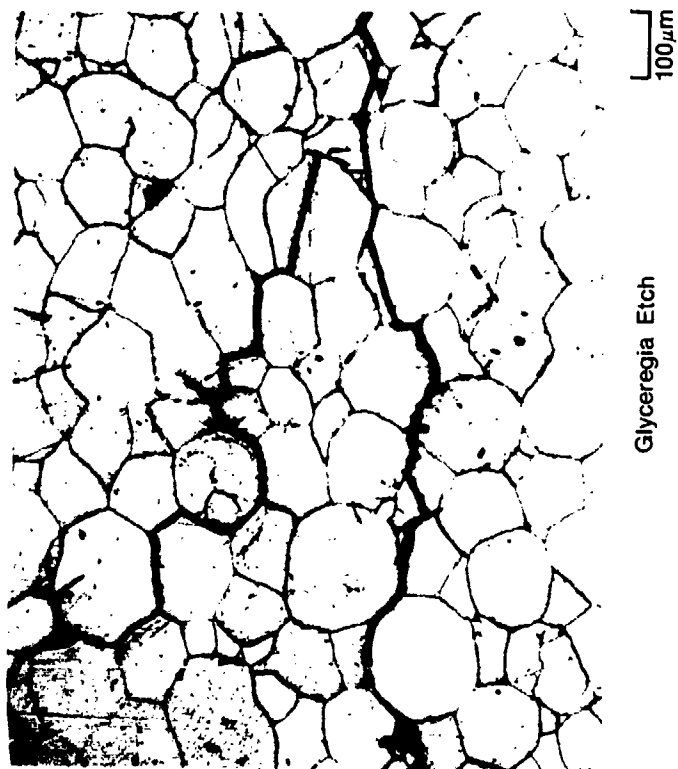
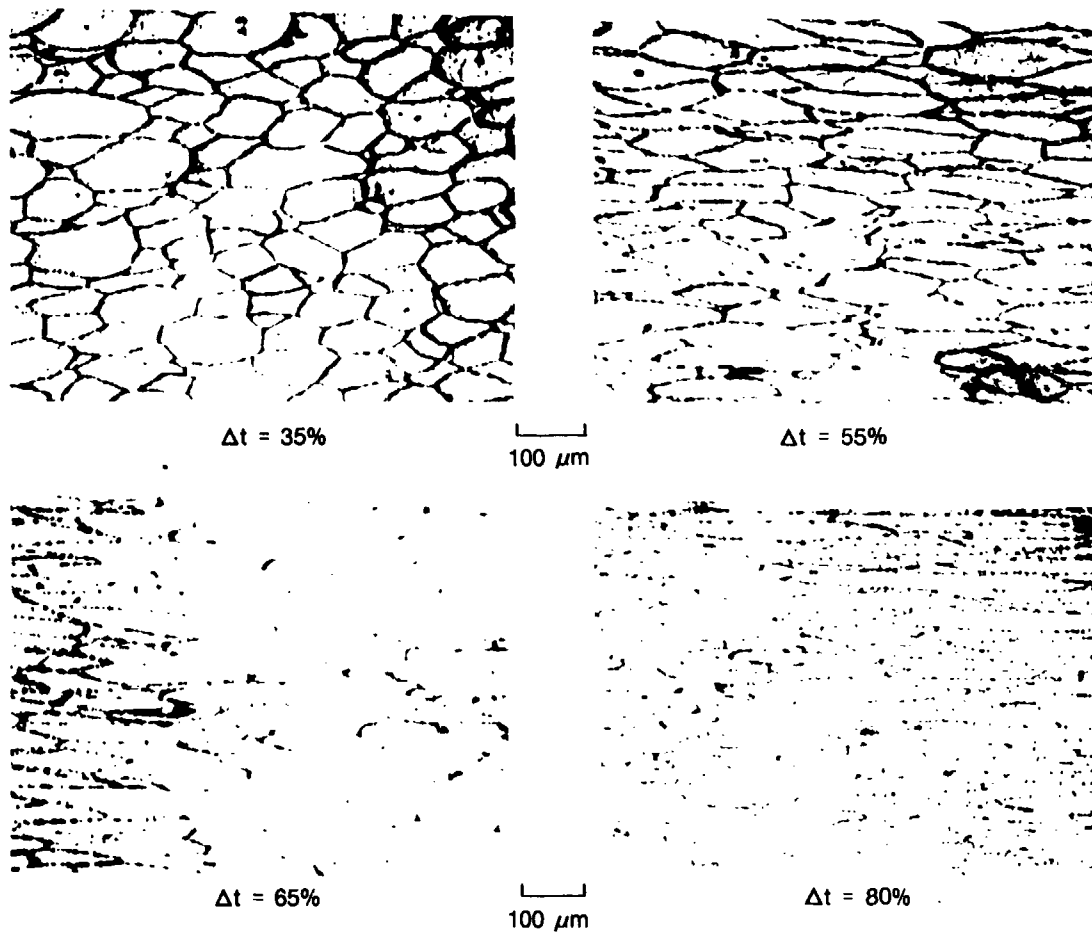
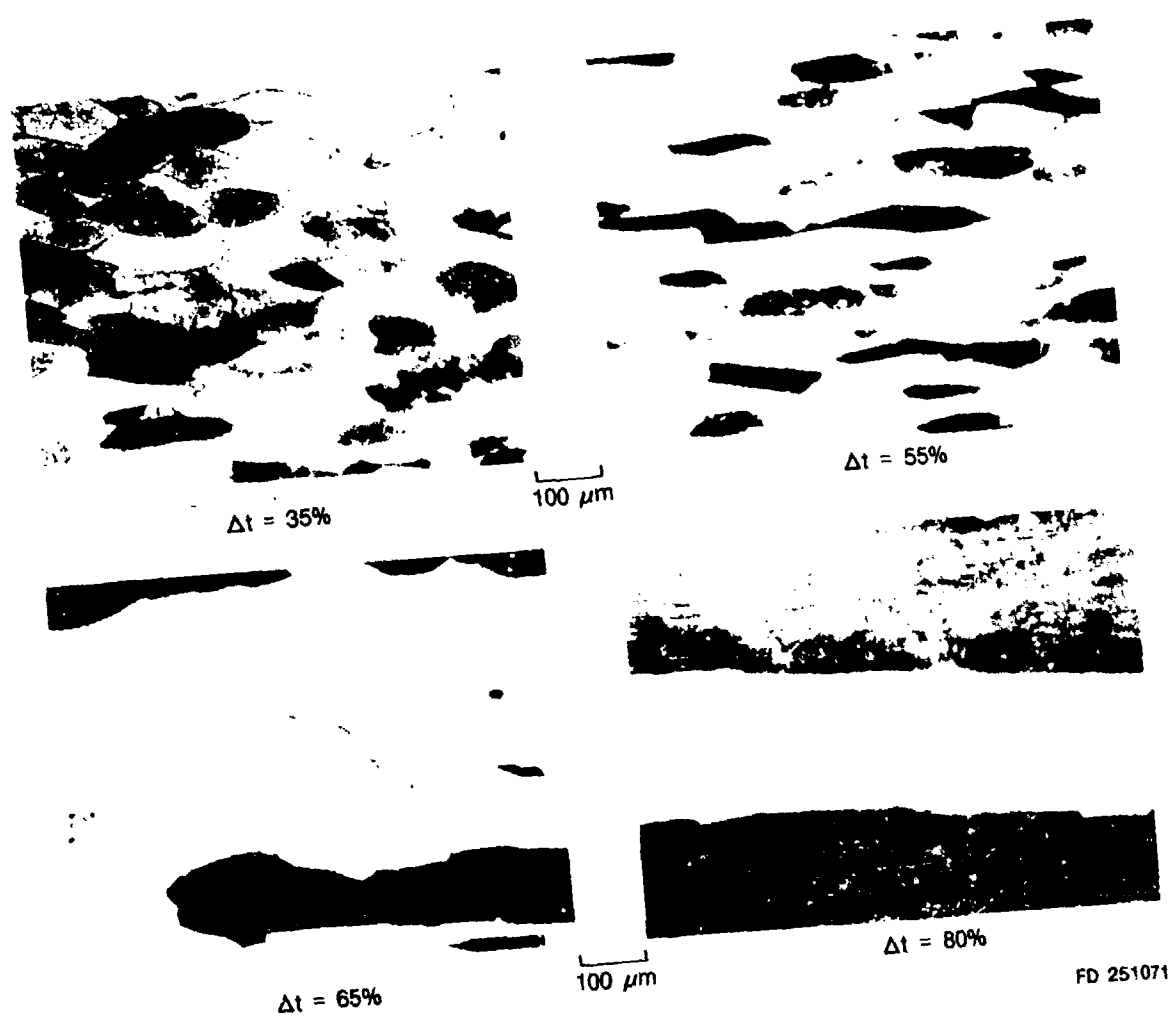


Figure 26. Alloy 729 (Fe_3Al) — HIP 2000°F (1093°C) — Roll 2100°F (1149°C) Kalling's Etch



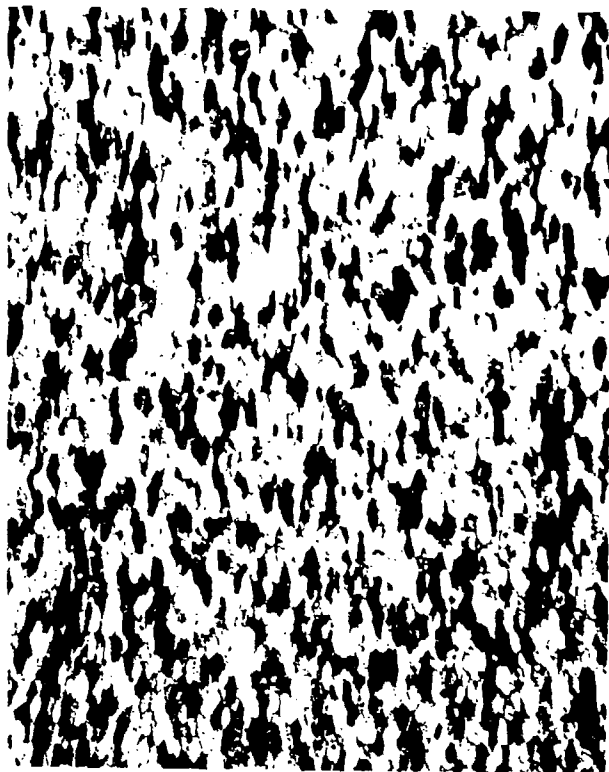
FD 251070

Figure 27. Development of Fiber Structure in Fe_3Al HIP at $2000^\circ F$ and Rolled at $2100^\circ F$



FD 251071

Figure 28. Alloy 729 (Fe_3Al) — HIP at 2000°F -140 +200 Mesh Powder



$\Delta t = 35\%$

500 μm



$\Delta t = 55\%$

500 μm



$\Delta t = 65\%$

500 μm



$\Delta t = 80\%$

500 μm

Figure 29. Alloy 729 (Fe_3Al) — HIP 2000°F (1093°C) — Roll 2100°F (1149°C) Kalling's Etch

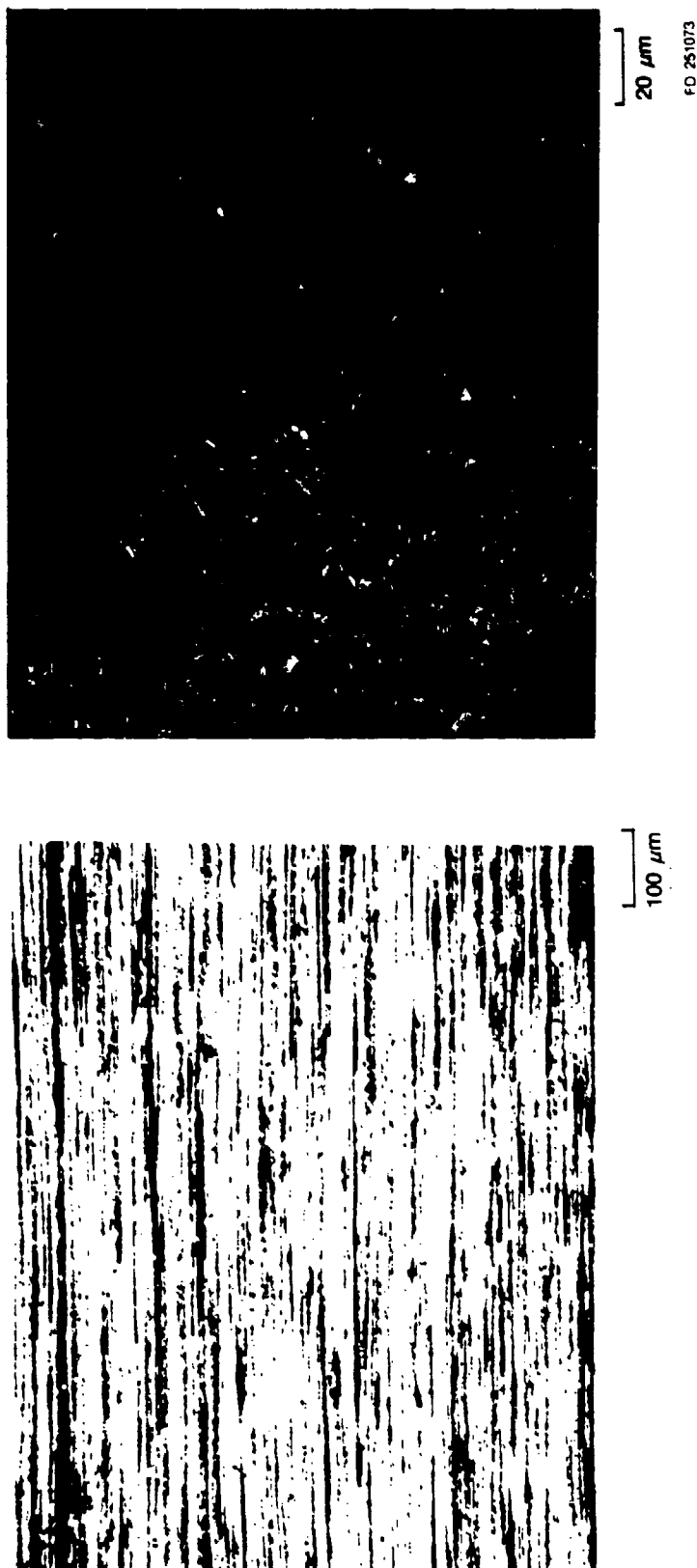


Figure 30. Alloy 729 (Fe₃Al) — HIP 2000°F (1093°C) — Roll 2100°F (1149°C) to 50% — Roll 1150°F (621°C) to 95% Total

FD 251073

As shown in Figure 31, Fe₃Al rolled sheet annealed at 1100°F to 1150°F (593 to 621°C) for 1 hour to relieve internal stress had a reasonable degree of ductility; whereas rolled sheet annealed at 1200°F (649°C) recrystallized and was embrittled. The fracture bend samples exhibited cleavage failure over the entire fracture surface as shown in Figure 32. No evidence was found of point initiation from defects.

The Fe₃Al alloy 729 consolidated by extrusion, warm rolled at 1150°F (621°C) to 0.055-inch thick sheet and annealed at 1200°F (649°C) for 1 hour, was examined by TEM microscopy. This alloy showed large regions of typically warm worked dynamically polygonized microstructural areas, with subgrain sizes of 0.1 to 0.5 microns, interspersed with very large areas showing abnormal grain growth and grain dimensions larger than 15 microns. Figure 33 shows a typical dynamically polygonized area, with the accompanying electron diffraction pattern showing ordered B2 (001) lattice reflections. The average grain dimensions in the microstructural areas showed evidence of partial recrystallization were 0.3 by 1 to 3 microns with the elongated grain axis parallel to the rolling direction. Microscopy clearly showed that abnormal grain growth had already commenced in this alloy after annealing at 1200°F (649°C) for 1 hour, and that it had progressed to the point where 15- to 20-micron diameter recrystallized grains had replaced the dynamically polygonized areas in some 30% of the microstructure examined. Figure 34 shows a typical area where a large grain of (111) zone axis orientation, adjacent to a heavily polygonized area typical of the recovered and dynamically polygonized structure, has replaced that structure by a process of abnormal recrystallization and grain growth.

CONSOLIDATION AND WORKING OF Fe₃Al + TiB₂

Laboratory Scale Processing

The consolidation and working of Fe₃Al + TiB₂ was carried out under the conditions specified in Table 4. The structure of alloy 723, after extrusion at 1750°F (954°C) and swaging to a 0.5-inch diameter rod at the same temperature, is shown in Figure 35. The microstructure of the alloy was found to be coarser and less fibrous than that of alloys of similar composition processed under equal conditions under a P&W in-house program. The Fe₃Al+TiB₂ alloy investigated (Table 5) includes the other alloy compositions (545 and 549) which have the microstructures shown in Figures 36 and 37. The difference in structure was found to be due to a relatively high carbon content with excess boron in the 723 alloy. The presence of carbon in the latter alloy apparently reduced the stability of the boride and its ability to resist grain coarsening during working. This section examines the difference in the microstructures of these alloys.

The evaluation of Fe₃Al + TiB₂ alloys was hampered initially by difficulties in preparing satisfactory metallographic samples. Various chemical etchants and examination by light and SEM produced poorly defined structures where neither the grain structure or even the coarse end of the TiB₂ dispersion could be resolved. The most satisfactory metallographic method currently available consists of etching with a low angle (approximately 5 degrees) ion beam for 24 hours followed by examination of samples in SEM using the back scatter mode. With this method, both the grain structure and TiB₂ dispersion of the alloys could be compared.

The microstructure of Fe₃Al + TiB₂ (alloy 723) HVC'ed at 1700°F and 30 ksi (927°C and 207 MPa) and at 2000°F and 30 ksi (1093°C and 207 MPa) are shown in Figures 38 and 39. The cellular or dendritic microstructure of as-quenched powder particles, with a secondary dendrite arm spacing of the order of 1 to 3 microns, is still partially defined in consolidated material by the TiB₂ in interdendritic cell walls. As shown in Figure 38, the smaller powder particles which were cooled at a higher solidification rate during atomization have the finer dendritic microstructures. The TiB₂, which is imaged but not clearly defined by SEM, appears to be

coarsening at the higher 2000°F (1093°C) temperature, and a subgrain structure has become better defined. The principal features of these consolidated microstructures include the following. The prior powder particles are clearly defined by apparent segregation of TiB_2 on the surface of the particles and in comparison with Fe_3Al with TiB_2 , the grain size is significantly finer since it is established by the borides within the powder particles. In addition, the structure at some of the triple points appears to have been modified to a considerable extent. Figure 40 shows one of these regions which contains a small undeformed particle adjacent to a larger particle. The titanium X-ray reveals the increased density of titanium and in all probability of TiB_2 in prior particle boundaries. In triple point regions, the absence of titanium suggests that the region forms by diffusion of iron and aluminum during consolidation. The small particle in the triple point area appears to have a finer TiB_2 compared to that in larger particles. Consequently, it is possible that finer particle size fractions will produce finer TiB_2 dispersions in consolidated material.

The microstructure of alloy 723 extruded 4 to 1 at 1700°F (927°C) is shown in Figure 40. The identity of the initial powder microstructure was retained by the presence of TiB_2 in interdendritic cell walls and prior particle boundaries are delineated by coarsened TiB_2 . The structure became aligned in the extrusion direction and the grain size which appears to be related to the size of original dendrites is not well defined. As shown in Figure 40, extrusion at 1750°F (954°C) and a 10 to 1 ratio followed by swaging at 1700°F (954°C) and a 3.5-to-1 ratio produced an aligned structure where coarsening of the TiB_2 as well as some grain growth across prior dendrite arms appears to have taken place. The latter structure, which was clearly defined by TEM, will be shown in a following section of this report. The microstructure of the lower carbon containing $\text{Fe}_3\text{Al} + \text{TiB}_2$ alloy 545 after extrusion and swaging is shown in Figure 41. At the lower magnification, the alloy extruded at 1700°F (927°C) and an 8-to-1 ratio appears to contain the same features found in alloy 723, but it has a finer structure. The same 545 alloy swaged at 1550°F (843°C) was found to have a still finer fibrous structure; thus, suggesting that processing at low temperatures will produce the finest structure.

A direct comparison of alloys 723 and 545 was made with the alloys extruded 10 to 1 and rolled 90% both at 1700°F (927°C). The results are shown in Figure 42. In general, the microstructures have aligned and partly recrystallized or coarsened grain structures with agglomeration or coarsening of the TiB_2 phase. These microstructures do not appear significantly different. However, in the simple bend test described previously, alloy 545 could be bent to a 2t radius, without failure while alloy 723 failed in every test. Figure 43 shows the effects of heat treatment on the ductility of $\text{Fe}_3\text{Al} + \text{TiB}_2$ (alloy 545) rolled strip. As-rolled or heat treated to 1900°F (1038°C) for 1 hour, the alloy could be bent to a 2t radius, but the heat treatment at 2000°F (1093°C) for 1 hour severely embrittled the alloy. Figure 44 shows a general coarsening of the structure of alloy 545 heat-treated at the higher temperature.

The foregoing results point to the importance of controlling the evolution of microstructure during working to obtain ductility in this class of alloys. The situation with Fe_3Al without TiB_2 was straightforward since the changes in microstructure with processing, unaffected by a dispersion, could be defined with standard metallographic techniques. With $\text{Fe}_3\text{Al} + \text{TiB}_2$ alloys, which have initially finer structures, the change in microstructure with deformation was far more difficult to define, because worked structures became ill defined with respect to both grain size and morphology. The work employing refined preparation and SEM techniques for the definition of microstructure was performed to define the structure on a macro-scale. The results are combined with TEM and texture results to fully define the structures developed in $\text{Fe}_3\text{Al} + \text{TiB}_2$. These results are discussed in a following section of this report.



As-Rolled



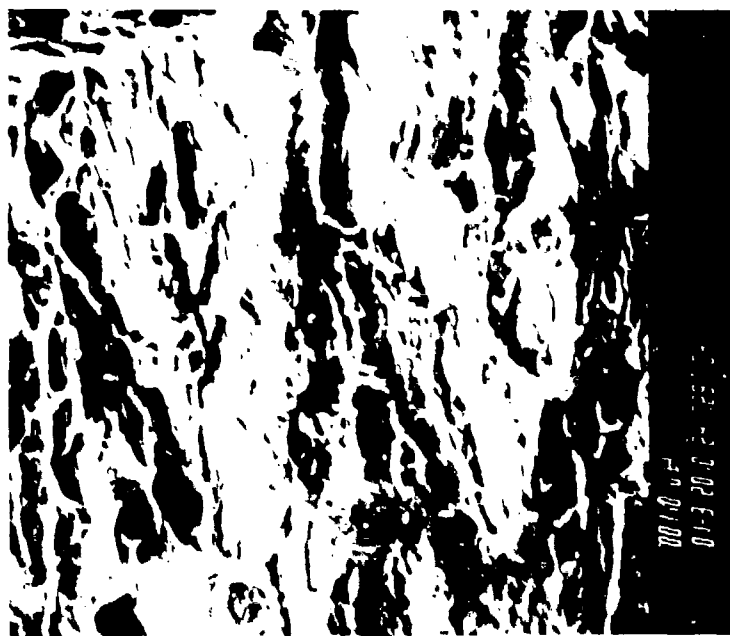
1100 to 1150°F (593 to 621°C) for 1 Hour



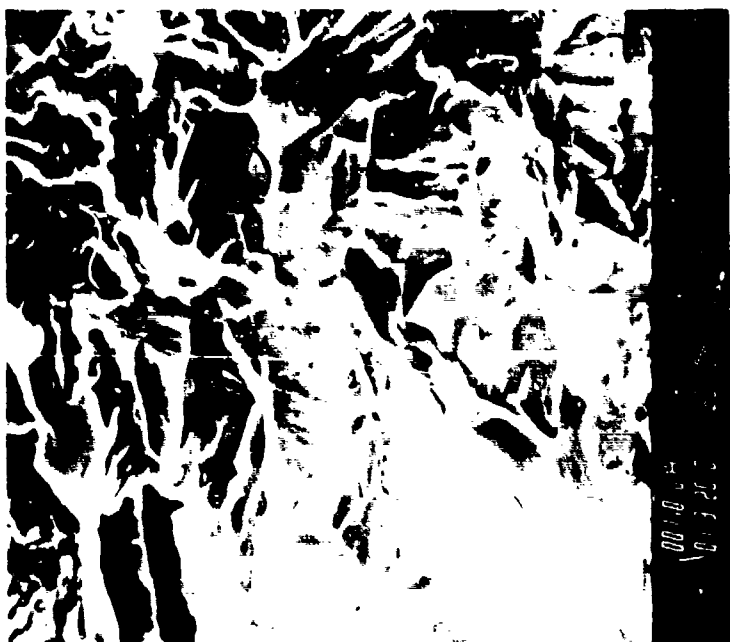
1200°F (649°C) for 1 Hour

FD 245607

Figure 31. Bend Samples Employed to Evaluate the Effect of Heat Treatment on Ductility of Fe₃Al Rolled Strip



As-Rolled



Rolled + 1200°F (649°C)/1 hour

FD 243008

Figure 32. Fracture Surface of Rolled Fe_3Al (729) Alloy Bend Samples



(001) Zone Axis, Fe_3Al B2 Structure Ordered:
Deformed, Recovered and Recrystallized

FD 243610

Figure 33. TEM of Fe_3Al (729) Alloy Consolidated, Post Worked and Annealed at 1200°F (649°C) — Polygonized Area, Partially Recrystallized

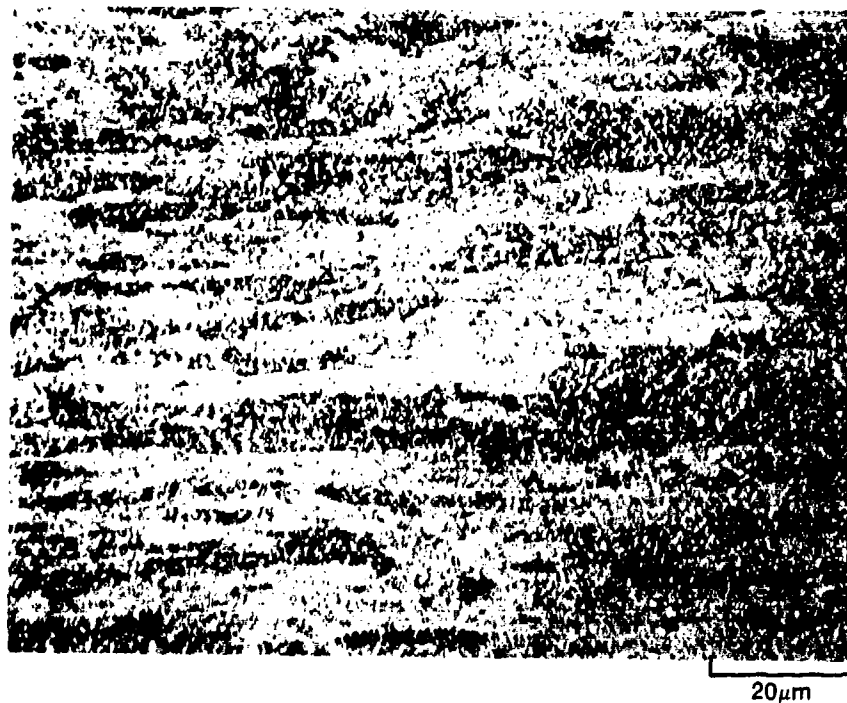
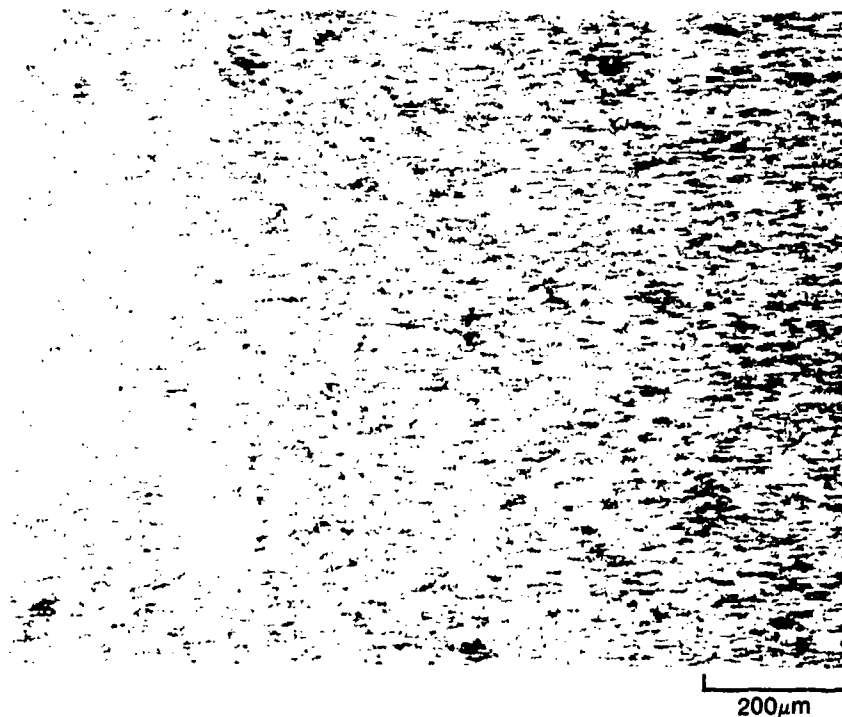


(111) Zone Axis FeAl B2 Structure:
Recrystallized Areas With Abnormal Grain Growth



Figure 34. TEM of Fe₃Al (729) Alloy Consolidated, Post Worked, and Annealed at 1200°F (649°C) — Recrystallized and Polygonized Area Showing Abnormal Grain Growth

FD 243611



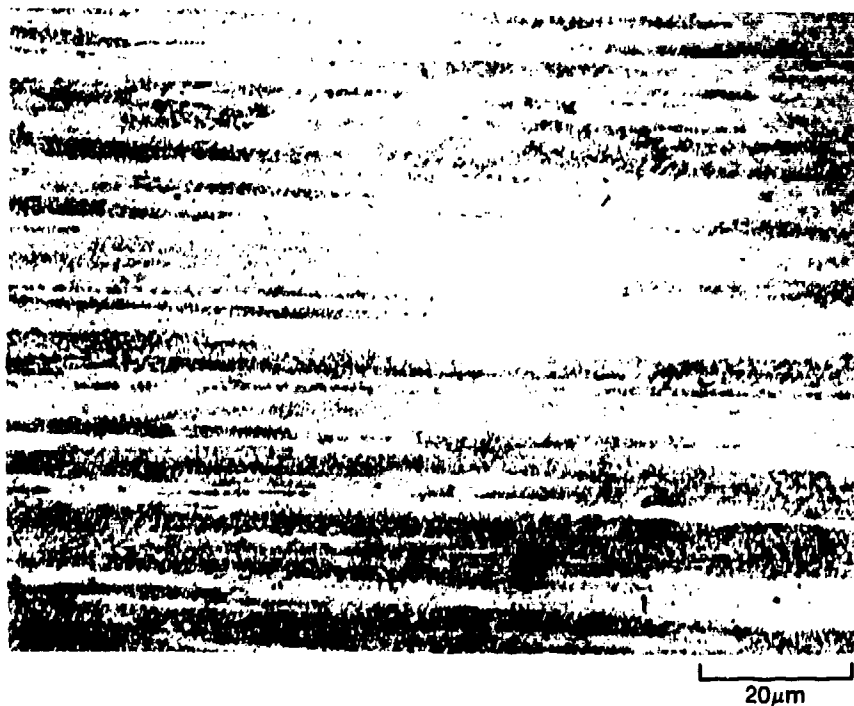
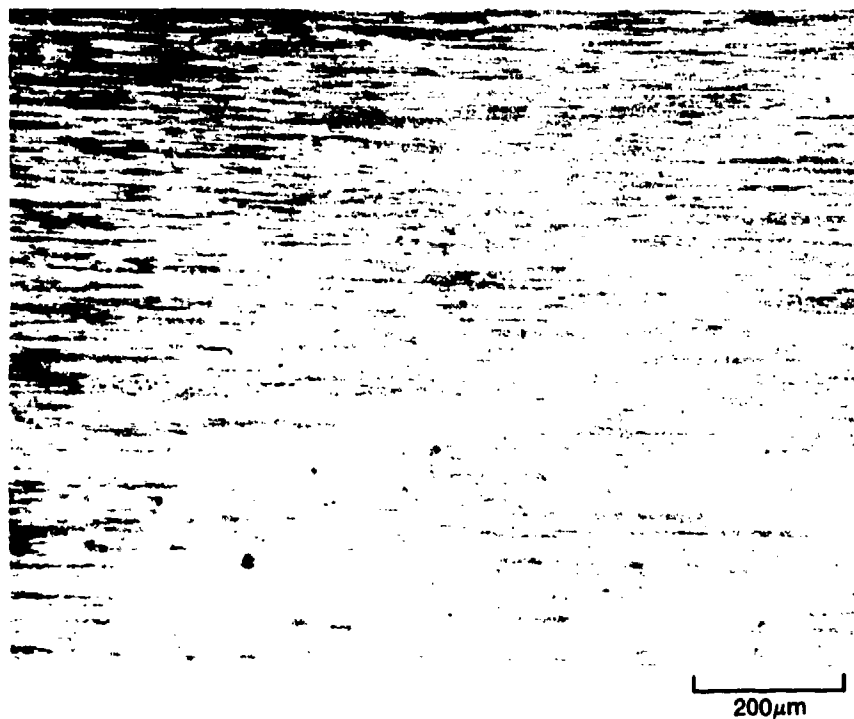
FD 243613

Figure 35. Microstructure of Extruded and Swaged $\text{Fe}_3\text{Al}+1.9\% \text{TiB}_2$ (723) Alloy

TABLE 5. COMPOSITION OF ALLOYS

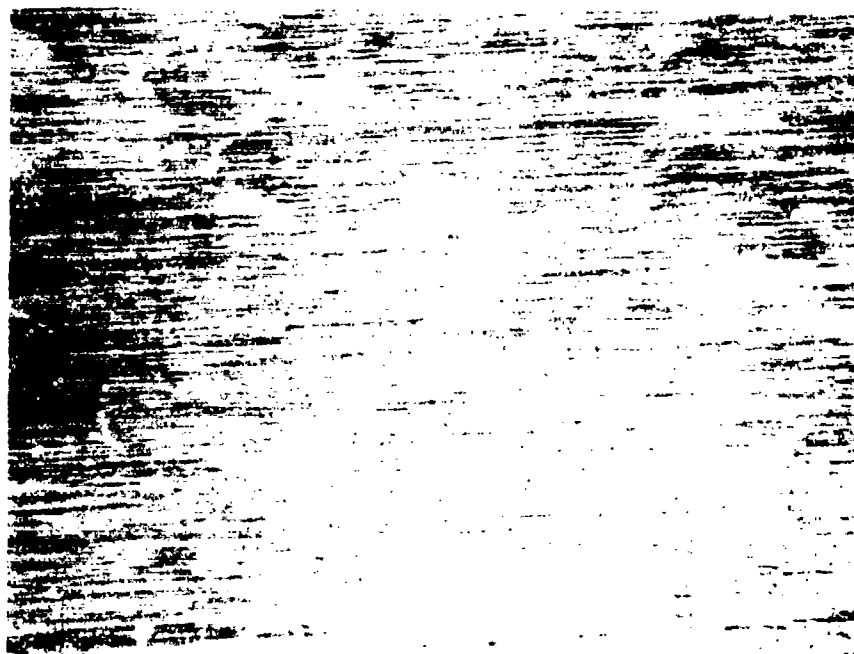
Alloy No.	Nominal Composition, wt%				Analysis of Master Heat, wt%				
	Fe	Al	Ti	B	Fe	Al	Ti	B	C
723, 724	bal	13.6	1.49	0.6	bal	11.3	1.5	0.69	~500
729	bal	13.9	—	—	bal	14.3	—	—	—
545	bal	13.6	1.33	0.6	—	—	—	—	~50
549	bal	13.3	2.82	1.2	—	—	—	—	—

2711C



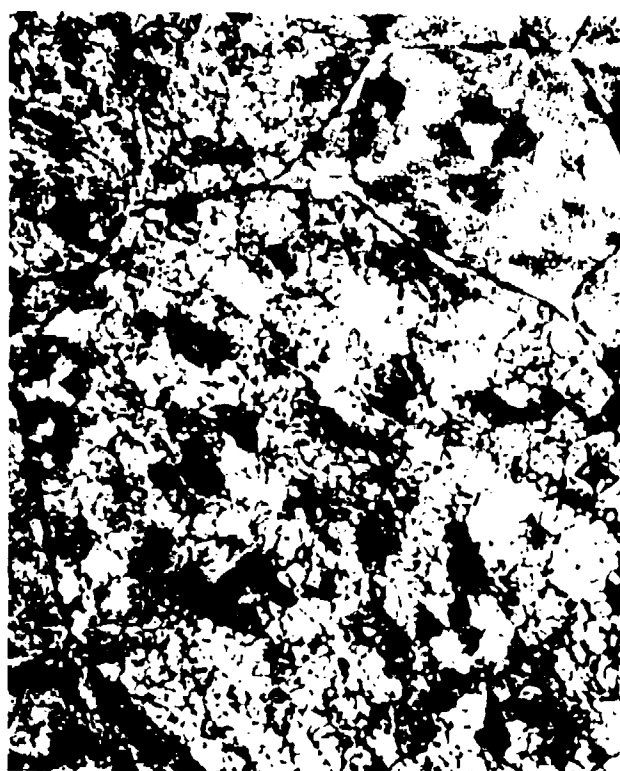
FD 243614

Figure 36. Microstructure of Extruded and Swaged $\text{Fe}_3\text{Al}+1.9\% \text{TiB}_2$ (545) Alloy

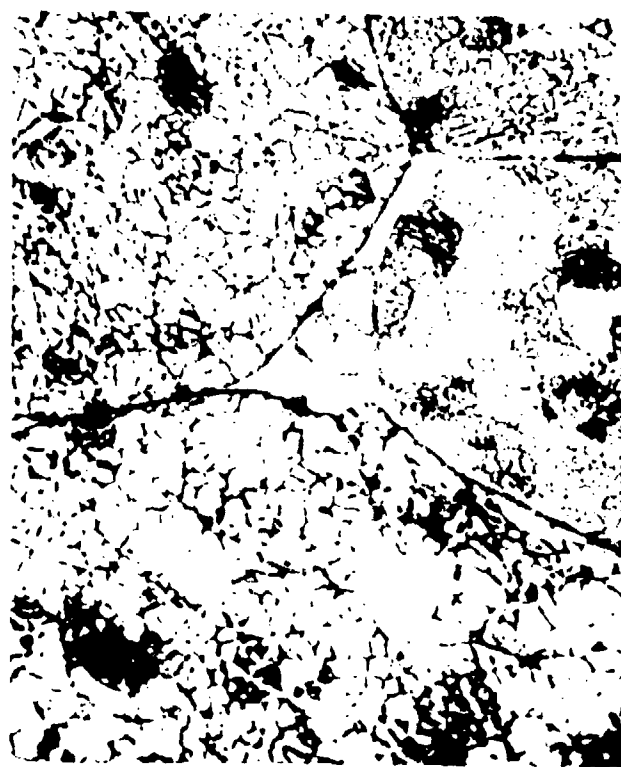


FD 243815

Figure 37. Microstructure of Extruded and Swaged $\text{Fe}_3\text{Al}+3.82\text{TiB}_2$ (549) Alloy



20 μm



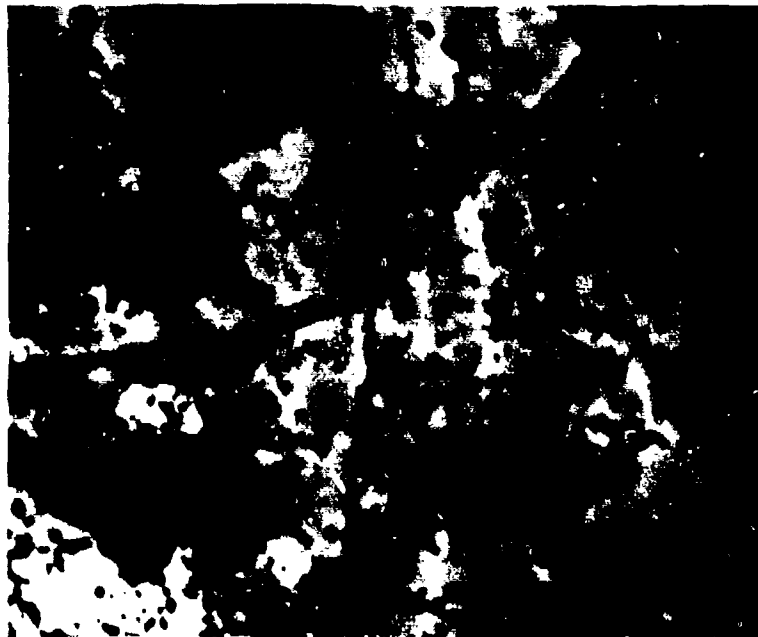
10 μm

FD 251074

Figure 38. Alloy 723 ($Fe_3Al + TiB_2$) — HVC 1700°F/30 ksi — Ion/Mill 5 deg -140 +200 Mesh Powder



20 μm



10 μm

FD 251075

Figure 39. Alloy 723 ($\text{Fe}_3\text{Al} - \text{TiB}_2$) — HVC 2000°F (1093°C)/30 ksi — Ion Beam Mill -140 +20 Mesh Powder



Extruded 4/1 at 1700°F (927°C)

10 μm



10 μm



Extruded 10/1 at 1700°F - Swaged 3.5/1
at 1700°F (927°C)

10 μm



10 μm

Figure 40. Microstructure of Extruded $\text{Fe}_3\text{Al} + \text{TiB}_2$ Powder Extruded 4 to 1 at 1700°F (927°C)



10μm



10μm



10μm

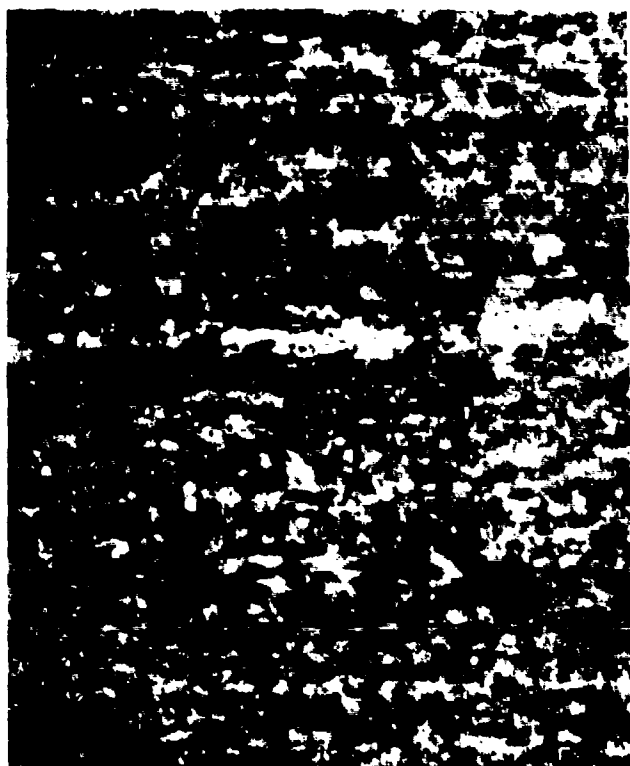
Extruded 8:1 at 1700°F (927°C)



10μm

Extruded 8:1 at 1700°F (927°C) - Swaged 4.5/1 at 1550°F

Figure 41. Alloy 545 ($\text{Fe}_3\text{Al} + \text{TiB}_2$) Extruded and Swaged Microstructures



Alloy 545

10 μ m



Alloy 723

10 μ m



Alloy 545

10 μ m

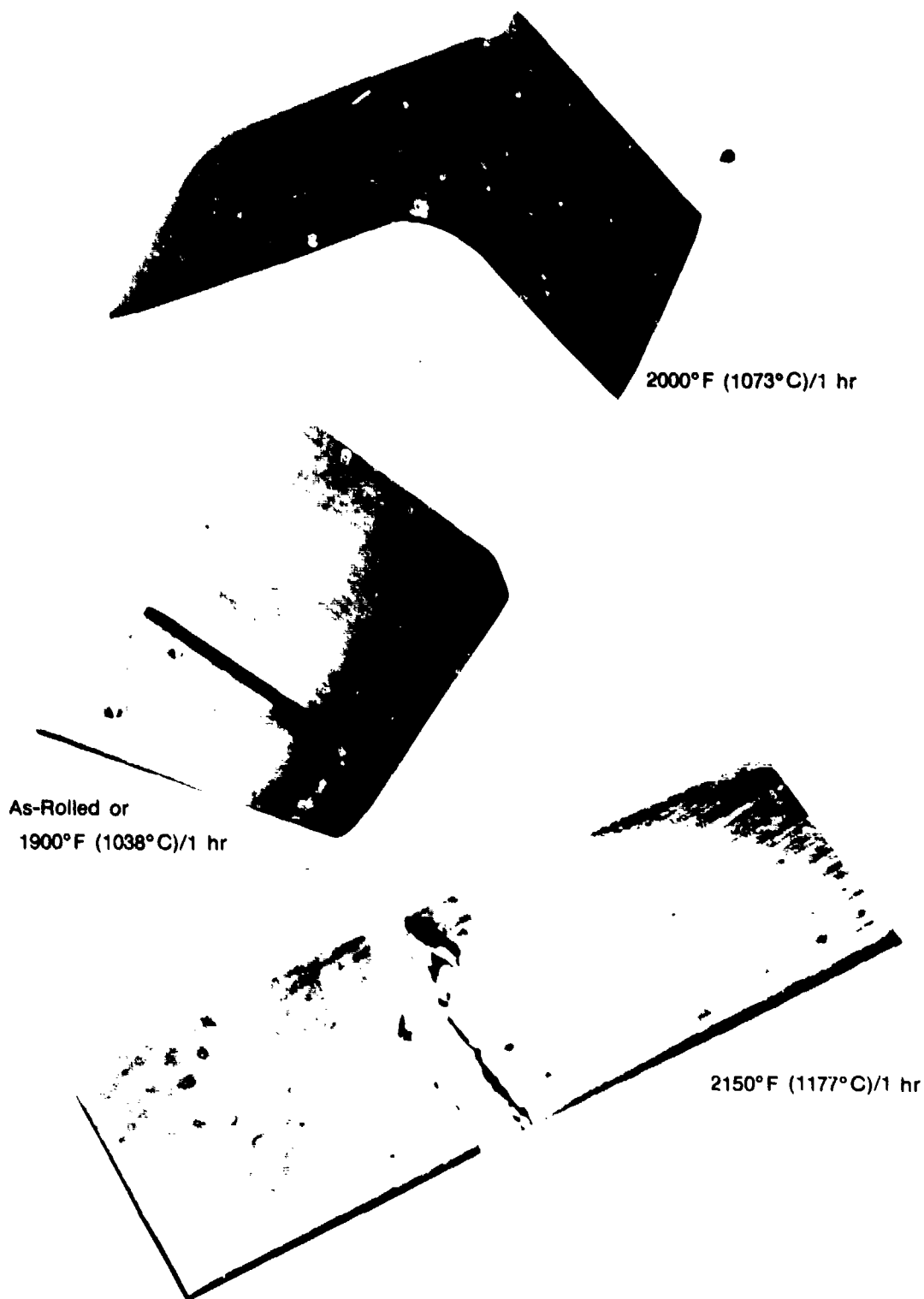


Alloy 723

10 μ m

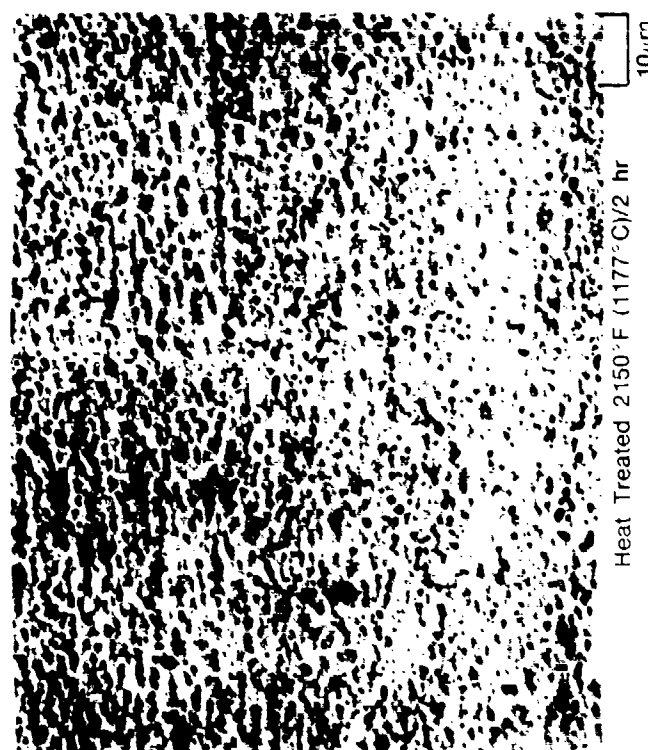
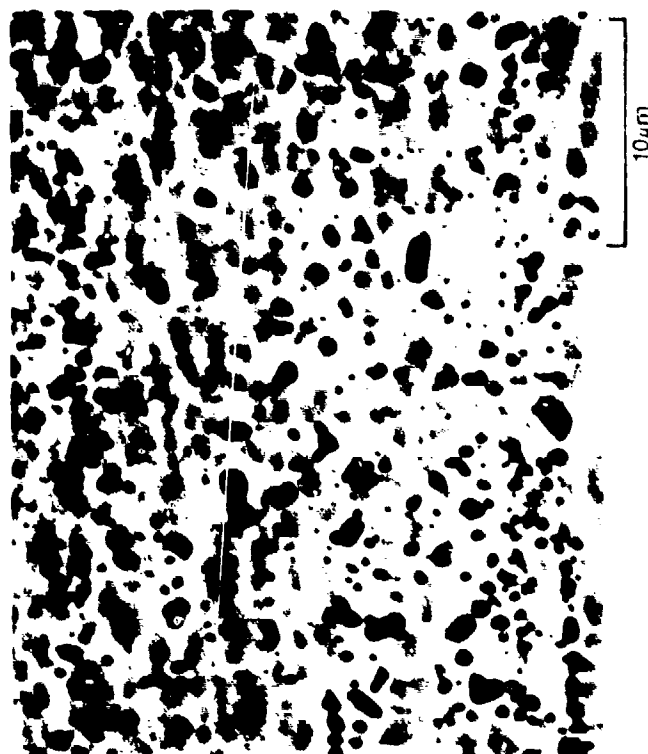
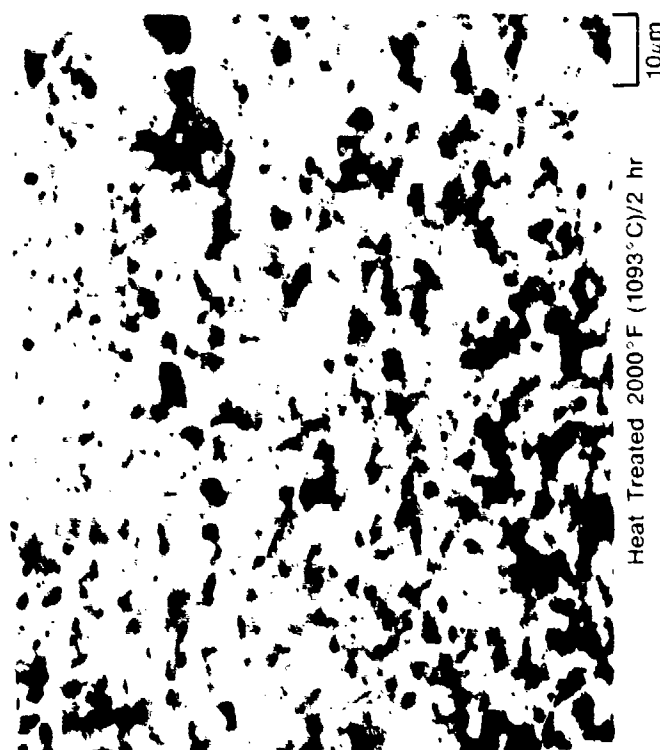
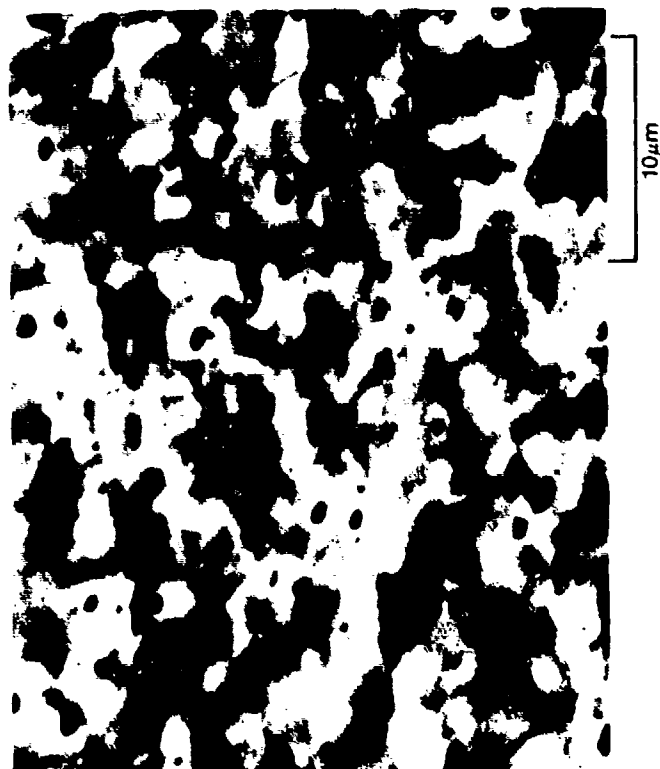
FD 251080

Figure 42. $Fe_3Al + TiB_2$ Extruded 10 to 1 at 1700°F (927°C) and Rolled 90% at 1700°F (927°C)



FD 251081

Figure 43. Bend Samples Employed to Evaluate the Effect on Heat Treatment on Ductility of Fe₃Al + TiB₂ (Alloy 545) Rolled Strip



FD 251083

Figure 44. Alloy 545 — Extruded 8 to 1 at 1700°F (927°C) — Rolled 90% at 1700°F (927°C) and Heat Treated

The processing of $\text{Fe}_3\text{AlTiB}_2$ to bar stock to evaluate the effects of processing on structure and mechanical properties was accomplished by extrusion and swaging. Stainless steel extrusion cans, 3-inch diameter containing about 6 pounds of powder each, were filled in a vacuum and soaked for 2 hours at temperature prior to extrusion. The $\text{Fe}_3\text{AlTiB}_2$ powder employed had been produced in a small experimental powder atomization device where the carbon content was held between 50 and 120 parts per million (ppm). The powder size fractions and processing employed are given in Table 4. The processing was separated into three lots with the first lot, R063 through R075, on the processing of -80 mesh powder; the entire powder size distribution. The second lot, R079 through R100, employed the fine (-270 mesh) and coarse (-80 +100 mesh) powder size fractions. The last lot, R105 through R108, employed four intermediate mesh size fractions with consolidation and working performed under the same conditions to determine the effects of varying powder size or solidification rate on alloy microstructure and properties.

Extrusions of all powder lots listed in Table 6 were at a nominal 8-to-1 ratio and subsequent swaging was carried out to a 75% reduction in area. The first lot of extrusions, R063 through R075, were extruded at temperatures from 1700 to 2250°F (927 to 1232°C) to determine the degree of structural coarsening with increasing temperature. Subsequent swaging was performed at 1500°F and 2000°F (815 to 1093°C). In some cases, one half of the swaging was performed at the higher (2000°F) temperature followed by swaging at the lower (1500°F) temperature. In other cases, the order of swaging was reversed. Subsequent annealing of swaged material was carried out at the final swaging temperature for times of 1 hour or less as indicated in Table 5. The second lot of extrusions, R079 through R100, which contained the fine and coarse powders, was extruded at temperatures of 1600 or 1650°F (871 or 899°C) and subsequently swaged at temperatures from 1200 to 1600°F (649 or 871°C). The third lot of extrusions which contained different powder size fractions, R105 through R108, were all extruded at 1650°F (899°C) and swaged at 1300°F (704°C).

Microstructural and mechanical property evaluations of the material produced in Table 5 are discussed in a following section of this report.

Large Scale Processing of Fe_3Al and $\text{Fe}_3\text{Al} + \text{TiB}_2$

Large scale consolidation and working of Fe_3Al and $\text{Fe}_3\text{Al} + \text{TiB}_2$ alloy powders were carried out to produce the cross sections of material required for transverse and other property measurements. The consolidation was carried out by the extrusion of 7.25-inch diameter stainless containers each filled with approximately 45 pounds of powder. The extrusion container used and a schematic of a hot dynamic outgassing unit employed to fill the containers are shown in Figures 45 and 46. The outgasser consists of mechanical and diffusion pumps, a transfer tube with heating furnace and means for attaching a reservoir prefilled with powder (transferred in a helium drybox) and an extrusion container. The system including the powder reservoir and extrusion container were evacuated to 10^{-5} torr and the furnace heated to 1000°F (538°C) prior to transfer of the powder. By this procedure, the powder was heated to about 500°F (260°C) to drive off absorbed gases as it was transferred to the extrusion container. Subsequent to filling of the container, the transfer tube was pinched off with a hydraulic press and welded with a tungsten arc to ensure that the sealed tube survives subsequent processing.

The extrusion conditions are stated in Table 7. The 1700°F (927°C) preheat temperature was determined from experience with small 3-inch diameter extrusions produced in a P&W press. The temperature selection was made on the basis of anticipated microstructure and mechanical properties and 1700°F (927°C) was selected instead of a somewhat lower temperature, i.e., 1650°F (900°C), to ensure that the billet would extrude satisfactorily. The 18 hours soak time was estimated from actual times required to heat powder billets of different sizes to different temperatures. The breakthrough pressures of 3050 tons for the Fe_3Al and 3100 and 3600 tons for

the $\text{Fe}_3\text{AlTiB}_2$ were well within press capacity. Extruded bar stock of each alloy or particle size distribution was 1.6 by 3.75 inches in cross section by about 6 feet long.

TABLE 6. THERMOMECHANICAL PROCESSING OF $\text{Fe}_3\text{Al} + \text{TiB}_2$

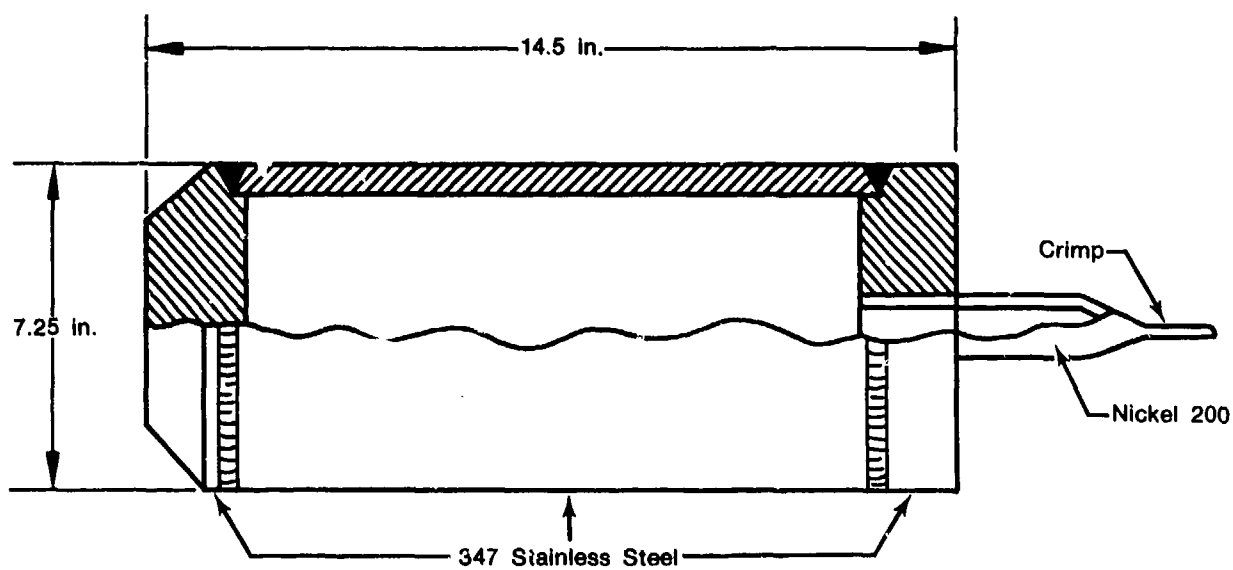
Lot	ID	Powder Mesh Size	Extrusion(a) Temperature (°F)	Swaging(b) Temperature (°F)	Annealing Temp/Time (°F/hr)
1	R063	-80	1700	2000/1500	1500/1
1	R064	-80	2050	2000/1500	1500/1
1	R065	-80	1700	1500	1500/1
1	R066	-80	2250	1500	1500/1
1	R068	-80	2050	1500	1500/1
1		-80	1700	2000	2000/0.25
1	R070	-80	2050	2000	2000/0.25
1	R071	-80	1700	1500/2000	2000/0.25
1	R072	-80	2250	1500/2000	2000/0.25
1	R073	-80	2050	1500/2000	2000/0.25
1	R075	-80	1850	1500/1900	1900/0.25
2	R079	-80 +100	1650	1600	1600/1
2	R080	-270	1650	1600	1600/1
2	R081	-80 +100	1650	1300	1300/1
2	R082	-270	1650	1300	1300/1
2	R088	-80+100	1650	1450	1450/0.5
2	R089	-80 +100	1600	1450	1450/0.5
2	R090	-270	1650	1450	1450/0.5
2	R091	-270	1600	1450	1450/0.5
2	R097	-80 +100	1650	1200	1200/0.25
2	R098	-80 +100	1600	1200	1200/0.25
2	R099	-270	1650	1200	1200/0.25
2	R100	-270	1600	1200	1200/0.25
2	R105	-80 +100	1650	1300	1300/0.5
3	R106	-120 +140	1650	1300	1300/0.5
3	R107	-170 -200	1650	1300	1300/0.5
3	R108	-230 -270	1650	1300	1300/0.5

(a) All extrusions were at a nominal 8 to 1 extrusion ratio.

(b) Where two temperatures are shown, one half of the swaging was at the first temperature listed and the balance at the second temperature.

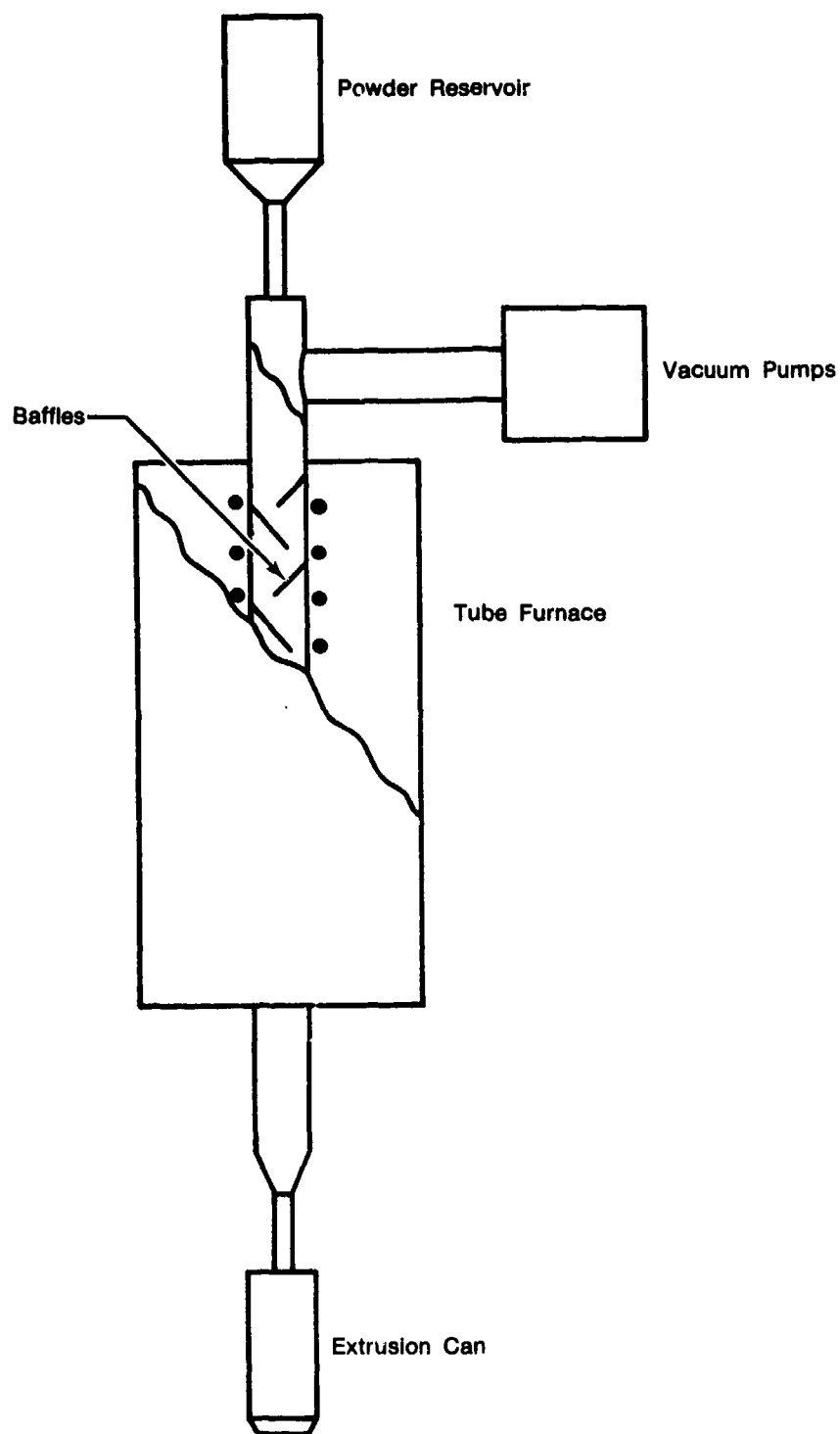
2711C

The three AMAX extrusions were cut into convenient lengths for subsequent rolling and forging. The cut surfaces of cross sections were sound, and all extrusions appeared satisfactory for subsequent working. The Fe_3Al extruded bar stock was rolled without de-jacketing at 1150°F (621°C) in 3 to 10% reduction steps (0.05-inch per pass) from 1.6- to 0.5-inch thick plate, Table 8. The total reduction was about 68%. Between each rolling pass, the material was reheated for approximately 10 minutes. The $\text{Fe}_3\text{Al} + \text{TiB}_2$ extruded bar stock produced with the two powder size fractions was rolled at 1500°F (815°C) by the same procedure except that the reduction per pass was increased to 6 to 13% (0.1 inch per pass). A portion of the $\text{Fe}_3\text{Al} + \text{TiB}_2$ extrusion was rolled to a total reduction of about 68% as for the Fe_3Al alloy, and another portion was rolled to a 0.9-inch thickness to provide plate from which to machine 0.5-inch thick fracture toughness samples.



FD 270900

Figure 45. Extrusion Can



FD 271839

Figure 46. Schematic of Hot Dynamic Outgasser

TABLE 7. LARGE SCALE EXTRUSION AT AMAX

	Alloy		
	Fe_3Al	$Fe_3Al + TiB_2$	$Fe_3Al + TiB_2$
Mesh Size	-80	-270	-80 + 140
Preheat Temperature	1700°F (927°C)	1700°F (927°C)	1700°F (927°C)
Preheat Time	18 hr	18 hr	18 hr
Press Temperature	700°F (371°C)	700°F (371°C)	700°F (371°C)
Extrusion Ratio	7.4:1	7.4:1	7.4:1
Ram Speed-Initial	3.5 in./sec	3.5 in./sec	3.5 in./sec
Ram Speed-Steady	2 in./sec	2 in./sec	2 in./sec
Breakthrough Load	3050T	3100T	3600T
Section Size	1.6 × 3.75 in. (4.06 × 9.52 cm)	1.6 × 3.75 in. (4.06 × 9.52 cm)	1.6 × 3.75 in. (4.06 × 9.52 cm)

2711C

TABLE 8. ROLLING CONDITIONS EMPLOYED FOR THE LARGE EXTRUSIONS OF $Fe_3Al + TiB_2$ ALLOY

	Light Pass Schedule	Heavy Pass Schedule
Roll Diameter	10 in.	10 in.
Roll Speed	30 fpm	60 fpm
Draft/Pass	5%	25%
No. Passes for 66% Reduction	24	5
No. Passes for 83% Reduction	37	8
Temperature	1500°F and 1750°F (815°C and 954°C)	1500°F and 1750°F (815°C and 954°C)

2711C

Heat Treatment

As discussed previously, the heat treatment of worked Fe_3Al at or above its recrystallization temperature of 1150 to 1200°F (621 to 650°C) caused grain growth which reduced the ductility of the alloy. In contrast, $Fe_3Al + TiB_2$ was found to be resistant to grain growth to significantly higher temperatures, for example, i.e., 2000°F (1093°C). Where growth did occur, it produced an abnormally large and aligned grain structure which also reduced ductility. A heat treatment study was carried out on the large $Fe_3Al + TiB_2$ extrusions after rolling under varying conditions to determine the stability of the alloy. Rolling parameters were stated in Table 7.

Table 9 gives the abnormal grain growth temperature of the rolled material as determined for samples heat treated for 2 hours at 100°F intervals from 1500 to 2200°F (815 to 1204°C). Included in the table are the results obtained with an $Fe_3Al + TiB_2$ containing 2 wt% molybdenum. These results obtained on P&W funded programs are included to show the pronounced effect of alloying on the resistance to grain growth in this class of alloys. The criterion used to define abnormal grain growth was the presence of at least one abnormally large grain in the polished section of the sample. Typically, abnormal grains were as large as one millimeter thick and one centimeter long and they appeared first on the outside surface in contact with the rolls. The results obtained are represented in Figures 47 and 48.

TABLE 9. TEMPERATURES FOR ABNORMAL GRAIN GROWTH IN $\text{Fe}_3\text{Al} + \text{TiB}_2$ ALLOYS

Rolling Temperature ($^{\circ}\text{F}$)	Reduction (%)	Type of Pass	$\text{Fe}_3\text{Al} + \text{TiB}_2^{(1)}$ -270 Mesh ($^{\circ}\text{F}$)	$\text{Fe}_3\text{Al} + \text{TiB}_2^{(2)}$ -80 +140 Mesh ($^{\circ}\text{F}$)	$\text{Fe}_3\text{Al}+2 \text{ w/o Mo}+\text{TiB}_2^{(3)}$ -80 Mesh ($^{\circ}\text{F}$)
1750	68	Light	2100	—	>2200
1750	68	Heavy	1800	2000	>2200
1750	83	Light	2000	—	>2200
1750	83	Heavy	1500	1700	>2200
1500	68	Light	1800	—	>2200
1500	68	Heavy	1600	2000	>2200
1500	83	Light	1800	—	>2200
1500	83	Heavy	1600	1700	>2200

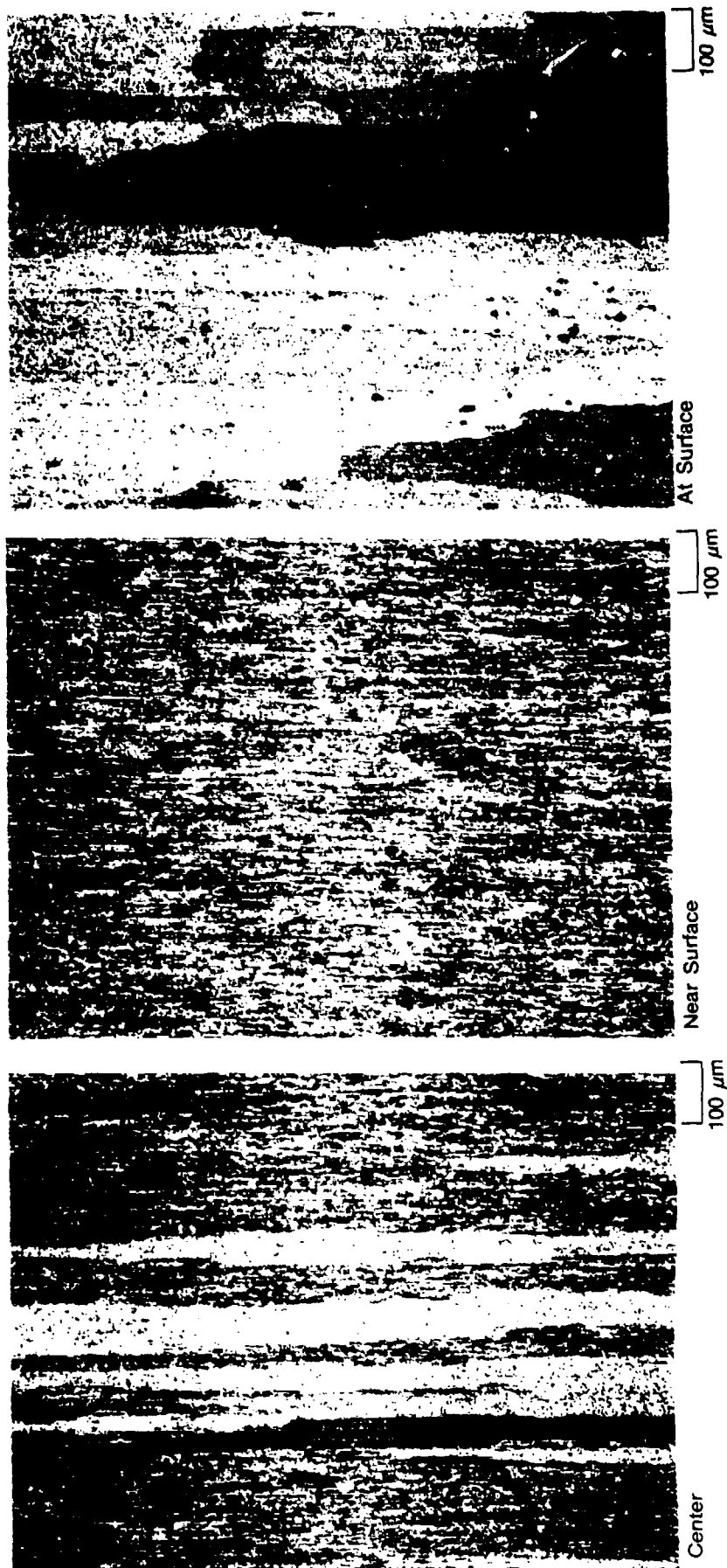
⁽¹⁾Growth Temperature of the Extrusion was 1800°F

⁽²⁾Growth Temperature of the Extrusion was 2000°F

⁽³⁾Growth Temperature of the Extrusion was 2200°F

2711C

As shown in Table 8, the effects of using fine (-270 mesh) instead of coarse (-80 +140 mesh) powder for the processing of $\text{Fe}_3\text{Al} + \text{TiB}_2$ were a decrease in the abnormal grain growth temperature of about 200°F (111°C), i.e., 2000 to 1800°F (1093 to 982°C). In addition, a decrease in abnormal grain growth temperature of at least 200°F (111°C) was obtained by increasing the reduction per pass from 5 to 25%. The combination of light reductions per pass and the higher 1750°F (954°C) rolling temperature raised the abnormal growth temperature at least 300°F (167°C) above the 1500°F (815°C) extrusion temperature. The lowering of the abnormal grain growth temperature (shown in Table 8), due to an increase in total reduction from 63 to 83%, may be as much a result of an increase in quenching from the rolls as it is from an increase in deformation. The effects of alloying with molybdenum were a high abnormal grain growth temperature over 2200°F (1204°C), irrespective of rolling schedule. The latter data are presented to show the high temperature microstructural stability of this class of alloys.

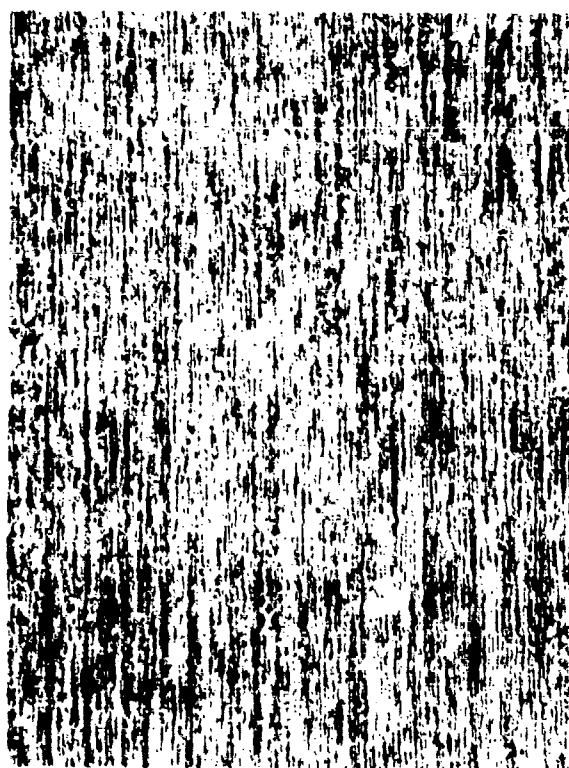


FD283031

Figure 47. $\text{Fe}_3\text{Al} + \text{TiB}_2$ Alloy Rolled 66% in Light Passes at 1500°F Showing Abnormal Grain Growth After 2-Hour Heat Treatment at 1800°C.



100 μm



20 μm

FD 271844

Figure 48. $Fe_3Al + TiB_2$ Alloy Rolled 66% in Heavy Passes at 1750°F Showing Resistance to Abnormal Grain Growth After 2-Hour Heat Treatment at 2200°F

The results of the heat treatment study may be summarized as follows. The recrystallization or abnormal grain growth temperature of $\text{Fe}_3\text{Al} + \text{TiB}_2$ was reduced from about 2100 to 1500°F (1149 to 815°C) by processing or rolling under conditions which increased the amount of strain in the material. The use of lower rolling temperatures, for example, 1500°F versus 1750°F (815°C versus 954°C), high reduction per pass; and increased amount of reduction (85% versus 68%), all tended to reduce the abnormal grain growth temperature. In addition, the use fine (-270 mesh) instead of coarse (-80 +140 mesh) powder also tended to lower the abnormal grain growth temperature. In contrast, $\text{Fe}_3\text{Al} + \text{TiB}_2$ with 2 wt% molybdenum had an abnormal grain growth temperature over 2200°F (1204°C) for material rolled under all conditions.

MICROSTRUCTURAL ANALYSIS

Microstructure of Material Processed in Small Lots

The extruded and swaged $\text{Fe}_3\text{Al} + \text{TiB}_2$ alloy produced from small 3-inch diameter extrusions and which was described in the last section was examined by TEM employing both carbon replicas and thinned foils of the material. The microstructure of Fe_3Al which was found to be considerably simpler was discussed in the section on the processing of Fe_3Al .

TEM With Carbon Replicas

The extruded and swaged $\text{Fe}_3\text{Al} + \text{TiB}_2$ alloy samples listed in Table 10 were produced with the fine (-270 mesh) and coarse (-80 +100 mesh) as well as with the entire (-80 mesh) particle size distribution. The alloy was extruded 8 to 1 at 1600 or 1700°F (871 or 927°C) and post swaged at 1300, 1600, 1700 and 2000°F (704, 871, 927 and 1093°C). The photomicrographs in Figures 49 through 52 were selected to describe, at a reasonably high magnification, the TiB_2 dispersion and grain structure obtained as a function of post working and powder particle size distribution. The following analysis which describes the TiB_2 obtained were found to be in agreement with the results obtained with thinned foils of the alloy. However, the thin foils gave a more accurate measure of the grain size produced in the alloy.

TABLE 10. $\text{Fe}_3\text{Al} + \text{TiB}_2$ ALLOY SAMPLES EXAMINED IN TEM WITH THINNED FOILS

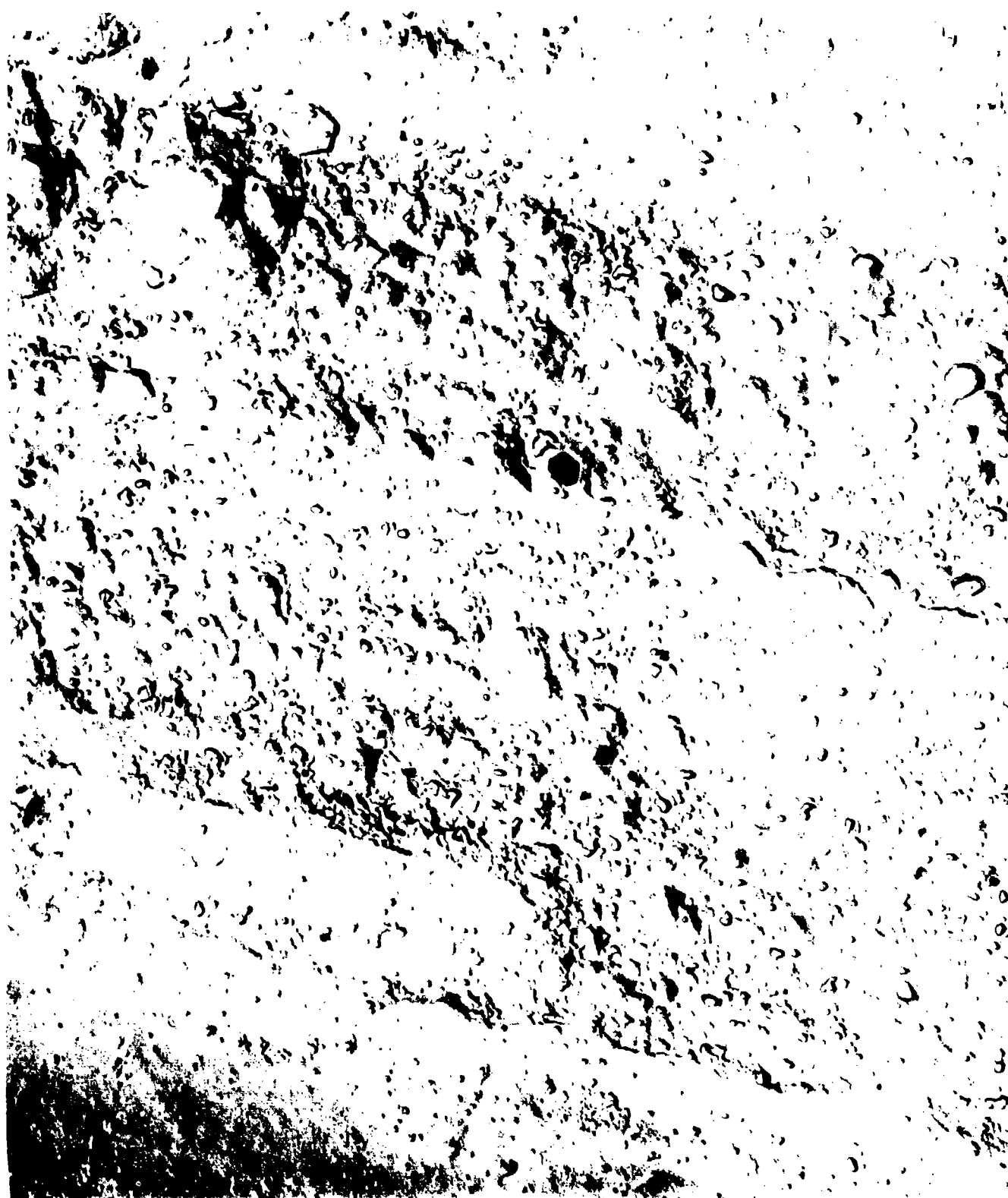
ID	Powder Mesh Size	Extrusion ¹ Temperature (°F)	Swaging ² Temperature (°F)
R069	-80	1700	2000
R079	-80 +100	1650	1600
R080	-270	1650	1600
R081	-80 +100	1650	1300
R082	-270	1650	1300

¹All extrusions at 8:1 ratio

²Swaging to 75% RA.

2711C

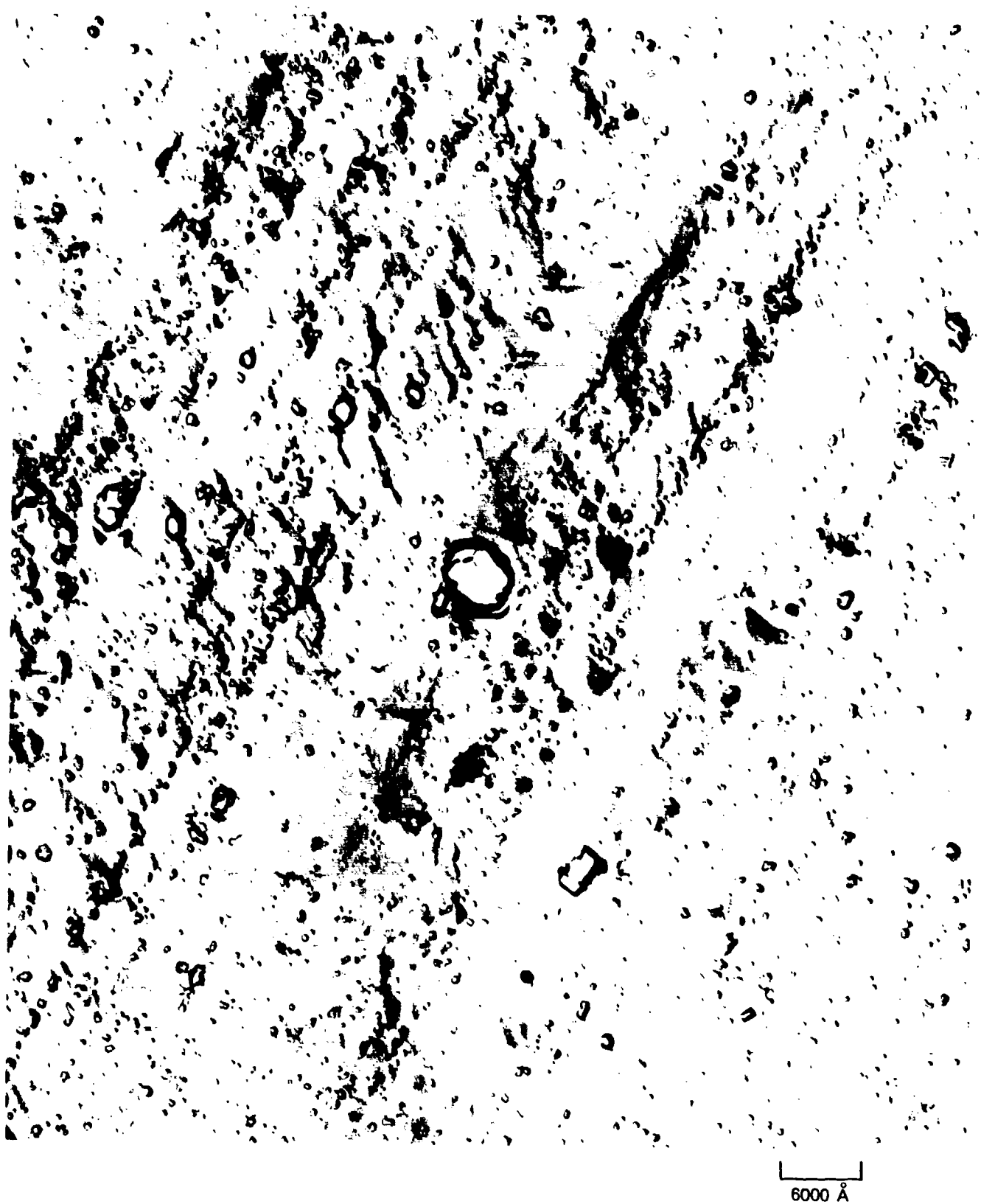
Comparison of Figures 49 through 52 shows that the fine (-270 mesh) powder produced a significantly higher density of a finer TiB_2 dispersion in the alloy than either the entire (-80 mesh) powder size distribution or the coarse (-80 +100 mesh) size fraction. The effect of working (swaging) temperature is pronounced also. Comparison of Figures 49 and 50 shows the increase in the density of TiB_2 obtained by lowering the swaging temperature from 1600 to 1300°F (871 to 704°C) for material produced with the finer (-270 mesh) powder. Figures 51 and 52 for the coarser (-80 mesh and -80 +100 mesh) powders show, as was expected, the coarser TiB_2 dispersion in the material swaged at the higher 2000°F (1093°C) temperature.



6000 Å

FD 267703

Figure 49. TEM of Sample R-82 ($\text{Fe}_3\text{Al} + \text{TiB}_2$) Extruded 8 to 1 at 1650°F and Swaged 75% at 1300°F Fine (-270 Mesh) Powder



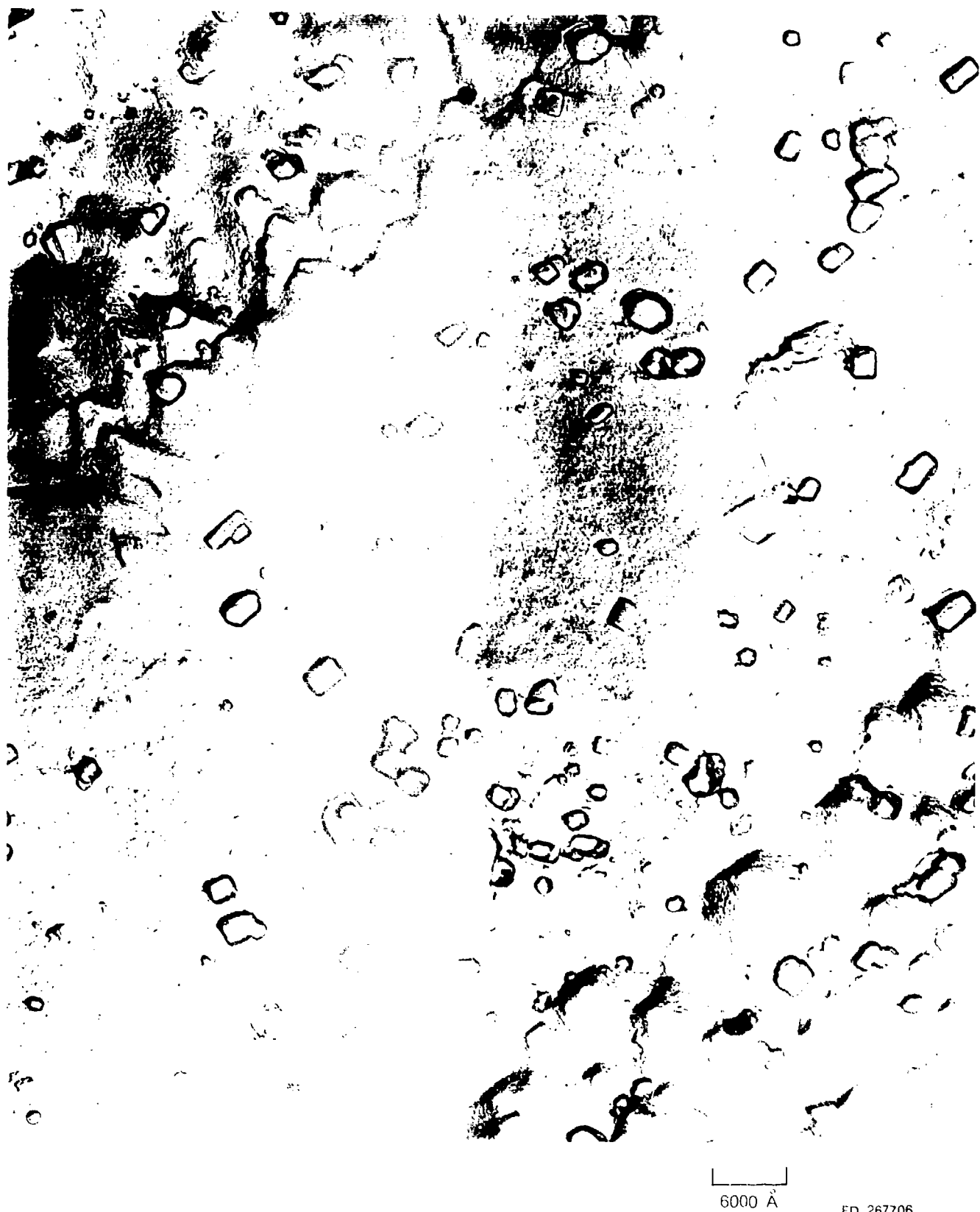
FD 267704

Figure 50. TEM of Sample R-80 ($\text{Fe}_3\text{Al} + \text{TiB}_2$) Extruded 8 to 1 at 1650°F and Swaged 75% at 1600°F Fine (-27C Mesh) Powder



FD 267705

Figure 51. TEM of Sample R79 ($\text{Fe}_3\text{Al} + \text{TiB}_2$) Extruded 8 to 1 at 1650°F and Swaged 75% at 1600°F Course (-80 +100 Mesh) Powder



6000 Å

FD 267706

Figure 52. TEM of Sample R69 ($\text{Fe}_3\text{Al} + \text{TiB}_2$) Extruded 8 to 1 at 1700°F and Swaged 75% at 2000°F Coarse (-80 Mesh Powder)

TEM With Thin Foils

The extruded and swaged $\text{Fe}_3\text{Al} + \text{TiB}_2$ samples listed in Table 10 were examined by TEM. A number of foils were employed for each sample to define the microstructures produced with two different powder size distributions and for material post worked under varying conditions. Previously, it was found that rolling of $\text{Fe}_3\text{Al} + \text{TiB}_2$ under conditions which produced a material with excellent ductility also produced a material with a high aspect ratio grain 1 micron wide by 10 to 20 microns long with a fine substructure 1000 to 5000 angstroms in size. The TiB_2 dispersion on the order of 200 angstroms was found effective in pinning grain and subgrain boundaries and in resisting subsequent grain coarsening during post working and annealing operations. The current investigation describes more fully the effect of powder size and post working on resulting TiB_2 particle size, grain size, and morphology in $\text{Fe}_3\text{Al} + \text{TiB}_2$ processed by extrusion and swaging.

The TEM photomicrographs in Figures 54 and 55 present an overview of the structures obtained in the alloy samples listed in Table 10. Figure 53 shows three areas at two magnifications which are representative of the structure obtained in $\text{Fe}_3\text{Al} + \text{TiB}_2$ produced with coarse (-80 +100 mesh) powder. The variation in structure which is due to partial recrystallization or grain growth was found to be characteristic of material produced with the coarse powder sizes. In comparison, Figure 54 shows four areas at a single magnification in material produced with fine (-270 mesh) powder extruded under the same conditions with post swaging at 1300°F. These figures show how the finer powder produced a more uniform structure with finer and higher aspect ratio grains. The third set of photomicrographs in Figure 55 for material produced with the coarse (-80 +100 mesh) powder extruded at 1650°F (899°C) and swaged at 1300 and 1600°F (704 and 871°C) again show the variation in structure but they also show the effect of working temperature on grain size. The following and closer examination of individual foil samples takes the foregoing findings under consideration to arrive at a correlation between powder mesh size, working temperature, grain size, and TiB_2 dispersion size.

The following table, which summarizes the results obtained, may be referred to in viewing the following photomicrographs selected to show both the structure and the role of the TiB_2 dispersion in the development of structure in $\text{Fe}_3\text{Al} + \text{TiB}_2$ alloys. The entire (-80 mesh) powder distribution and the coarse (-80 +100 mesh) powder size fractions extruded at 1700°F (927°C) and swaged at 2000°F (1093°C) produced the coarsest structure of the series (sample R069 in Table 11) with a grain size averaging 1.5 micron wide by 2 to 10 microns long. The grains were relatively strain free as shown in Figure 56 with dislocations tied to the TiB_2 dispersions. The grain boundaries were also pinned by the dispersion. The TiB_2 which was uniformly dispersed in the structure was found to have a particle diameter in the range of 700 to 1800 angstroms.

As shown in Figure 57, a decrease in the swaging temperature from 2000 to 1600°F (1092 to 871°C) for $\text{Fe}_3\text{Al} + \text{TiB}_2$ produced with the coarse (-80 +100 mesh) powder resulted in a substantial increase in matrix deformation, with a decrease in the size of the dispersion to the range of 300 to 900 angstroms. Variations were observed in the structure, as previously indicated, with grain width 1 to 1.5 microns and corresponding lengths from 2 to about 10 microns. A matrix substructure, approximately 0.5 micron in size was observed where subgrain boundaries are pinned by TiB_2 . In general the TiB_2 dispersion was associated with dislocations, grain boundaries, and sub boundaries in all regions of the sample. The dispersion played a dominant role in the development of the fine structures in the alloy.

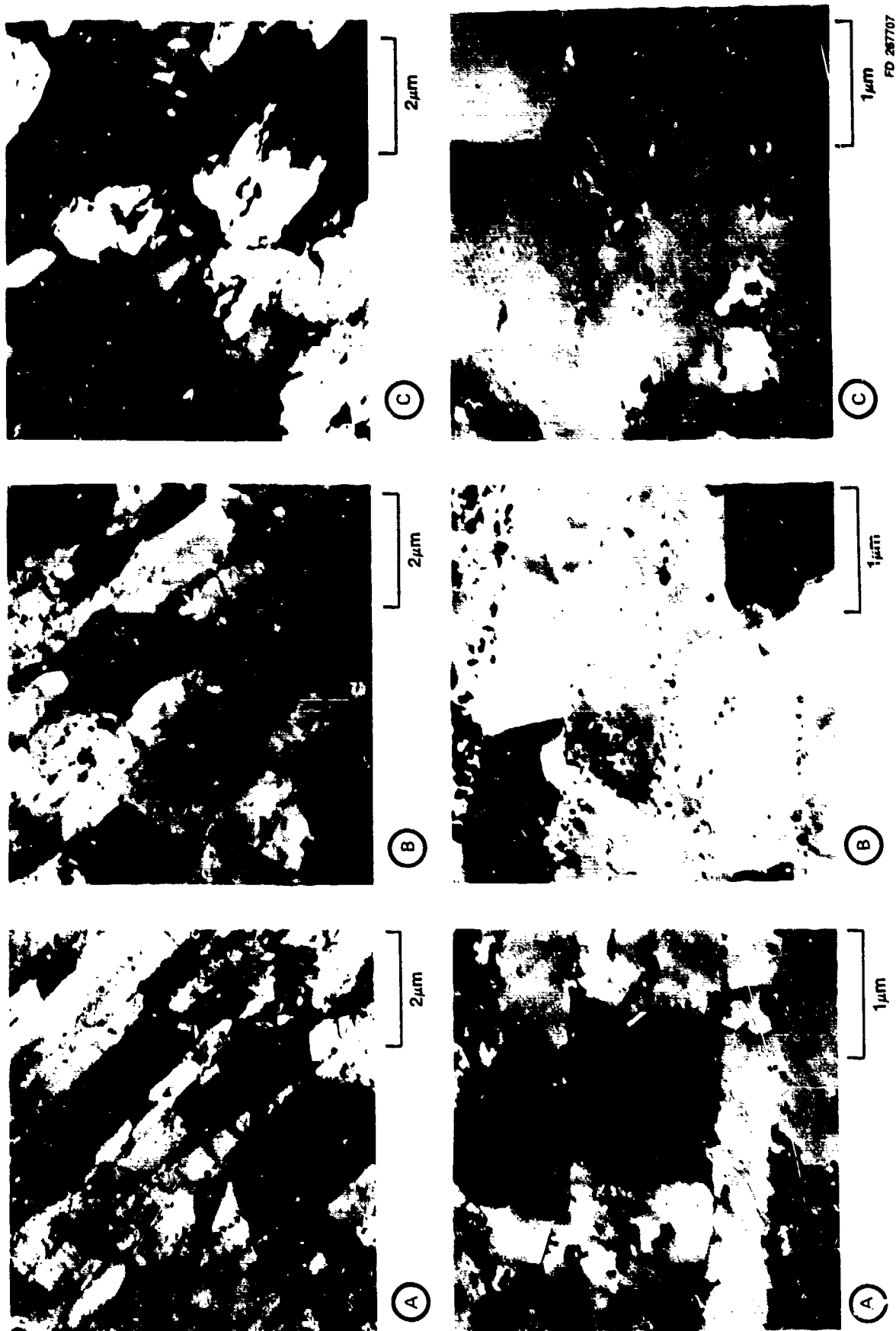


Figure 53. TEM of $\text{Fe}_3\text{Al} + \text{TiB}_2$ Extruded 8 to 1 at 1650°F -80 + 100 Mesh Powder — Three General Areas A, B, and C



Ⓐ



1 μ m



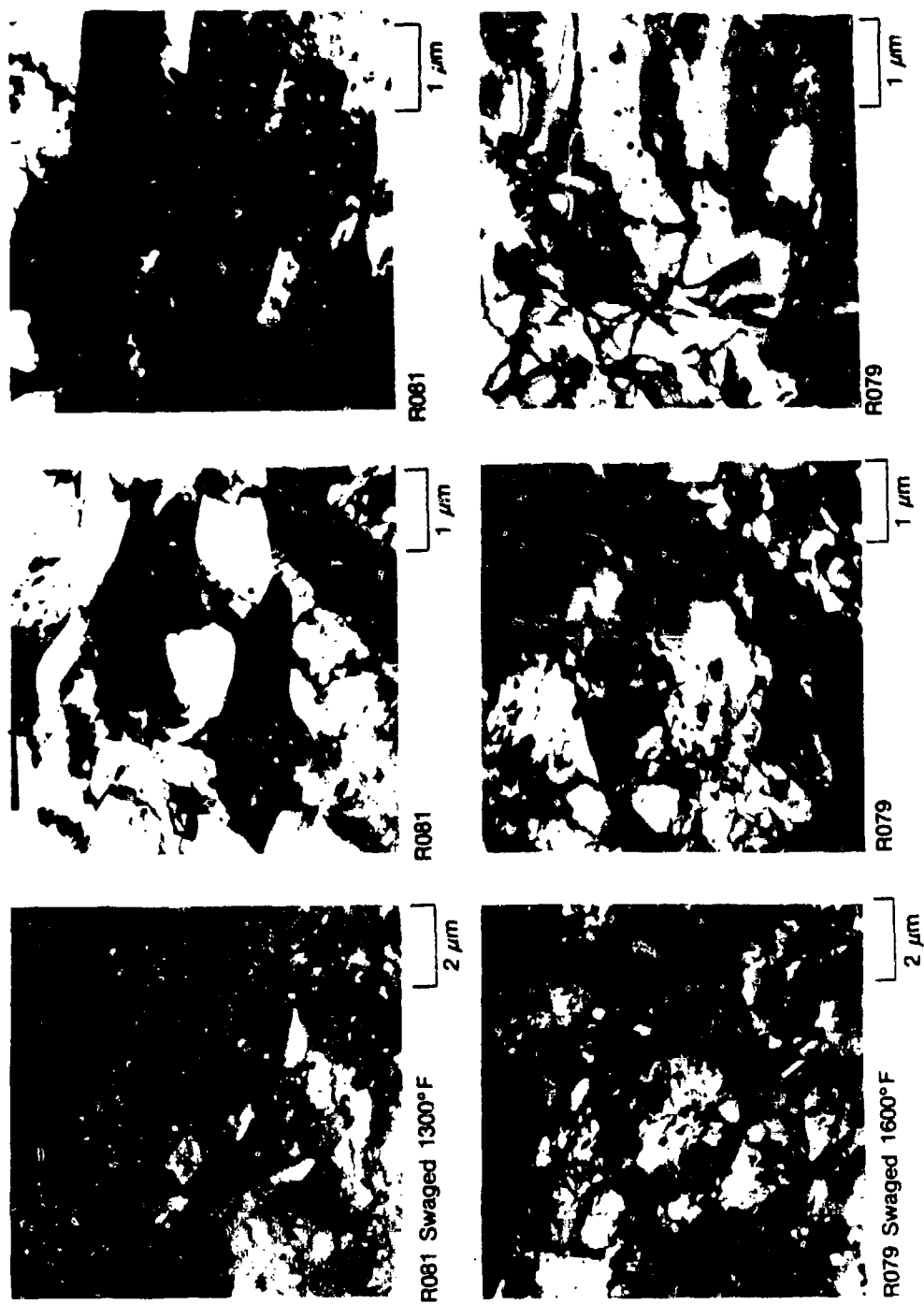
Ⓒ



1 μ m

FD2677J8

Figure 54. TEM of $\text{Fe}_3\text{Al} + \text{TiB}_2$ Extruded 8 to 1 at 1650°F and Swaged 75% at 1300°F (-270 Mesh Powder) — Four General Areas A, B, C, and D



F3087770

Figure 55. TEM of Fe₃Al + TiB₂ Extruded 8 to 1 at 1650°F and Swaged 75% at Two Different Temperatures (~80 + 100 Mesh Powder)

TABLE 11. GRAIN ASPECT RATIO AND TiB_2 DISPERSION SIZE FOR $Fe_3Al + TiB_2$ PRODUCED WITH FINE AND COARSE POWDERS

ID/Mesh	Swaging Temperature		
	1300°F	1600°F	2000°F
R069 -80	—	—	1.5 × 2-10 μm 700Å-1800Å
R079 -80 +100	—	A. 1.5 × 10 μm B. 1 × 2-4 μm 300Å-900Å	—
R081 -80 +100	A. 0.5 × 6 μm B. 0.5 × 2 μm C. 1 × 2 μm 250Å-700Å	—	—
R080 -270	—	1 × 10 μm 200Å-400Å	—
R082 -270	0.5 × 10 μm 200Å-400Å	—	—

All material extruded 8:1 at 1650-1700°F and swaged 75% at temperature indicated A-C grain aspect ratio — thickness × length.

771C



FD 267709

Figure 56. TEM of Sample R069 ($\text{Fe}_3\text{Al} + \text{TiB}_2$) Extruded 8 to 1 at 1700°F and Swaged 75% at 2000°F (-80 Mesh) Powder



FD 267771

Figure 57. TEM of Sample R079 ($\text{Fe}_3\text{Al} + \text{TiB}_2$) Extruded 8 to 1 at 1650°F and Swaged 75% at 1600°F (-80 +100 Mesh) Powder

A further decrease in swaging temperature from 1600 to 1300°F (871 to 704°C) refined the structure as shown in Figure 58. The structure which was derived from the initial powder dendritic structure was found to degenerate to the extent shown in Table 10 for sample R081. The finer structures (region A and B) are fiber structures approximately 0.5 micron in width with lengths varying from 6 to about 2 microns depending on the degree of recovery or partial recrystallization in the alloy. The third structural variation (C) appears as a more equiaxed and somewhat coarser structure with a lower concentration of TiB_2 generally at triple points in the structure.

In contrast with the structures obtained with coarse (-80 +100 mesh) powder, the structure with fine (-270 mesh) powder produced a fiber structure with greater continuity and uniformity. The structure also contained a finer TiB_2 dispersion which was more effective in resisting recrystallization and grain growth. The material produced with fine powder and swaged at 1600°F (871°C), sample R080 in Table 11, has the structure shown in Figure 59. The material contains a moderate dislocation density with a fine polygonized subgrain structure and uniform TiB_2 dispersion 200 to 400 angstroms in size. The fiber structure which is more uniform than found in material produced with coarse (-80 +100 mesh) powder has an average width of 1 micron and length of approximately 10 microns. In comparison to the above, the R082 sample swaged at a lower temperature of 1300°F (704°C) has a similar but finer structure. The structure shown in Figure 60 is completely fibrous with one half the fiber width (0.5 micron) and an equivalent length. The matrix dislocation and TiB_2 dispersion density shown in Figure 61 is moderate, and no greater than observed in the R080 sample swaged at a higher temperature. The TiB_2 dispersion, 200 to 400 angstroms, is about the same as in sample R080, but the lower swaging temperature resulted in a finer structure.

In summary, the use of fine (-270 mesh) instead of coarse (-80 +100 mesh) powder or the entire (-80 mesh) powder size distribution produced $\text{Fe}_3\text{Al} + \text{TiB}_2$ with a higher concentration of a finer TiB_2 dispersion. The finer dispersion offered greater resistance to recrystallization and grain growth during consolidation and post working operations. The use of the finer powder size fraction also produced a more uniform fiber structure of reduced size with a higher aspect ratio and a finer and more uniform TiB_2 dispersion size. The grain size was found to be dependent on swaging temperature with the finer and higher aspect ratio grains produced at the lowest temperature.

Microstructure of Large Scale Extruded and Worked Material

Fe_3Al

Extruded Fe_3Al produced with -80 mesh powder was found to have an equiaxed recrystallized grain structure as shown in Figure 62A. The grain size is seen to be on the order of 50 to 100 microns and coincidentally close to the average powder particle size employed. In TEM's there was little evidence of strain in the material.

As shown in Figure 63A, strings of small irregular particles were found in the structure of extruded Fe_3Al . These particles spaced at intervals of 3.5 to 10 microns in some boundaries were identified as aluminum oxide. They are believed to be spheroidized oxides originating on the surface of the prior powder particles. Also shown in the figure are occasional fine grains, approximately 2 microns, inside boundaries pinned by the oxide particles.



FD 267762

Figure 58. TEM of Sample R081 ($\text{Fe}_3\text{Al} + \text{TiB}_2$) Extruded 8 to 1 at 1650°F and Swaged 75% at 1300°F (-80 +100 Mesh) Powder



6000 Å

FD 267773

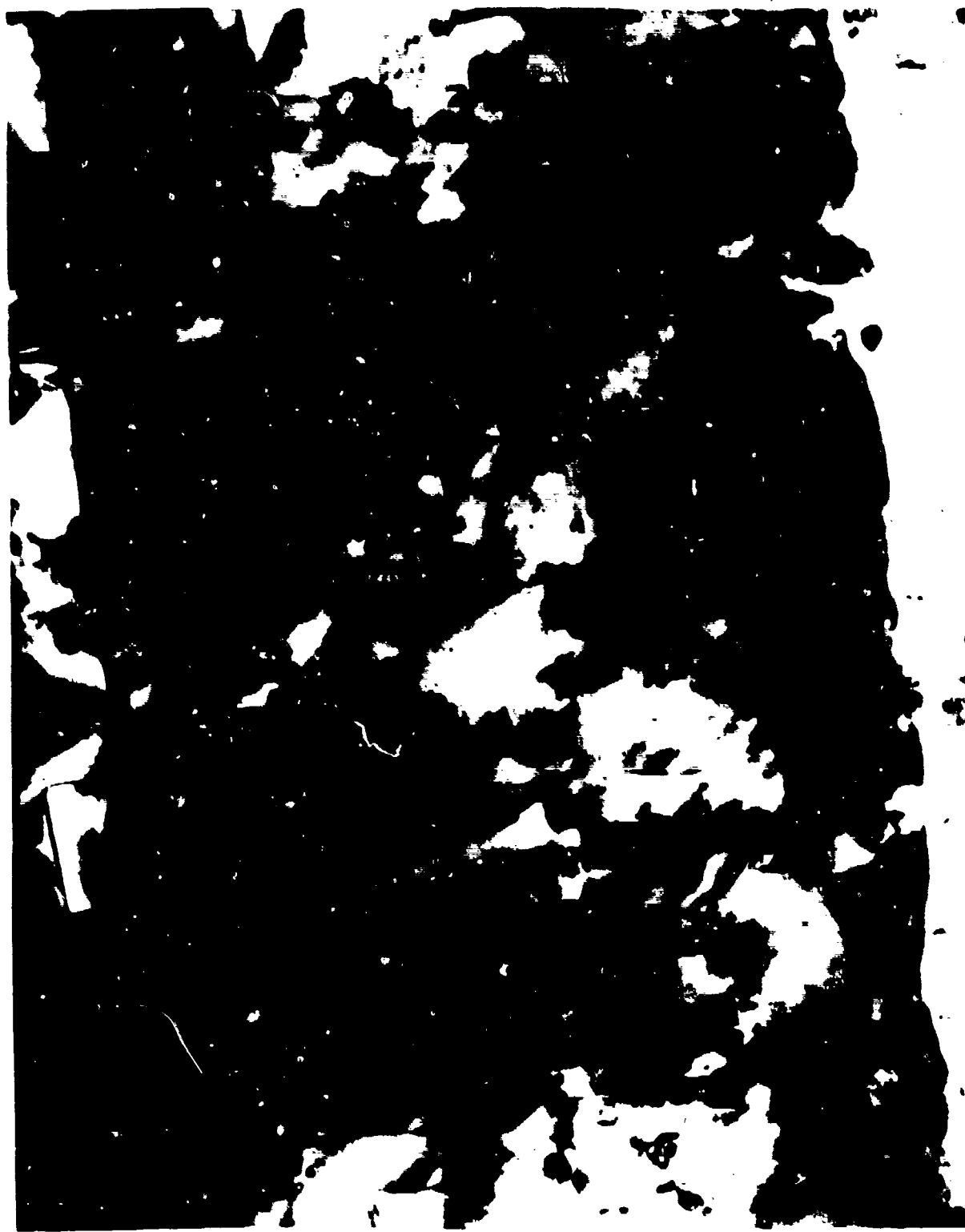
Figure 59. TEM of Sample R080 ($\text{Fe}_3\text{Al} + \text{TiB}_2$) Extruded 8 to 1 at 1650°F and Swaged 75% at 1600°F (-270 Mesh) Powder



6000 Å

FD 267774

Figure 60. TEM of Sample R082 ($\text{Fe}_3\text{Al} + \text{TiB}_2$) Extruded 8 to 1 at 1650°F and Swaged 75% at 1300°F (-80 +100 Mesh) Powder



1000 Å

FD 267775

Figure 61. TEM of Sample P⁸² ($\text{Fe}_3\text{Al} + \text{TiB}_2$) Extruded 8 to 1 at 1650°F and Swaged 75% at 1390°F (-80 +100 Mesh) Powder

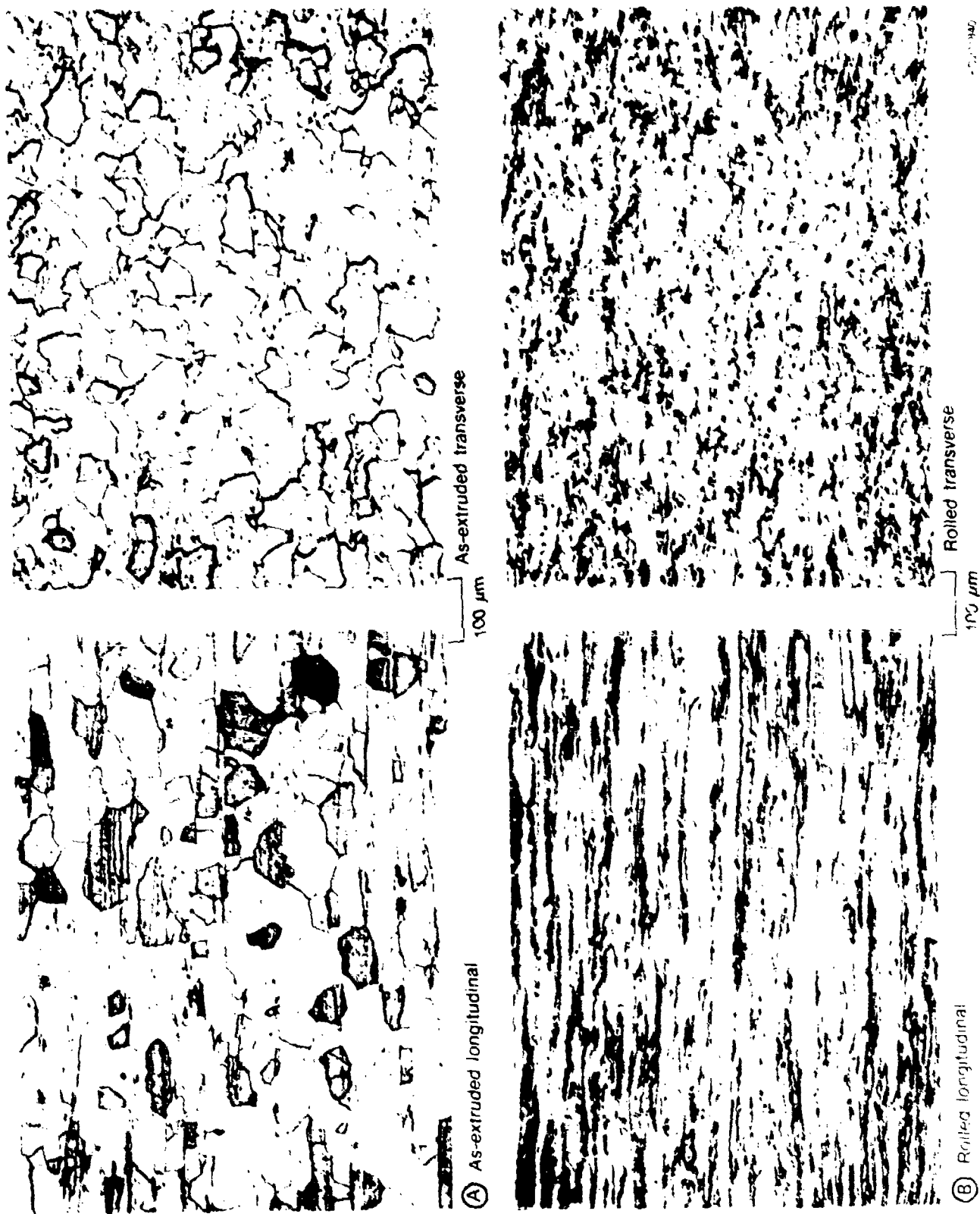
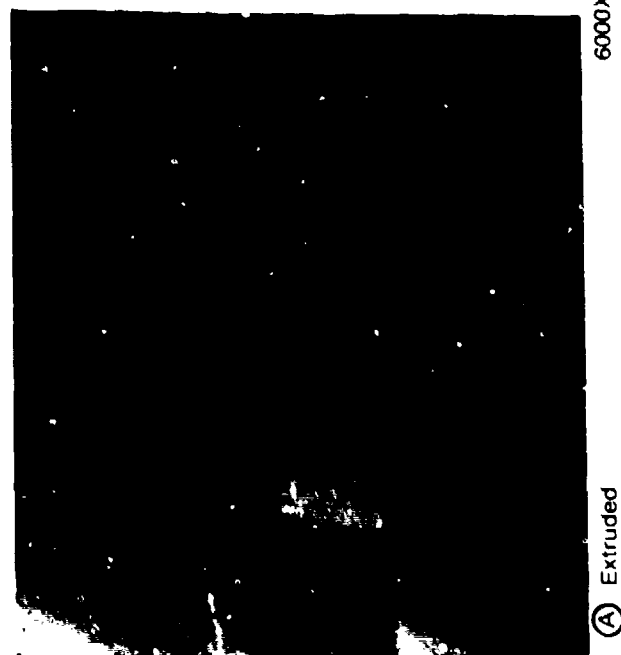
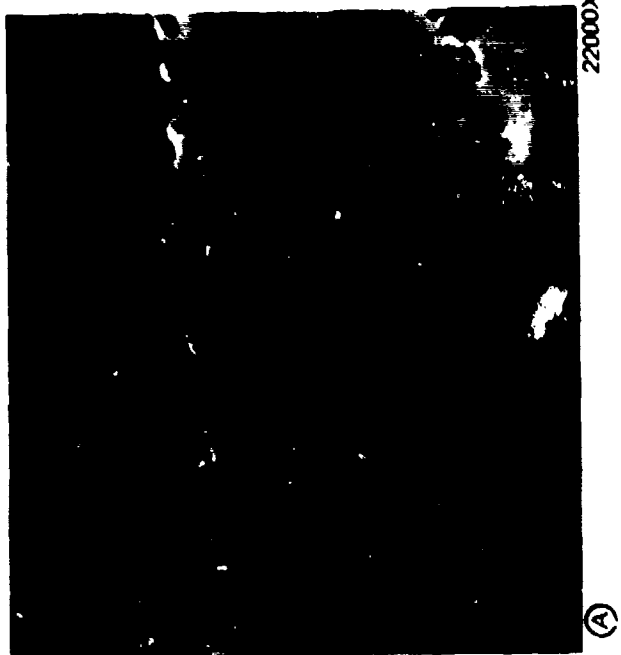


Figure 62. Microstructure of Fe_3Al (A- as Extruded 7.4 to 1 at 1700°F; B- as Rolled 68% at 1150°F)



(A) Extruded

6000X



(A)

22000X



(B) Rolled

6000X



(B)

22000X

FF 270896

Figure 63. Fe_3Al from (-80 Mesh) Powder (A- as Extruded 8 to 1; B- as Rolled 73% at 1150°F.

The structure of rolled Fe_3Al 1150°F (621°C) rolling and annealing temperatures) shown in Figures 62B and 63B, revealed grain refinement and a moderate dislocation density as a result of rolling just below the recrystallization temperature. The aligned grains also contained a ¼- to 2¼-micron subgrain structure. The strings of aluminum oxide particles found in the extruded material were also observed in the rolled structure. The presence of aluminum oxide particles in Fe_3Al was not unexpected since they were found previously in the alloy produced from different batches of powder and consolidated by both HIP and extrusion.

$\text{Fe}_3\text{Al} + \text{TiB}_2$

The $\text{Fe}_3\text{Al} + \text{TiB}_2$ extruded from fine (-270 mesh) and coarse (-80 +140 mesh) powder fractions were found to have few but significant differences in microstructure. A relatively large rod type precipitate was found in the material produced from fine powder. As shown in Figure 64, the precipitates about 0.1 to 0.5 micron thick and 0.4 to 2 microns in length were located in grain boundaries and oriented parallel to the extrusion/rolling direction. These precipitates were identified as TiB_2 possibly deficient in boron. In comparison, the extrusion from coarse powder, Figure 66A, did not contain these large precipitates. Differences in processing should not account for the presence of these coarse precipitates in the material produced with fine powder since the extrusions were carried out sequentially with the extrusion billets pre-heated in the same furnace. However, this type of precipitation was not found in prior small 6-pound extrusions produced previously with the same or equivalent fine (-270 mesh) powder size. Therefore, the precipitation or accelerated coarsening of the TiB_2 phase could be a result of the relatively long soak time (18 versus 2 hours) employed for the larger extrusion billets.

The $\text{Fe}_3\text{Al} + \text{TiB}_2$ extrusion produced with coarse (-80 +140 mesh) powder had a somewhat more elongated grain structure and localized areas containing a higher dislocation density. The elongated grains, ½ to 2 microns in thickness and 1 to 3 microns in length, were essentially strain free while equiaxed grains ½ to 3 microns in the localized areas contained the higher dislocation density. In comparison, the extrusion produced with fine powder, Figure 64 versus 66, had a more equiaxed and relatively strain free structure with grains about 2 to 6 microns with an aspect ratio less than 2 to 1.

The TiB_2 dispersion in the extrusion produced with fine powder, excluding the relatively large rod TiB_2 precipitate, was estimated to be 350 to 650 angstroms in size. The TiB_2 in the extrusion produced with coarse powder was somewhat larger and in the range of 400 to 1000 angstroms.

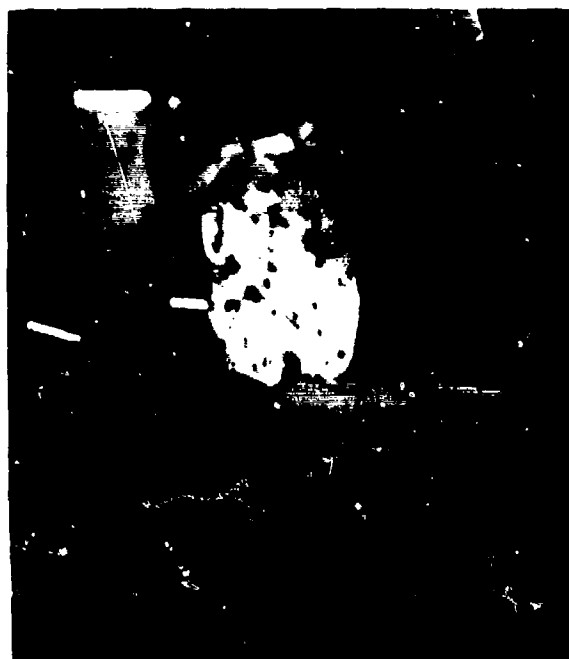
Rolling of the $\text{Fe}_3\text{Al} + \text{TiB}_2$ alloy produced from fine (-270 mesh) and coarse (-80 +140 mesh) powder, Figure 65 and 66, generated similar microstructures (except for the large TiB_2 rod precipitate mentioned above). The rolled alloy produced with the fine and coarse powders had an elongated grain structure with the average grain sizes given in Table 12. The material from fine powder had about half the grain size of the material produced with coarse powder. The microstructures of both extrusions also contained, in different regions, a subgrain structure approximately ¼ by 1 micron. There appeared to be a somewhat higher dislocation density in the subgrain structure of the material produced with the coarse powder. The difference in the microstructures of the extrusions produced with fine and coarse $\text{Fe}_3\text{Al} + \text{TiB}_2$ were retained during rolling except for an increase in the aspect ratio of the grains and a reduction in the grain size for rolled material. The grain aspect ratio of the extrusions were found to vary, and it was difficult to assign values to the length of the grains. The TiB_2 dispersion size apparently did not change as a result of rolling.



2800X



6000X



10000X



36000X

FD270687

Figure 64. $\text{Fe}_3\text{Al} + \text{TiB}_2$ from Fine (-270 Mesh) Powder, A- as Extruded 8 to 1 at 1700°F and B- as Rolled 73% at 1500°F



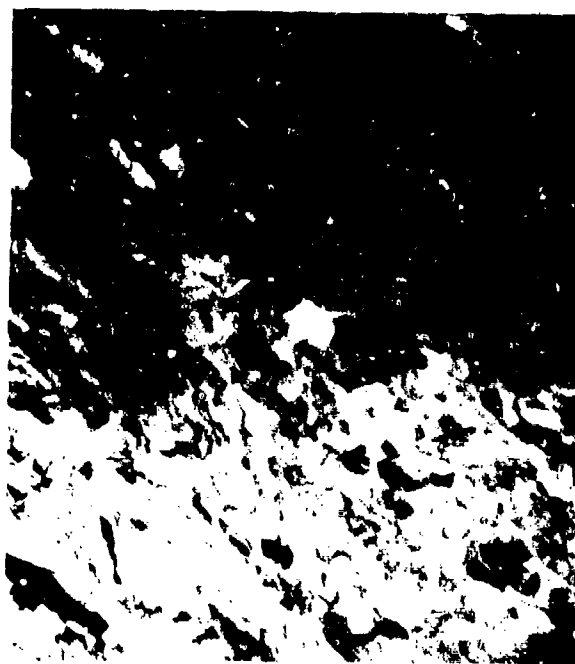
(A) Extruded

2800X



(A)

10000X



(B) Rolled

2800X



(B)

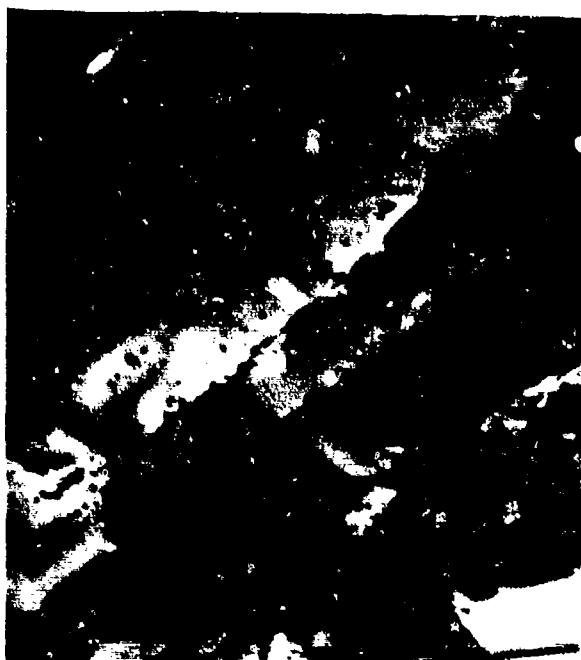
10000X

FD270898

Figure 65. $\text{Fe}_3\text{Al} + \text{TiB}_2$ from Fine (-270 Mesh) Powder a. Extruded 8:1 at 1700°F b. Rolled 65% at 1500°F

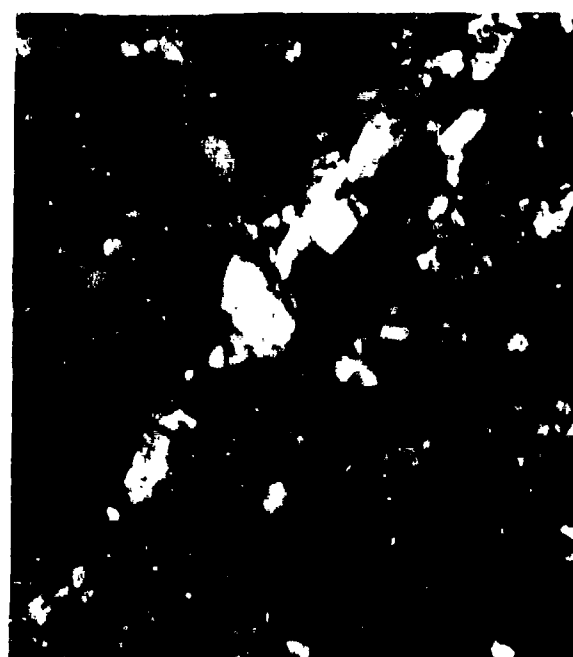


Ⓐ Extruded



Ⓑ

1 μ m



Ⓐ Extruded



Ⓑ

FD 270699

Figure 66. $\text{Fe}_3\text{Al} + \text{TiB}_2$ from Coarse (-80 +140 Mesh) Powder, A- as Extruded 8 to 1 at 1700°F and B- as Rolled 69% at 1500°F

TABLE 12. GRAIN SIZE IN Fe_3Al AND $\text{Fe}_3\text{Al} + \text{TiB}_2$ AFTER EXTRUSION AND ROLLING

	$\text{Fe}_3\text{Al} + \text{TiB}_2$					
	Fe_3Al		Extruded			Rolled
	Extruded	Rolled	-270	-80 +140	-270	-80 +140
Grain Size	50-100	¼-30	2-6	½-2	1-3	¼-1¼
TiB_2	—	—	0.1-0.5 by 0.4-2 microns 350-850Å			350-650Å

2711C

In summary, the results obtained with $\text{Fe}_3\text{Al} + \text{TiB}_2$ processed in larger 45-pound powder lots were different in some respects from the results reported previously for the same alloy, and equivalent particle sizes, produced from small 6-pound powder lots. Extrusion and rolling parameters were not equal, but a sufficiently broad range of conditions had been covered with the small extrusions for a comparison to be made between the microstructures of small and the large extrusions. Comparison of the grain size results in Table 5 and those presented in Table 9 for swaged material produced from small extrusion suggests the following conclusions.

The grain size of ¼ to 1¼ microns in the rolled material (large extrusion) produced from coarse (-80 +140 mesh) powder was not significantly different from the 1- to 1¼-micron grain size of the swaged material (small extrusion) produced with -80 mesh powder. The latter grain size range for the swaged material was for material swaged at 1600°F (871°C). In contrast, the 1- to 3-micron grain size in the rolled material (large extrusion) produced with fine powder was much larger than the measured 1 micron grain size of the swage material (small extrusion) produced from the same -270 mesh powder size. In addition, the grain size as well as the grain aspect ratio were found to vary to a much greater extent in the large extrusion produced with fine powder.

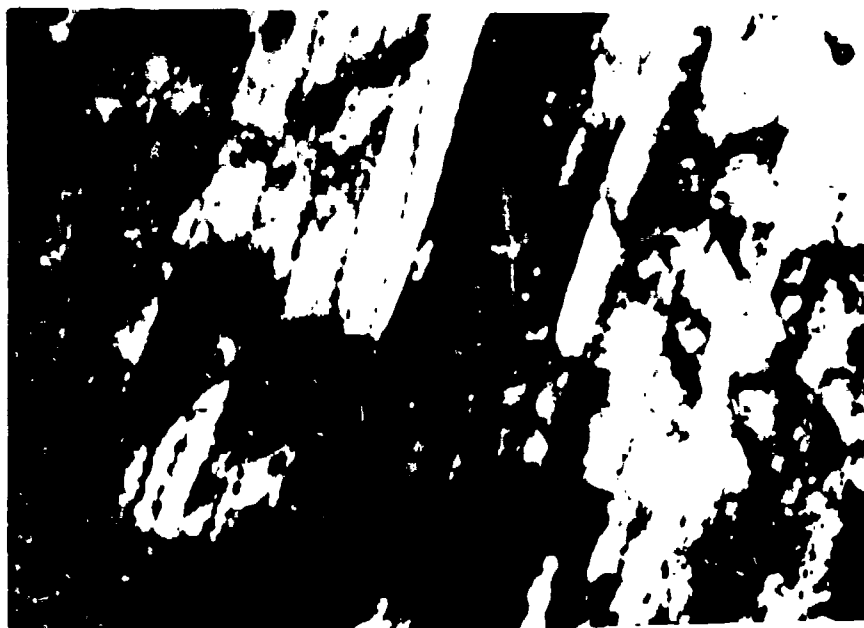
The relatively coarse TiB_2 phase found in the large extrusion from fine powder was not present in the extrusion from coarse powder or in any of the small extrusions previously produced with fine powder. The normal TiB_2 dispersion present in all $\text{Fe}_3\text{Al} + \text{TiB}_2$ in both small and large extrusions were close to the same size in the material produced from coarse powder. These were 400 to 1000 angstroms for the coarse powder and 300 to 900 angstroms for the fine powder swaged at 1600°F (871°C). However, the TiB_2 particle size in material produced in the large extrusion with fine powder was 350 to 650 angstroms compared to 200 to 400 angstroms in the material from fine powder produced in the small extrusions. In addition, the material from the small extrusion produced with fine powder did not contain the relatively coarse TiB_2 precipitate found in the large extrusion produced during this period. As mentioned previously, the differences noted in the microstructures, including the accelerated coarsening of the TiB_2 , appears to be due to the long soak time which was required to achieve a uniform temperature in the large extrusion billets prior to extrusion.

DEFORMATION PROCESS MODELING

In a previous section, both Fe_3Al and $\text{Fe}_3\text{Al} + \text{TiB}_2$ were investigated by optical and SEM/TEM microscopy to discern the major features related to grain size and orientation, and to quantify the TiB_2 distribution. In this section, the macroscopic crystallographic orientation of Fe_3Al grains was determined by standard X-ray texture analysis. The deformation texture of those alloys which performed successfully in bend tests, shown previously, were investigated in an attempt to determine the succession of microstructural stages during thermomechanical

processing which led to extremely ductile behavior in bend tests. TEM showed that these alloys had a fine polygonized subgrain structure which when combined with a (110) sheet normal rolling texture produced ductile behavior.

During the extrusion process, spherical powder particles become aligned with aspect ratios (length/diameter) which are a function of the extrusion ratio. The diameter of the elongated grains was found to be related to both the extrusion ratio and the diameter of the powder particles. In $\text{Fe}_3\text{Al} + \text{TiB}_2$, a significantly finer diameter grain structure was produced which originated from the powder particle solidification structure. This structure is shown in Figure 67. The linear distribution of TiB_2 which in this case was found to be $\frac{1}{4}$ to $\frac{1}{2}$ microns apart was derived from the dendrite arm spacing of the original powder and the extrusion ratio used in consolidation. Figure 68 shows a distribution of 3000 angstroms transverse spacing with sizes ranging from 200 to 800 angstroms. Dark field microscopy showed that the average transverse grain size in the extruded alloy 545 was 1.5 microns, with up to several TiB_2 distributions within each Fe_3Al grain. The average grain dimensions were 1.5 microns in the transverse direction and up to 20 microns long. X-ray texture analysis showed that the deformation was $\langle 110 \rangle$ fiber texture (Figure 69 with approximately nine times random intensity. Work on nickel-base and aluminum alloys (References 10 and 11) has shown that textural intensity is dependent on extrusion reduction ratio (at least below the recrystallization temperature) with the strongest textures being produced by the highest extrusion ratios.



FD 253152

Figure 67. TEM of $\text{Fe}_3\text{Al} + \text{TiB}_2$ (Alloy 545) Extruded 8 to 1 at 1700°F (927°C) Showing Elongated Grains and the Distribution of TiB_2 Inherited from the Original Solidification Structure

The effects of thermomechanical processing on texture evolution in bend test samples described previously and in the $\text{Fe}_3\text{Al} + \text{TiB}_2$ alloys produced from different powder lots are shown in Table 13. The ductile behavior refers to bending a sample through 180 degrees around a $3t$ radius where " t " is the sheet thickness, and "fracture" behavior refers to failure to pass this test. As shown in a following section, alloy 723 had up to several percent elongation on tensile testing; however, considerably more ductility appears to be required for successful completion of

3t bend test. In comparing the two alloys containing TiB_2 (545 and 723) with the alloy without TiB_2 (729) it is apparent that attainment of a simple deformation texture will not explain the differences in bend fracture behavior of these alloys. The sequence of textural changes associated with thermomechanical processing of each alloy type are shown in Figures 70 and 71, indicating that the Fe_3Al alloy 729 processed to a $(112) \langle 110 \rangle$ texture survived the bend test but has a significantly different texture from the also successful $\text{Fe}_3\text{Al} + \text{TiB}_2$ alloy (545) texture shown in Figure 72. This deformation texture was very close to that of the extruded alloy, indicating that the role of TiB_2 in alloy 545 may be to prevent major grain reorientation, with its deformation texture showing some of the characteristics of a polygonized structure, for example, a reduction in the central $\langle 110 \rangle$ intensity and a broad distribution of orientations in the rolling direction ranging from $\langle 110 \rangle$ to $\langle 223 \rangle$.

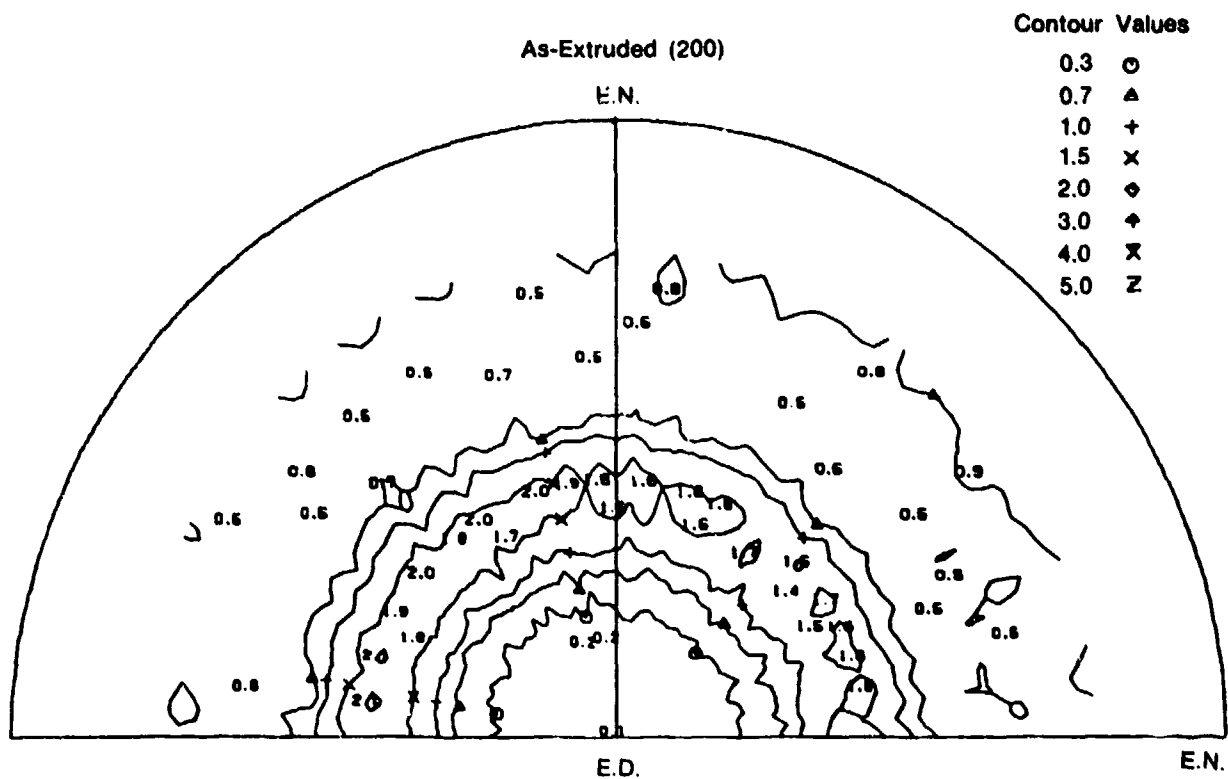
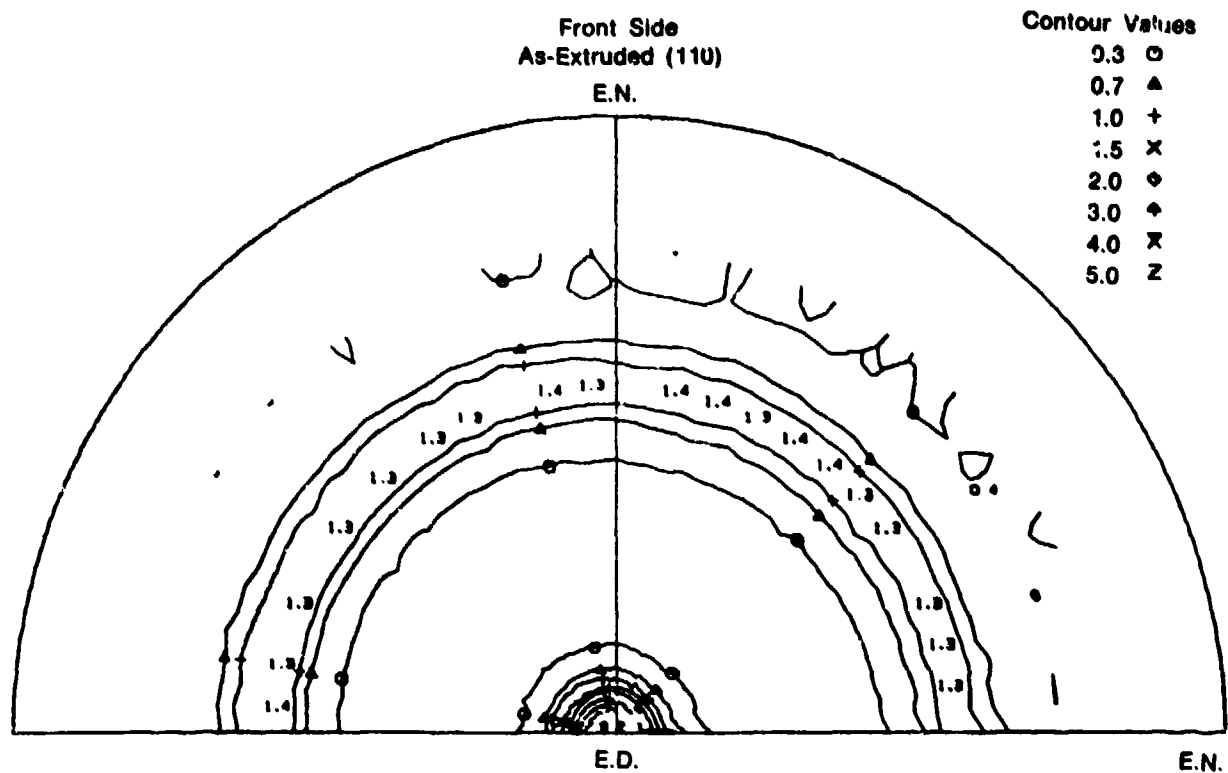
700°F AT 8/1



FD 253153

Figure 68. TEM of $\text{Fe}_3\text{Al} + \text{TiB}_2$ (Alloy 545) Extruded 8 to 1 at 1700°F (927°C) Showing the Distribution of TiB_2 in Prior Dendrite Arms

The alloys whose textures were described in Table 13 were examined by both bright field and dark field TEM. The onset of "brittle" behavior in the 3t bend test samples of alloy 729 annealed at 1200°F (649°C) for 1 hour was shown to result from premature abnormal grain growth. The sample annealed at 1150°F (621°C) for one hour showed elongated grains of Fe_3Al with extensive subgrain boundary polygonization networks (Figure 73) and a few strain free grains. Those strain-free grains, Figure 74, resulted from static recrystallization of the dynamically polygonized structure. In the several thin foils examined, only two areas of recrystallization were observed, indicating that recrystallization nuclei were present but not widely developed after annealing for 4 hours at 1150°F (621°C). It is those recrystallization nuclei which presumably are responsible for the gross textural changes in which the $(112) \langle 110 \rangle$ polygonized structure is systematically replaced by the $(110) \langle 110 \rangle$ structure with a corresponding increase in grain size from the 1- to 2-micron size present at 1150°F (621°C) to 20 to 50-micron size after one hour at 1200°F (649°C).



FD 253154

Figure 69. (110) and (200) Pole Figures of Extruded Alloy $\text{Fe}_3\text{Al} + \text{TiB}_2$ (RSR 545)
Showing Strong $\langle 110 \rangle$ Fiber Textures

TABLE 13. TEXTURE ANALYSIS

Processing	Fe ₃ Al (eg., Alloy 729)	Fe ₃ Al + TiB ₂ (eg., Alloy 545, 723)
As Extruded		<110> Fiber Texture
As-Rolled, Parallel to Extrusion Direction	900°K (1180-1100°F) (110) <001>	1200K (1700°F) (110) <001> (723) (110) <110> and (110) <223> (545)
As-Rolled and Annealed	900°K (1180°F)/1 hr (112) <110> Ductile	1200K (1700°F)/1 hr (223) <110> Ductile (720) (110) <001> Fracture (723) (110) <113> Ductile (545)
As-Rolled and Annealed	920°K (1300°F)/1 hr Weak (112) <110> Stronger (110) <110>	1300K (1900°F)/1 hr (223) <110> Ductile (720) (110) <110> Fracture (723) (110) <113> Ductile (545)
Cross Rolled	—	1200K (1700°F)/1 hr Strong (001) <110> Fracture

2711C

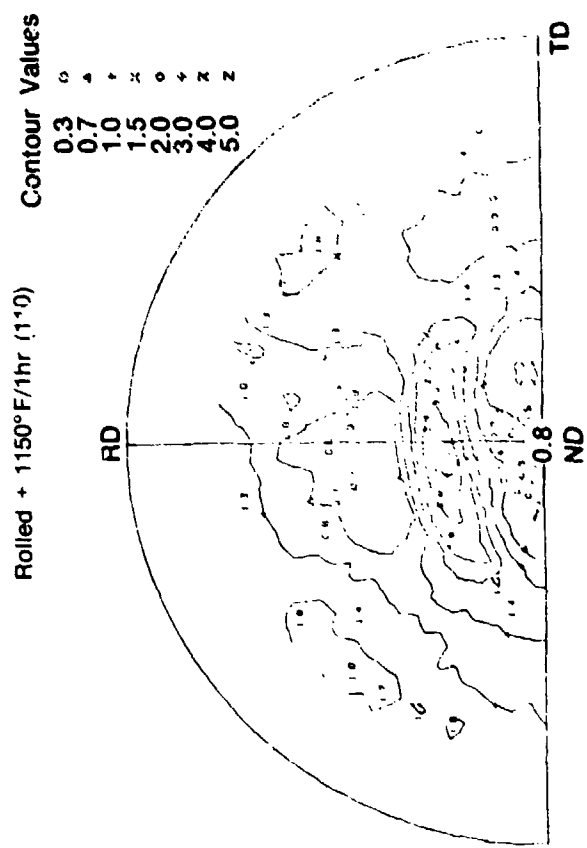
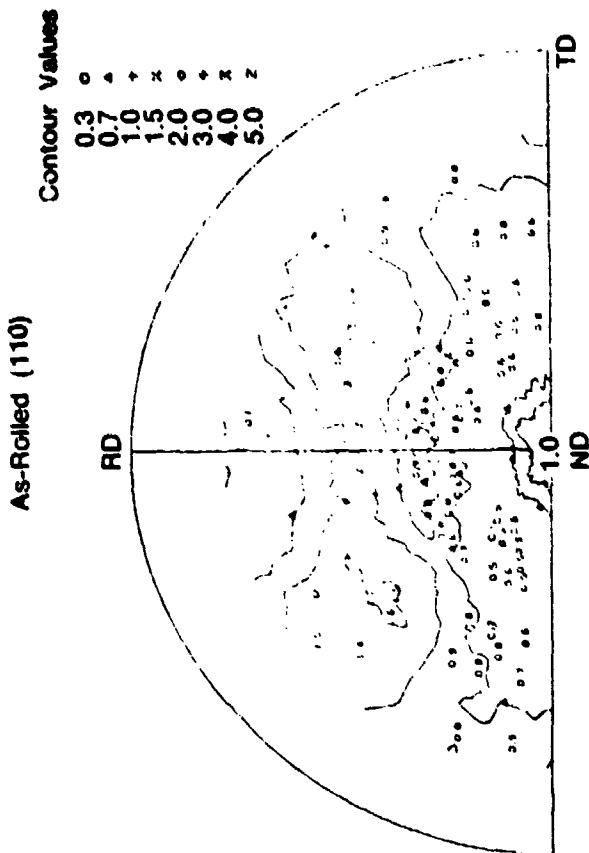
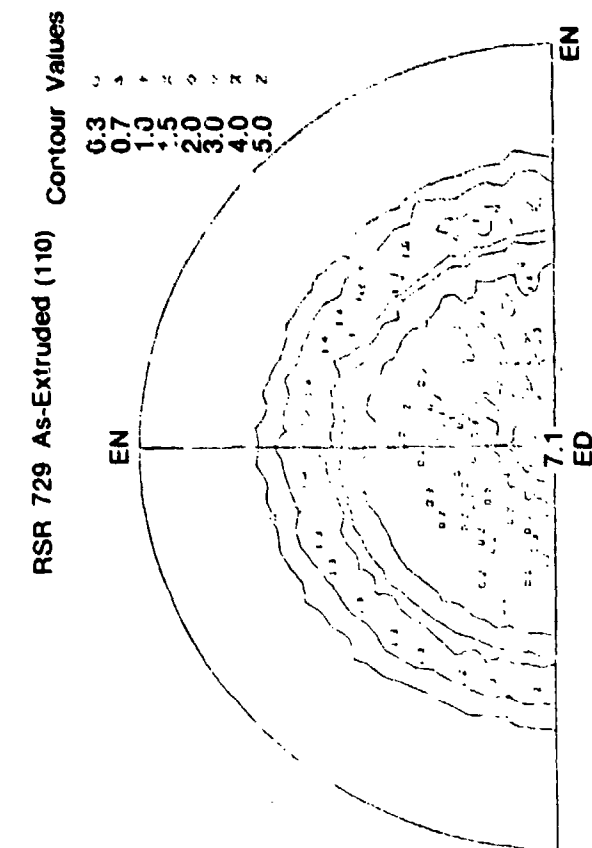
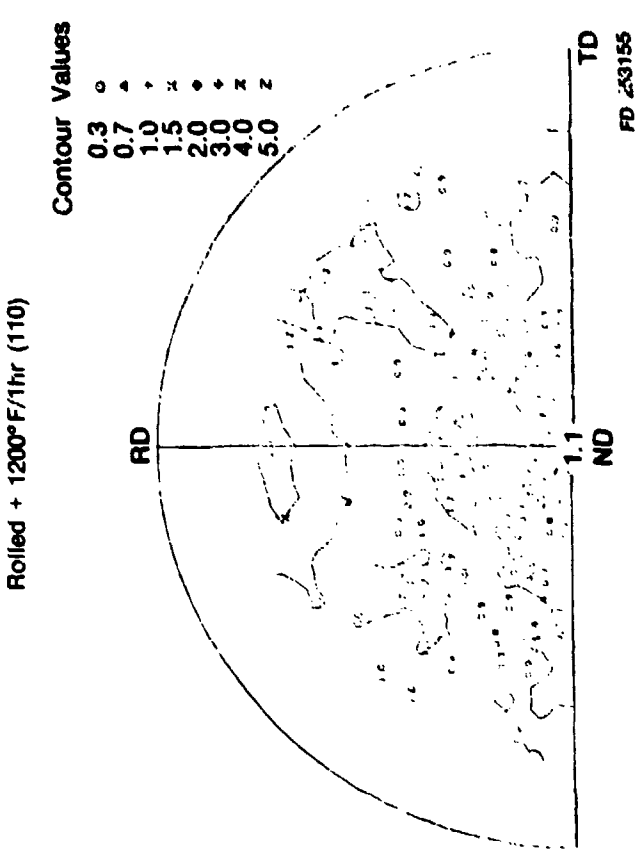
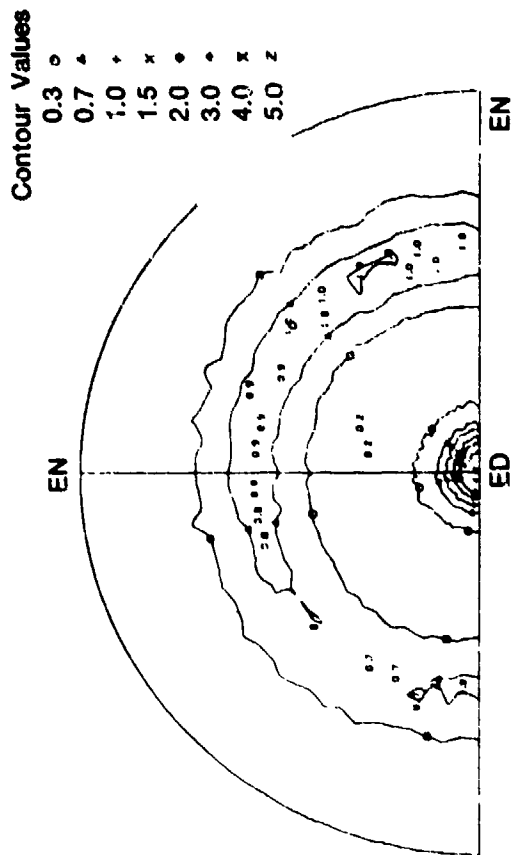


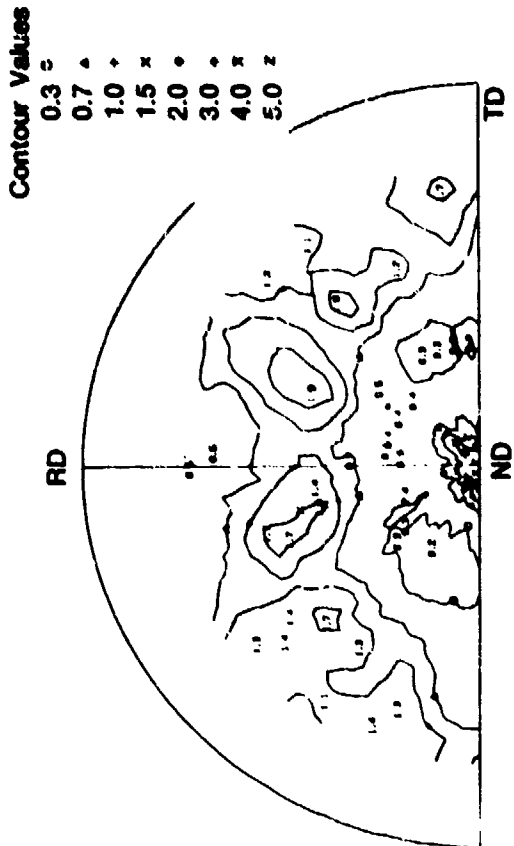
Figure 70. (110) Pole Figures for Different Thermomechanical Processing Sequences for Alloy 729 (Fe_3Al)



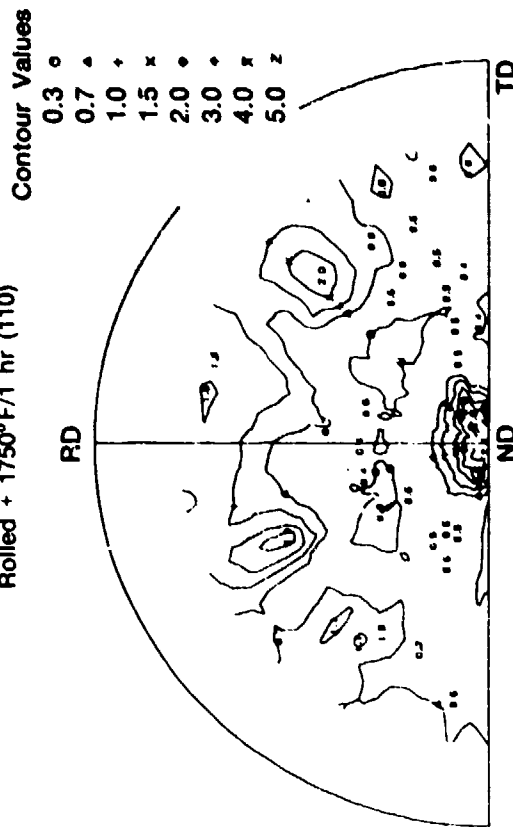
Extruded 4 to 1 (110)



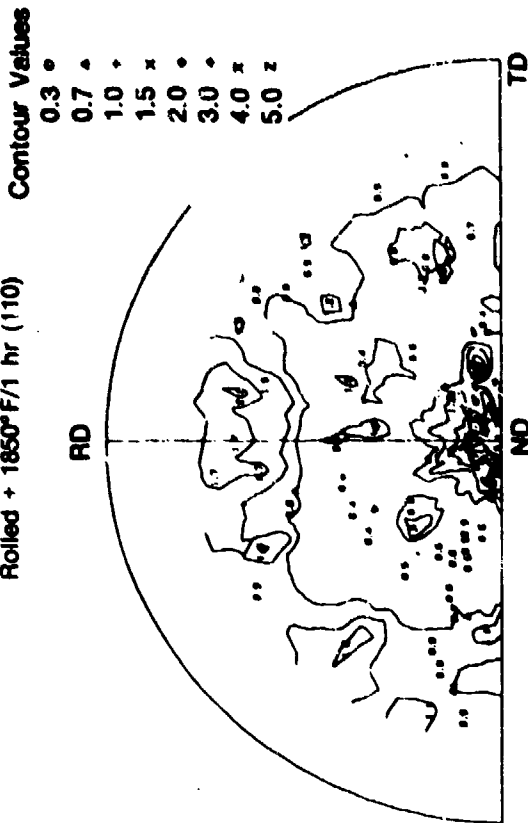
As-Rolled (110)



Rolled + 1750°F/1 hr (110)

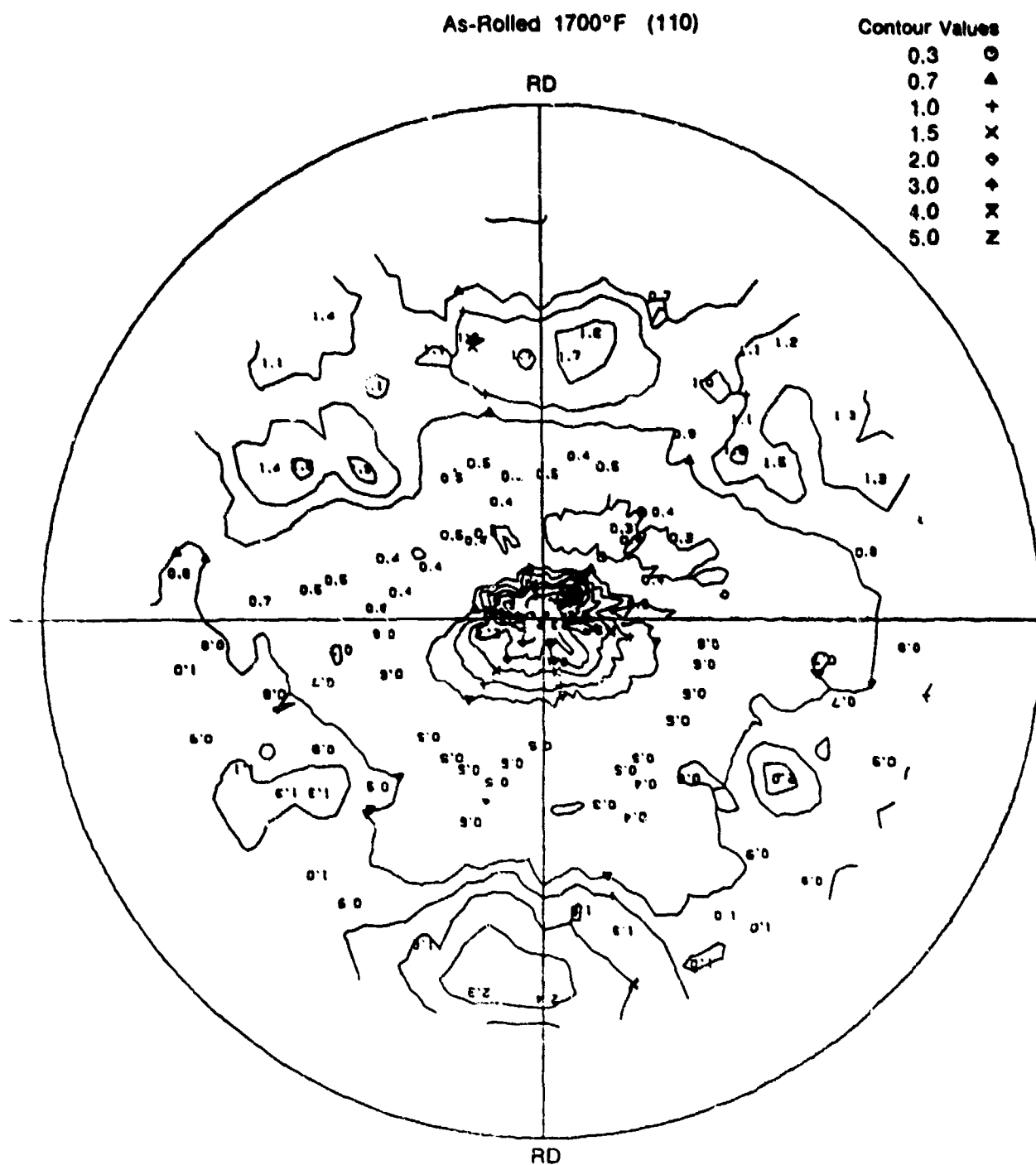


Rolled + 1850°F/1 hr (110)



FD 253156

Figure 71. (110) Pole Figures from Different Thermomechanical Processing Sequences for $\text{Fe}_3\text{Al} + \text{TiB}_2$ (Alloy 723)



FD 253157

Figure 72. (110) Pole Figure of $\text{Fe}_3\text{Al} + \text{TiB}_2$ (Alloy 545) Rolled at 1700°F (927°C)
Showing Ductile at Bend Test Behavior



FD 263938

Figure 73. Bright Field TEM of Alloy 729 (Fe_3Al) Rolled and Annealed at 1150°F (521°C) for 1 Hour, Showing Extensive Polygonization Networks



FD 253159

Figure 74. Bright Field TEM of Alloy 729 (Fe_3Al) Rolled and Annealed at 1150°F (621°C) for 1 Hour, Showing Nucleation of New Strain Free Grains Within the Deformed Matrix

Alloys containing TiB_2 showed distinctly different microstructural behavior on rolling. The ductile 545 alloy after rolling and annealing at 1700°F (926°C), Figures 75 and 76 showed elongated pairs of 1 micron thickness and 10- to 20-microns long, with 200 angstroms TiB_2 particles uniformly distributed throughout the microstructure. Figure 75 shows clearly that dynamic deformation and static annealing have produced a very fine matrix substructure of 1000 to 5000 angstrom size in which subgrain boundaries are pinned by TiB_2 . The presence of TiB_2 within subgrains is responsible for a high degree of slip "delocalization" during which cross-slip off the primary slip plane is necessary to bypass TiB_2 obstacles, with the associated generation of both partial dislocations and Orowan segments. This increasing dislocation density with plastic deformation is ultimately responsible for the development of polygonization networks and the establishment of a fine polygonized subgrain structure which showed development in dispersion strengthened aluminum alloys (Reference 11). A basic difference between the recrystallization and grain growth behavior of alloys with and without TiB_2 is that alloys with TiB_2 can store a high level of deformation energy in subgrain boundaries, which are prevented from movement by Zener drag forces, while in alloys without TiB_2 , subgrain boundaries become quickly unstable and the stored energy is adequate for the onset of grain growth. Based on these observations, the presence of TiB_2 confers an approximate 500 to 600°F (260 to 315°C) processing advantage before grain coarsening consumes the stored deformation energy in polygonized subgrain boundaries.

Texture of Material Processed in Small Lots

X-ray analysis was performed with $\text{Fe}_3\text{Al} + \text{TiB}_2$ alloy samples R069 and R079 through R082 listed in Table 14. The samples produced with fine (-270 mesh), coarse (-80 +100 mesh) and the entire (-80 mesh) powder size distribution had been extruded 8 to 1 at 1650 or 1700°F (89 or 927°C) and swaged at 1300, 1600, and 2000°F (704, 871, and 1093°C). Post annealing of swaged material was carried out at the swaging temperatures, and for this study a number of samples were given an additional anneal at 1800°F (982°C) for 30 minutes.

As shown in Table 14 and Figures 77 and 78, extruded $\text{Fe}_3\text{Al} + \text{TiB}_2$ with a $\langle 110 \rangle$ crystallographic fiber texture approximately nine times random was found only to strengthen in texture with swaging. The deformation texture increased with decreasing swaging temperature, as for a number of alloys, while the material produced with fine (-270 mesh) and coarse (-80 +100 mesh) powders behaved differently. The fine powder sample swaged at 1300°F (704°C) had a stronger texture than the coarse powder sample swaged at the same temperature. However, the order was reversed for the same powder size fractions swaged at 1600°F (899°C). There are currently no explanations for this anomaly.

Annealing of swaged samples at 1800°F (982°C) for 30 minutes did not change the texture of the samples except that of sample R081 (-80 +100 mesh powder swaged at 1300°F) which changed to a $\langle 111 \rangle$ fiber texture. However, the change in texture was limited to the periphery of the swaged bar where recrystallization and grain coarsening had taken place. In addition, sample R081 may have been swaged at a lower temperature thereby increasing strain energy and reducing the recrystallization temperature. Gross textural change with a corresponding increase in grain size was reported previously for rolled Fe_3Al which had been annealed at a temperature which caused partial recrystallization and grain coarsening.



FD 253160

Figure 75. Dark Field TEM of Rolled and Annealed 545 Alloy ($\text{Fe}_3\text{Al} + \text{TiB}_2$) Showing the General Grain Elongation and Subgrain Polygonization Within the Grain



FD 253161

Figure 76. TEM Alloy 545 ($\text{Fe}_3\text{Al} + \text{TiB}_2$) Showing the Distribution of $\sim 200\text{\AA}$ Diameter TiB_2 and Their Relationship to Polygonized Subgrain Boundaries

TABLE 14. STRENGTH OF $\langle 110 \rangle$ FIBER TEXTURE (TIMES RANDOM) VERSUS SWAGING TEMPERATURE

Powder Size	Temperature ($^{\circ}\text{F}$)		
	1300	1600	2000
-80	—	—	16X (R069)
-80 +100	38X (R081)	30X R079	
-270	49X (R082)	20X (R080)	

mic

Swaged $\text{Fe}_3\text{Al} + \text{TiB}_2$ analyzed by X-ray diffraction was found to have a BCC iron base structure with some DO_3 type (Fe_3Al) ordering. In the coarse grain region of annealed sample R081, some B2 type ordering was observed. The dispersion was identified as TiB_2 in both swaged and 1800°F annealed samples. The TiB_2 was found to possess a $\langle 001 \rangle$ texture in the swaged samples produced with coarse ($-80 +100$ mesh) powder but the TiB_2 was randomly oriented in samples produced with fine (-270 mesh) powder. The difference in textural response of the TiB_2 dispersion may be due to the difference in the size of the dispersion derived from the fine (-270 mesh) and coarse ($-80 +100$ mesh) powder size fractions. This is discussed in the following section.

Texture of Material Processed in Large Lots

Iron aluminides (Fe_3Al and $\text{Fe}_3\text{Al} + \text{TiB}_2$) produced from fine (-270 mesh) and coarse ($-80 +140$ mesh) powder were extruded in 50 pound lots at an 8-to-1 ratio and 1700°F (927°C). The Fe_3Al was subsequently rolled at 1150°F (621°C) and the $\text{Fe}_3\text{Al} + \text{TiB}_2$ rolled at 1500°F (815°C) to 0.9-inch thick slabs. The latter consolidated and worked conditions were selected from results of prior investigations with small extrusions post worked by swaging or rolling. The material produced in the larger size was investigated to verify the deformation mode or mechanisms identified previously, and to measure mechanical properties including tensile properties, in the transverse (to rolling) direction, and fracture toughness properties.

The deformation structures obtained in extruded and rolled Fe_3Al and $\text{Fe}_3\text{Al} + \text{TiB}_2$ were similar to those obtained with small extruded lots of material post worked by swaging and rolling except for the differences noted below. In small extrusions, the alloys developed $\langle 110 \rangle$ fiber textures which increased in strength with increasing extrusion ratios or amount of subsequent swaging. The presence or absence of TiB_2 in the alloy did not markedly affect the texture in symmetrically extruded material. In the larger Fe_3Al rectangular extrusion, the alloy developed a $\langle 110 \rangle$ fiber texture with some secondary sheet type texture component. In the larger $\text{Fe}_3\text{Al} + \text{TiB}_2$ rectangular extrusions, the alloy developed an axial texture about 15 degrees off the $\langle 110 \rangle$. The rolling textures were typical of BCC materials, but differed somewhat from prior results with rolled material produced from small extrusions. The texture of Fe_3Al rolled from small extrusions was $(112) \langle 110 \rangle$ and in some cases $(110) \langle 110 \rangle$ while the texture of rolled $\text{Fe}_3\text{Al} + \text{TiB}_2$ was $(110) \langle 001 \rangle$, $(110) \langle 113 \rangle$ and $(110) \langle 110 \rangle$. The deformation textures of material produced as large extrusions were as follows.

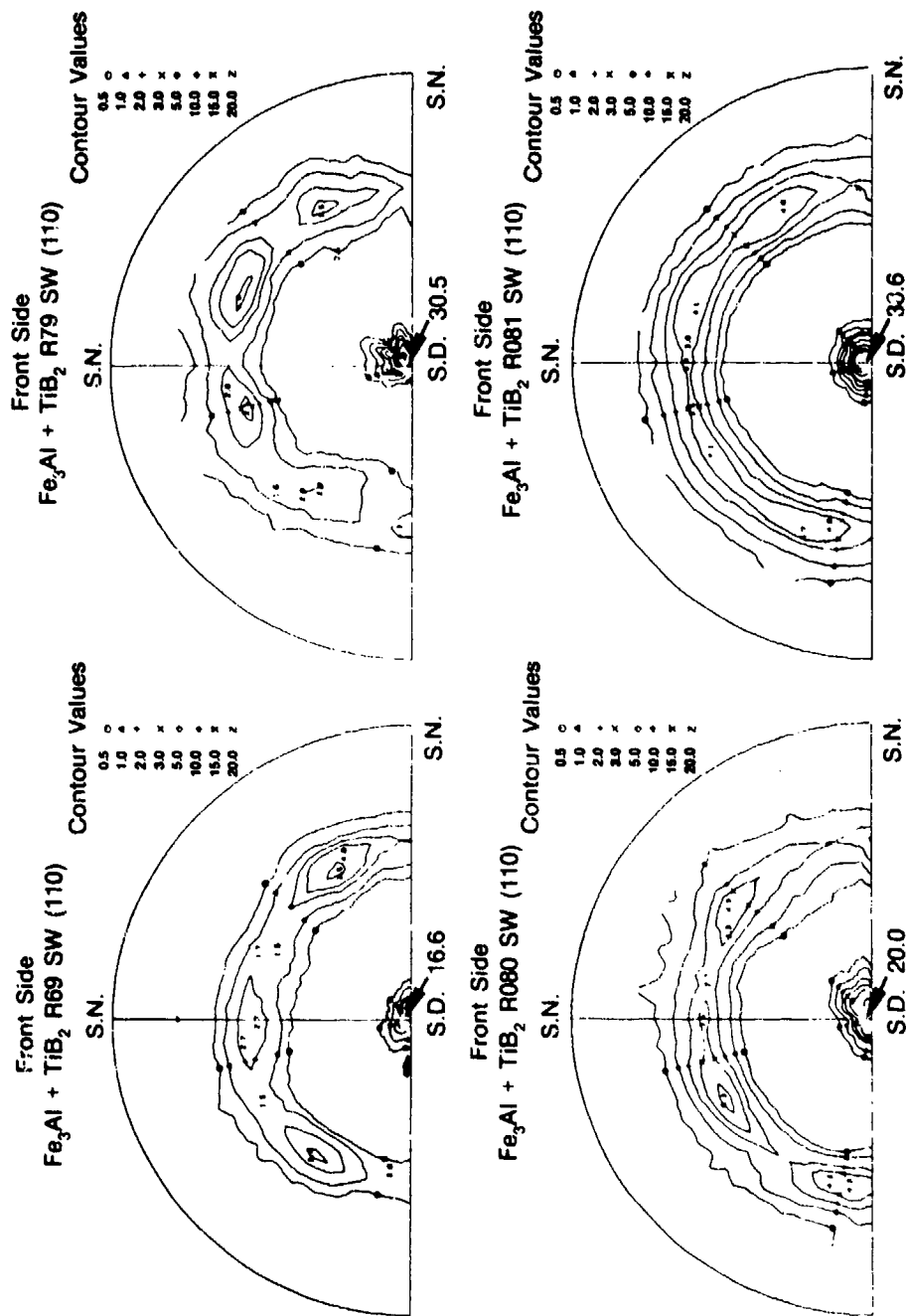
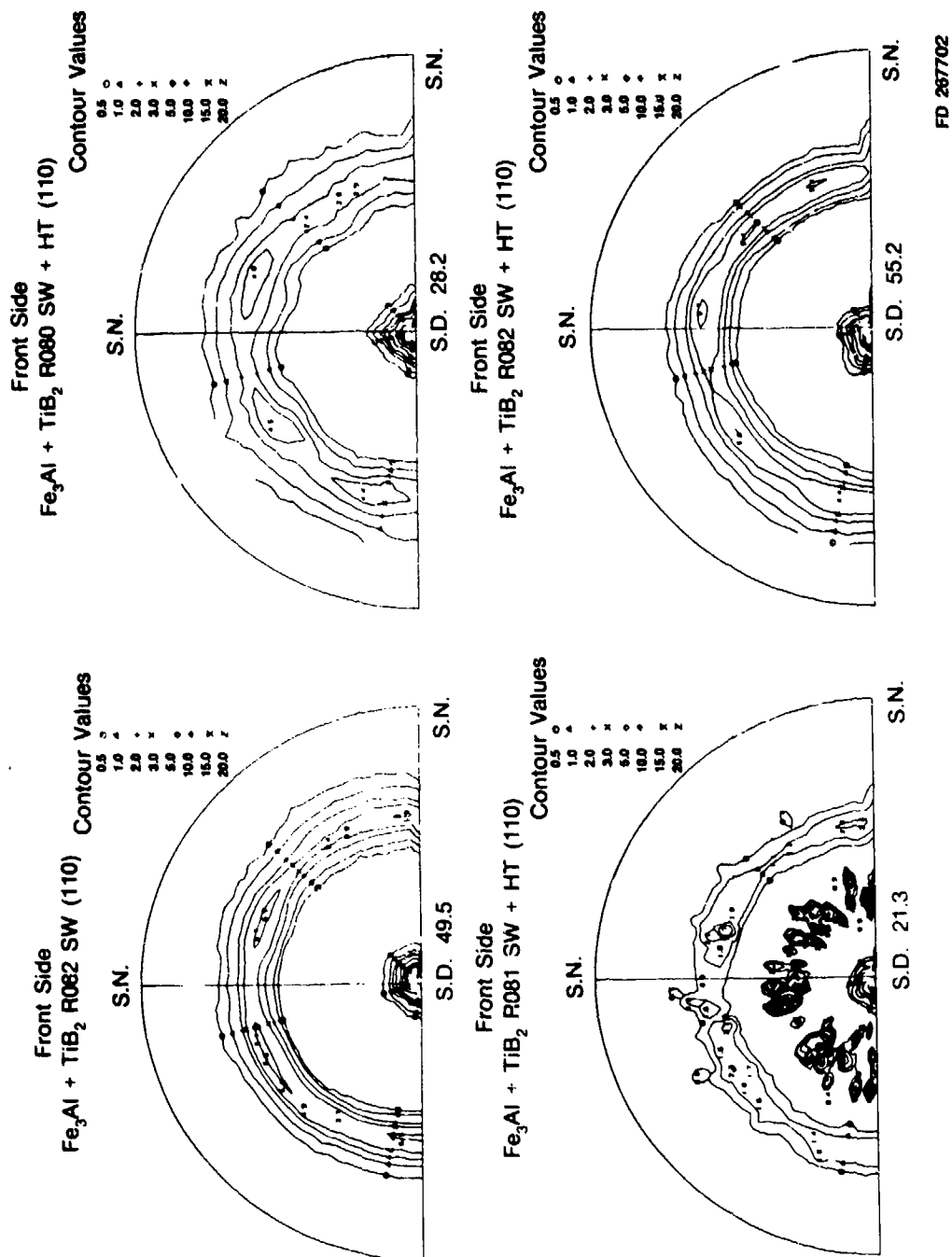


FIG 267701

Figure 77. (110) Pole Figures of Extruded and Swaged Fe₃Al + TiB₂



FD 267702

Figure 78. (110) Pole Figures of Extruded, Swaged, and Annealed Fe₃Al + TiB₂

Extruded Fe_3Al

A strong 14 times random $\langle 110 \rangle$ fiber texture with a weak sheet texture spread from a (001) $\langle 110 \rangle$ to (112) $\langle 110 \rangle$ is shown in Figure 79.

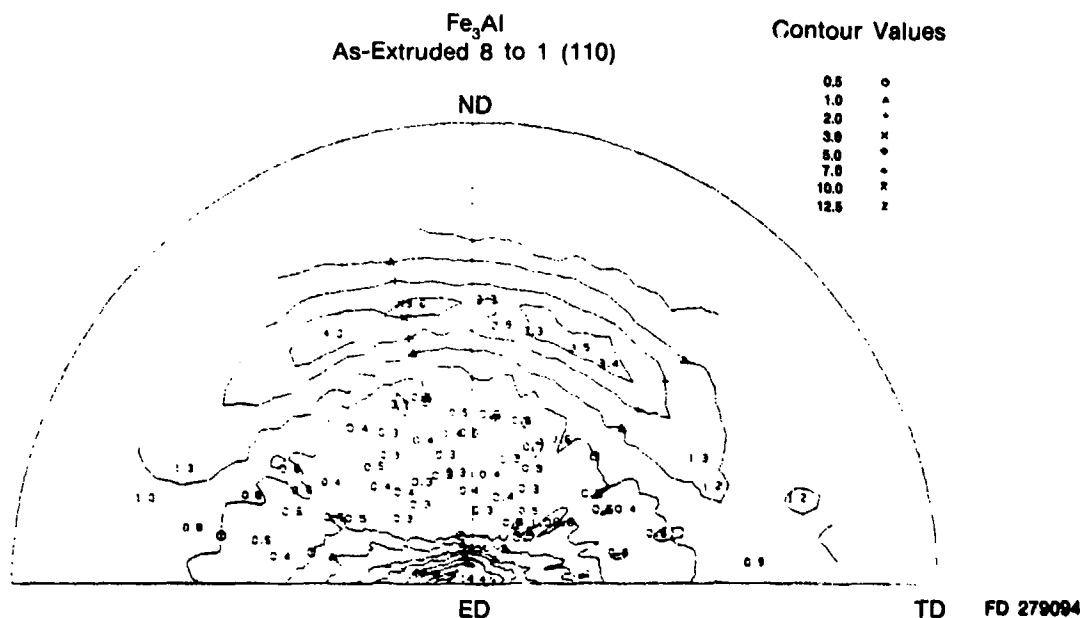


Figure 79. $\langle 110 \rangle$ Pole Figure Resulting from the Extrusion of Fe_3Al to a Rectangular Cross Section

Rolled Fe_3Al

A moderate rolling texture five times random formed with a spread from (112) $\langle 110 \rangle$ to (001) $\langle 110 \rangle$ is shown in Figure 80.

Extruded $\text{Fe}_3\text{Al} + \text{TiB}_2$

Material produced from both powder fractions were found to have extrusion or fiber textures similar to those of the Fe_3Al alloy except that the orientation was $\langle 133 \rangle$ or about 15 degrees off the $\langle 110 \rangle$. In addition, since the extrusion was rectangular, a weak sheet texture from (611) $\langle 133 \rangle$ to (321) $\langle 113 \rangle$ was also found as shown in Figures 81 and 82. Areas near the surface of the extruded bar could have a texture varying by as much as 10 degrees, but it is possible that the texture in the large extrusions was a result of partial recrystallization especially in the material produced with fine powder. These textures were relatively weak. The extrusion produced with fine powder was 1.8 times random, while the extrusion produced with coarse powder was five times random.

Rolled $\text{Fe}_3\text{Al} + \text{TiB}_2$

The deformation texture which developed in rolled material produced with both fine and coarse powder was similar to that found in rolled $\text{Fe}_3\text{Al} + \text{TiB}_2$. As shown in Figure 83, rolling of the material produced with fine powder was found to have a five times random texture spread from (001) $\langle 110 \rangle$, (112) $\langle 110 \rangle$ to (111) $\langle 110 \rangle$. Rolling of the material produced with the

coarse powder was found to have a stronger 12 times random texture from (012) $\langle 110 \rangle$ to (001) $\langle 110 \rangle$ as shown in Figure 84. All of the above textures are found in BCC alloys.

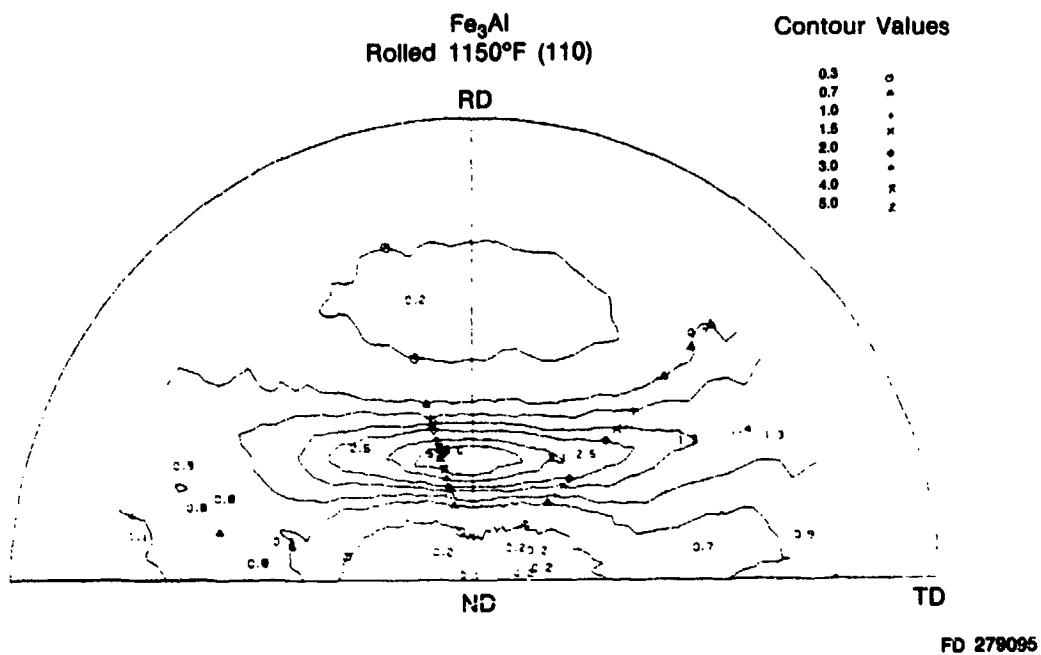


Figure 80. $\langle 110 \rangle$ Pole Figure Resulting from the Warm Rolling of Fe₃Al Which Had Been Extruded to a Rectangular Cross Section

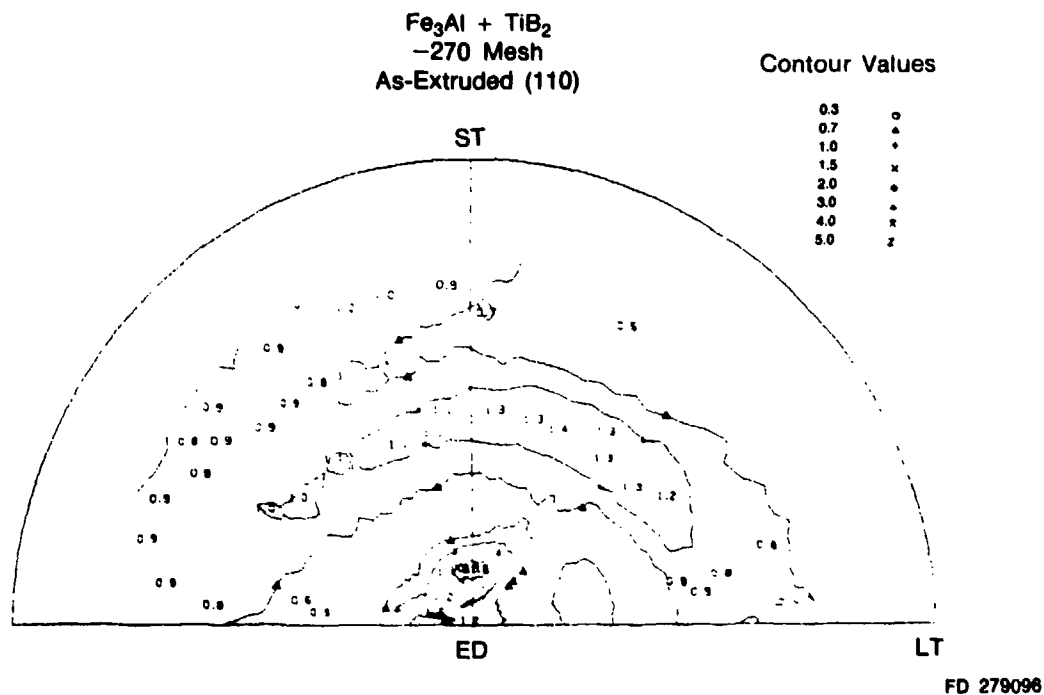
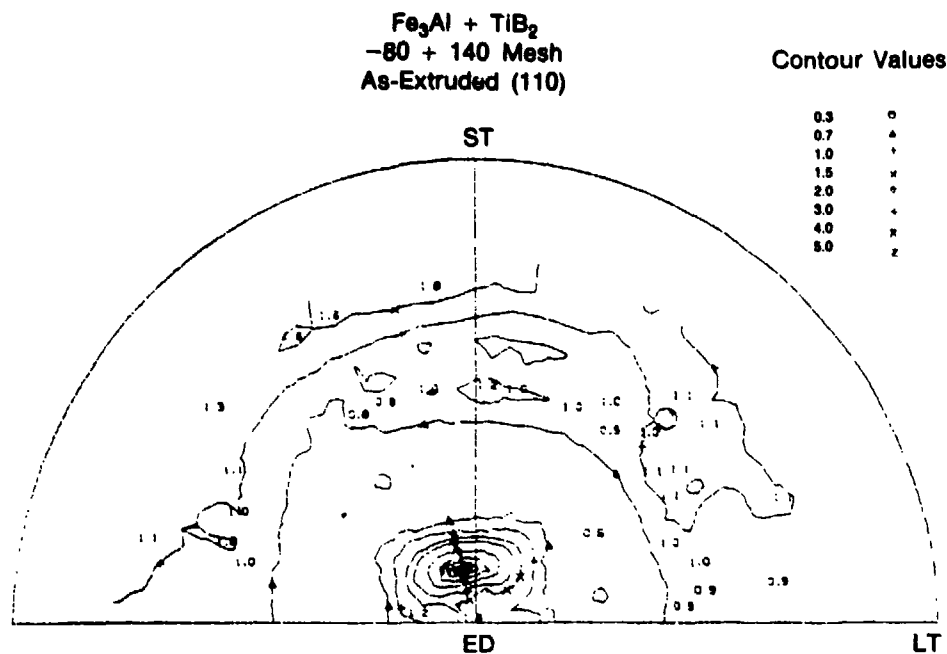
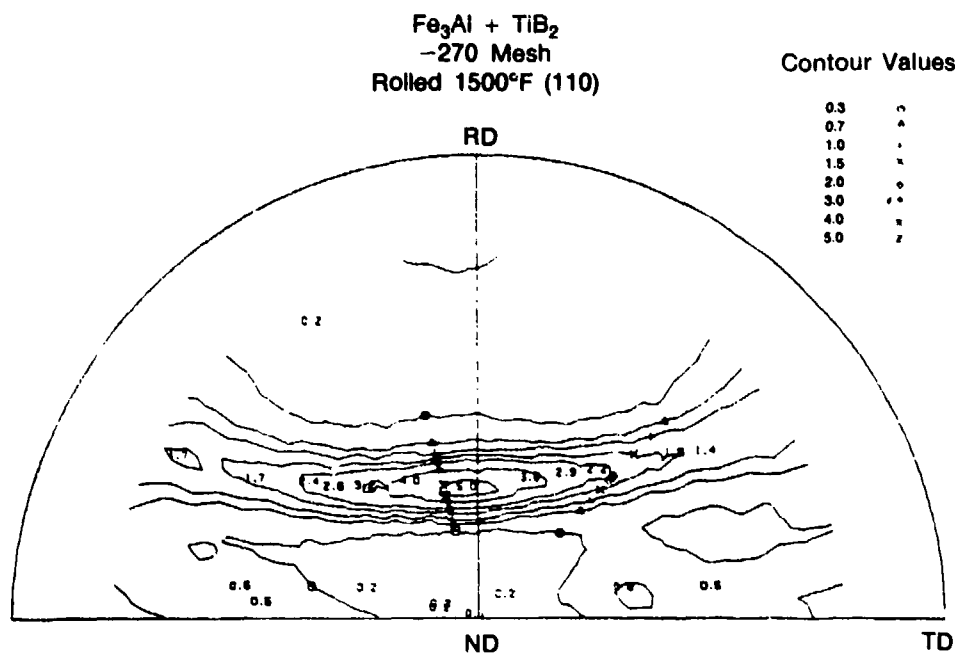


Figure 81. $\langle 110 \rangle$ Pole Figure of As-Extruded Fe₃Al + TiB₂ Produced from Fine (-270 Mesh) Powder



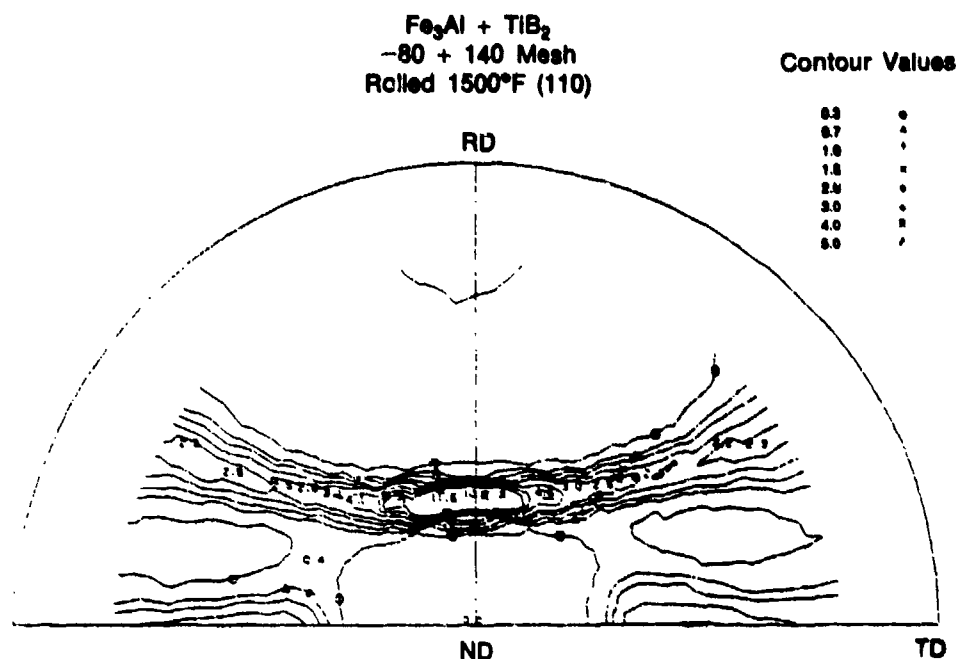
FD 279097

Figure 82. $\langle 110 \rangle$ Pole Figure of As-Extruded $\text{Fe}_3\text{Al} + \text{TiB}_2$ Produced from Coarse (-80 +140 Mesh) Powder



FD 279098

Figure 83. $\langle 110 \rangle$ Pole Figure of Rolled $\text{Fe}_3\text{Al} + \text{TiB}_2$ Produced from Fine (-270 Mesh) Powder



FD 27:083

Figure 84. $\langle 110 \rangle$ Pole Figure of Rolled $\text{Fe}_3\text{Al} + \text{TiB}_2$ Produced from Coarse (-80 +140 Mesh) Powder

The following table, Table 15, summarizes the texture results obtained with the large extrusions produced during the last reporting period.

TABLE 15. TEXTURE RESULTS

Alloy	Fraction	Extrusion Texture	Rolling Texture
Fe_3Al	-80 mesh	14 × random $\langle 110 \rangle$ fiber + (001) $\langle 110 \rangle$ to	5 × random (112) $\langle 110 \rangle$ to (001) $\langle 110 \rangle$
$\text{Fe}_3\text{Al} + \text{TiB}_2$	-270 mesh	1.8 × random $\langle 133 \rangle$ fiber + (611) $\langle 113 \rangle$ to (321) $\langle 113 \rangle$	5 × random $\langle 001 \rangle$ $\langle 110 \rangle$ to (112) $\langle 110 \rangle$ to (111) $\langle 110 \rangle$
$\text{Fe}_3\text{Al} + \text{TiB}_2$	-80 +140	5 × random $\langle 133 \rangle$ fiber + (611) $\langle 133 \rangle$ to (321) $\langle 133 \rangle$	12 × random (001) $\langle 110 \rangle$ to (112) $\langle 110 \rangle$ to

271:0

PROPERTY EVALUATION

Tensile Properties of Swaged Fe_3Al and $\text{Fe}_3\text{Al} + \text{TiB}_2$

The Fe_3Al alloy 729 extruded 10 to 1 at 1750 and 1950°F (954 and 1065°C) was swaged to strains of 1.3 and 1.8, and was annealed for 1 hour at various temperatures, the swaging

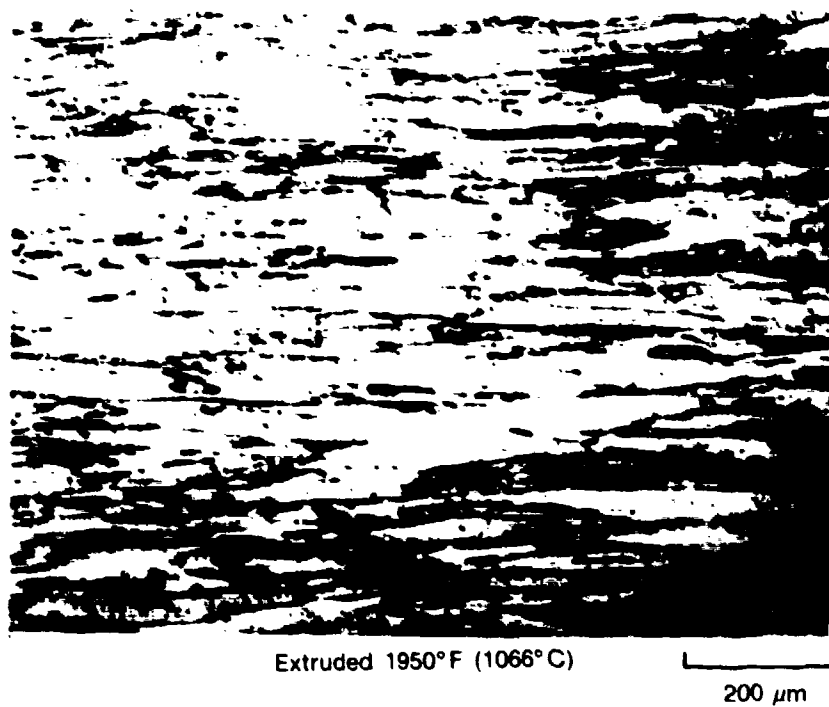
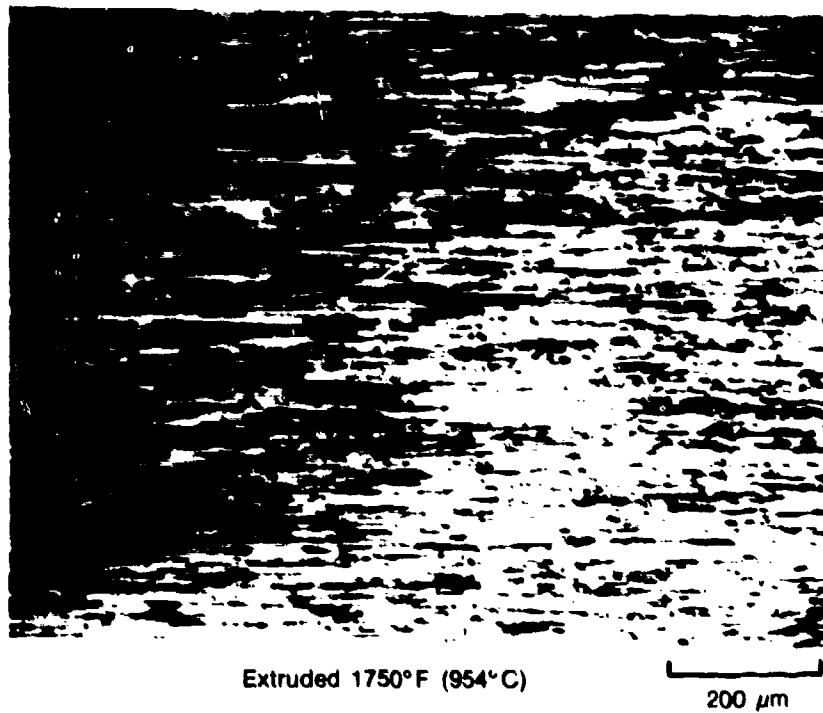
temperature was 1250°F (621°C) for the first swaging pass, and was reduced for each of the succeeding three passes to 1150°F (621°C), and held constant for the remaining passes. The room temperature tensile properties of the swaged material are given in Table 16. The tensile properties and especially the elongation are seen to be related to processing. The higher strength and more ductile samples had been extruded at the lower temperature, swaged to the higher strain and annealed at 1150°F (621°C). The 18% elongation measured is the highest obtained on this contract for Fe₃Al. Figure 85 shows that the alloy extruded at 1750 and 1950°F (954 and 1065°C), and subsequently swaged at 1150°F (621°C) reflects the initial grain size of the extruded material. The elongations of the latter swaged material were 18 and 9% respectively.

TABLE 16. TENSILE PROPERTIES OF Fe₃Al (729) ALLOY

Extrusion Temperature		Swaging Strain	Anneal Temperature		0.2% Yield Strength		Ultimate Tensile Strength		Elongation (%)	Reduction of Area (%)
(°F)	(°C)		(°F)	(°C)	(ksi)	(MPa)	(ksi)	(MPa)		
1750	954	1.8	*	*	177	1220	189	1363	15	35.2
1750	954	1.8	1150	621	150	1034	171	1179	18	30.9
1750	954	1.8	1200	649	142	979	162	1117	10	15.4
1750	954	1.3	*	*	147	1014	166	1145	13	32.5
1750	954	1.3	1150	621	141	972	160	1103	12	15.7
1750	954	1.3	1200	649	130	896	150	1134	9	12.2
1950	1065	1.8	*	*	174	1200	185	1276	6	11.6
1950	1065	1.8	1150	621	145	1000	163	1124	9	6.5
1950	1065	1.8	1200	649	132	910	149	1027	8	6.5
1950	1065	1.3	*	*	142	979	158	1080	4	6.5
1950	1065	1.3	1150	621	111	972	161	1110	9	9.6
1950	1065	1.3	1200	649	140	965	160	1103	9	10.7

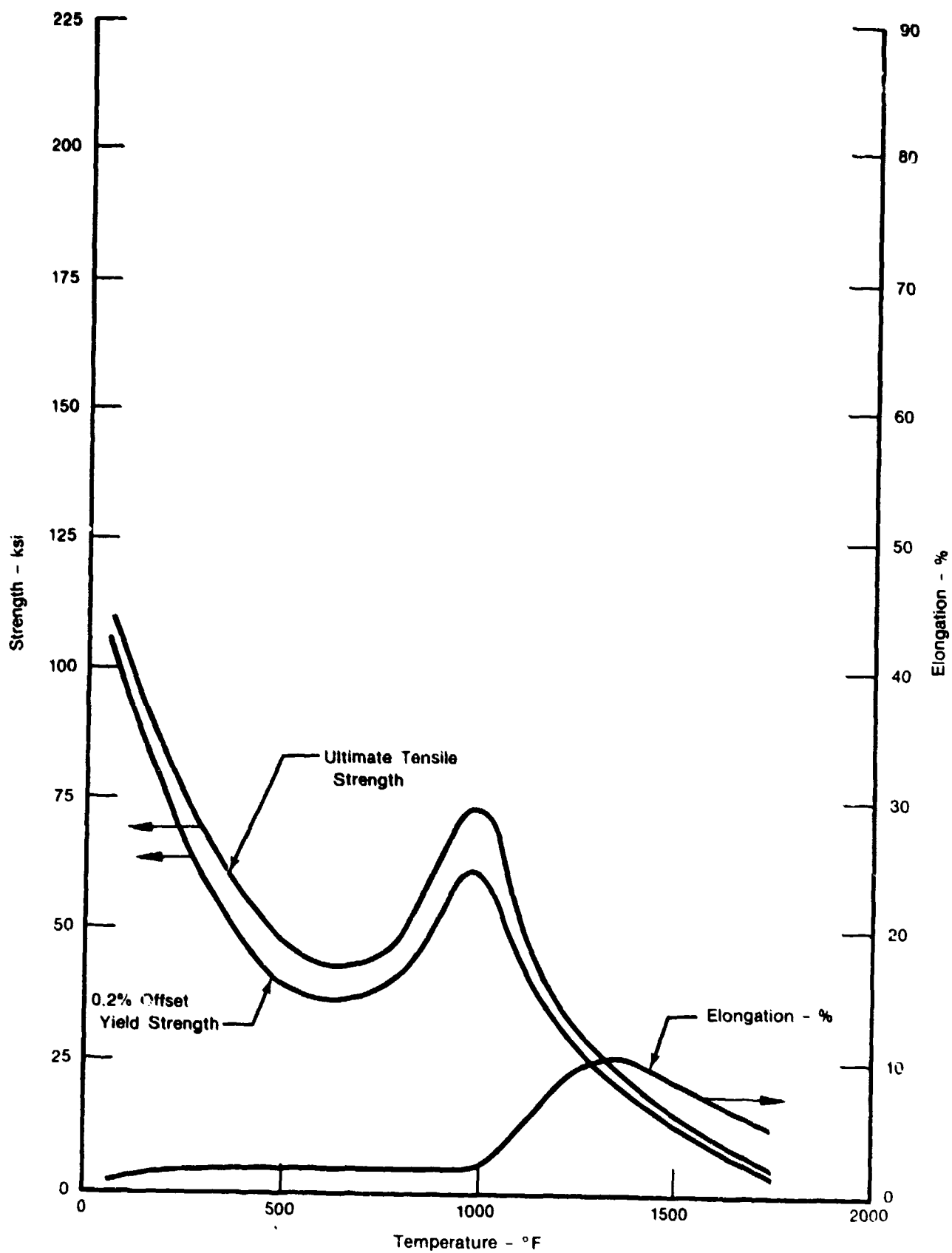
mic

The tensile properties of consolidated Fe₃Al (alloy 729) and Fe₃Al + TiB₂ (alloy 723) were measured as a function of temperature. The consolidated material was produced by extrusion at a low 4-to-1 ratio and by HIP. Figure 86 gives the tensile properties of Fe₃Al (alloy 729) HIP at 2000°F (1093°C) and 15 ksi (103 MPa). As previously discussed, this material was difficult to work due to apparent weak bonding of prior powder particles and this was reflected in the low ductility of the alloy. The increase in strength to 1000°F (538°C) which should be a result of a change in ordering from the B2 to DO₃, was also found in Fe₃Al after a 4-to-1 extrusion at 1700°F (927°C), Figure 87. The extruded Fe₃Al alloy also has a low ductility at ambient temperature, but the elongation increases rapidly with increasing temperature. As a result of improved interparticle bonding, the extruded Fe₃Al could be hot rolled to sheet without difficulty. In comparison with the latter results, the tensile properties of Fe₃Al + TiB₂ (alloy 723) extruded 4 to 1 at 1700°F (927°C) shown in Figure 88, includes a higher elongation and tensile strength which are believed to be a consequence of a finer grain size, retained by the TiB₂ dispersion. However, the HIP or extruded Fe₃Al with and without a dispersion worked under conditions, which produced or retained a fine grain size, were found to have a tensile elongation to 20%. The difference between the alloys is related to the role of TiB₂ in preventing grain growth above a temperature of approximately 1150°F (621°C). Without a dispersion, abnormal grain growth in an Fe₃Al alloy causes the alloy to fail in a brittle manner in a simple bend test.



FD 243612

Figure 85. Microstructure of Fe₃Al (729) Alloy Extruded and Swaged



FD 251085

Figure 86. Tensile Properties of Alloy 729 (Fe₃Al) HIP at 2200°F (1093°C)

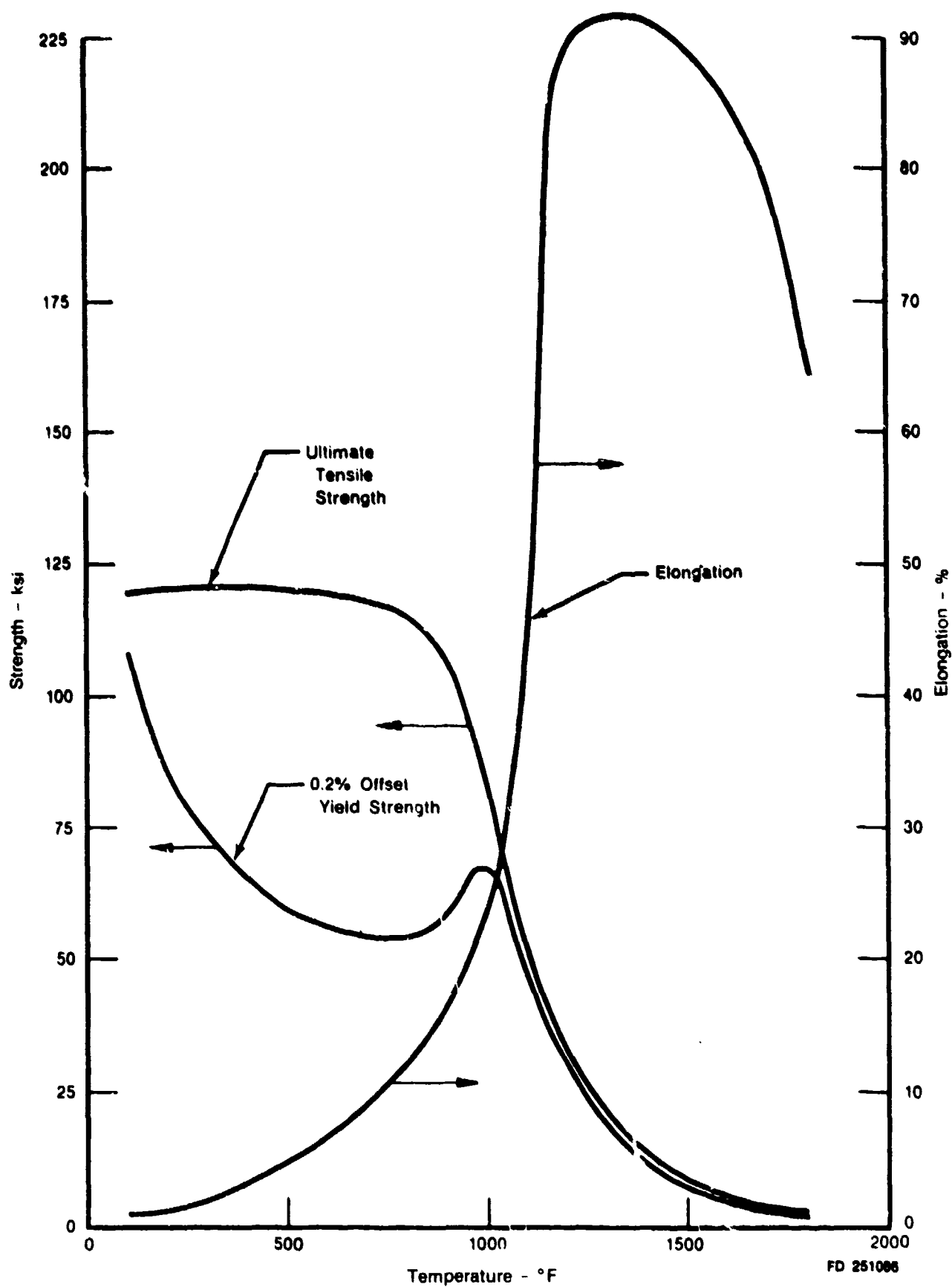
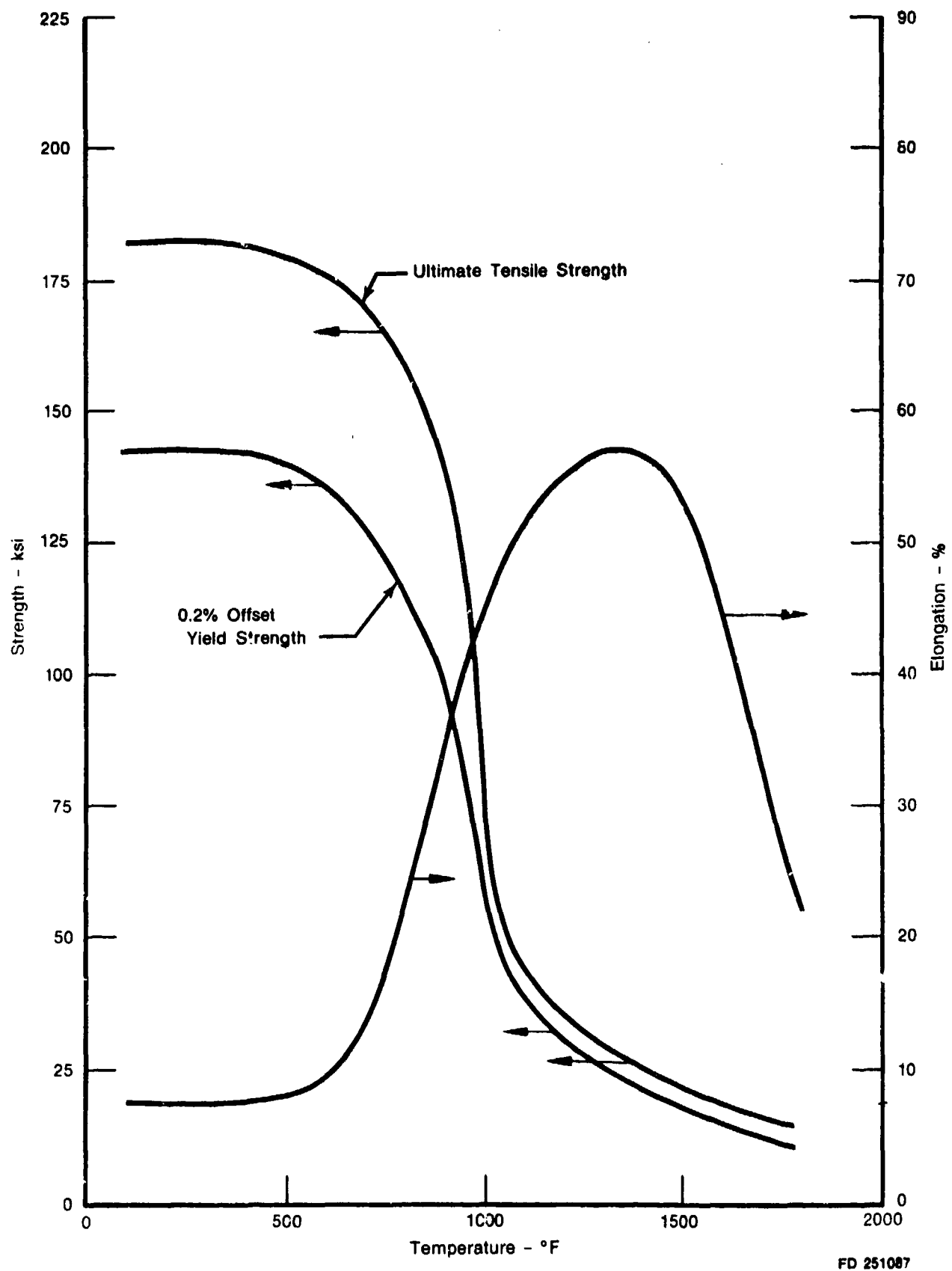


Figure 37. Tensile Properties of Alloy 729 (Fe₃Al) Extruded 4 to 1 at 1700°F (927°C)



FD 251087

Figure 88. Tensile Properties of Alloy 723 ($\text{Fe}_3\text{Al} + \text{TiB}_2$) Extruded 4 to 1 at 1700°F (927°C)

Properties as a Function of Powder Size

The tensile properties of $\text{Fe}_3\text{Al} + \text{TiB}_2$ produced from three lots of powder are given in Tables 17 through 22. The powder particle sizes and processing conditions employed were given in Table 6. The results of the first lot of extrusions produced at different extrusion and swaging temperatures with -80 mesh powder show that consolidation and post working at the lowest temperature produced the highest yield and ultimate strengths at all test temperatures. The lowest temperature sequence, extrusion at 1700°F (926°C) followed by swaging at 1500°F (815°C), produced strengths at ambient temperature that were 11 to 12% greater than the average of the lot. Corresponding increases at 1200°F (649°C) were 19% greater in yield and 24% greater in tension than the average of the lot while the increases in strength at 1800°F were 62 and 76% respectively. Processing at a relatively high temperature such as extrusion and swaging at temperatures over 2000°F (1093°C), produced material of slightly lower strength but with excellent ductility. Extrusion at a high temperature followed by swaging at a lower temperature, for example, 2000°F extrusion and 1500°F swaging, yielded similar results. The latter processing sequences produced material with elongations in the range of 18 to 20%. In comparison, working at a low temperature, for example, 1500°F (815°C), followed by working at a higher temperature, for example, 2000°F (1093°C), significantly lowered the ductility of the alloy. The reduction in ductility from 18 to 20% to 4% was due to abnormal grain growth and, as is known, a large grain size in $\text{Fe}_3\text{Al} + \text{TiB}_2$ is associated with a low ductility. In summary, the lowest consolidation and working temperatures produced the highest strength material with the magnitude of the change increasing with increasing temperature to 1800°F (982°C). The ductility did not vary appreciably except with material worked at a high temperature subsequent to working at an appreciably lower temperature. As shown in the following section on microstructure, processing, which introduces strain in the material, will cause partial recrystallization or grain growth and an increase in grain size is a primary cause for reduced ductility in this class of alloys. However, it needs to be pointed out that $\text{Fe}_3\text{Al} + \text{TiB}_2$ can be processed at relatively high temperatures and that a fine grain and ductile alloy will be produced.

The second and third lots of extrusions (R079 through R108) were produced with different powder size fractions. The material was extruded at 1600 or 1650°F (871 or 899°C) and swaged at temperatures from 1200 to 1600°F (649 to 871°C). Tensile data for these extrusions are listed also in Tables 16 through 21. In general, decreasing the swaging temperature from 1600 to 1300°F (871 to 704°C) increased tensile strength some 15%. This increase, however, was probably due to work hardening. Interestingly, the ductility of the alloy did not change.

Analysis of the data in Tables 17 through 22 for the second and third lots of extrusions revealed a strong correlation between alloy strength and powder size (solidification rate). Figure 89 shows the increase in strength obtained with the fine (-270 mesh) powder and the increase in strength as it relates to the working temperature. The average working temperature was the weighted average of the extrusion and swaging temperatures. Figure 90 presents the data plotted as a function of average powder particle diameter. The increase in yield strength with decreasing powder size, which is related to the strength of the coarsest powder, is on the order of 10% or less at ambient temperature and over 80% at the 1800°F test temperature. The increase in yield strength at ambient temperature may be due to a finer grain size, a finer TiB_2 dispersion or a combination of these factors. The larger increase in yield strength obtained at the higher test temperatures with the finer powder fraction is believed to be due to a uniform microstructure, a high aspect ratio grain and a fine TiB_2 dispersion.

TABLE 17. TENSILE PROPERTIES OF $\text{Fe}_3\text{Al} + \text{TiB}_2$ AT AMBIENT TEMPERATURE

<i>Lot</i>	<i>Identification</i>	<i>0.2% Offset Yield Strength (ksi)</i>	<i>Ultimate Tensile Strength (ksi)</i>	<i>Elongation (%)</i>	<i>Reduction in Area (%)</i>
1	R063	124	166	18	46
1	R064	121	159	18	48
1	R065	134	180	18	44
1	R068	124	164	20	50
1	R069	120	162	20	49
1	R070	115	156	18	41
1	R071	124	167	19	50
1	R073	105	130	4	8
2	R079	130	177	19	46
2	R080	144	191	16	38
2	R081	129	188	18	41
2	R082	169	205	18	36
2	R088	130	176	18	45
2	R089	133	180	17	34
2	R090	147	196	18	40
2	R091	151	201	17	34
2	R097	156	196	17	38
2	R098	154	195	13	33
2	R099	169	213	15	27
2	R100	170	214	17	33
3	R105	148	190	17	37
3	R106	155	199	15	31
3	R107	160	203	17	38
3	R108	163	205	14	29

2711C

TABLE 18. TENSILE PROPERTIES OF $\text{Fe}_3\text{Al} + \text{TiB}_2$ AT 500°F (260°C)

<i>Lot</i>	<i>Identification</i>	<i>0.2% Offset Yield Strength (ksi)</i>	<i>Ultimate Tensile Strength (ksi)</i>	<i>Elongation (%)</i>	<i>Reduction in Area (%)</i>
1	R063	116	161	15	54
1	R064	105	154	14	50
1	R065	139	177	14	36
1	R068	124	164	20	50
1	R069	98	158	14	46
1	R070	115	156	18	41
1	R071	114	165	15	45
1	R073	65	133	12	29

2711C

With respect to ductility, the data in Tables 17 through 22 show the elongation increasing with test temperature with the smallest change for material swaged at the lowest temperature. However, the elongation also decreased with increasing temperature over 1000°F (538°C) and the stronger material produced with the finer powder has the lowest ductility. The level of ductility in this case should be related to the level of strain in the material. The same trend was observed to some extent with reduction in area, but in either case the ductility of $\text{Fe}_3\text{Al} + \text{TiB}_2$ was quite good, and for its strength level it is not unlike that of a conventional steel.

TABLE 19. TENSILE PROPERTIES OF Fe₃Al + TiB₂ AT 1000°F (538°C)

<i>Lot</i>	<i>Identification</i>	<i>0.2% Offset Yield Strength (ksi)</i>	<i>Ultimate Tensile Strength (ksi)</i>	<i>Elongation (%)</i>	<i>Reduction in Area (%)</i>
2	R079	73.8	79.8	23	86
2	R080	81.0	88.8	17	82
2	R081	83.6	91.6	18	85
2	R082	83.6	90.3	24	82
2	R088	77.2	80.4	60	88
2	R089	73.2	80.3	15	87
2	R090	75.8	82.6	20	83
2	R091	77.2	84.6	15	81
2	R097	82.5	89.7	80	88
2	R098	83.2	91.0	105	89
2	R100	82.6	98.1	69	87
3	R105	85.2	91.0	16	86
3	R106	86.9	92.6	9	84
3	R107	80.0	83.7	13	84
3	R108	88.0	95.1	6	81

2711C

TABLE 20. TENSILE PROPERTIES OF Fe₃Al + TiB₂ AT 1200°F (649°C)

<i>Lot</i>	<i>Identification</i>	<i>0.2% Offset Yield Strength (ksi)</i>	<i>Ultimate Tensile Strength (ksi)</i>	<i>Elongation (%)</i>	<i>Reduction in Area (%)</i>
1	R063	27.6	33.1	83	94
1	R064	26.0	32.7	82	94
1	R065	33.1	39.4	67	93
1	R068	26.4	32.7	72	95
1	R069	26.4	34.6	101	95
1	R070	24.4	29.8	93	95
1	R071	26.3	32.8	115	95
1	R073	22.9	29.5	122	95
2	R079	29.2	34.5	23	92
2	R080	35.9	40.6	45	90
2	R081	29.4	37.7	20	91
2	R082	39.1	47.0	33	87
2	R088	30.9	35.8	28	91
2	R089	29.7	34.8	22	91
2	R090	37.3	43.1	26	86
2	R091	38.2	43.4	49	86
2	R097	28.6	39.2	108	94
2	R098	32.0	41.0	75	93
2	R099	38.5	45.9	22	36
2	R100	41.9	48.2	69	88
3	R105	32.4	40.7	16	89
3	R106	35.6	47.6	23	88
3	R107	40.4	48.7	18	86
3	R108	39.0	45.1	30	82

2711C

TABLE 21. TENSILE PROPERTIES OF Fe₃Al + TiB₂ AT 1800°F (982°C)

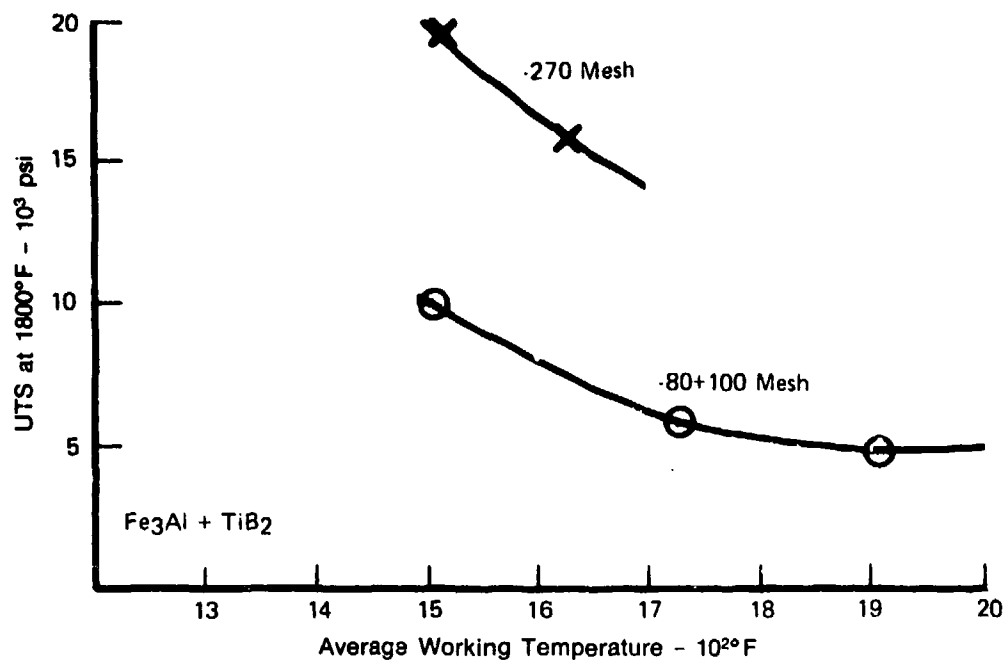
<i>Lot</i>	<i>Identification</i>	<i>0.2% Offset Yield Strength (ksi)</i>	<i>Ultimate Tensile Strength (ksi)</i>	<i>Elongation (%)</i>	<i>Reduction in Area (%)</i>
1	R063	4.2	6.9	63	96
1	R064	4.2	4.4	72	94
1	R065	9.6	11.0	50	87
1	R068	4.1	6.7	86	96
1	R069	5.7	8.9	83	97
1	R070	4.4	5.5	88	96
1	R071	7.1	8.0	71	95
1	R073	4.4	5.3	92	94
2	R079	7.3	10.1	13	84
2	R080	12.3	15.7	16	62
2	R081	7.4	10.0	64	81
2	R082	14.6	18.8	8	56
2	R088	7.7	10.6	42	84
2	R089	8.3	10.5	6	80
2	R090	14.3	15.9	11	61
2	R091	16.5	19.3	9	53
2	R097	8.5	11.5	23	76
2	R098	8.0	11.1	39	83
2	R099	15.0	17.9	16	62
2	R100	15.2	19.1	18	65
3	R105	8.1	12.8	26	81
3	R106	9.6	12.8	22	80
3	R107	11.2	15.6	24	79
3	R108	14.0	17.5	13	70

2711C

TABLE 22. TENSILE PROPERTIES AT ELEVATED TEMPERATURES

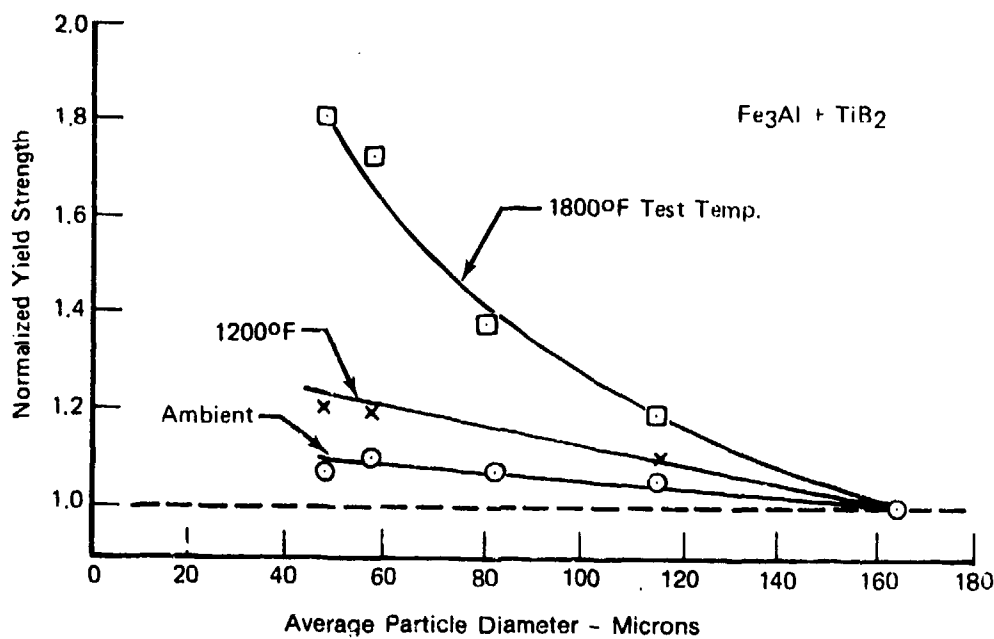
<i>Lot</i>	<i>Identification</i>	<i>Test Temperature (°F) (°C)</i>		<i>0.2% Offset Yield Strength (ksi)</i>	<i>Ultimate Tensile Strength (ksi)</i>	<i>Elongation (%)</i>	<i>Reduction in Area (%)</i>
3	R105 (-80 mesh)	300	149	150.8	188.5	13	25
		300	315	145.1	188.2	13	30
		1400	760	17.2	23.3	14	88
		1600	871	11.7	16.0	28	88
3	R106 (-120 mesh)	600	315	150.8	191.8	15	31
3	R107 (-170 mesh)	600	315	159.3	193.9	13	30
3	R108 (-230 mesh)	300	149	162.2	201.4	13	20
		600	315	167.6	197.5	13	25
		1400	760	23.8	30.0	24	81
		1600	871	18.7	23.4	18	72

2711C



FD 261840

Figure 89. Effect of Particle Size and Working Temperature on the 1800°F Tensile Strength of $Fe_3Al + TiB_2$



FD 261849

Figure 90. Effect of Particle Size on Yield Strength of $Fe_3Al + TiB_2$ at Different Test Temperatures

The stress rupture properties at 1800°F (932°C) listed in Table 23, for $Fe_3Al + TiB_2$ were obtained for both fine (-270 mesh) and coarse (-80 +100 mesh) powder. The trend observed in the data, especially for material produced with the coarser powder, is that of stress rupture life

increasing with decreasing swaging temperature. The data extrapolated to a 100-hour rupture life, and presented in Figure 91, show that the rupture strength at 1800°F (982°C) of material produced with coarse powder increased from about 3.5 to 4.7 ksi (over 30%) by lowering the swaging temperature to 1200°F. However, the material produced with the coarse (-80 +100 mesh) powder swaged at 1200°F (649°C) was found to have recrystallized to an abnormally large grain size during the 1800°F test. In this case, a large grain size alone can account for the increase in stress rupture strength. In comparison, the stress rupture strength of material produced with the fine (-270 mesh) powder did not vary with working temperature. The increased stability of material produced with fine powder which is believed to be related to a more uniform structure and finer TiB₂ distribution was discussed in a prior section describing the microstructure of this alloy. Figures 92 and 93 shows the abnormal grain growth in samples swaged at the lowest temperatures and the fine structure of material processed under conditions which limited strain in the material.

TABLE 23. STRESS RUPTURE PROPERTIES OF Fe₃Al + TiB₂ AT 1800°F (932°C)
(-270 MESH FINE POWDER)

ID	Stress (ksi)	0.2% Creep (hr)	Rupture Life (hr)	Prior Elongation	Total Elongation	RA (%)	Swaging ¹ Temp (°F)
R108 ²	9.0	0.5	1.8	0.475	5.1	—	1300
R103	6.8	<0.4	1.0	0.751	13.4	94	1300
R108	5.2	2.0	4.9	0.402	13.0	94	1300
R108	4.3	3.0	6.8	0.851	13.1	93	1300
R082	4.3	3.4	7.3	2.44	10.9	75	1300
R082 ^A	4.3	10.5	18.5	0.733	4.4	17	1300
R080	4.3	6.0	8.6	0.829	7.8	57	1600
R080 ^A	4.3	0.5	2.0	1.477	9.7	38	1600
R080	3.5	13.0	23.3	2.58	21.5	74	1600

(-80 +100 Mesh Coarse Powder)

R097	4.3	—	442	0.11	6.6	—	1200
R105	5.2	1.4	5.8	0.564	10.9	71	1300
R105	4.3	57.2	64.6	0.369	7.7	40	1300
R105	4.0	99	103.7	0.386	6.7	55	1300
R079	4.3	1.9	14.2	2.746	8.2	45	1600
R079 ^A	4.3	5.9	14.2	0.049	6.7	23	1600

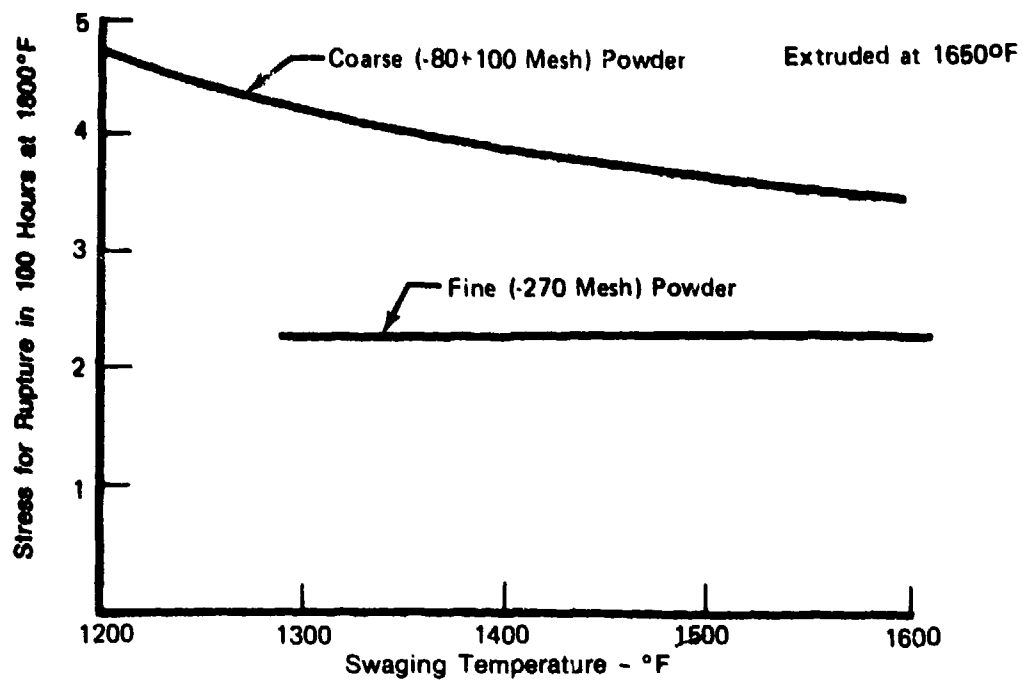
¹Alloys extruded at 1650°F (899°C)

²-230 +270 mesh powder

^AAnnealed 2100°F/4 hr (1150°C) after swaging

2711C

The stress rupture strength at high temperatures of Fe₃Al + TiB₂ compared favorably with that of some nickel-base alloys. For example, the 100- and 1000-hour rupture strength of Hastelloy "X" at 1800°F (982°C) are about 3.8 and 2 ksi respectively, while the equivalent rupture strength of Fe₃Al + TiB₂ with a fine structure is not that much lower.



FD 261850

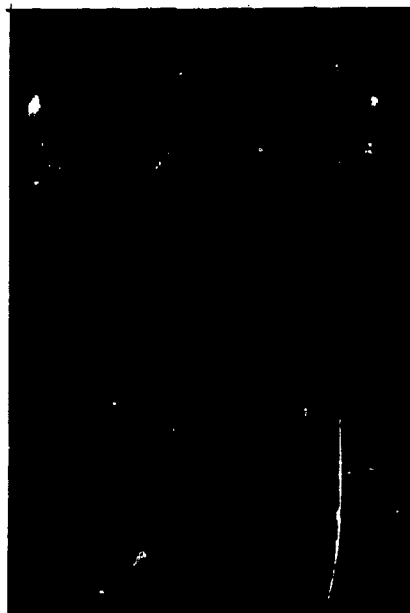
Figure 91. Effect of Swaging Temperature on 1800°F Stress Rupture Strength of $Fe_3Al + TiB_2$



R1087

4.3 ksi - 442 hr

SW1200F



R079

4.3 ksi - 4.2 hr

SW1600F



R108

4.3 ksi - 6.6 hr

SW1300F



R080

4.3 ksi - 8.6 hr

SW1600F
FD 257768

Figure 92. Stress Rupture Samples Tested at 1800 °F (982°C)



R097 4.3 ksi - 442 hr

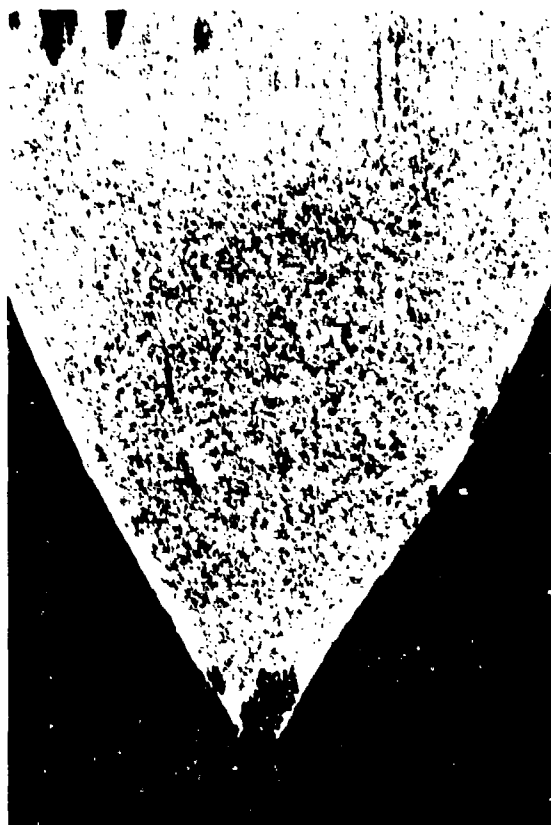
SW1200F



R079

4.3 ksi - 4.2 hr

SW1600F



R108

4.3 ksi - 6.8 hr

SW1200F



R080

4.3 ksi - 8.6 hr

SW1600F

FD 267769

Figure 9a. Stress Rupture Samples Tested at 1800°F (982°C)

Tensile Properties of Alloys Produced in Large Lots

Mechanical properties of the Fe_3Al and $\text{Fe}_3\text{Al} + \text{TiB}_2$ alloy plate rolled from 1.6 to 3.75 (4.06 by 9.52 cm) 50 pound extrusions were determined in both the longitudinal and transverse directions. The Fe_3Al alloy produced from -80 mesh powder was produced in the rolled and annealed condition (1150°F (621°C) rolling and annealing temperatures) as well as in the rolled and recrystallized condition (1150°F (621°C) rolling and 1350°F (732°C) annealing temperatures) while the $\text{Fe}_3\text{Al} + \text{TiB}_2$ alloy was tested in the rolled and annealed condition (1500°F (815°C) rolling and annealing temperatures). Tensile properties were determined from ambient temperature to 1400°F (760°C), fracture toughness at ambient temperature, and rupture strength at 1000, 1200, and 1800°F (538, 650, and 982°C).

The tensile properties of the Fe_3Al and $\text{Fe}_3\text{Al} + \text{TiB}_2$ alloys are given in Tables 24 and 25. The longitudinal yield and tensile strengths of the Fe_3Al in the rolled and annealed, and rolled and recrystallized conditions, and of the $\text{Fe}_3\text{Al} + \text{TiB}_2$ produced with fine and coarse powder are plotted in Figures 94 and 95. The yield and tensile strengths of the $\text{Fe}_3\text{Al} + \text{TiB}_2$ alloy produced from both fine and coarse powders were nearly equal.

The yield and tensile strengths of the Fe_3Al in the rolled and annealed condition were found to be greater than the strengths of the recrystallized material from room temperature to about 900°F (482°C). The difference in strength could be related to the difference in both grain size and degree of grain alignment. At higher temperatures, as could be expected, the strengths of the recrystallized Fe_3Al were somewhat greater. In contrast to the latter results, the yield and tensile strengths of the $\text{Fe}_3\text{Al} + \text{TiB}_2$ were significantly higher from room temperature to about 900°F (482°C) than those of the Fe_3Al . For example, at 700°F (371°C), the yield strength of the TiB_2 containing alloy was at least 2.5 times that of the recrystallized Fe_3Al alloy (139.8 ksi versus 54.5 ksi). The increase in strength, in this case, should be derived from both a fine aligned grain size and the presence of the TiB_2 dispersion. At higher temperatures to 1200°F (650°C), the strengths of the TiB_2 containing alloy fell in the range of the strengths for the Fe_3Al alloy, but at still higher temperatures, 1400°F (760°C) and above, its tensile strength increased due to the aligned grain structure and pinning of grain boundaries.

The elongation at room temperature of as-rolled and annealed Fe_3Al was found to be at least twice (15 to 16% versus 6 to 8% elongation) that of recrystallized Fe_3Al as shown in Table 24 and Figures 96 and 97. The higher elongation of the rolled and annealed material could be related to both a fine and aligned grain structure. As shown previously, recrystallized Fe_3Al has an equiaxed and appreciably coarser grain size. The room temperature elongation for the $\text{Fe}_3\text{Al} + \text{TiB}_2$ produced from coarse (-80 +140 mesh) powder was close to that of the rolled and annealed Fe_3Al alloy and somewhat lower (11 to 15% versus 15 to 20%) than for the same alloy produced from extruded and swaged material, Figure 25. The lower ductility of the rolled alloy could be due to a somewhat coarser grain size and a different texture. This was discussed in a prior section. The apparent lower elongation of 11% for $\text{Fe}_3\text{Al} + \text{TiB}_2$ produced from fine powder could be related to residual strain in the material rolled at 1500°F (815°C). The reduction in area measurements plotted in Figure 12 for the same alloys reflect the results obtained for tensile elongation.

The transverse tensile properties are given in Tables 24 and 25. The transverse yield and ultimate strengths of Fe_3Al at room temperature were nearly equal to the longitudinal strengths, but the elongation in the transverse direction was significantly lower. With increasing temperatures, the transverse and longitudinal strength and ductility of the alloy were more nearly equal. Additional data is required to verify these measurements.

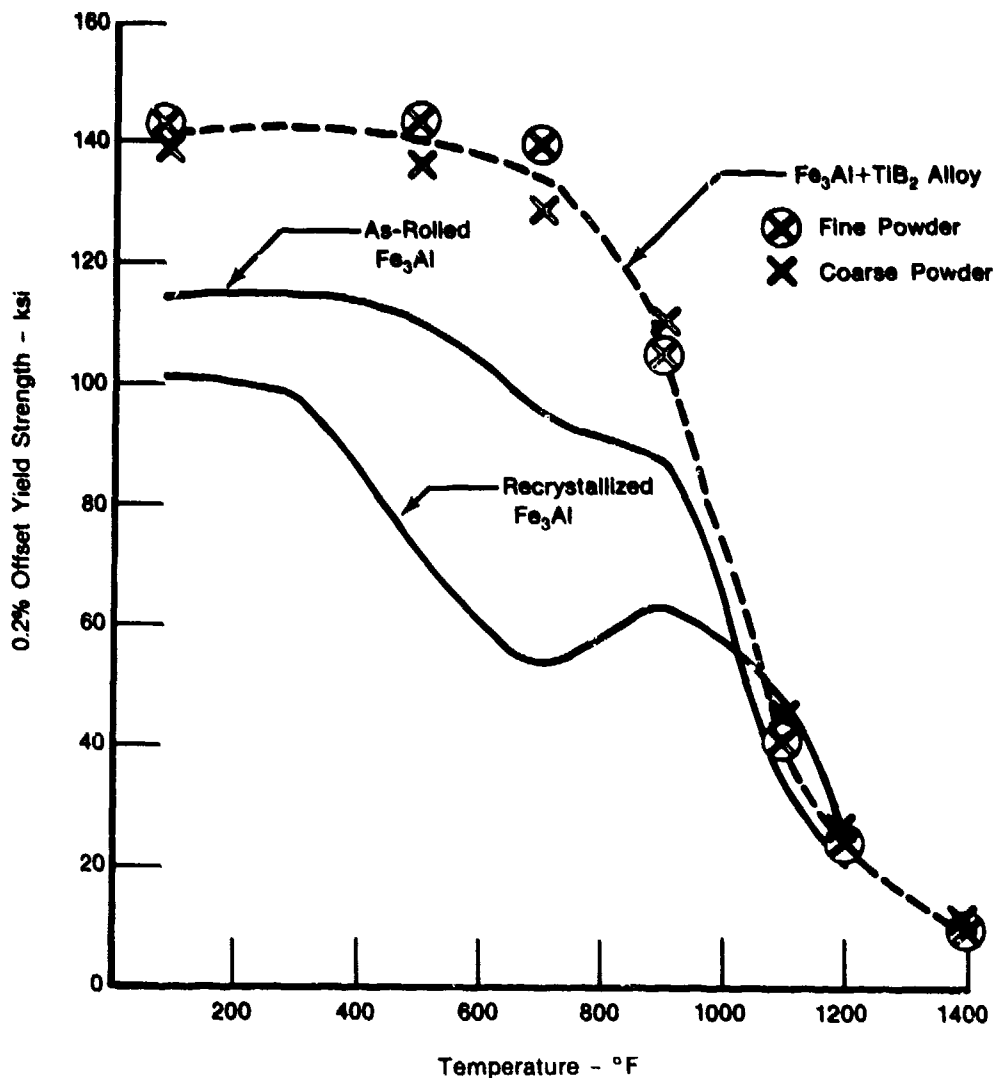
TABLE 24. LONGITUDINAL AND TRANSVERSE TENSILE PROPERTIES OF Fe₃Al ALLOY AS ROLLED AT 1150°F (621°C) AND RECRYSTALLIZED AT 1350°F (732°C)

Test Temperature (°F)	0.2% Offset Yield Strength (ksi)						Ultimate Tensile Strength (ksi)						Elongation (%)						Reduction in Area (%)					
	Annealed (1150°F)			Recrystallized (1350°F)			Annealed (1150°F)			Recrystallized (1350°F)			Annealed (1150°F)			Recrystallized (1350°F)			Annealed (1150°F)			Recrystallized (1350°F)		
	Long		Trans	Long		Trans	Long		Trans	Long		Trans	Long		Trans	Long		Trans	Long		Trans	Long		Trans
	Long	Trans	Long	Long	Trans	Long	Long	Trans	Long	Long	Trans	Long	Long	Trans	Long	Long	Trans	Long	Long	Trans	Long	Long	Trans	Long
Ambient	113.2	126.4	101.3	112.6	138.9	142.7	126.7	139.6	15	9	6	8	20	13	6	9	9	9	20	13	6	9	9	9
Ambient	114.8	125.2	101.2	111.8	137.7	142.7	129.5	138.2	16	4	8	8	29	8	12	9	9	9	29	8	12	9	9	9
300	114.6	—	98.4	—	132.4	—	122.4	—	16	—	15	—	36	—	41	—	—	—	36	—	41	—	—	—
500	112.2	120.7	72.0	82.4	135.7	140.8	132.0	137.8	12	10	14	9	36	13	45	18	18	18	36	13	45	18	18	18
700	94.3	—	54.5	—	138.7	—	128.8	—	12	—	19	—	32	—	40	—	—	—	32	—	40	—	—	—
900	87.0	96.4	63.6	69.1	101.5	106.7	90.9	98.1	38	24	64	37	63	26	74	43	43	43	63	26	74	43	43	43
1100	34.7	37.1	48.2	47.9	38.5	41.9	46.2	47.9	54	48	25	10	84	53	83	72	72	72	84	53	83	72	72	72
1200	20.9	22.6	24.6	26.6	23.7	25.0	24.6	26.6	41	48	22	17	83	68	89	74	74	74	83	68	89	74	74	74

TABLE 25. LONGITUDINAL AND TRANSVERSE TENSILE PROPERTIES OF Fe₃Al + TiB₂ ALLOY AS ROLLED AT 1500°F
(815°C)

Test Temperature (°F)	0.2% Offset Yield Strength (ksi)				Ultimate Tensile Strength (ksi)				Elongation (%)				Reduction in Area (%)			
	Fine Powder		Coarse Powder		Fine Powder		Coarse Powder		Fine Powder		Coarse Powder		Fine Powder		Coarse Powder	
	Long	Trans	Long	Trans	Long	Trans	Long	Trans	Long	Trans	Long	Trans	Long	Trans	Long	Trans
Ambient	143.1	157.4	140.7	154.0	179.0	181.7	180.7	177.4	11	4	14	4	17	5	25	6
Ambient	137.4	139.3	144.3	155.7	173.7	178.1	183.0	182.0	11	12	15	5	15	18	32	6
350	—	—	139.4	—	—	—	175.5	—	—	—	11	—	—	—	30	—
500	143.8	136.6	136.0	—	177.8	175.0	177.1	—	9	9	8	—	18	18	21	—
700	139.8	119.1	128.9	141.8	179.7	162.8	169.1	167.7	4	11	14	7	5	18	24	8
800	—	—	119.0	—	—	—	147.4	—	—	—	30	—	—	—	58	—
900	105.7	108.5	110.4	109.2	113.2	117.6	119.2	118.5	24	18	46	11	64	39	12	37
1100	41.9	—	42.6	—	49.5	—	50.1	—	70	—	49	—	80	—	87	—
1200	24.2	26.0	26.1	25.8	31.6	32.9	34.8	34.3	73	32	45	35	85	64	97	70
1400	9.8	9.2	11.1	10.1	14.5	13.8	15.7	15.9	44	32	52	40	86	71	90	74

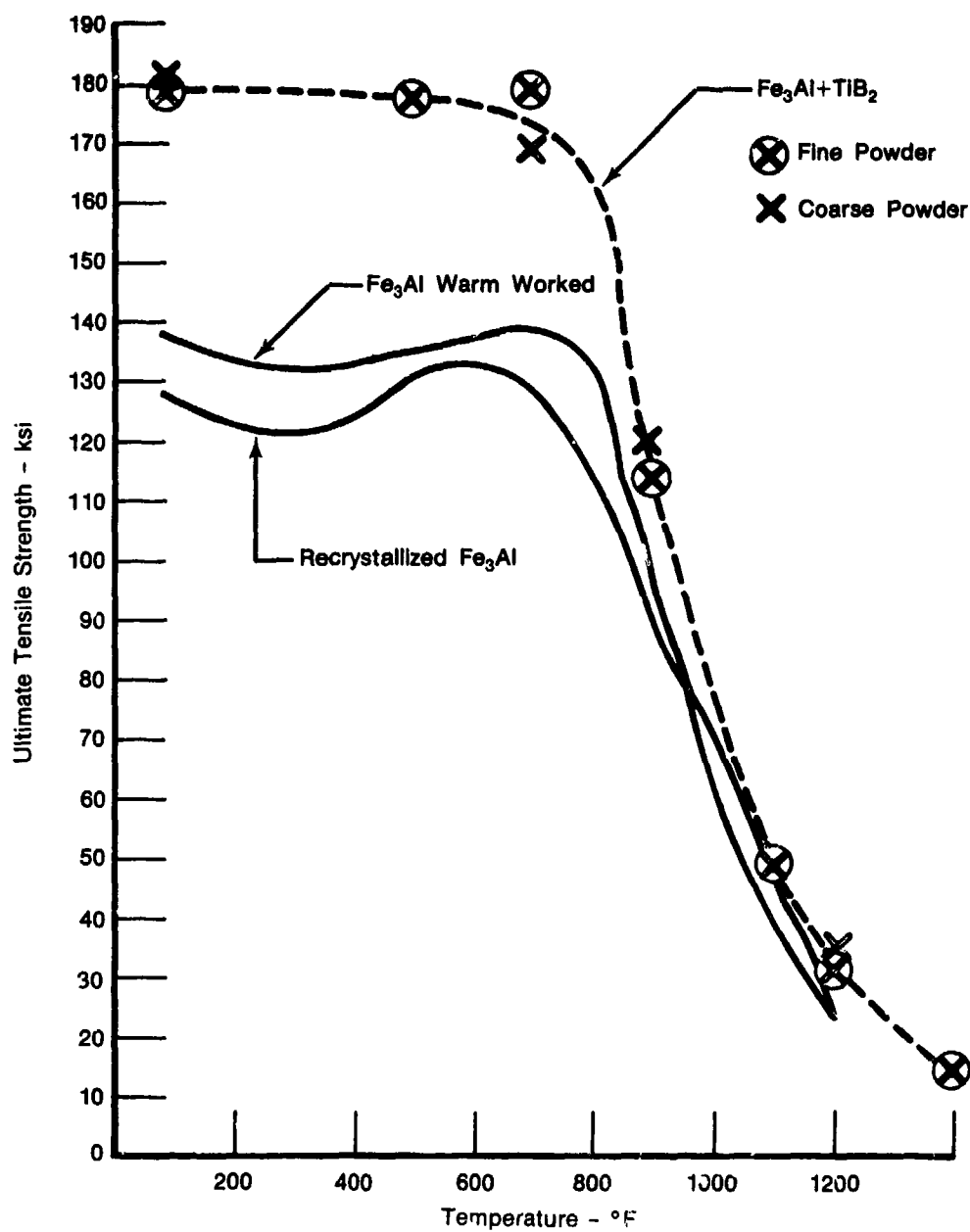
THICK



FD 271845

Figure 94. Yield Strength Versus Temperature for Extruded and Rolled Fe₃Al With and Without TiB₂

As shown in Table 25, the transverse yield and tensile strengths of Fe₃Al + TiB₂, were found to be similar in both the longitudinal (rolling) and transverse directions. However, greater scatter in the data and a lower ductility, as measured by elongation and reduction in area, was measured for the transverse direction. At room temperature, the elongation in the transverse direction was lower by 60 to 80%, but lower by only 15 to 40% at 900 to 1400°F (482 to 760°C). Differences in the elongation of fine and coarse powder material were also measured and anomalies were found which indicate that the use of finer powder may provide a significant advantage. For example, with three of seven samples, the elongation in the transverse direction of material produced with the finer (-270 mesh) powder was equal to or greater than for the same material tested in the longitudinal or rolling direction.



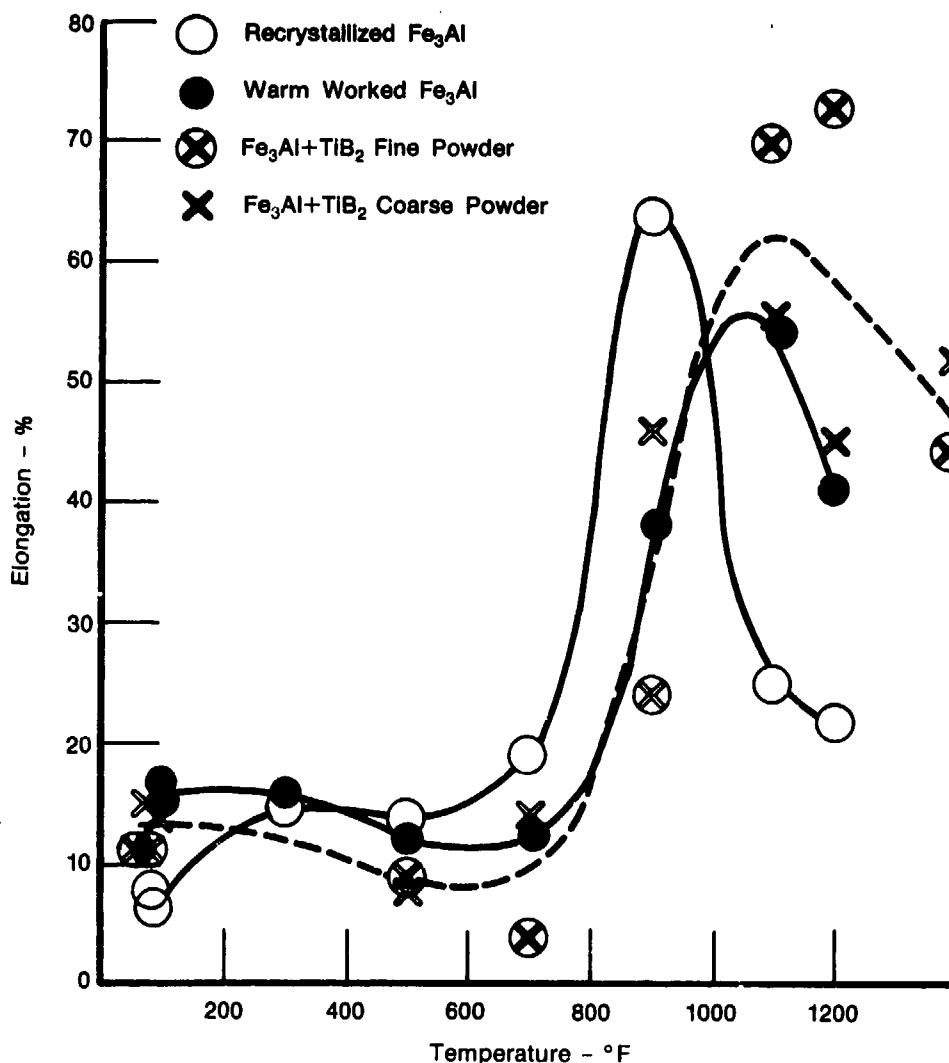
FD 271846

Figure 95. Tensile Strength Versus Temperature for Extruded and Rolled Fe₃Al With and Without TiB₂

Stress Rupture Properties of Alloys Produced in Large Lots

Fe₃Al

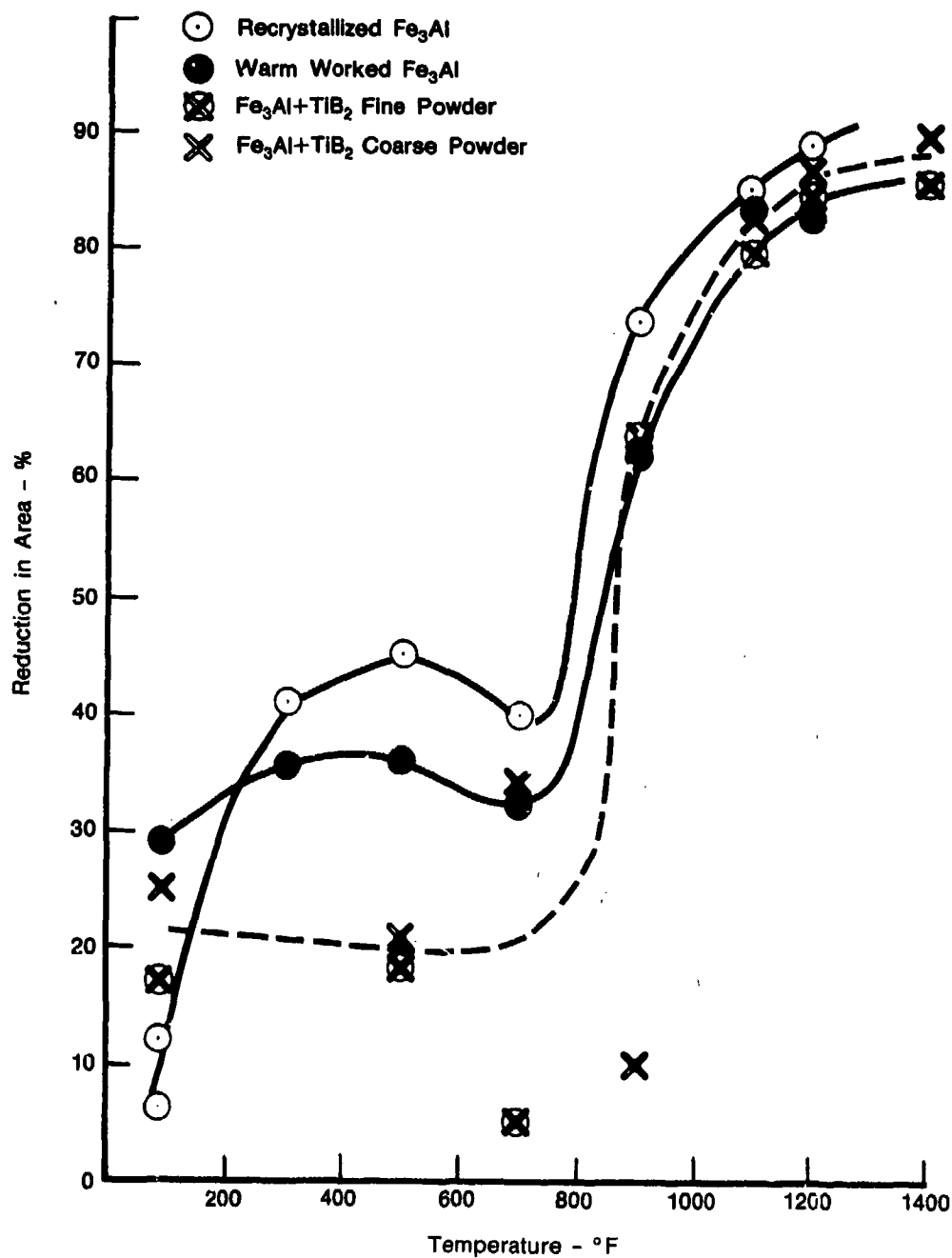
The stress rupture properties of Fe₃Al after rolling and annealing at 1150°F (621°C) (below the recrystallization temperature) and rolling at 1150°F (621°C) followed by annealing at 1350°F (732°C) (above the recrystallization temperature) are presented in Table 26. The measurements at 900, 1000, and 1200°F (482, 538 and 643°C) were made with samples machined in the longitudinal or rolling direction.



FD 271847

Figure 96. Elongation Versus Temperature for Extruded and Rolled Fe₃Al With and Without TiB₂

The effects of recrystallization are a decrease in elongation, especially in the total elongation, at the lower 900°F (482°C) temperature, and an appreciable increase, i.e., 28% to 101%, at the higher 1200°F (650°C) test temperature. These results are at variance with the results obtained in tensile where the elongation at 1200°F (650°C) for recrystallization Fe₃Al was about half (22% versus 41%) that of the as worked material. At the lower 900°F temperature, the tensile elongation of the recrystallized material was significantly higher, 64 versus 38%. This difference in elongation between tensile and creep may be related to strain rate and grain boundary effects since at higher stresses, in stress rupture tests, the elongation, as shown in Table 27, became more nearly equal at 1200°F (650°C).



FD 271848

Figure 97. Reduction of Area Versus Temperature for Extruded and Rolled Fe_3Al With and Without TiB_2

TABLE 26. STRESS RUPTURE PROPERTIES OF Fe₃Al IN THE LONGITUDINAL (ROLLING DIRECTION)

ID ⁽¹⁾	Temperature (°F)	Stress (ksi)	0.2% Creep (hr)	Rupture Life (hr)	Prior Elongation (%)	Total Elongation (%)	RA (%)
A	900	35.0	2.0	127.0	33.7	55	67
B	900	35.0	17.7	129.6	22.2	26	55
A	1000	20.0	0.9	55.4	25.8	36	71
B	1000	15.0	5.2	418.5	48.7	69	77
B	1000	20.0	3.3	60.6	45.6	62	71
B	1000	15.0	12.1	312.4	—	78	62
A	1200	7.5	0.1	8.0	39.7	116	86
A	1200	5.0	0.2	19.9	19.4	29	85
A	1200	3.5	13	439.5	27.0	28	66
B	1200	7.5	<0.1	7.1	41.5	89	89
B	1200	5.0	0.6	27.7	29.1	42	89
B	1200	3.5	6.4	388.7	81.7	101	70

(1) A — Fe₃Al Rolled and Annealed at 1150°F (621°C)

B — Fe₃Al Rolled at 1150°F and Annealed at 1350°F (732°C)

2711C

TABLE 27. STRESS RUPTURE PROPERTIES OF Fe₃Al PRODUCED FROM FINE AND COARSE POWDER TESTED IN THE LONGITUDINAL/ROLLING DIRECTION

ID ⁽¹⁾	Temperature (°F)	Stress (ksi)	0.2% Creep (hr)	Rupture Life (hr)	Prior Elongation (%)	Total Elongation (%)	RA (%)
F	1000	26.0	0.3	36.7	43.5	54	65
F	1000	20.0	0.7	161.5	44.8	51	51
C	1000	20.0	1.4	659.1	38.9	37	70
F	1200	20.0	<0.1	6.8	4.6	71	81
F	1200	12.0	<0.1	14.0	45.0	69	74
F	1200	10.0	0.2	41.6	49.4	61	63
F	1200	8.5	0.3	98.4	24.7	67	64
C	1200	12.0	0.1	34.1	12.6	18.6	73
C	1200	11.0	<0.8	226.9	36.1	38.9	78
C	1200	9.0	0.5	513 Disc	—	—	—
F	1800	4.0	3.2	9.2	1.51	8	18
F	1800	3.0	—	344.7	0.43	7	65
C	1800	4.0	<0.1	1.5	4.9	46	91
C	1800	3.0	0.3	36.3	9.7	12	25
C	1800	2.0	9.3	510 Disc	—	—	—

(1) F — Fe₃Al Fine (−270 mesh) Powder Rolled and Annealed at 1500°F

C — Fe₃Al Coarse (−80 mesh) Powder Rolled and Annealed at 1500°F

2711C

The stress rupture life was apparently little affected by the recrystallization. This is surprising in view of the difference in grain structure which is aligned ½ to 30 microns in diameter in the worked Fe₃Al and equiaxed 50 to 100 microns in the recrystallized material.

Fe₃Al + TiB₂

The stress rupture properties of Fe₃Al + TiB₂ produced from fine (-270 mesh) and coarse (-80 +140 mesh) powder extruded 8 to 1 at 1700°F (927°C) and rolled 65% at 1500°F (815°C) are given in Table 28. The tests were conducted at 1000, 1200, and 1800°F (538, 649, and 982°C) with samples machined in the longitudinal or rolling direction.

TABLE 28. STRESS RUPTURE PROPERTIES OF Fe₃Al PRODUCED FROM FINE AND COARSE POWDER TESTED IN THE TRANSVERSE DIRECTION

ID ⁽¹⁾	Temperature (°F)	Stress (ksi)	0.2% Creep (hr)	Rupture Life (hr)	Prior Elongation (%)	Total Elongation (%)	RA (%)
C	1000	20.0	<1.0	252.7	31.5	35	26
F	1200	20.0	<0.1	0.4	28.4	37	49
F	1200	10.0	<0.1	13.3	33.6	35	32
F	1200	8.5	0.1	23.8	30.8	31	28
C	1200	9.0	0.1	85.8	23.6	24	24
C	1200	7.0	0.6	363.3	8.9	10.4	13.8
F	1800	2.0	(2)	29.8	—	2	0
F	1800	1.4	—	154.3	—	8	3
F	1800	4.0	—	<0.1	—	51	21
F	1800	2.0	—	2.4	—	31	2
F	1800	1.4	—	23.3	—	16	14

(1) F — Fe₃Al + TiB₂ Fine (-270 mesh) Powder Rolled and Annealed at 1500°F

C — Fe₃Al + TiB₂ Coarse (-80 +140 mesh) Powder Rolled and Annealed at 1500°F

(2) — Not Measured

2711C

The material produced with coarse powder was found to have a significantly greater stress rupture life (659.1 versus 161.5 hours) at the lower 1000°F (538°C) test temperature. The reverse (36.3 versus 344.7 hours) was found to be the case at the higher 1800°F (982°C) test temperature. At the intermediate 1200°F (650°C) test temperature, the increase in stress rupture life for the material produced from coarse powder was 34.1 versus 14.0 for the material produced from fine powder. These results suggest that some change in structure is taking place with increasing temperature, and that the rupture life of both materials could be equal at about 1600°F (871°C).

The elongation of the alloys was found to be related to the rupture life with the correlation being different at the higher 1800°F temperature. That is, the total elongation at 1800°F was lower (7 versus 12%) for the material produced with fine powder. However, the reduction in area which could be more accurately measured was greater (65 versus 25%) for the material produced with the fine powder. According to the stress rupture results discussed previously, the 1800°F (982°C) test samples of Fe₃Al + TiB₂ produced from fine powder and swaged at 1600°F (871°C) retained a fine grain size during test, while the same material swaged at a lower 1200°F (650°C) temperature recrystallized during test to an abnormal grain size in the gauge section of the sample. In comparison, the 1800°F (982°C) test samples of material produced from coarse powder and swaged at a low temperature, for example, 1200°F (650°C), recrystallized to an abnormal grain size in the gauge as well as in the grip section of the samples while the same material swaged at 1600°F (871°C) retained a fine aligned worked structure throughout.

The stress rupture results obtained with the large extrusions, and discussed above, were found to be related to their microstructures as shown in Figure 98. The Fe₃Al + TiB₂ samples produced with fine powder and rolled at 1500°F (815°C) and tested at 1800°F (982°C) were found

to have an abnormally large grain structure. In comparison, the material produced with coarse powder and tested under the same conditions retained a fine grain size. As noted in Figure 98, the stress rupture life (highest for the sample with large grains) correlated very well with microstructure. The microstructure of stress rupture samples tested at the lower temperatures (1000 and 1200°F) were fine grain as in the gage section of Figure 97B. The higher stress rupture lives, for example, 659.1 versus 161.5 hours, were for the material produced with coarse powder which had the finer and higher ratio grain structure.

The stress rupture results described previously, especially the 1800°F (982°C) results, are at variance with the results for swaged material discussed previously. The variance which was related to the microstructures of the alloys also demonstrated the difficulties which can be encountered with scale up of a new alloy. The significance of the stress rupture results obtained with the large extrusions of $\text{Fe}_3\text{Al} + \text{TiB}_2$ are believed to be as follows.

The stress rupture properties of $\text{Fe}_3\text{Al} + \text{TiB}_2$ in the transverse direction are shown in Table 27. The stress rupture life at 1800°F (982°C) for the material produced with fine powder was appreciably greater (153.3 versus 23.3 hours) than the material produced with coarse powder. The reverse was obtained for the 1200°F (650°C) tests. These results are comparable to the results obtained in the longitudinal direction except that rupture life was generally much lower in the transverse direction. The longitudinal to transverse stress rupture life from Tables 27 and 28 is in some cases more than an order of magnitude greater. However, the difference in rupture strength is considerably less. The correlation between microstructure and stress rupture results are essentially the same as described for the stress rupture results in the longitudinal direction.

The relative stress rupture properties of Fe_3Al and $\text{Fe}_3\text{Al} + \text{TiB}_2$ are shown in Figure 99. The $\text{Fe}_3\text{Al} + \text{TiB}_2$ was found to be stronger than the Fe_3Al , and especially at the higher 1800°F (982°C) temperature. The TiB_2 dispersion in an aligned fine (or coarse) grain $\text{Fe}_3\text{Al} + \text{TiB}_2$ alloy greatly enhanced stress rupture strength attaining a level comparable to that of Hastelloy "X." Although the use of fine versus coarse powder and varying processing schedules could affect grain size, grain alignment, dispersion size, and resistance to abnormal grain growth, the stress rupture results for $\text{Fe}_3\text{Al} + \text{TiB}_2$ shown in Figure 99 did not vary over that wide a range. Of greater concern was the effect of grain size on alloy ductility, and this could be controlled to a large extent. The resistance to grain coarsening was found to be related to the level of residual strain in the material, but as was discussed in a prior section, alloying was found to be more effective in raising the recrystallization or abnormal grain growth temperature in this class of alloys. The alloying of $\text{Fe}_3\text{Al} + \text{TiB}_2$ with molybdenum, studied under Company-funded IR&D programs, also increased the stress rupture of the alloy to a comparatively high level. These results are presented to show the relatively high temperature strengths as well as the potential of the alloys for use in aircraft engine applications.

Fracture Toughness Properties of Alloys Produced in Large Lots

The fracture toughness properties of Fe_3Al and $\text{Fe}_3\text{Al} + \text{TiB}_2$ were determined using compact tensile samples. Tests were made with crack propagation parallel and transverse (perpendicular) to the rolling direction. The Fe_3Al alloy was tested after rolling and annealing at 1150°F (621°C) and after recrystallization at 1350°F (732°C). The $\text{Fe}_3\text{Al} + \text{TiB}_2$ alloy derived from fine (-270 mesh) and coarse (-80 +140 mesh) powder was tested after rolling at 1500°F (815°C).



Ⓐ Fine Powder Gauge

200 μm



Ⓐ 3 ksi - 344.7 hr - Grip

100 μm



Ⓑ Coarse Powder Gauge

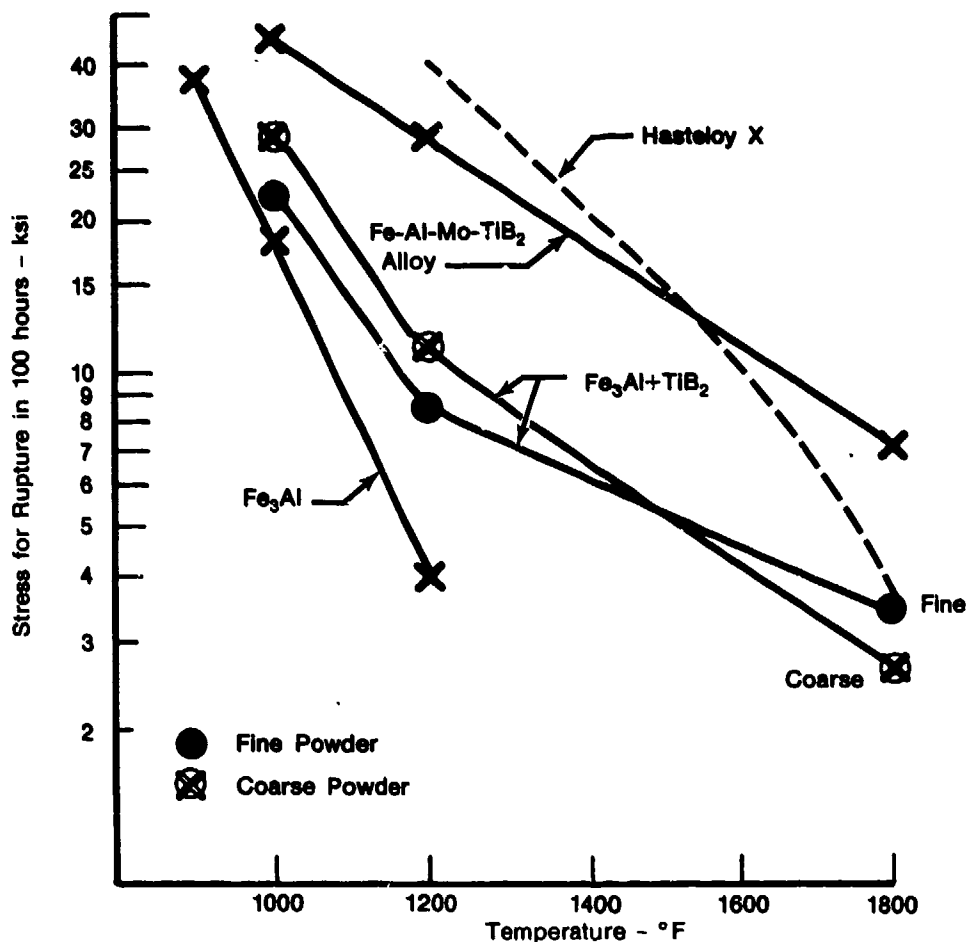
200 μm



Ⓑ 3 ksi - 36.3 hr - Grip

200 μm
FD 271849

Figure 98. Stress Rupture Samples of $\text{Fe}_3\text{Al} + \text{TiB}_2$ Produced from Fine (A) and Coarse (B) Powder and Tested at 1800°F



FD 271850

Figure 99. Stress Rupture in 100 Hours for Fe_3Al and $Fe_3Al + TiB_2$ Provided from a Large Rolled Extrusion

In accordance with ASTM E399, "Plane Strain Fracture Toughness of Metallic Materials," sample size must be such that linear elastic behavior is obtained. Analysis of the load/displacement data for the iron aluminides indicated that sample thickness was inadequate to obtain plane strain conditions. Since all test load ratios (P_{max}/P_Q) exceeded the maximum (1.10), the presence of considerable plastic deformation was implied. However, pure plane strain fractures were obtained for all samples tested.

Examination of samples fractures, Figure 100, revealed a "lamellar type" structure with considerable secondary cracking. It appears that the failure mechanism in these alloys contributed to the plastic behavior observed in the recorded data, and consequently the tests were judged as meeting basic plane strain conditions. Nevertheless, the calculated K_Q values presented in Tables 29 and 30 should be qualified as approximations for engineering comparison, and should not be considered as critical plane strain K_{IC} values.



FD 270894

Figure 100. Typical Fracture Surface of the Fe_3Al and $Fe_3Al + TiB_2$ Alloys

TABLE 29. FRACTURE TOUGHNESS PROPERTIES OF ROLLED Fe_3Al

	K_Q ksi $\sqrt{in.}$	
	Direction of Crack Propagation	
	Longitudinal	Transverse
Rolled and Annealed at 1150°F	36.8	34.1
	36.2	
Recrystallized at 1350°F	27.9	—

2711C

TABLE 30. FRACTURE TOUGHNESS PROPERTIES OF ROLLED $Fe_3Al + TiB_2$ ALLOY PRODUCED WITH FINE AND COARSE POWDER

	K_Q ksi $\sqrt{in.}$	
	Direction of Crack Propagation	
	Longitudinal	Transverse
-270 Mesh	69.6	43.6
-80 +140 Mesh	62.7	71.4
	50.7	65.8

2711C

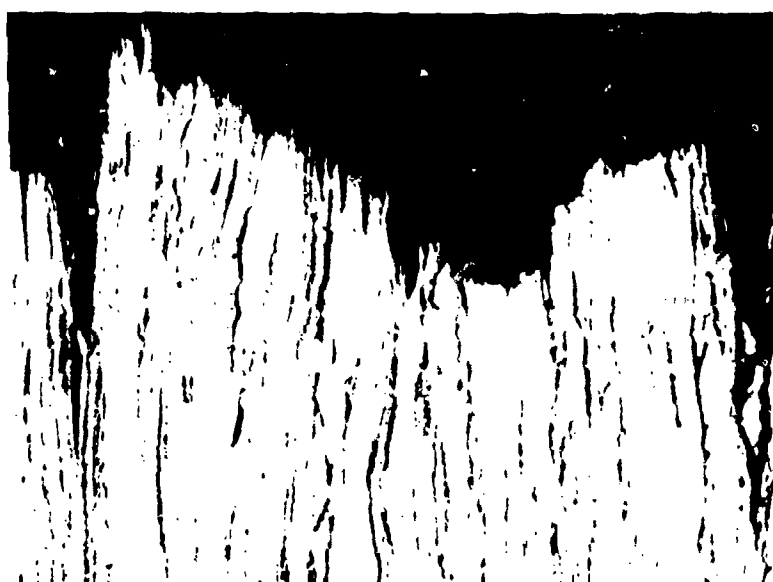
As shown in Figure 101, metallographic sections of fracture samples showed considerable plastic deformation in the Fe_3Al and $Fe_3Al + TiB_2$ alloys, and much less in the Fe_3Al with the recrystallized grain structure. Numerous cracks in the rolling plane of the fracture surface emphasized the lamella structure of the rolled alloys. These were over 400 microns in thickness in the Fe_3Al and 100 to 200 microns in the $Fe_3Al + TiB_2$. As indicated previously, the deformation within the structure no doubt contributed to the deformation in the alloys. Although the K_Q values listed in Tables 28 and 29 cannot be equated to K_{IC} , it appears that the alloys do possess a significant fracture toughness.



Fe₃Al Rolled and Recrystallized

100 μ m

FD 20040



Fe₃Al Rolled 1150°F



Fe₃Al + TiB₂ Rolled 1500°

Figure 101. Cross Sections of Fracture Toughness Samples Produced from Extruded and Rolled Material Longitudinal Fractures

SEM examination of the fracture surfaces, shown in Figure 102, revealed occasional secondary cracks and large cleavage facets. In comparison, the fracture surface of $\text{Fe}_3\text{Al} + \text{TiB}_2$, shown in Figure 103, revealed relatively large cracks spaced about 100 microns apart along with finer cracks on the order of 10 microns apart. At high magnification, the latter fracture surface consists of fine dimples characteristic of void coalescence as well as cleavage.



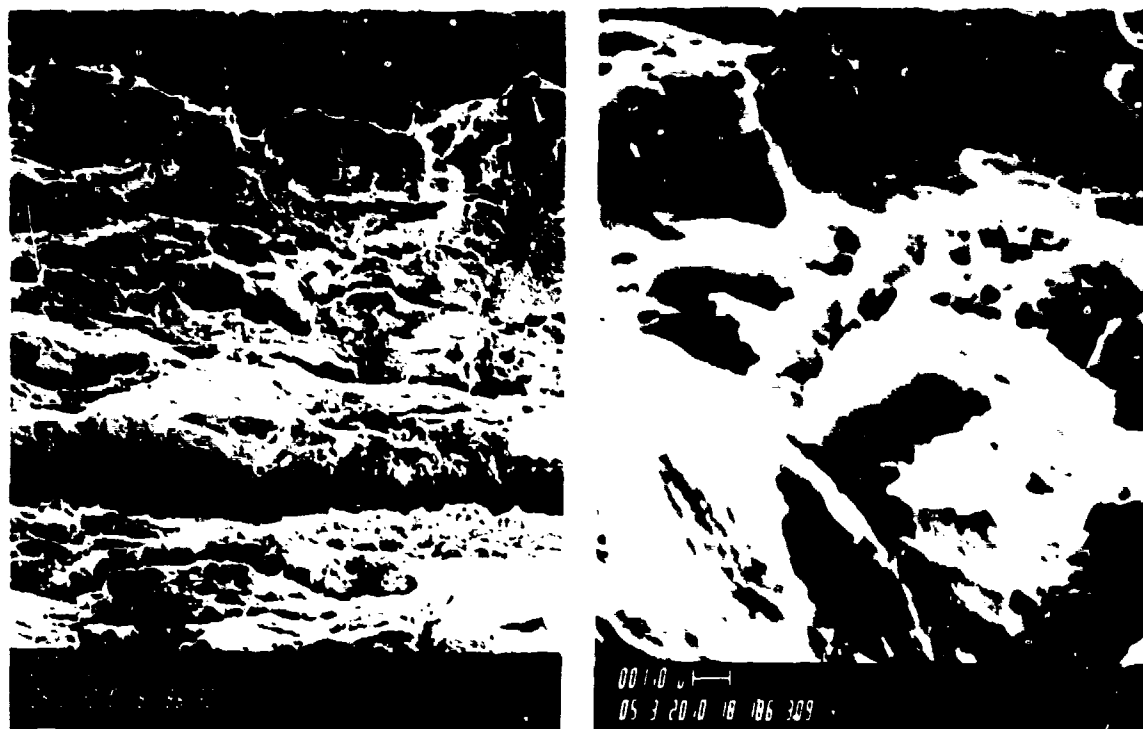
Rolled at 1150°F



Rolled 1150°F and Recrystallized at 1350°F

FD 276875

Figure 102. Fracture Surface of Fe_3Al Alloy



FD 276888

Figure 103. Fracture Surface of $\text{Fe}_3\text{Al} + \text{TiB}_2$ Alloy

The average K_Q of 65.8 ksi $\sqrt{\text{in.}}$ for $\text{Fe}_3\text{Al} + \text{TiB}_2$ compared to 33.8 ksi $\sqrt{\text{in.}}$ for the Fe_3Al alloy is believed to be due to its finer structure and the type of fracture obtained. As expected, the recrystallized Fe_3Al had the lower K_Q of 27.5 ksi in. The difference in transverse K_Q of the $\text{Fe}_3\text{Al} + \text{TiB}_2$ produced from fine and coarse powder was related to alloy structure. The alloy produced with the coarse powder had the finer and higher aspect grain structure and the higher K_Q .

Evaluation of Dispersoids — Task I Extension

The goal of this task was to increase the specific modulus of iron aluminum from 112 (10)⁶ for Fe_3Al to at least 140 (10)⁶ by increasing the aluminum content of the alloy. This goal was to be accomplished in an alloy with a tensile elongation approaching 10%. Three alloys, (1) Fe-18.3Al-8Cr-2Mo-1.9TiB₂, (2) Fe-18.3Al-1.3Mo-1.9TiB₂, and (3) Fe-18.8Al-1.9TiB₂ (in wt%), produced on a P&W program in sufficient quantities for use on this program, were selected for processing. The alloy without chromium or molybdenum extruded 8 to 1 at 1700°F (927°C) and swaged 4 to 1 at 1500°F (816°C) had been found to have a modulus of 29.3 (10)⁶ psi. (specific modulus of 129 (10)⁶ in.) and a tensile elongation of 5%, but the first alloy with both chromium and molybdenum was believed to be the most promising in terms of microstructural stability and strength.

Processing

Alloy powders were screened through a -80 mesh screen in a high purity helium atmosphere and transferred to stainless steel extrusion cans. Fourteen extrusions were produced at temperatures from 1750 to 2250°F (954 to 1232°C) at ratios from 8 to 1 to 30 to 1. Processing parameters for alloy number (1) are listed in Table 31. The first six samples (00688 to 00693) were extruded 8 to 1 subsequent to a blank die precompact. Extrusion of the remaining

samples in Table 31 (00750 to 00764) was carried out without pre-compaction. Extrusion and swaging conditions for alloys number (2) and (3) (samples 00807 to R251) are listed in Table 32. High extrusion ratios, feasible at the highest temperatures, were employed to extend processing conditions and to produce a high texture directly with little or no subsequent working. Subsequent swaging of the extruded material was carried out at a temperature of 1450°F (788°C), where swaging was laborious, to a temperature of 2100°F (1149°C). All extruded bars were swaged to 0.5-inch bar stock. Subsequent to swaging, the material was annealed at the swaging temperature for one hour.

TABLE 31. PROCESSING PARAMETERS FOR ALLOY (1)

<i>Fe-18.3Al-8Cr-2Mo-1.9TiB₂</i>								
<u>Extrusion</u>			<u>Swaging Temperature (a)</u>					
<i>I.D.</i>	<i>Temp (°F)</i>	<i>Ratio</i>	<i>Low</i>		<i>Medium</i>		<i>High</i>	
(With Precompaction)								
00688	1750	8:1	1450°F (R197)		1750°F (R198)		2000°F (R199)	
00689	1850	8:1	1450°F (R200)		1850°F (R201)		2000°F (R202)	
00690	1950	8:1	1550°F (R203)		1950°F (R204)		2100°F (R205)	
00691	2250	8:1	1550°F (R206)		1750°F (R207)		2100°F (R208)	
00692	2250	20:1	1550°F (R209)		1750°F (R210)		2100°F (R211)	
00693	2250	30:1	1550°F (R212)		1750°F (R213)		2100°F (R214)	
(Without Precompaction)								
00750	1950	8:1	—		—		—	
00751	2250	8:1	—		—		—	
00752	2250	20:1	—		—		—	
00764	2250	30:1	—		—		—	

(a) All extrusions swaged to 0.5 inch bars and the bars annealed 1 hour at the swaging temperature.

2711C

TABLE 32. PROCESSING PARAMETERS FOR ALLOYS (2) AND (3)

<u>Composition w/o</u>				<u>Extrusion</u>		<u>Swaging</u>	
<i>I.D.</i>	<i>Al</i>	<i>Mo</i>	<i>TiB₂</i>	<i>Temp. (°F)</i>	<i>Ratio</i>	<i>Temp (°F)</i>	<i>Ratio</i>
00807	18.3	1.3	1.9	2250	30:1	—	—
00808	18.8	—	1.9	2250	30:1	—	—
R250	18.8	—	1.9	1900	8:1	1700	4:1
R251	18.3	1.3	1.9	1900	8:1	1700	4:1

(a) All extrusions swaged to 0.5 inch bars and the bars annealed 1 hour at the swaging temperature.

2711C

Longitudinal cracking plagued the processing of the first Fe-Al-Cr-Mo-TiB₂ alloy during hot working and machining operations. This did not occur with the chromium-free alloys except for less extensive longitudinal cracking of sample 00808 during machining.

Alloy Evaluation

Alloy number (1) (samples 00688 to 00693) extruded at an 8-to-1 ratio at 1750 to 2250°F (954 to 1232°C) were found to contain near diametrical longitudinal cracks. Subsequent swaging at temperatures from 1450 to 2100°F (788 to 1149°C) did not seal these cracks. These results were unexpected, since the same alloy had been processed without much difficulty on a P&W program. Subsequent extrusions (00750 to 00764) in Table 1 were carried out without a blank die pre-compaction.

Sample 00692 extruded at a 20-to-1 ratio at 2250°F (1232°C), subsequent to precompaction, was sound for part of the extrusion. The material swaged satisfactorily to 0.5-inch diameter bar stock, however, the material could not be machined without cracking. Examination of cracked material revealed transgranular fracture.

Sample 00693 extruded at a 30-to-1 ratio at 2250°F (1232°C), subsequent to pre-compaction, was sound and swaged at 1750°F (954°C) without difficulty. Interestingly, the microstructure of this 30-to-1 extrusion was not significantly different than that of the 8-to-1 extrusion. Therefore, a greater apparent ductility of the 30-to-1 extrusion may be due to higher grain or prior particle boundary strength.

Samples 00750 and 00751 extruded at 1950 and 2250°F (1065 and 1232°C) and an 8-to-1 extrusion ratio, without pre-compaction, were found to be cracked diametrically along the entire length of the bars. It appears that the precompaction step was not responsible for the cracking, but that it was due to marginal tensile properties which could not sustain the tensile stressed generated during nonuniform cool down from the extrusion temperature.

The 20-to-1 extrusion (sample 00752) carried out at 2250°F resulted in a nonuniform extrusion where the can material periodically stuck to the die and thickened locally (about every 3 inches) possibly due to failure of the lubricant. This failure of the canning material resulted in extrusion of the alloy at ratios varying from 20 to 1 to as high as 80 to 1, and the process repeating over the entire length of the extrusion. However, the material was crack free, and a 20-to-1 extrusion could be produced with better lubrication.

Sample 00764 extruded at 2250°F (1232°C) and a 30-to-1 ratio, without precompaction, was sound for part of the extrusion. The material swaged satisfactorily to 0.5-inch diameter bar stock, however, the material could not be machined without cracking. Examination of cracked material revealed partial transgranular fracture.

From the preceding processing work, material suitable for evaluation was produced. The 30-to-1 as-extruded alloy (1) (sample 00764) and the 8-to-1 extruded and swaged alloys (2) and (3) (samples 00807, 00808, R250 and R251) were tested. The room temperature tensile properties are presented in Table 33 and dynamic modulus data in Table 34.

TABLE 33. ROOM TEMPERATURE TENSILE PROPERTIES

Alloy	YS — ksi		UTS — ksi		% Elong.	
	A*	B*	A	B	A	B
Fe-Al-TiB ₂	69.5	91.5	114.4	131.7	4	4
Fe-Al-Mo-TiB ₂	89.0	106.0	164.6	180.0	8	6
Fe-Al-Cr-Mo-TiB ₂	108.0	—	184.7	—	6	—

*A Extruded 30:1 at 2250°F B Extruded 8:1 at 1900°F plus swage 4:1 at 1700°F

2711C

TABLE 34. DYNAMIC ELASTIC MODULUS

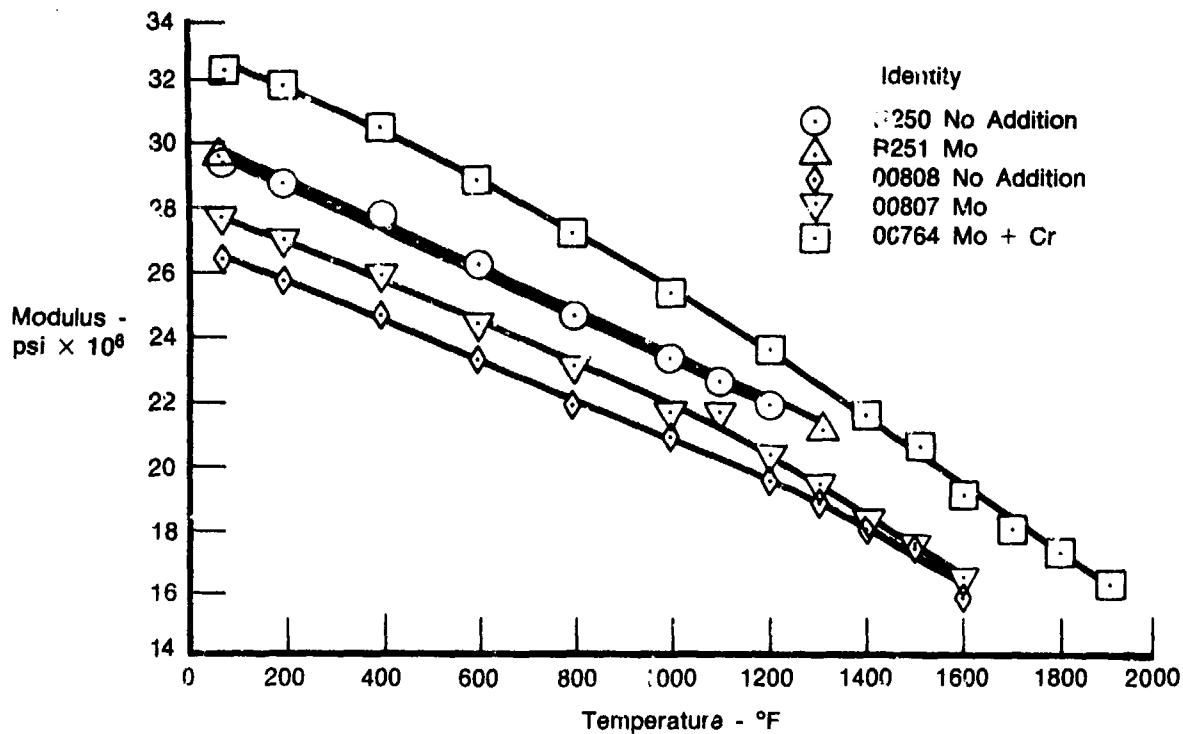
Alloy	Elastic Modulus psi $\times 10^6$		Specific Modulus in. $\times 10^6$	
	A*	B*	A	B
Fe-Al-TiB ₂	26.5	29.6	116	130
Fe-Al-Mo-TiB ₂	27.7	29.6	121	130
Fe-Al-Cr-Mo-TiB ₂	32.5	—	142	—

*A Extruded 30:1 at 2250°F, B Extruded 8:1 at 1900°F plus swage at 1700°F

2711C

The Fe-Mo-TiB₂ alloy was stronger and more ductile than the Fe-Al-TiB₂ alloy for both thermomechanical treatments. The room temperature ductility fell short of the goal of 10% elongation. However, the elongation in a tensile test may be misleading in that the ductility in these materials is anisotropic. For example, the chromium-containing alloys cracked longitudinally while the Fe-Al-TiB₂ alloy did not. Yet the chromium-containing alloy had the higher elongation. Apparently the ductility in the longitudinal direction is greater than in the circumferential direction.

The dynamic elastic modulus of the alloys with various thermomechanical treatments are given in Table 34 and Figure 104.



FD 319851

Figure 104. Dynamic Modulus vs. Temperature

The modulus was affected by composition and the thermomechanical treatment. The chromium-containing alloy extruded 30 to 1 had the highest modulus, 32.5 10^6 psi, while the

Fe-Al-TiB₂ alloy had the lowest, 26.5 10⁶ psi. While the metal chromium has a higher elastic modulus (36.6 10⁶ psi) than iron (28.5 10⁶ psi), for which it substituted, the rule of mixtures would predict a smaller effect than was obtained and, as shown below, it was not apparent that the chromium increased the modulus by increasing texture.

For both the Fe-Al-TiB₂ and the Fe-Al-Cr-Mo-TiB₂, the process of extrusion plus swaging produced higher moduli than the extrusion process alone, but the program goal of a specific modulus of 140×10^6 -inch was achieved only with the chromium containing alloy.

The (110) and (200) pole figures of the five alloy/treatments listed in Table 31 are given in Figures 105 through 107. All of the materials had a (110) wire type texture with varying strengths depending on composition and thermomechanical processing. The strength of the textures are given in Table 35.

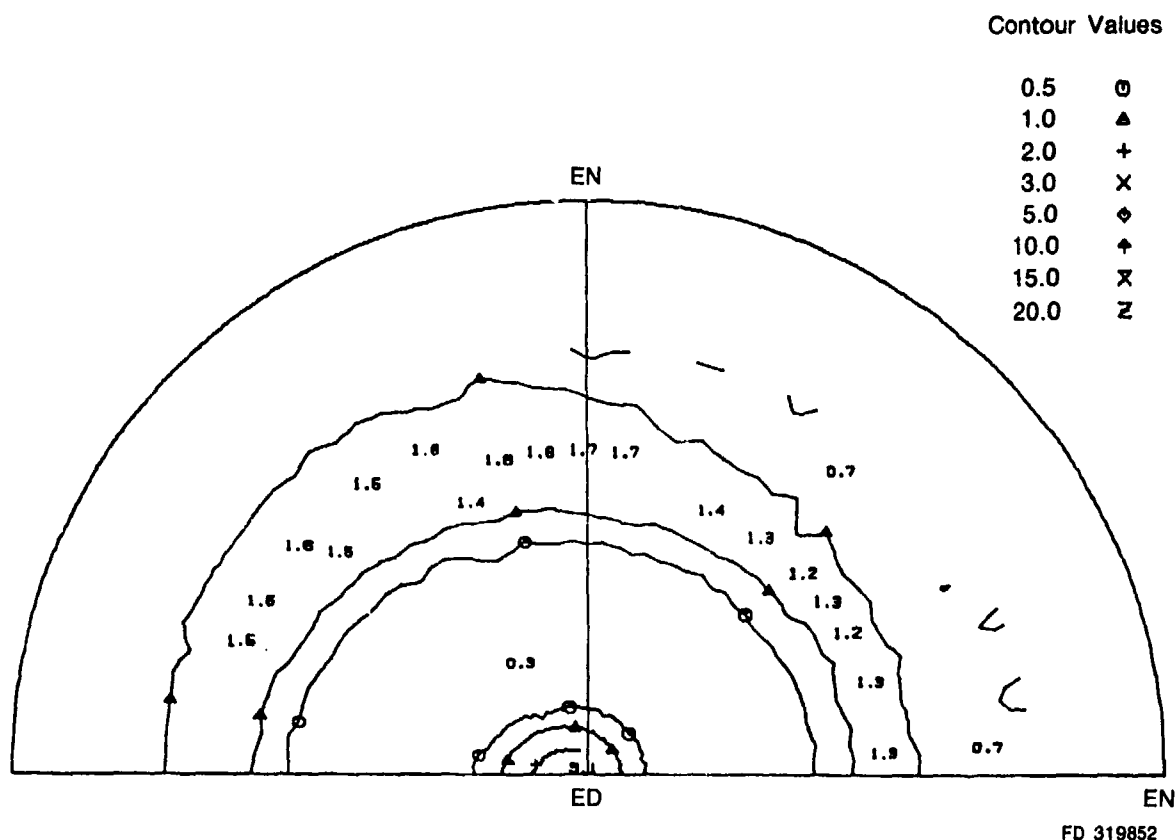


Figure 105. (110) Pole Figure for Extruded Fe-Al-TiB₂ Alloy

The strength of the (110) texture varied with processing; the textures of the extruded plus swaged materials were stronger than those of the 30-to-1 extruded materials.

Summary of Task 1 Extension

The Fe-18.5 wt% Al alloys were found to be far more difficult to extrude and work, without cracking, than the Fe₃Al base alloy. A high specific modulus over $140 (10)^6$ inches was obtained with the chromium and molybdenum alloy, and this was coupled with a tensile elongation of 6%. Changes in the composition of 18.5% Al alloys along with further processing investigations would be needed to produce a satisfactory material for aircraft engine application.

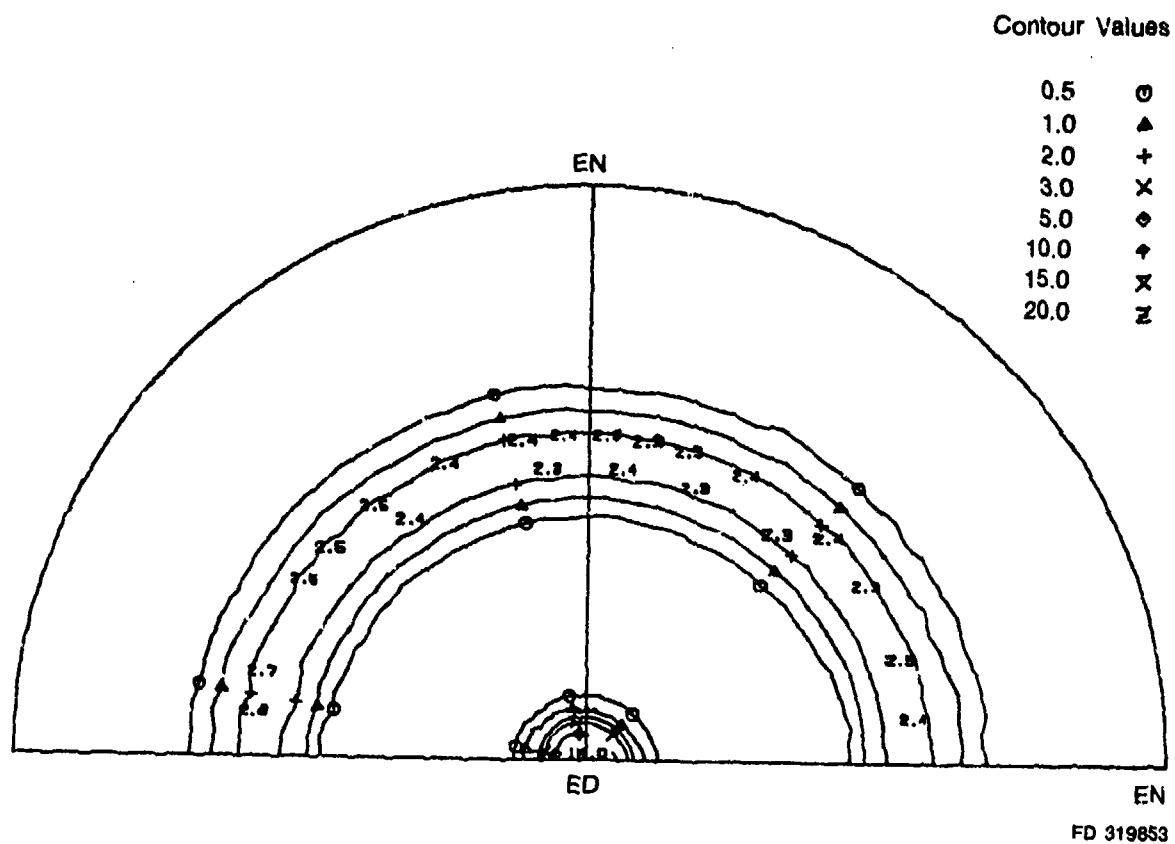


Figure 106. (110) Pole Figure for Extruded Fe-Al-Cr-Mo-TiB₂ Alloy

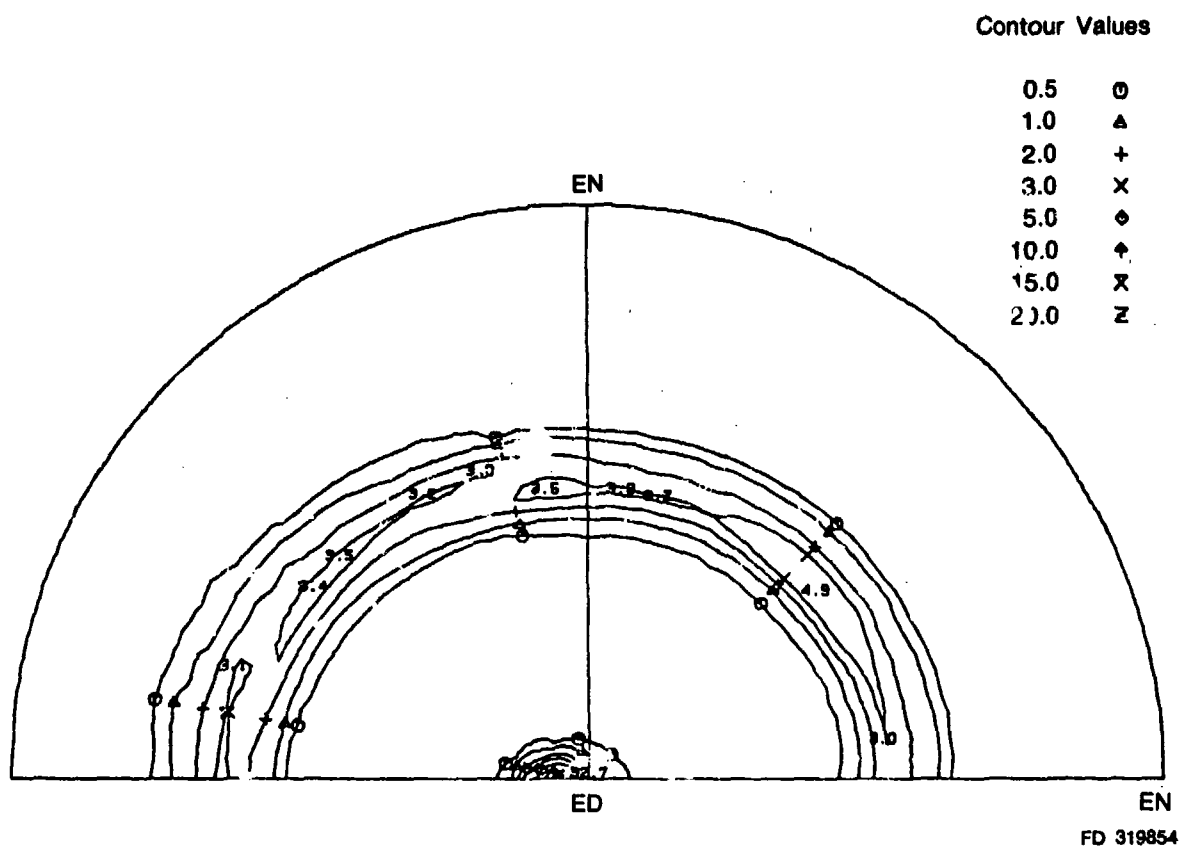


Figure 107. (110) Pole Figure for Extruded and Swaged Fe-Al-Mo-TiB₂ Alloy

TABLE 35. TEXTURE STRENGTH (X RANDOM)

	A*	B
Fe-Al-TiB ₂	3.1	24.0
Fe-Al-Mo-TiB ₂	9.6	32.7
Fe-Al-Cr-Mo-TiB ₂	15.0	—

*A Extruded 30:1 at 2250°F, B

Extruded 8:1 at 1900°F plus swaged

4:1 at 1700°F

2711C

SECTION IV

CONCLUSIONS — TASK 1

The following conclusions are offered with regard to the study of iron aluminides.

1. Fe_3Al produced as rolled plate from a rectangular extrusion was found to have a tensile strength of 140 ksi and an elongation of 15 to 16%. The alloy rolled at 1150°F (621°C) was found to recrystallize at about 1200°F (650°C) and transform from an aligned to an equiaxed grain structure with an elongation reduced to about 8%. The alloy should be limited in use to a temperature below 1000 to 1100°F (538 to 595°C).
2. $\text{Fe}_3\text{Al} + \text{TiB}_2$ produced in rolled plate from a rectangular extrusion was found to have a tensile strength of 180 ksi and an elongation of 11 to 15%. The alloy which was rolled at 1500°F (815°C) resisted recrystallization (abnormal grain growth in this case) to about 1800°F (982°C), and this temperature could be raised to over 2000°F (1093°C) by alloying or by working under conditions which limit residual stresses. Abnormal grain growth significantly reduced the ductility of the alloy, but this could be avoided and an alloy produced which has a use temperature to at least 2000°F (1093°C).
3. The transverse (perpendicular to the rolling direction) strengths of Fe_3Al and $\text{Fe}_3\text{Al} + \text{TiB}_2$ were similar to the strength in the longitudinal direction, but the elongations were reduced by about one half. The rupture strength of $\text{Fe}_3\text{Al} + \text{TiB}_2$ at 1800°F (982°C) in the transverse direction was found to be about half that in the longitudinal direction. For comparison, the rupture strength of $\text{Fe}_3\text{Al} + \text{TiB}_2$ in the longitudinal direction at 1800°F was about equal to that of Hastelloy "X." The elongation in stress rupture and in the transverse direction at 1800°F (982°C) was found to vary over a wide range (<10 to about 50%) depending on stress or strain rate.
4. Variations in consolidation and working conditions for the processing of $\text{Fe}_3\text{Al} + \text{TiB}_2$ and the use of fine versus coarse powder caused variations in microstructure which were found to be the major reason for variation in strength and ductility. In general, the finer and more continuous grain structures produced the best combination of mechanical properties.
5. The fracture toughness properties of the iron aluminides as defined by K_{Q} was 65.8 ksi $\sqrt{\text{in.}}$ for $\text{Fe}_3\text{Al} + \text{TiB}_2$ compared to 33.8 ksi $\sqrt{\text{in.}}$ for Fe_3Al . The difference is believed to be due to a finer lamellar structure in the latter alloys. Examination of fracture surfaces revealed considerable secondary cracking which contributed to the plastic behavior observed in the recorded data. The recrystallized Fe_3Al with a larger grain size had a lower K_{Q} of 27.5 ksi $\sqrt{\text{in.}}$ as was expected.
6. The Fe-18.5 wt% Al alloys were found to be far more difficult to extrude and work, without cracking, than the Fe_3Al base alloy. A high specific modulus over 140 (10)⁶ inches was obtained with the chromium and molybdenum alloy, and this was coupled with a tensile elongation of 6%. Changes in the composition of 18.5% Al alloys along with further

processing investigations would be needed to produce a satisfactory material for aircraft engine application.

POWDER FOR ALLOY DEVELOPMENT — TASK II

Powder Processing

Quantities of rapidly solidified aluminide powders were produced by the Pratt & Whitney rapid solidification rate (RSR) rotary atomization process for delivery to the Air Force Material Laboratory. Table 36 lists the alloy compositions and the amounts of -80 mesh powder produced and delivered.

TABLE 36. ALUMINIDE POWDERS PRODUCED FOR AFML

<i>Alloy ID</i>	<i>Composition (wt%)</i>	<i>Yield in Pounds</i>
1	Fe-13.87Al	35
2	Fe-32.57Al	57
394	Fe-20.65Al	16.5
395	Fe-20.25Al-1.40Ti-0.60B	15
434	Fe-19.78Al-2.19V-1.98W	13.4
435	Fe-13.50Al-6.51Nb	12.3
436	Fe-12.10Al-1.72Si-1.96Mo	11.9
437	Fe-11.85Al-1.68Si-1.92Mo-1.49Ti-0.59B	16.3
438	Supplied by Howmet	16.7
439	Supplied by Howmet	14.1
468	Fe-13.66Al-3.76Nb	17.6
469	Fe-13.06Al-3.75Nb-0.97Ti	17.1
471	Fe-20.11Al-3.80Hf	16.3
472	Fe-10.76Al-2.80Si-1.92Mo-1.49Ti-0.59B	15.7
476	Fe-12.79Al-3.68Nb-2.42Ti-0.59B	9.6
477	Fe-13.77Al-1.86Zr	9.7
400	Fe-10.65Al-6.13Ti-0.6B	12.1
403	Fe-13.21Al-0.94Ti-7.09Ta	19.2
441	Ni-13.28% Al	19.7
442	Ni-14.53% Al	16.5
443	Ni-4.80% Al-15.20% Fe	7.1
444	Ni-4.90% Al-15.00% Mn	22.5

7450C

The processing of Fe₃Al (Alloy No. 1) in a AGT 400,000 P&W atomization device met with limited success in terms of powder yield. The difficulty was due to reaction between a SiO₂ bonded MgO crucible and the liquid metal which had to be held at a temperature of 3100°F (1704°C) for its metering prior to atomization. In some cases, the liquid metal reacted to such an extent that it had to be discarded. In comparison, only 2850°F (1565°C) was required for the atomization of alloy No. 2, and it atomized without difficulty. Additional Fe₃Al was processed in a smaller 30-pound capacity experimental atomization device where alumina crucibles were available for use. Nevertheless, 35 pounds of Fe₃Al were produced and delivered to the Air Force. The Fe32.57Al alloy (No. 2) was produced without difficulty in the larger AGT 400,000 atomization device. The remaining alloy compositions were converted to powder in a 30-pound capacity experimental atomization device.

The alloys were obtained from vendors or produced by vacuum induction melting of the metals in alumina crucibles and cast in copper molds. Cast billets were normally 30 pounds in weight.

SECTION V

TASK III

INTRODUCTION

Task III effort was conducted at P&W/Engineering Division — North to develop wrought austenitic iron aluminides with low strategic element contents which can be used at temperatures up to about 650°C. The material should be capable of replacing 12% Cr stainless steel such as H-46 and perhaps iron-base superalloys of the A286 type in engine applications.

Austenitic iron aluminides are known to form in three alloy systems: Fe-Mn-Al, Fe-Mn-Al-C, and Fe-Ni-Al/Ti. Extensive work (References 1 and 2) in the 1950's and the early 1960's showed that Fe₃Al-based alloys had the potential to replace titanium alloys and some stainless steels. However, reservations over the ductility of these ferritic materials at lower temperatures prompted the development of a second alloy series with an austenitic structure. It was shown that the best, and lowest cost, system for such a development was Fe-Mn-Al. Although Fe-Mn-Al alloys were investigated about 20 years ago, the physical metallurgy of the alloys and the strengthening mechanisms were not studied in any detail. One of the goals of this program task is to further develop Fe-Mn-Al alloys. The approach taken here is to achieve an understanding of the microstructure as a basis for further improvement.

Formation of an ordered face-centered cubic phase of the L1₂ type in the Fe-Mn-Al-C system is a recent discovery by Japanese workers. They concluded that the austenitic phase was a metastable phase produced as a result of rapid solidification. This phase was found to have excellent strength and ductility (Reference 3). Improved Fe-Mn-Al-C alloys will be formulated and produced as rapidly solidified powder for study in this program.

The third alloy system, Fe-Ni-Al/Ti has also been studied extensively in the past. It is the basis for the development of superalloys. The goal is to determine if the material cost can be reduced by substitution of Ni with Mn, both of which are austenitic stabilizers.

Thus, three series of alloys based on the Fe-Mn-Al, Fe-Mn-Al-C, and Fe-Ni-Al/Ti systems were screened in the first 2 years of this program task. The formulation of these alloys is provided in the following section. Results from the alloy screening were used to select the alloys which were studied in greater detail during the 3rd-year program described at the end of this section.

ALLOY SCREENING

Alloy Formulation

Fe-Mn-Al Alloys

Alloys for Basic Studies

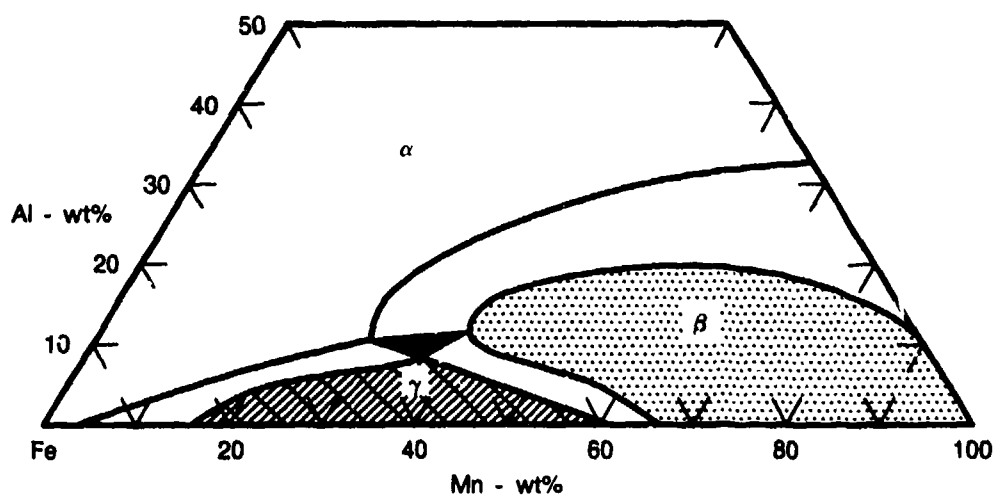
The nominal compositions of the alloys formulated for basic studies are given in Table 37. The base alloy, containing 30 at. % Mn, 12 at. % C, and balance Fe (alloy 103), lies well within the fcc phase field in the Fe-Mn-Al ternary diagram, Figure 108, so that with modest additions of ferrite stabilizers the alloys should remain completely austenitic. The relatively high C level was selected since a preliminary internal study indicated that the yield strengths of alloys with lower C contents decreased significantly at elevated temperatures. Further, the higher C content may also prevent formation of ferrite which is considered to have deleterious effects on creep-rupture

properties. Si and Ni were selected as the major alloying elements in the initial phase of this study, again based on results of previous (1950) studies which indicated that these elements significantly improved the tensile and rupture strength of Fe-Mn-Al alloys. Chromium was chosen as the first carbide former to be studied, as Cr carbides are probably the best characterized interstitial compounds in commercial steels in terms of crystallography, phase transformation, etc., thus providing a good reference system for studying carbides in the Fe-Mn-Al system. To study the individual and interactive effects, Si, Ni, and Cr were added singly and in various combinations. Note that in alloys 107 through 110, Ni substitutes for Mn with a Ni/Mn ratio of 0.2. Alloy 111, with a Ni/Mn ratio of 1.0, will yield information on the effects of higher Ni substitutions, and will provide a basis for comparing nonequilibrium phase formation in the rapidly solidified powder alloys described below.

TABLE 37. ALLOYS FOR BASIC STUDIES, AT.%, (WT%)

Alloy	Fe	Mn	Al	C	Si	Cr	Ni
103	Bal.	30 (32.7)	12 (6.4)	4 (0.95)	—	—	—
104	Bal.	30 (33.4)	12 (6.6)	4 (0.97)	4 (2.3)	—	—
105	Bal.	30 (32.8)	12 (6.4)	4 (0.95)	—	2 (2.0)	—
106	Bal.	30 (33.1)	12 (6.5)	4 (0.97)	2 (1.1)	2 (2.1)	—
Cast							
107	Bal.	25 (27.2)	12 (6.4)	4 (0.95)	—	—	5 (5.8)
108	Bal.	25 (27.2)	12 (6.4)	4 (0.95)	2 (1.1)	P	5 (5.8)
109	Bal.	25 (27.2)	12 (6.4)	4 (0.95)	—	2 (2.1)	5 (5.8)
110	Bal.	25 (27.5)	12 (6.5)	4 (0.96)	2 (1.1)	2 (2.1)	5 (5.9)
111	Bal.	15 (16.2)	12 (6.4)	4 (0.94)	—	—	15 (17.3)

7448C



FDA 318367

Figure 108. Fe-Mn-Al Ternary Diagram at 760°C, (Schmatz, 1959). The Approximate Position of the Base Alloy (Alloy 103) Is Indicated by the Filled Circle in the Austenitic Phase Field

Alloys Based on Previous Investigations

The compositions of the most promising alloys studied during the 1950's are summarized in Table 38 together with the modified alloy compositions (alloys 67 and 68) for the present investigation. Alloy BA28-2 showed good stress rupture properties (Reference 12); however, the high Ni, Mo, and W contents, which had beneficial influence on creep rupture properties, led to difficulties in mechanical working of this alloy, which was subsequently modified to BA36-1 (Reference 1). The compositions of both alloys are rather complex. Schmatz (Reference 2) took a simpler approach and determined, based on tensile properties and oxidation resistance, promising alloy composition ranges.

TABLE 38. PROMISING ALLOYS OF THE 1950'S AND PRESENT MODIFICATIONS, WT%

Alloy	Fe	Mn	Al	C	Si	Ni	Mo	W	V	Others	Ref.
BA28-2	Bal.	36	7.0	0.6	—	6.0	2.0	2.0	0.5	1.5 Cu	5
BA36-1 (140)	Bal.	33	7.0	0.7	0.5	3.0	1.0	0.5	0.5	0.01 B	1
Ford	Bal.	25 to 35	8.0 to 9.0	0.8 to 1.0	1.0 to 2.0	—	—	—	—	—	2
67	Bal.	32	8.0	0.2	0.5	6.0	3.0	—	0.3	—	Present
68	Bal.	32	8.0	0.2	0.5	6.0	3.0	—	—	0.2 Ti, 0.2 Nb, 0.01 B	Study

7480C

In the present studies, it was considered that the powder metallurgy techniques may overcome early workability problems associated with BA28-2-type alloys. However, the high C contents in the alloys of the 1950's could present a prior powder particle boundary decoration problem in the consolidated materials, as experienced during the early stage of the nickel-base powder alloy development program. Therefore, the C level was reduced to 0.2 at.% for alloys 67 and 68. In alloy 68, V is replaced by Ti and Nb, which are also strong carbide formers. Further, structural characterization was also conducted on BA36-1, designated alloy 140 in the present studies, to provide insights for further improvements.

Alloys for Corrosion Studies

Studies in the 1950's have shown the good oxidation resistance of Fe-Mn-Al alloys can be attributed to the high Al content. Unfortunately, the sulfidation resistance of Fe-Mn-Al alloys could be lower due to the absence of Cr. A minimum of 12 at.% Cr is generally considered necessary to impart corrosion and oxidation resistance to stainless steels. It was considered worthwhile to study small Cr additions (5 at.%) to Fe-Mn-Al alloys to determine if the element would act synergistically with Al and/or Si.

Simple alloys, Table 38, similar to those studied by Schmatz, were selected for this study. Si, which was determined to be beneficial to oxidation resistance and tensile strength, was maintained at a recommended level of 1.5 at.%. The concentrations of Al were set at 8 and 10 at.% and Cr, at 0, 3, and 5 at.%. Sulfidation resistance of these alloys in an environment of Na₂SO₄ and NaCl were studied under three different conditions: (1) uncoated surface, (2) surface protected by an aluminized coating, and (3) by a chromized coating. For comparison, the oxidation and sulfidation resistances of commercial alloys A286 and H46, Table 38, under the same conditions were also evaluated. Results are given in Section 2.C.(7).

TABLE 39. NOMINAL COMPOSITIONS OF ALLOYS (WT%) STUDIED IN CYCLIC OXIDATION AND SULFIDATION TESTS

Alloy	Fe	Mn	Al	Cr	Si	C	Ni	Mo	Ti	V
50	Bal.	30.0	8.0	—	1.5	1.0	P	—	—	—
74	Bal.	30.0	8.0	3.0	1.5	1.0	—	—	—	—
75	Bal.	30.0	8.0	5.0	1.5	1.0	—	—	—	—
76	Bal.	30.0	10.0	3.0	1.5	1.0	—	—	—	—
A286	Bal.	1.5	—	15.0	0.7	—	25.5	1.3	2.1	0.3
H46	Bal.	0.7	—	11.0	0.4	0.2	0.5	1.0	—	0.3

7480C

Fe-Mn-Al-C Alloys — First Series

Table 40 shows the composition of the powder alloys selected for the present studies. Alloy 97 is one of the alloys which forms a metastable single phase $L1_2$ structure under rapid solidification conditions, as recently reported by Japanese workers (Reference 3), Figure 109. Alloy 101, which differs significantly from alloy 97, is predicted to behave similarly under rapid solidification conditions according to the Japanese studies. Chromium is added to increase the thermal stability and strength of the metastable phase (Reference 3). Alloy 102 is a variant of alloy 101 with Ni substituting for half of the Mn, because Ni has also been shown to be an $L1_2$ stabilizer.

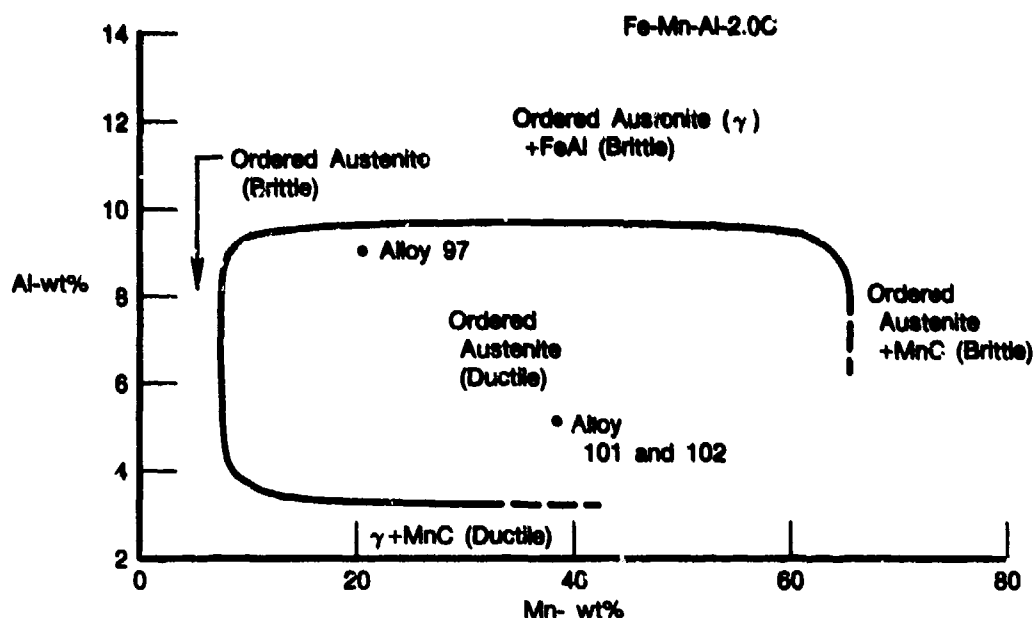
TABLE 40. COMPOSITIONS OF Fe-Mn-Al-C ALLOYS, AT.% (WT%)

	Alloy	Fe	Mn	Al	C	Cr	Ni
	97	Bal.	20.0 (23.1)	16.0 (9.1)	8.0 (2.0)	—	—
Powder	101	Bal.	35.8 (40.0)	9.1 (5.0)	8.2 (2.0)	— (5.0)	—
	102	Bal.	17.9 (19.7)	9.1 (4.9)	8.2 (2.0)	— (4.9)	17.9 (21.1)

7480C

Fe-Ni-Al/Ti Systems

Two systems which show formation of coherent face-centered cubic phases, γ and γ' , are Fe-Ni-Al and Fe-Ni-Ti, Figures 110 and 111, respectively. These alloys are the prototypes of superalloys, the most creep-resistant alloys currently available. The key questions are the effectiveness of replacing Ni with Mn, and whether the $\gamma + \gamma'$ phase field can be shifted to higher Fe contents. The stabilization of the γ' phase (rather than the ordered bcc phase) is anticipated to be difficult. Work on phase stability in the austenitic Fe-Ni alloys in the early 1960's showed that with Al additions, the ordered bcc phase was formed. However, if most of the Al was replaced by Ti, then the γ' phase was stable. It may be noted that the iron base superalloy, A286, illustrates this trend in that Ti is the γ' former rather than Al. The role of carbon in such systems will have to be carefully evaluated as there is a very close relationship between γ' and perovskite structures. However, the addition of Ti may cause the formation of MC carbides, thus upsetting the desired phase balance.



FDA 318368

Figure 109. Compositional Dependence of As-Quenched Structure of Fe-Mn-Al-2.0C Alloys Formed by Rapid Quenching (Melt Spinning) Technique. After Inoue et al, 1981 (Ref. 3)

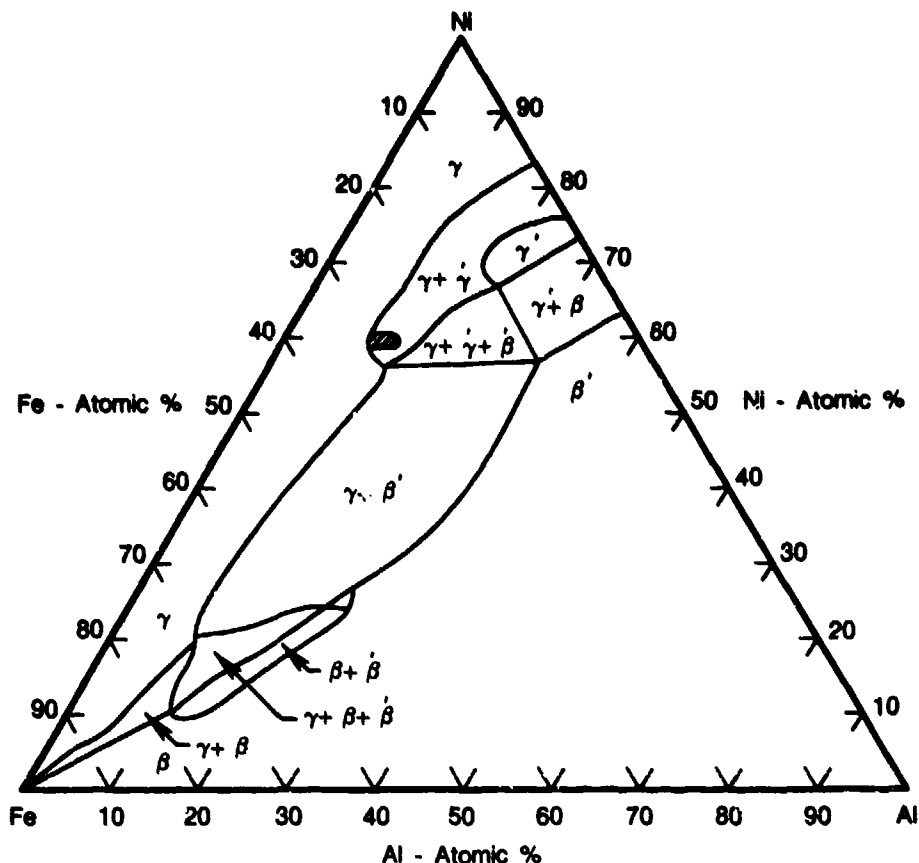
Fe-Ni/Mn-Al Alloys

To explore the Fe-Ni-Al systems, alloys indicated in Table 41 were formulated for the present studies. Alloys 147 and 149 lie at the boundary of the (γ +) phase field and alloys 150 and 151 well within the (γ +) phase field. The effects of Ti and C in the formation of the γ phase are to be evaluated in alloys 148, 149 and 151. Alloys 152 and 153 are intended to be baseline alloys.

Fe-Ni/Mn-Ti Alloys

To further pursue the development of a γ and γ' phase mixture, alloys were also selected from the Fe-Ni-Ti ternary system as shown in Figure 111. An interesting feature of this system is that for alloys which lie in the γ +Ni₃Ti phase field or its vicinity, an Ni₃Ti phase with an L1₂-type structure will be produced initially as a metastable precipitate which will eventually transform to the equilibrium Laves phase (Fe,Ni)₂Ti and/or the DO₂₄ structure, depending on the specific alloy composition. For this type of alloy to be an attractive alternative to commercial iron-base superalloys, a significant cost advantage is essential which can only be achieved if the Ni content can be reduced. Thus, the predominant variable to be studied was the extent to which Mn can be substituted for Ni without upsetting the desired phase balances. The compositions of alloys formulated for the present studies are given in Table 42. Nickel at levels of 30, 45 and 60 at% will be studied, each at Mn:Ni ratios of 0, 1.6 and 3.0. Assuming that Ni and Mn are interchangeable, the relative positions of the alloys are indicated in Figure 111. Further, following the development experience of iron-base superalloys, 0.1 wt% Al is added to the alloy to reduce the propensity of cellular phase reaction, and 1 wt% Mo is added to increase the temperature capability. Alloying additions with high electron-to-atom ratios (e/a) have been considered important for the stabilization of the L1₂ structure in iron-base alloys. In order to compensate for the lower average e/a in alloys No. 244 and 245, which have reduced levels of Ni

(e/a=10), additions of Cu (e/a=11) to alloys No. 250 and 251 were included in this study. The effect of the Ti level should be defined by alloys 169 and 170 which contain 2 and 4 a/o Ti, respectively.



FDA 318369

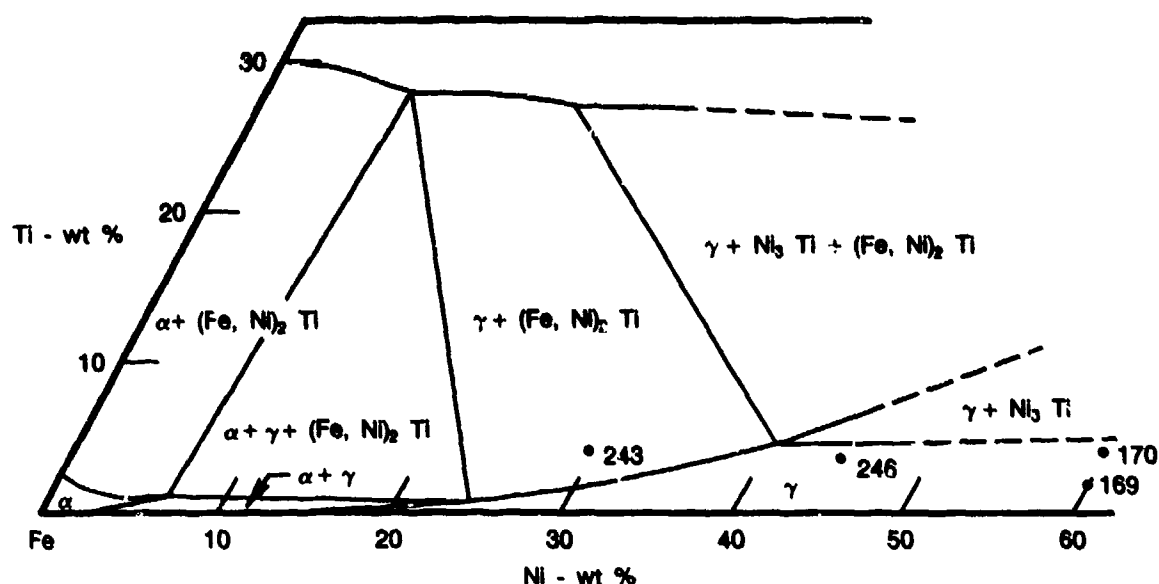
Figure 110. Fe-Ni-Al Ternary System at 950°C. After Bradley, 1949*. Positions of Alloys in the Present Studies Are Shaded, Assuming Interchangeability of Ni and Mn in These Types of Alloys. γ =fcc, γ' =Ni₃Al, β =bcc, β' =FeAl, NiAl

Experimental

Preparation of Materials

The cast alloys were produced by nonconsumable arc melting of pure raw materials, Table 43, in an inert atmosphere and casting into a water-cooled copper mold. The dimensions of the castings for alloys listed in Table 37 are about 33 mm × 33 mm × 100 mm, and weigh about 0.77 kg each. These castings were hot rolled at 2100°F (1150°C) to about 60% reduction in thickness with a reheating after about 30% reduction. To study the effect of dislocation substructure on aging behavior, sections of the hot-rolled alloys were solution heat treated at 2048°F (1120°C) for 1 hour followed by an oil quench, and then further rolled at 1112°F (593°C) to a thickness of about 6 mm. Smaller castings of alloys listed in Table 39 were produced in the form of hemispherical buttons weighing about 0.1 kg each using the same raw materials and casting technique.

* A. J. Bradley: Iron and Steel Inst. J. 1949, Sept., p. 9.



FDA 318376

Figure 111. Isothermal Section of the Fe-Ni-Ti System at 700°C. After Speich, 1963**. The Positions of Some of the Alloys Selected for the Present Studies Are Indicated by Dots

TABLE 41. Fe-Mn-Ni-Al ALLOYS AT % (WT%)

Alloy	Fe	Mn	Ni	Al	Ti	C
147	Bal.	37.0 (38.2)	23.0 (25.3)	10.0 (5.1)	— —	— —
148	Bal.	37.0 (37.4)	23.0 (24.9)	5.0 (2.5)	5.0 (4.4)	— —
149	Bal.	33.0 (35.2)	23.0 (26.2)	10.0 (5.2)	— —	4.0 (0.9)
150	Bal.	50.0 (52.8)	10.0 (11.3)	12.5 (6.5)	— —	— —
151	Bal.	46.0 (50.2)	10.0 (11.7)	12.5 (6.7)	— —	4.0 (1.0)
152	Bal.	35.0 (35.6)	— —	5.0 (2.5)	— —	— —
153	Bal.	35.0 (35.8)	— —	5.0 (2.5)	5.0 (4.5)	— —

7448C

The powder alloys, with the exception of alloy 97, were produced by vacuum atomization at Homogenous Metals, Inc. (HMI) and screened to -80 mesh. Alloy 97 was produced as a 11.4 kg ingot by vacuum induction melting, and then atomized at P&W/GPD using the RSR powder process and equipment. Alloys 67 and 68 were consolidated by vacuum hot pressing using a 32 mm diameter molybdenum (TZM) die. The other powder alloys (97, 101, and 102) were consolidated by HIP.

** G. R. Speich: Trans. AIME, 1963, p. 754

TABLE 42. NOMINAL COMPOSITIONS OF Fe-Mn/Ni-Ti/Al ALLOYS, AT.% (WT%)

Alloy	Fe	Mn	Ni	Ti	Mo	Al	(Mn+Ni)	Mn: Ni
169	38 (37.89)	37 (36.29)	23 (24.11)	2 (1.71)	—	—	60	1.6
243	65.2 (64.37)	— —	30.0 (31.14)	4.0 (3.39)	0.59 (1.00)	0.21 (0.10)	30	0
244	65.2 (65.15)	18.5 (18.19)	11.5 (12.09)	4.0 (3.43)	0.59 (1.01)	0.21 (0.10)	30	1.6
245	65.2 (65.35)	22.5 (22.19)	7.5 (7.90)	4.0 (3.44)	0.59 (1.02)	0.21 (0.10)	30	3.0
246	50.2 (49.19)	— —	45.0 (46.36)	4.0 (3.36)	0.59 (0.99)	0.21 (0.10)	45	0
247	50.2 (50.11)	27.7 (27.12)	17.3 (18.15)	4.0 (3.42)	0.59 (1.01)	0.21 (0.10)	45	1.6
248	50.2 (50.31)	33.75 (33.28)	11.25 (11.85)	4.0 (3.44)	0.59 (1.02)	0.21 (0.10)	45	3.0
170	36.0 (36.00)	37.0 (36.39)	23.0 (24.18)	4.0 (3.43)	—	—	60	1.6
249	35.2 (35.09)	37.0 (36.28)	23.0 (24.10)	4.0 (3.42)	0.59 (1.01)	0.21 (0.10)	60	1.6
<u>Cu</u>								
250	63.2 (63.00)	18.5 (18.14)	11.5 (12.06)	4.0 (3.42)	0.59 (1.01)	0.21 (0.10)	2.0 (2.27)	
251	63.2 (63.17)	22.5 (22.13)	7.5 (7.88)	4.0 (3.43)	0.59 (1.01)	0.21 (0.10)	2.0 (2.27)	

7448C

TABLE 43. PURITY OF RAW MATERIALS USED FOR MELTING

Iron	99.9%
Aluminum	99.9%
Carbon	99.99%
Silicon	99.99%
Chromium	99.9%
Nickel	99.9%
Manganese	*

7448C

Microstructural Characterization

Microstructural characterization was performed using optical metallography, analytical electron microscopy, and X-ray diffraction techniques. Standard specimen preparation procedures for ferrous alloys were followed for the optical metallography. Thin foils for electron microscopy were prepared using a twin-jet polishing technique. The electrolyte consists of a mixture of 150 ml each of ethanol, methanol, and butanol and 30 ml of perchloric acid used at -10 to 0°C and 45 volts, producing a current of 60 mA. To study the structures of phases by X-ray samples consisting of -400 mesh, filings were taken from solution heat treated alloys, evacuated, and encapsulated in quartz. The capsules were then aged at 650°C for 16 hours which

also reduced the residual stresses in the filings, and resulted in more distinctive diffraction peaks. This procedure was observed to yield more reliable results than annealing in a vacuum or inert atmosphere without encapsulation, which could result in depletion of Mn in the filings and produce misleading results. The annealed filings were examined using a diffractometer technique with CrK α radiation.

To extract carbides from Fe-Mn-Al alloys, various digestive solutions were tried including: (1) an electrolyte (consisting of 10 volume % hydrochloric acid, 90 volume % methanol with 1g of tartaric acid added per 100 ml of mixture) was used at a current density of 200 mA/cm² at 20°C; (2) a bromine solution consisting of 10% bromine and 1% tartaric acid in methanol; and (3) an aqueous electrolyte consisting of 15g of sodium citrate, 1.2g of potassium bromine, and 30g of citric acid in a volume of 100 ml. The first two digestive solutions were found to be unsatisfactory

for the Fe-Mn-Al alloys as the hydrochloric acid electrolyte attacked the alloys at an extremely slow rate; the bromine solution produced insoluble reactants during the digestion process. The aqueous electrolyte tends to dissolve both the matrix and the major precipitates.

Cyclic Oxidation and Sulfidation Tests

The specimens for these tests were cut from the cast buttons of compositions given in Table 38 and have dimensions of approximately 17 mm \times 17 mm \times 2 mm. For comparison, similar specimens from two commonly used alloys, A286 and H46, were also included in these tests. All the specimens were polished to a No. 600 grit finish prior to testing. The cyclic oxidation tests were conducted in static air between 68 and 1400°F (20 and 760°C) in 2-hour cycles with 10 minutes per cycle for cooling. Sulfidation resistance to mixtures of NaCl and Na₂SO₄ was studied isothermally at 1200°F (650°C) in static air. Two mixtures with Na₂SO₄ concentrations of 50 and 75% by weight were used. A layer of the salts was applied by air-spraying a preheated 302°F (150°C) specimen with a saturated aqueous solution. The salt-layer thickness of 0.5 mg/cm² was maintained throughout the tests. Sulfidation resistance of specimens protected by either a chromized or aluminized coating was also studied. The coatings were applied following the procedures described in the PWA specifications PWA 7C and PWA 73, respectively. Both the oxidation and sulfidation tests were interrupted periodically for weight change measurements and visual inspections. A fresh coating of salt was applied to the sulfidation specimen after each measurement.

Mechanical Tests

Three types of properties, creep, yield, and bend ductility, were used for screening alloys in the present studies. Creep and yield tests were conducted in compression using rectangular specimens of 5 mm \times 5 mm \times 13 mm (approximate dimensions). The specimens were compressed between two alumina platens to which extensometer fixtures were attached. Deformation of the specimens were measured by a linear voltage differential transformer with output continuously recorded by a strip chart for the creep tests and by a X-Y recorder for the yield tests. All creep tests were conducted at 1200°F (650°C) and (42.5 ksi) 293 MPa. Yield stresses at 0.2% plastic strain were determined in compression using the same experimental set up. As a measure of low temperature ductility, bend tests were conducted at 68°F (20°C) using specimens 2 mm thick, 13 mm wide, and 65 mm long.

Results and Discussions

Fe-Mn-Al Alloys

Workability and Aging Response

The analyzed compositions of the alloys in this study are given in Table 44. Small castings of these alloys weighing about 0.77 kg were hot rolled at 2102°F (1150°C) to about 60% reduction

in thickness. Rolling was performed without difficulty, and no edge cracking was observed. A portion of each hot-rolled alloy was solution heat treated at 2048°F (1120°C) for 1 hour, oil quenched, and then further warm rolled at 1100°F (593°C) for a total thickness reduction of slightly over 80%. After this operation, the majority of the alloys were uncracked, except for the high-Ni alloy (Alloy 111) which split open after several rolling passes along the midplane parallel to the rolling plane. The results of the rolling experiments confirm the generally good hot workability observed in the previous studies of this class of alloys.

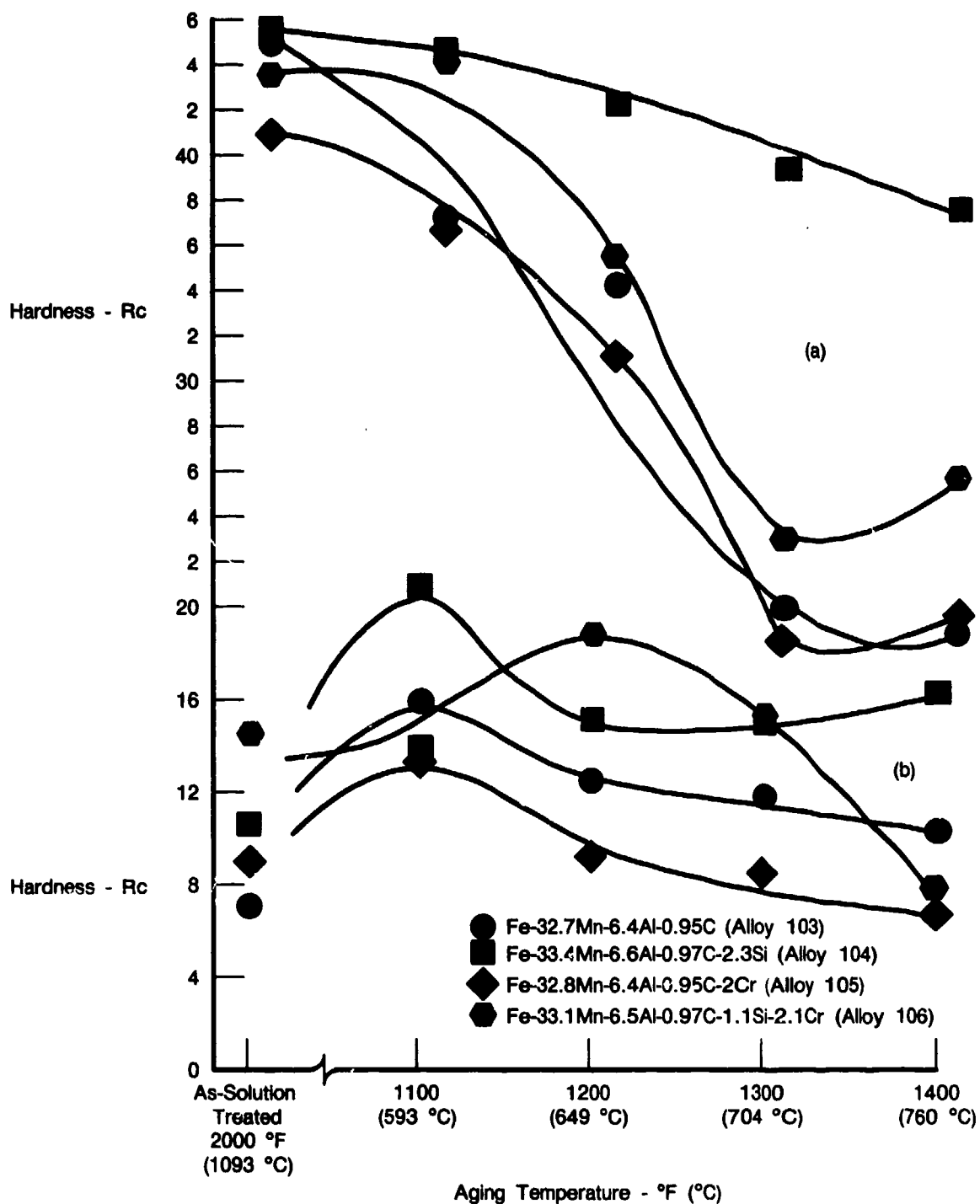
TABLE 44. ANALYZED COMPOSITIONS OF CAST + WROUGHT ALLOYS, WT%

Alloy	Fe	Mn	Al	Ni	Cr	Si	C
103	Bal.	30.2	6.6	—	—	—	0.89
104	Bal.	32.0	6.5	—	—	2.24	0.87
105	Bal.	31.4	6.4	—	2.10	—	0.96
106	Bal.	31.9	6.4	—	2.16	1.12	1.04
107	Bal.	25.7	6.4	5.8	—	—	0.82
108	Bal.	25.8	6.4	5.8	—	1.06	0.66
109	Bal.	25.6	6.4	5.8	2.10	—	0.81
110	Bal.	26.0	6.6	5.8	2.10	1.04	0.74
111	Bal.	15.9	6.5	17.5	—	—	0.84

7450C

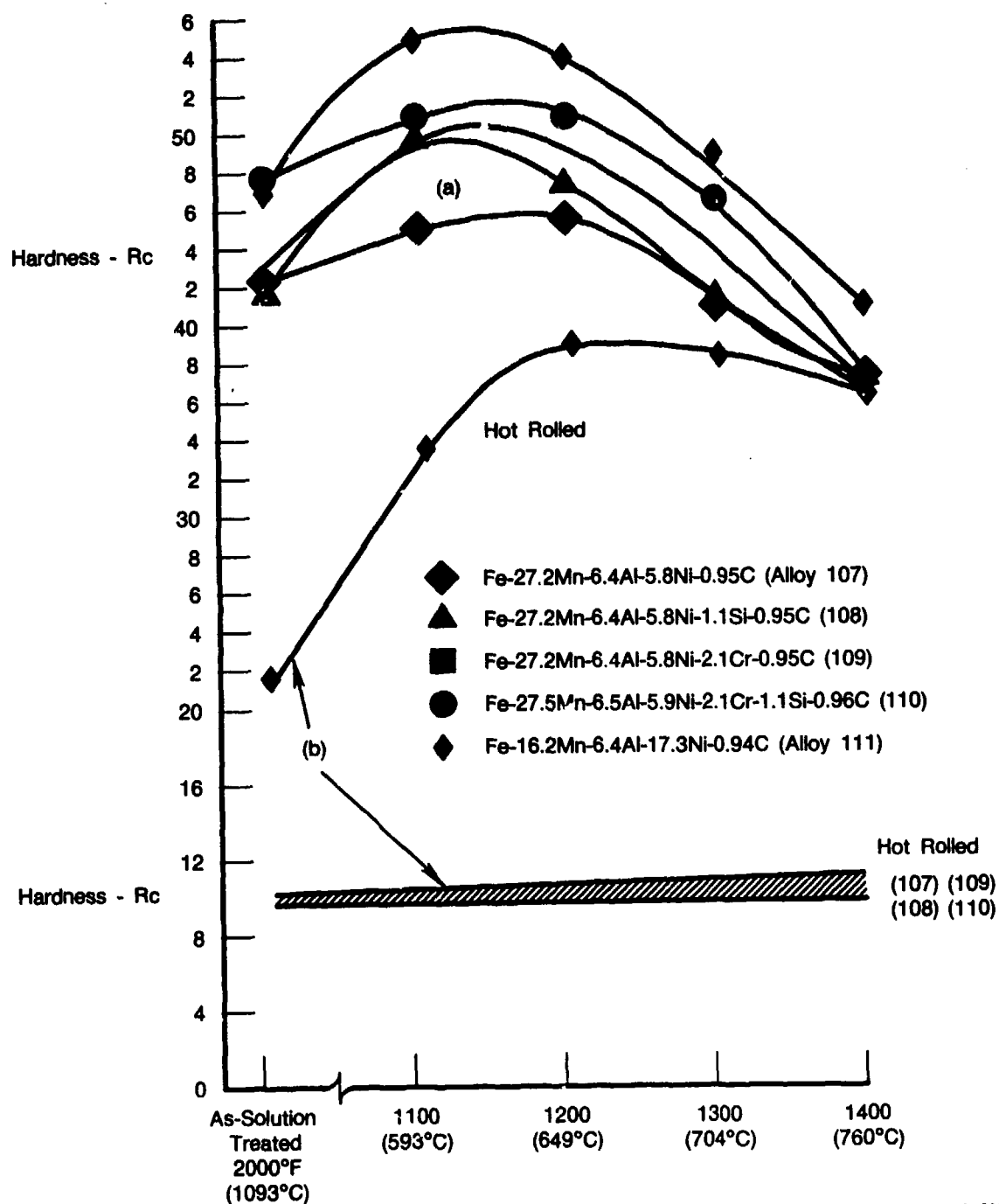
Room temperature hardness measurements of the warm-rolled and hot-rolled alloys aged at 1100, 1200, 1320, and 1400°F (593, 650, 705, and 760°C) for 16 hours are shown in Figures 112, and 113. Prior to aging, the hot-rolled alloys were given a solution treatment of 2000°F (1095°C) for 45 minutes followed by an oil quench. Figure 112a shows that in the warm-worked condition, the baseline alloy (alloy 103) softened during aging treatments. Addition of 2 at.% Cr (alloy 105), 2 at.% Si (alloy 104), and 1 at.% Si + 2 at.% Cr (alloy 106) did not change the aging response. The rapid hardness decrease in these alloys above 1200°F (650°C) will be shown to be accompanied by recrystallization. Figure 112b shows the aging response of the hot-rolled, nickel-free alloys after solution heat treatment. The initial hardness is about four times lower than that of the warm-rolled alloys. Aging at temperatures around 1112°F (600°C) produced some hardening; however, the general hardness levels of the alloys are low, around Rc 16 which is about two and one half times lower than those in the warm-rolled alloys. These observations underscore the important role of thermomechanical history in the strengthening of the Fe-Mn-Al alloys.

In contrast to the nickel-free alloys, the hardness of all the warm-rolled nickel-containing alloys shows a peak at aging temperatures between 1090 and 1200°F (590 and 650°C) (Figure 113a). Strengthening is amplified by small additions of Si and Cr either singly or in combination, but the highest hardness is associated with the alloy with the highest Ni content (alloy 111). From Figure 113a, the hardness decreases much more slowly after aging at temperatures above 1200°F (650°C) compared with the Ni-free alloys. Figure 113b shows that, with the exception of alloy 111, the hardness of the hot-rolled alloys is very low, about Rc 10, and did not respond to aging treatments. The initial hardness of alloy 111 is about Rc 20 and increases to a peak hardness of about Rc 40 at 1200°F (650°C). As will be shown, the large difference between the warm-rolled and the hot-rolled alloys can be explained in terms of grain size and precipitation structure.



FDA 318371

Figure 112. Hardness of Alloys 103 Through 106 vs Aging Temperature. Specimens Aged for 16 Hours at the Indicated Temperatures. a. Alloys Rolled at 593°C, b. Alloys Rolled at 1150°C



FDA 318372

Figure 113. Hardness of Alloys 107 Through 111 vs Aging Temperature. Specimens Aged for 16 Hours at the Indicated Temperatures. (a) — Alloys Rolled at 593°C, (b) — Alloys Rolled at 1050°C

Microstructure

Figures 114 and 115 show the microstructures of alloys 106 and 110 which are representative of those observed in the Ni-free alloys and the Ni-containing alloys. Elongated

grains and linear features due to precipitation on specific crystallographic planes can be observed in all alloys after rolling at 1100°F (593°C). It is evident from Figures 114 and 115 that an important difference between the Ni-free and the Ni-containing alloys is in the kinetics of recovery and recrystallization. With the exception of alloy 104, all the warm-rolled Ni-free alloys show evidence of recrystallization in the optical micrographs when aged at temperatures around 1290°F (700°C). Alloy 104, which contains 2% Si, Figure 116, and the nickel-containing alloys show no evidence of recrystallization after aging treatments at temperatures at least up to 1400°F (760°C). These differences in recovery and recrystallization kinetics between the alloys are entirely consistent with the observed variations in hardness as a function of age temperature, Figures 112a and 113a. Microstructures of alloys, after rolling at 2100°F (1150°C) and solution heat treated at 2050°F (1120°C), at various temperatures are shown in Figure 117 for the Ni-free alloys and Figure 118 for the Ni-containing alloys. The equiaxed coarse grain structure in the heat treated alloys shows that recrystallization and grain growth had occurred in both types of alloys during the solution heat treatment.

A microstructural difference between the warm-rolled and the corresponding hot-rolled alloys is in the amount of precipitate observed after aging. Comparison of Figure 114 with Figure 119 for alloy 106 and Figure 115 with Figure 118 for alloy 110 shows a higher density of precipitate is formed in the warm-rolled material than in the hot-rolled material. This difference is illustrated in greater detail in Figure 119 showing the secondary electron micrographs in alloy 111 in warm-rolled and hot-rolled conditions. It is not clear at this time if these observations are due to differences of the kinetics of precipitation, or to the working operation changing the nature of the precipitates.

More detailed microstructural and compositional information has been obtained by transmission electron microscopy studies which were conducted on warm-rolled materials after the 1200°F (650°C) 16-hour aged treatment, which produced high hardness, especially in the Ni-bearing alloys 107 through 111. High dislocation densities were observed in all warm-rolled alloys, Figure 116. The major precipitate phases in all the Ni-containing alloys are morphologically similar, having an ellipsoidal shape, and are distributed uniformly in the matrix. Figure 120, taken from alloy 111, illustrates the typical appearance of the major precipitates in the Ni-containing alloys. The dimensions and density of the ellipsoidal precipitates vary somewhat, depending on specific alloy compositions. In alloy 111, the precipitates are 100 to 200 Å in diameter and 500 to 1000 Å in length. Analysis of electron diffraction patterns indicates that the structure of the major precipitates in alloys 107 to 111 is an ordered body-centered phase with an CsCl-type structure, having a Kurdjumov-Sach and Nishiyama-type crystallographic relationship with the austenitic matrix.

The precipitation behavior in the warm-rolled Ni-free alloys (103 through 106) is distinctly different from that of the Ni-containing alloys described in the preceding paragraphs. In Alloys 103 through 106 the precipitates are coarser and tend to be heterogeneous, occurring in both grain boundaries and intergranularly (Figure 116). Results of compositional studies by energy dispersive spectroscopy (EDS) and analysis summarized in Table 45 indicated that in most cases there are little differences between matrix and precipitate chemistries. Limited analysis of the hot-rolled alloys showed the same trend. For comparison, the alloy compositions determined by chemical analyses are also included in Table 44. Whenever several precipitate phases have been observed in a given alloy, the major one is indicated as Precipitate A in Table 45. By comparing the matrix compositions with the alloy compositions, it can be concluded that the EDS gives a reasonably accurate measurement for elements with high concentrations of Fe and Mn. For Al, it is obvious that the EDS results are less reliable in the absolute sense, but may still be meaningful in a relative sense. Relative to the matrix compositions, the major precipitates in the Ni-containing alloys are enriched in Al and the Mn content is equal to or less than that of the

matrix. The opposite trends appear to be true for the Ni-free alloys. Further, for a given alloy, the Al concentrations in the precipitates increase with increasing Ni contents. These observations indicate strong affinity of Ni for Al, which may account for the differences in precipitate morphology and distribution between the Ni-containing and the Ni-free alloy series.

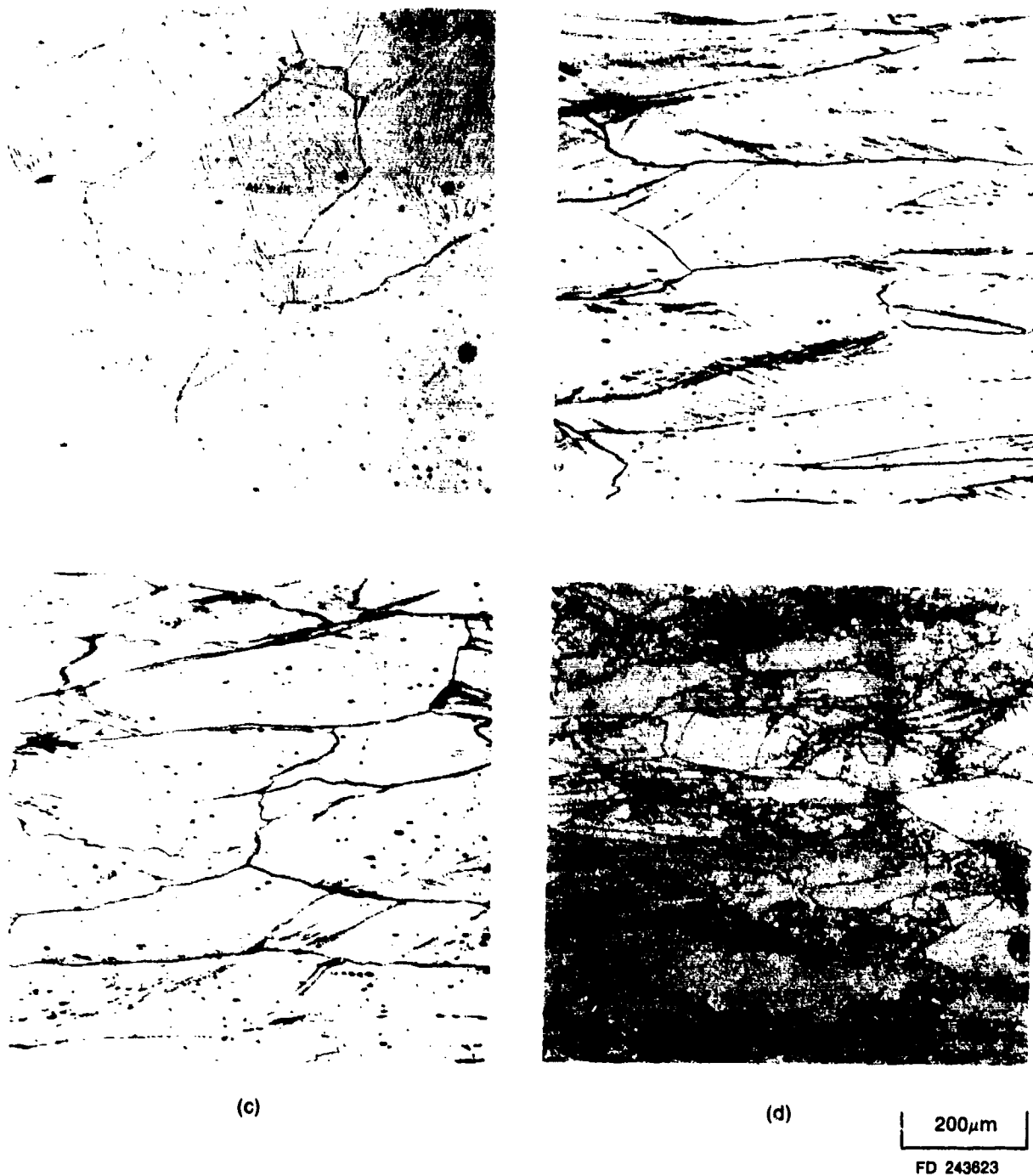
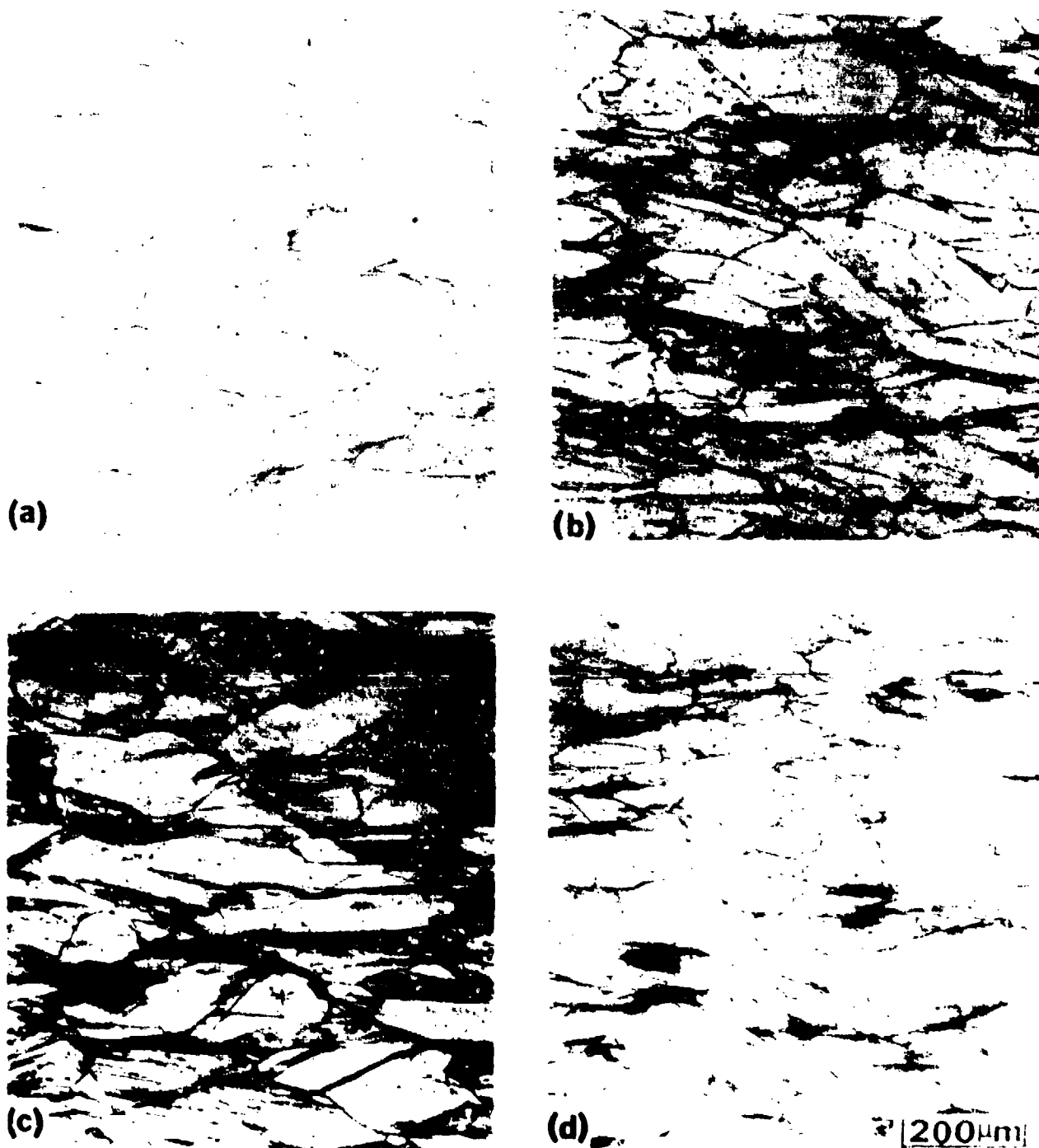


Figure 114. Microstructure of Alloy 106 (a) After Rolling at 593°C and After Aging for 16 Hours at (b) 593°C (c) 649°C (d) 704°C



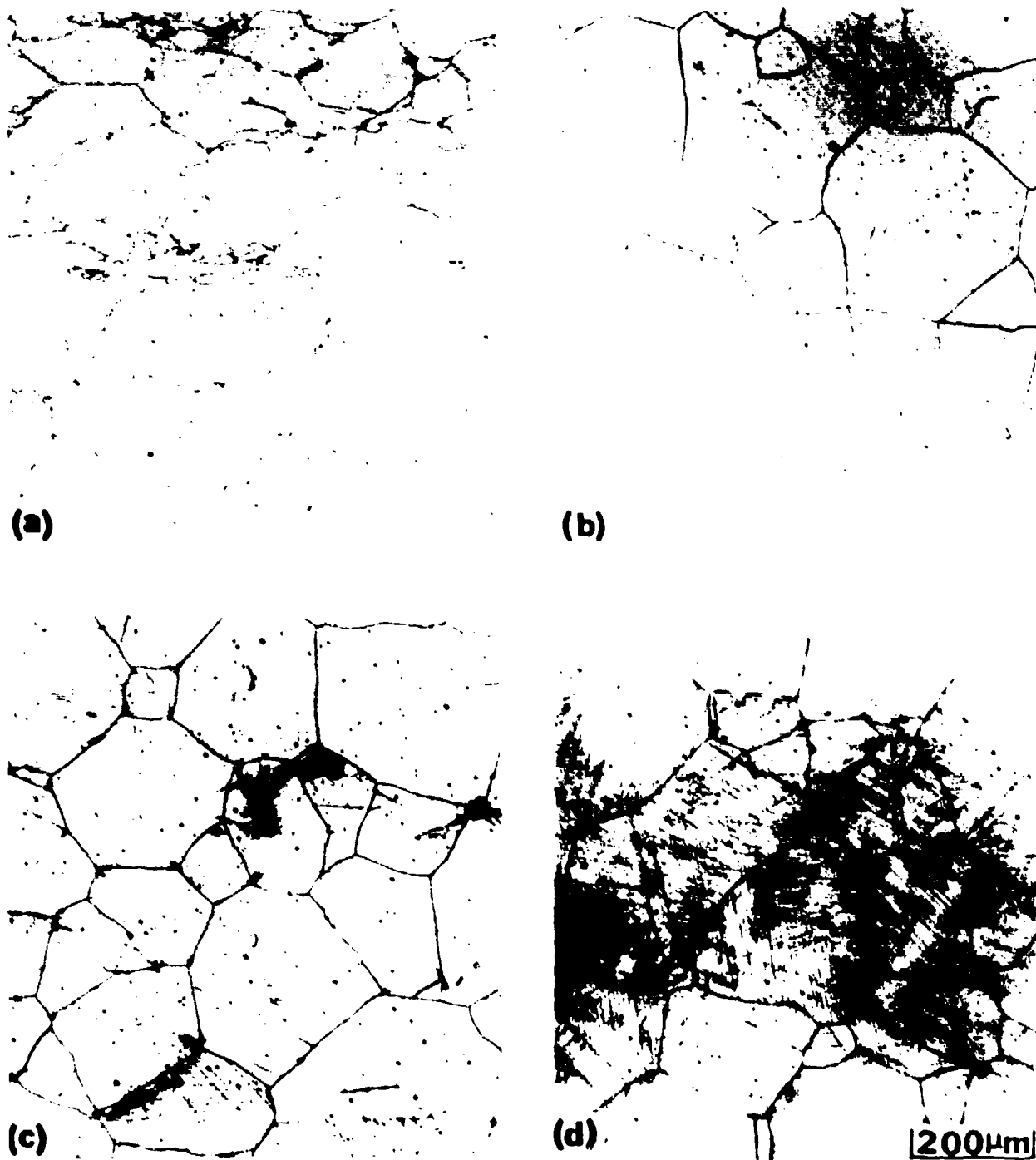
FU 3163/5

Figure 115. Microstructure of Alloy 110 (a) After Rolling at 593°C and After Aging for 16 Hours at (b) 593°C (c) 649°C (d) 704°C



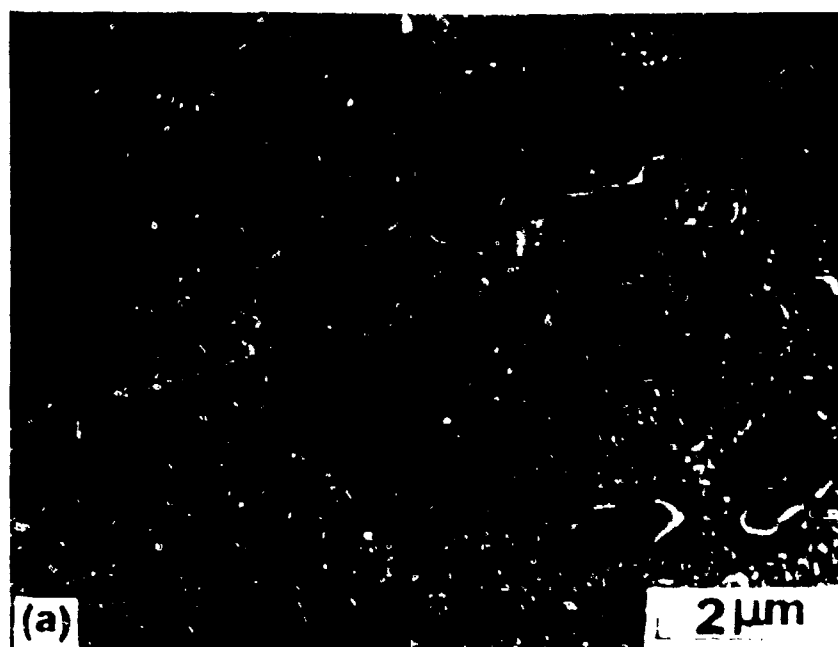
FD 318374

Figure 116. Microstructure of Alloy 104 After Rolling at 593°C and Aging for 16 Hours at 704°C (a) Optical Micrograph Showing No Evidence of Recrystallization, (b) Secondary Electron Micrograph Illustrating the Morphology and Distribution of the Precipitates, (c) Transmission Electron Micrograph Showing High Dislocation Density in the Warm-Rolled Alloy



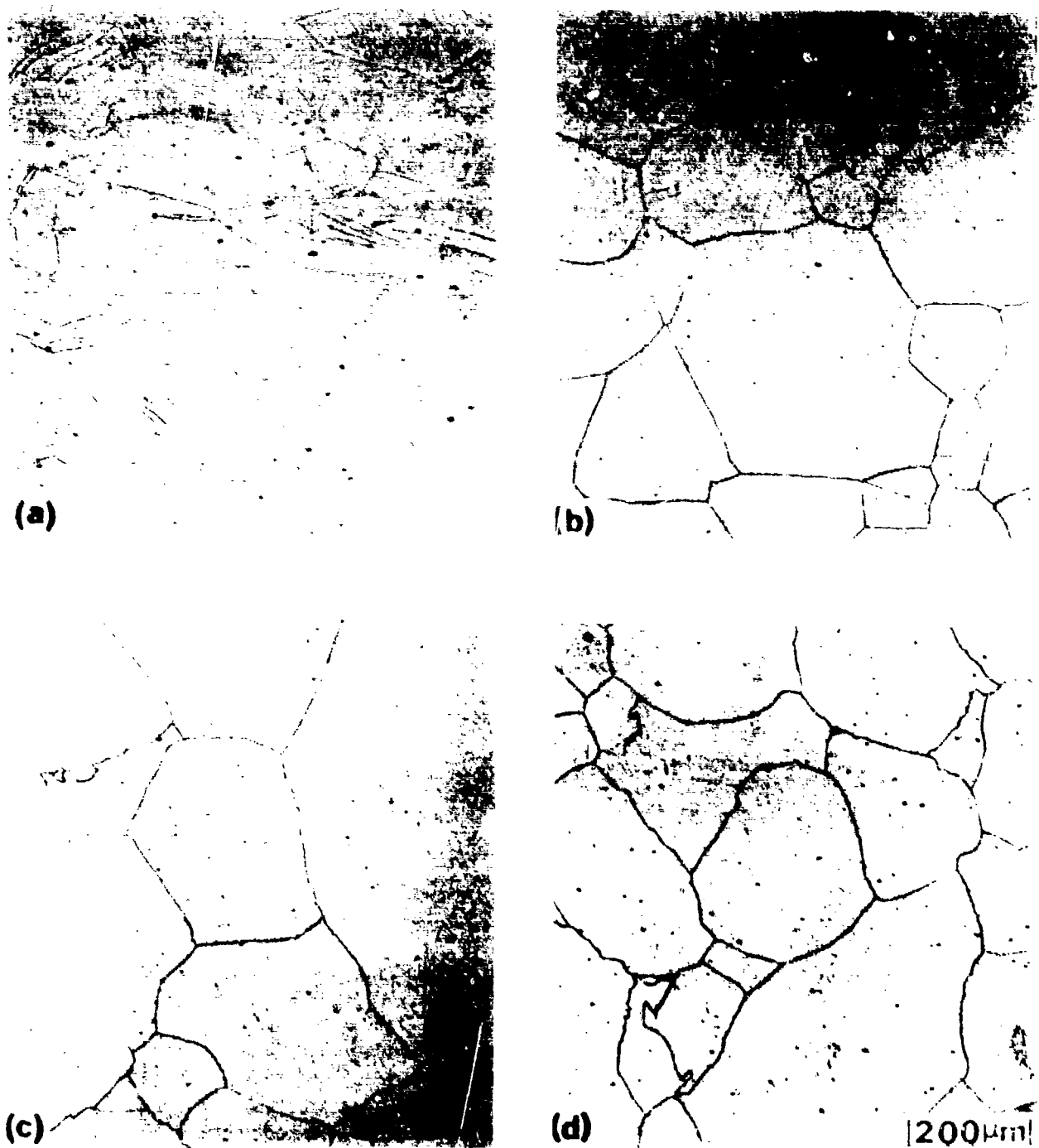
FD 318376

Figure 117. Microstructure of Alloy 110 (a) After Rolling at 1150°C. After Solution Heat Treatment at 1120°C for 1 Hour Followed by an Oil Quench and Aged for 16 Hours at (b) 593°C (c) 649°C (d) 704°C



FD 318377

Figure 118. *Secondary Electron Micrographs Illustrating the Relative Quantity of Precipitates Formed in Alloy 111. (a) After 593°C Rolling (b) After 1150°C Rolling. The Alloy Was Aged at 649°C for 16 Hours After Rolling in Both Cases*



FD 318375

Figure 119. *Microstructure of Alloy 106 (a) After Rolling at 1150°C. After Solution Heat Treatment at 1120°C for 1 Hour Followed by an Oil Quench and Aged for 16 Hours at (b) 593°C (c) 649°C (d) 704°C*



FD 318378

Figure 120. Transmission Electron Micrographs Illustrating the Major Precipitates in Alloy 111 After Warm Rolling and Aging Treatment at 650°C for 16 hours. (a) Bright Field (b) Dark Field

**TABLE 45. COMPOSITIONS OF MATRIX AND PRECIPITATES BY ENERGY
DISPERSIVE SPECTROSCOPY
593C ROLLED + 650C/16H AGED**

	Composition, Wt%						
	Fe	Al	Mn	Si	Cr	Ni	C
Alloy 103	62.3	6.6	30.2	—	—	—	0.9
Matrix	61.7	7.2	31.1	—	—	—	*
G.B. Ppt**	55.7	8.6	35.7	—	—	—	*
Alloy 104	58.4	6.5	32.0	2.2	—	—	0.9
Matrix	60.7	4.4	32.9	2.0	—	—	*
Ppt	62.0	4.6	31.7	1.7	—	—	*
Alloy 105	59.1	6.4	31.4	—	2.1	—	1.0
Matrix	60.7	5.8	31.0	—	2.5	—	*
G.B. Ppt**							
A	47.8	2.9	41.0	—	8.3	—	*
B	39.2	1.6	46.7	—	12.5	—	*
C	54.3	4.5	35.8	—	5.4	—	*
Alloy 106	57.4	6.4	31.9	1.1	2.2	—	1.0
Matrix	61.8	3.0	31.8	0.7	2.6	—	*
Ppt							
A	46.5	1.4	43.0	2.1	6.9	—	*
B	57.0	2.3	36.1	0.8	3.8	—	*
Alloy 107	61.3	6.4	25.7	—	—	5.8	0.8
Matrix	64.8	4.9	26.9	—	—	3.4	*
Ppt	59.8	6.1	26.5	—	—	7.6	*
Alloy 108	60.2	6.4	25.3	1.1	—	5.8	0.7
Matrix	61.5	5.9	26.2	1.7	—	4.7	*
Ppt							
A	56.7	7.6	24.6	1.7	—	9.4	*
B	46.1	10.7	21.1	1.2	—	20.8	*
Alloy 109	59.3	6.4	25.6	—	2.1	5.8	0.8
Matrix	62.8	5.7	24.7	—	2.3	4.4	
Ppt							
A	58.7	6.8	23.9	—	2.4	7.8	*
B	52.2	2.6	35.1	—	6.6	3.2	*
Alloy 110	57.7	6.6	26.0	1.1	2.1	5.8	0.7
Matrix	63.9	4.8	23.7	1.4	2.5	3.8	*
Ppt	55.5	7.2	23.8	1.2	2.4	9.9	*
Alloy 111	59.3	6.5	15.9	—	—	17.5	0.8
Matrix	64.8	4.5	16.1	—	—	14.6	*
Ppt							
A	62.2	4.9	15.7	—	—	17.2	*
B	11.9	14.5	13.3	—	—	60.3	*
C	37.3	7.7	12.9	—	—	42.1	*
D	25.9	13.6	11.7	—	—	48.8	*

* Cannot be detected by EDS

** Grain boundary precipitate

7448C

X-ray diffraction techniques were used to determine the structure of the precipitates. Initial attempts involved extraction of precipitates by selective dissolution of the matrix phase using

various electrolytes and a bromine solution. Such efforts were unsuccessful, since the major precipitates, which have similar chemical compositions as the matrices, Table 45, also tended to be dissolved. The digestive process yielded only chemically inert residues such as carbides, as indicated in Table 46, but the presence of the ordered phase $L1_2$ -type structure in alloys 103 and 104 should be noted. The formation of this ordered phase will be described in detail later in a following Section. Powder diffraction technique was used subsequently, and proved far more successful. Filings from the hot-rolled materials were produced from machining chips and aged at 650°F (342°C) for 16 hours. The phases and structures identified by subsequent X-ray analyses are presented in Table 47. The major precipitate in all the annealed filings from the hot-rolled alloys, with the exception of alloy 103, has been identified as an ordered bcc phase with a $CsCl$ -type structure having lattice constants of about 2.89 Å. The minor precipitate phases identified include $M_{23}C_6$ -type fcc carbide and tetragonal sigma phase. The analyzed compositions of powder alloys are given in Table 48.

TABLE 46. STRUCTURES OF EXTRACTED PRECIPITATES FROM 593C ROLLED + 650°C/16H AGED ALLOYS

Alloy	X-Ray Results
103	$L1_2$ -type, $a_0 = 3.84$ to 3.90 Å
104	MC -type, $a_0 = 4.32$ Å $L1_2$ -type, $a_0 = 3.87$ to 3.94 Å
105	$M_{23}C_6$ -type, $a_0 = 10.58$ Å
106	One diffraction peak, possible $M_{23}C_6$

7450C

The powder diffraction data obtained from the annealed filings of the warm-rolled alloys are, with minor variations in amount of precipitates and lattice parameters, rather similar to those given in Table 47. The only notable exception is alloy 103 in which 5 vol percent of an ordered phase with $L1_2$ -type structure ($a_0 = 3.812$ Å) was observed in the annealed filings of the warm-rolled

The microstructural observations presented above show that the physical metallurgy of the Fe-Mn-Al-X-C alloys is quite complex. According to the Fe-Mn-Al ternary diagram given in Figure 108, alloys 103 through 111 were expected to be essentially single-phase austenitic alloys. This is found to be true only for alloy 103, the base composition. Remarkably, small additions of Si, Cr, and Ni to the base composition led to the formation of moderate amounts of ordered bcc phase, which is not anticipated from the Fe-Mn-Al ternary diagram. Note that a more recent Fe-Mn-Al ternary by Chakrabarti (7), given in Figure 121, does predict formation of the ordered bcc phase. However, as noted by this author, ordering was not detectable by X-ray diffraction until the Al content in the alloy is above 35 at.%. Since the Al content in alloys 104 through 111 is no more than half this amount, the observation of the ordered bcc phase in these alloys can only be explained if one assumes that small additions of Si, Cr or Ni reduce significantly the solubility of Al in the Mn-stabilized austenite. Alternatively, the formation of the ordered bcc phase can be rationalized using the Fe-Ni-Al ternary, given in Figure 122. The approximate position of alloys 104 through 111, assuming Mn behaves like Ni, is indicated by a dot which lies within the austenite and ordered bcc phase field. The formation of the ordered phase with a $L1_2$ -type structure in alloy 103 will be discussed later.

TABLE 47. PHASES AND STRUCTURES IN ANNEALED FILINGS OF HOT-ROLLED ALLOYS 103-111*

Alloy	
103	≥ 99 v/o fcc ($a_0 = 3.656\text{\AA}$) ≤ 1 v/o fcc $M_{23}C_6$
104	55 v/o fcc ($a_0 = 3.651\text{\AA}$) 35-40 v/o ordered bcc ($a_0 = 2.886\text{\AA}$) 10-5 v/o tetragonal sigma phase plus a phase (a) ≤ 1 v/o SiO_2 as hexagonal α -quartz
105	90-95 v/o fcc ($a_0 = 3.664\text{\AA}$) 5 v/o ordered bcc ($a_0 = 2.883\text{\AA}$) ≤ 3 v/o fcc $M_{23}C_6$ ($a_0 = 10.60\text{\AA}$)
106	75 v/o fcc ($a_0 = 3.653\text{\AA}$) 15-20 v/o ordered bcc ($a_0 = 2.897\text{\AA}$) 10-5 v/o tetragonal sigma phase plus a phase (a)
107	85 v/o fcc ($a_0 = 3.642\text{\AA}$) 13-15 v/o ordered bcc ($a_0 = 2.894\text{\AA}$) ≤ 2 v/o fcc $M_{23}C_6$
108	80 v/o fcc ($a_0 = 3.638\text{\AA}$) 18-25 v/o ordered bcc ($a_0 = 2.893\text{\AA}$) ≤ 5 v/o tetragonal sigma phase + fcc $M_{23}C_6$
109	85 v/o fcc ($a_0 = 3.637\text{\AA}$) 10 v/o ordered bcc ($a_0 = 2.893\text{\AA}$) 5 v/o fcc $M_{23}C_6$ ($a_0 = 10.56\text{\AA}$)
110	80 v/o fcc ($a_0 = 3.634\text{\AA}$) 13-15 v/o ordered bcc ($a_0 = 2.891\text{\AA}$) 4-3 v/o fcc $M_{23}C_6$ 3-2 v/o tetragonal sigma phase
111	70 v/o fcc ($a_0 = 3.612\text{\AA}$) 25-30 v/o ordered bcc ($a_0 = 2.899\text{\AA}$) 5-3 v/o fcc $M_{23}C_6$ ($a_0 = 10.55\text{\AA}$)

* Alloys were solution heat treated at $1120^\circ\text{C}/1$ hr./OQ and aged at $650^\circ\text{C}/16$ hr. Filings annealed at $650^\circ\text{C}/16$ hr.

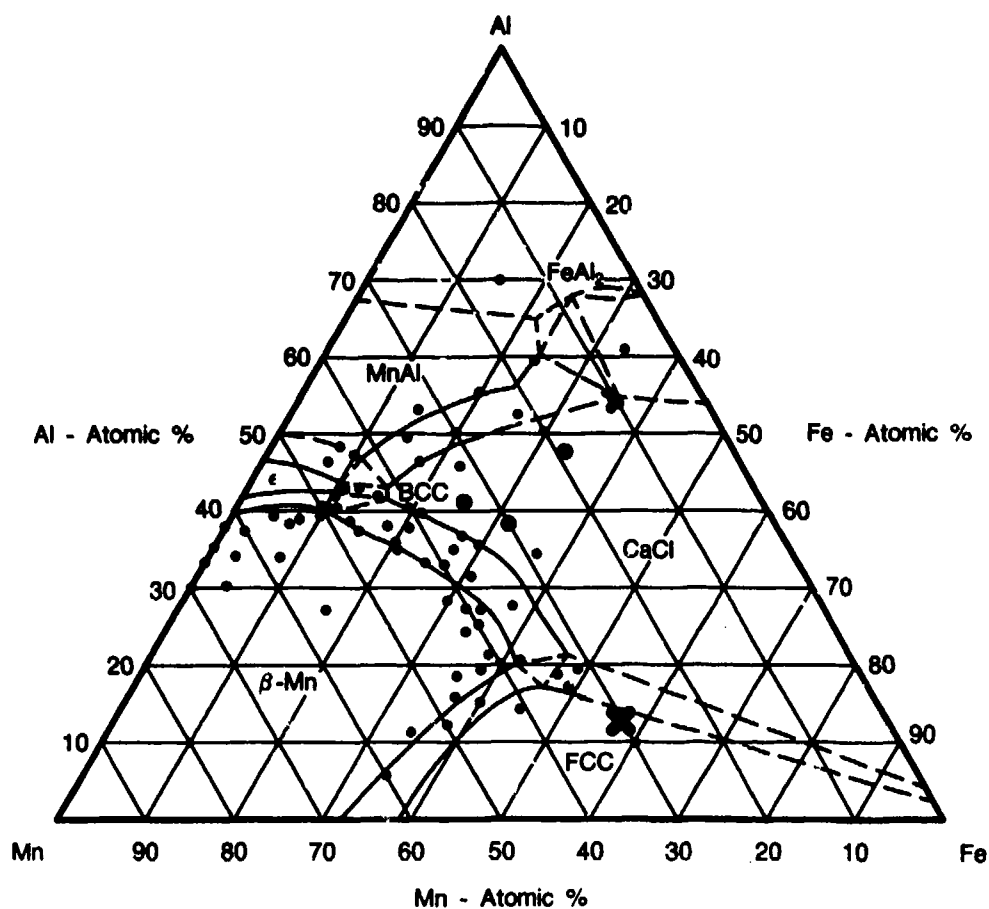
Phase (a): either with Mn_5Si_3 -type hexagonal structure or $Mn_{23}Th_6$ -type fcc structure

7480C

TABLE 48. ANALYZED COMPOSITIONS OF POWDER ALLOYS

Alloy	Fe	Mn	Al	C	Cr	Ni
97						
Ingot	Bal.	23.4	9.2	1.94	—	—
97	Bal.	24.1	9.4	1.92	—	—
101	Bal.	39.8	5.1	1.81	5.0	—
102	Bal.	19.6	4.8	1.74	4.9	20.6

7480C



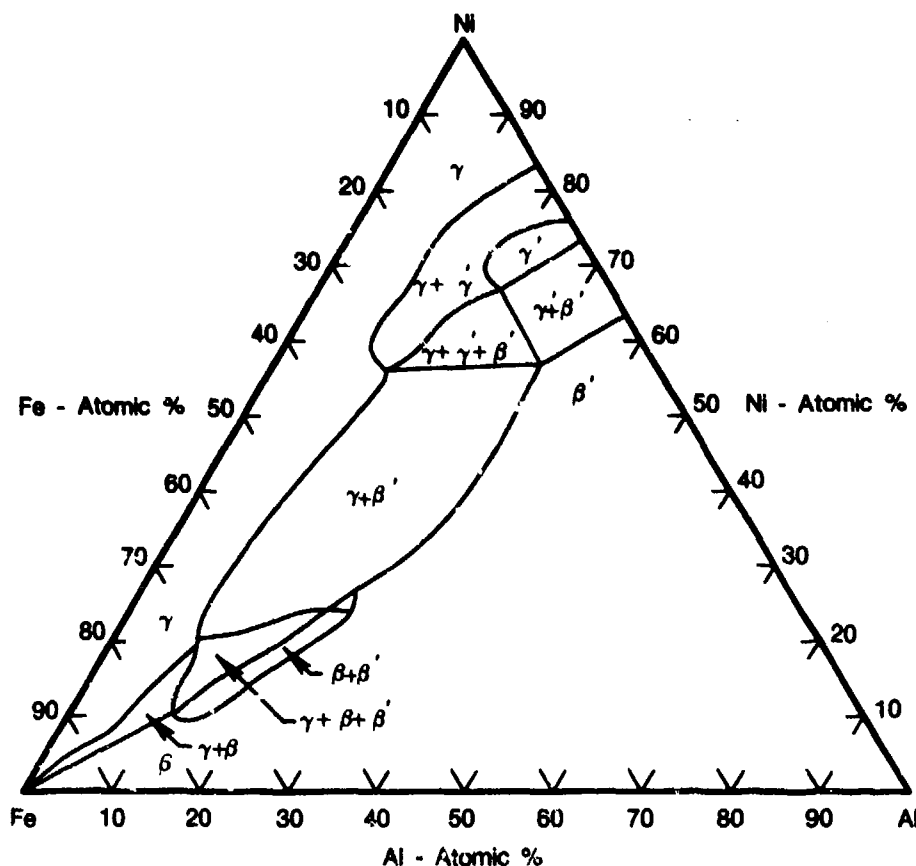
FDA 318379

Figure 121. Part of 1000°C Ternary Isothermal Section of Mn-Fe-Al System (Chakrabarti, 1977). Within the bcc Phase Field, Alloys Showing CsCl-Type Superlattice Lines Are Indicated By Filled Circles (•), and Disordered Alloys by Open Circles (O). The Approximate Position of the Base Alloy (103) Is Indicated by the (X) in the Austenite Phase Field

It may also be noted that although the precipitation of an ordered bcc phase occurred in most alloys, the hardening produced varied considerably. The rather fine precipitates formed in the Ni-containing alloys caused quite high levels of hardness, but the much coarser precipitates formed in the other alloys produced little or no hardness change.

Creep Behavior

Creep data have been obtained primarily on the cast alloys (alloys 103 through 111) in warm-rolled and hot-rolled conditions. All tests were conducted at 1200°F (650°C) and a stress of 42.5 ksi (293 MPa).



FDA 318380

Figure 122. Fe-Ni-Al Ternary System at 950°C (Bradley, 1949). The Approximate Compositions of Alloys 107 Through 111, Assuming Mn Behaves Like Ni, Is Indicated by the Filled Circle in the $(\gamma + \beta)$ Phase Field. β = bcc, γ = fcc, γ' = Ni_3Al , β' = FeAl , NiAl

The creep behavior of warm-rolled and 1200°F (650°C) aged materials is shown in Figure 123 for alloys 103 through 106, and Figure 124 for alloys 107 through 111. For comparison, the creep curve of H46 steel, determined under identical test conditions, was also included in the figures. It can be observed that the creep resistance of the warm-rolled alloys is lower than the H46 steel. The alloys which show the highest hardness, alloy 104 in the Ni-free series, and alloy 111 in the Ni-containing series, exhibit the lowest creep resistance. Thin foil samples from selected creep specimens for TEM studies have been prepared to determine the cause for this poor performance of the warm-rolled alloys.

Prior to creep test, the hot-rolled alloys were given a solution heat-treatment at 1900°F (1040°C) for 1 hour followed by an oil quench and then aged at 1200°F (650°C) for 16 hours. The hardness numbers of the hot-rolled Ni-containing alloys after this heat-treatment are Rc 8, 30, 13 and 8 for alloys 107 through 110, respectively, compared with Rc 10 when the solution heat treatment was performed at a higher temperature, 2050°F (1120°C), as in the aging studies.

The hardness of alloy 111 was not changed by the lower solutioning temperature. Creep curves of the hot-rolled Ni-containing alloys, given in Figure 125, show some important differences from the warm-rolled alloys. The hot-rolled alloys show a prominent primary creep

stage followed by a secondary stage with creep rates comparable to H46 steel. The creep resistance of alloy 110 appears to be close to that of H46 steel.

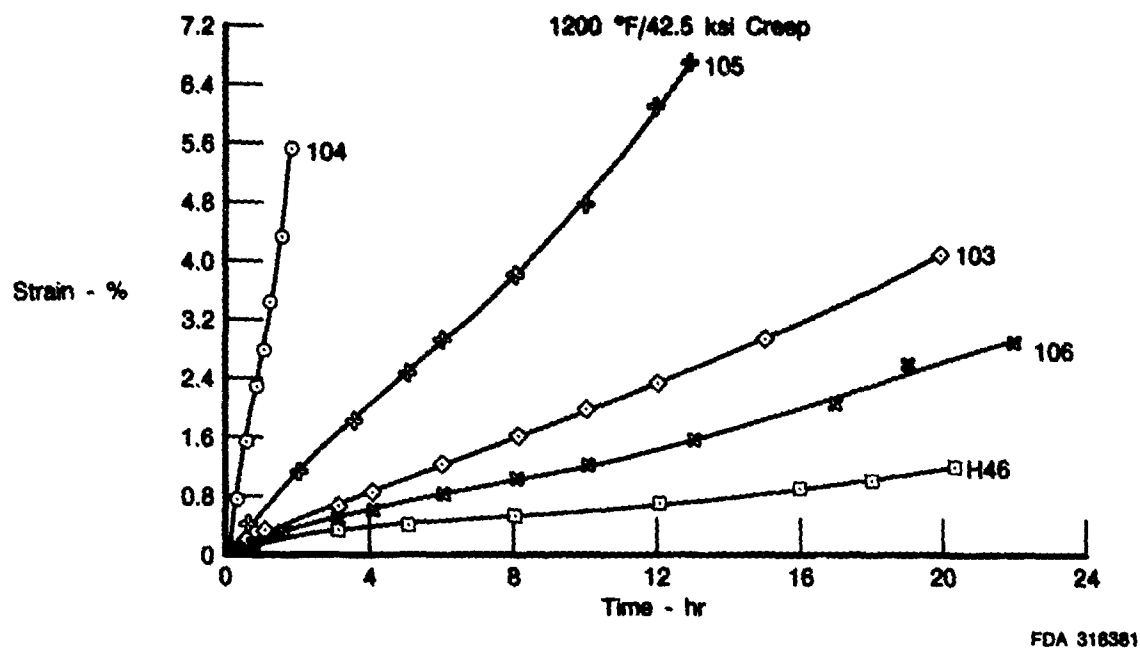


Figure 123. Creep Behavior of Alloys 103 Through 106 in Warm-Rolled, 650°C/16 Hours Aged Condition at 650°C and 293 MPa

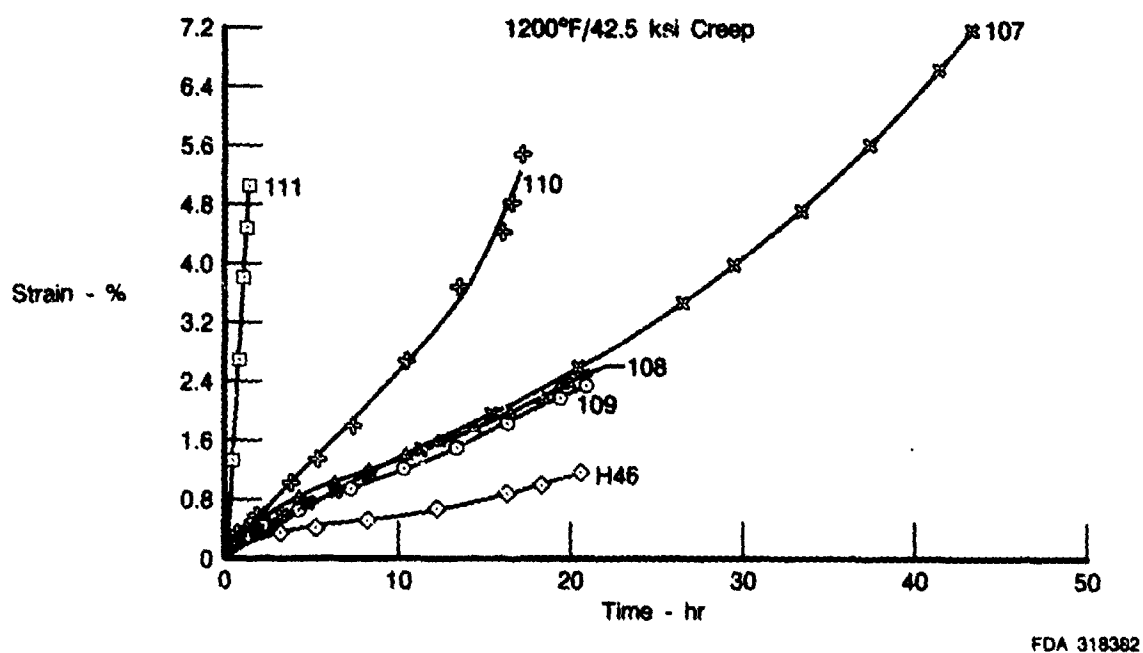


Figure 124. Creep Behavior of Alloys 107 Through 111 in Warm-Rolled, 650°C/16 Hours Aged Condition at 650°C and 293 MPa

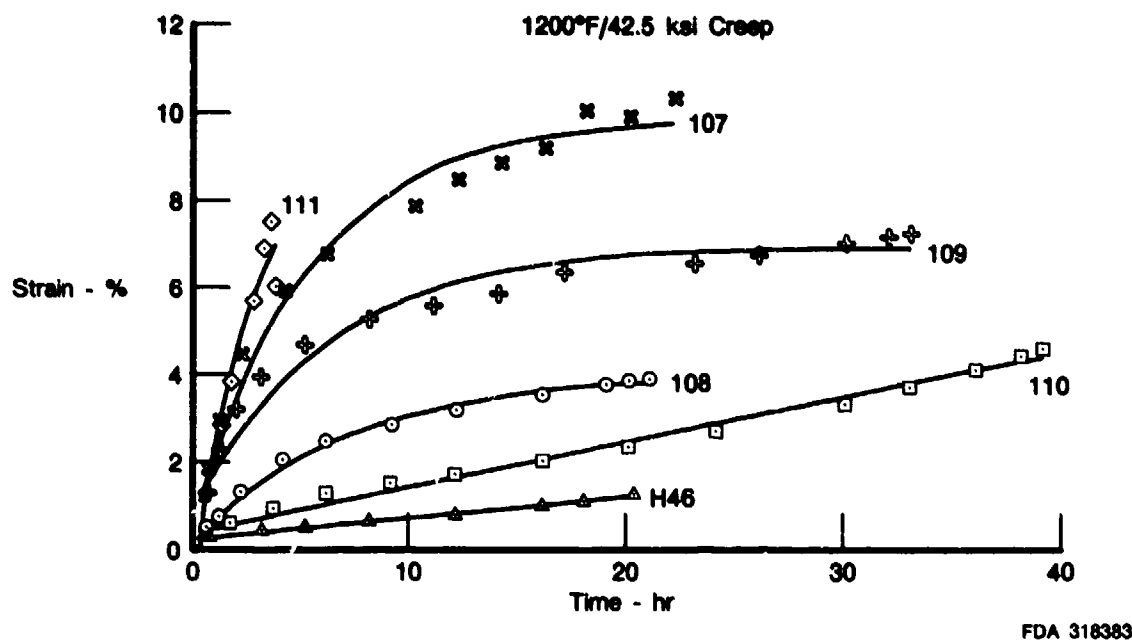


Figure 125. Creep Behavior of Alloys 107 Through 111 in Hot-Rolled, Solution Heat Treated (1038°C/1hr/OQ) and Aged (650°C/16 Hours) Condition at 650°C and 293 MPa

Fe-Mn-Al Alloys Based on Previous Investigation

Three alloys were chosen for the present studies. Alloy 140, formerly designated BA36-1 in the 1950's, was produced as a small casting and two of its modifications, alloys 67 and 68, were produced as powder which was consolidated using vacuum hot pressing. The analyzed compositions of the three alloys are given in Table 49 which shows no major deviations from the aim compositions except for the Mn content in alloy 67, which is 16% lower.

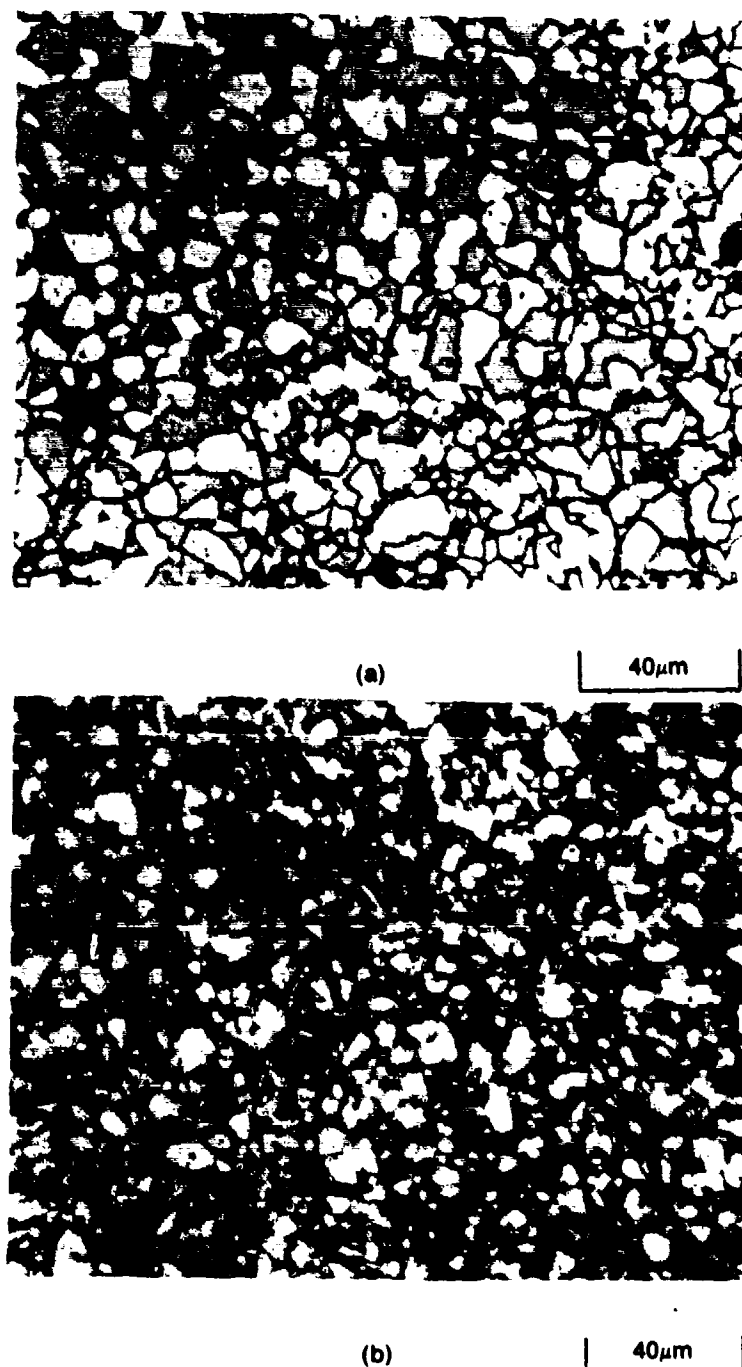
TABLE 49. ANALYZED COMPOSITIONS, WT%

Alloy	Fe	Mn	Al	C	Cr	Ni	Si	Mo	Nb	Ti	V	B	W
67	Bal.	27.0	7.9	0.24	—	6.1	0.49	2.9	0.17	—	0.27	—	—
68	Bal.	32.5	8.0	0.19	—	6.1	0.48	2.7	0.22	0.16	—	0.02	—
140	Bal.	32.4	6.6	0.7	—	3.0	0.5	1.1	—	—	0.6	0.01	0.6

7448C

Microstructure (Alloys 67, 68 and 140)

X-ray diffraction analyses indicates that the structures of the loose powders of both alloys 67 and 68 consist primarily of ferrite with a lattice parameter of 2.91Å. However, upon annealing the powders at 1904°F (1040°C) for 2 hours, the structural changes to an approximately equivolume mixture of bcc and fcc phases with lattice parameters of 2.90Å and 3.66Å, respectively. Figure 126 shows the duplex phase structure of alloys 67 and 68 consolidated by vacuum hot pressing at 1904°F (1040°C) at 3000 psi (21 MPa) for 0.5 hour. Full density was achieved in both alloys using this hot pressing condition.



FD 243630

Figure 126. *Duplex Phase Microstructures of Powder Compacts of (A) Alloy 67, and (B) Alloy 68 Consolidated by Vacuum Hot Pressing at 1040°C, 3 ksi for 0.5 Hour*

The compositions of the bcc and fcc phases in alloy 67 were determined using an analytical electron microscope (AEM), and results are given in Table 50 together with the bulk alloy composition. The partitioning behavior of the alloying elements in the Fe-Mn-Al-X system follows the expected trend except for Ni, which shows a higher concentration in ferrite than in austenite. As a check for the accuracy of AEM results, the alloy composition was calculated from

the phase compositions, and results are presented in Table 49 which show reasonable agreements between the calculated and the actual alloy contents.

TABLE 50. ANALYZED PHASE COMPOSITIONS OF ALLOY 67, WT %

	Fe	Mn	Al	C	Si	Ni	Mo	Nb	V
Bulk	Bal.	27.0	7.9	0.2	0.5	6.1	2.9	0.17	0.3
Ferrite	Bal.	23.6	12.4	—	—	8.3	2.4	—	—
Austenite	Bal.	31.0	7.0	—	—	5.2	2.1	—	—
Bulk (Calc.)	Bal.	26.5	10.3	—	—	7.1	2.3	—	—

7480C

The third alloy, No. 140, was prepared to verify the reported excellent creep system results from the 1950's, and to characterize the microstructure of the alloy which was not studied in any detail in the previous work. Such characterization was considered essential for insight into design of improved alloys. Alloy 140 casting was hot-rolled under the same conditions as other alloys.

The X-ray results from alloy 140 are summarized in Table 51. The heat treatment No. 1, Table 51, which was that used in the studies during the 1950's, results in a rather inhomogeneous grain structure consisting of recrystallized grains mixed with irregular grains containing a high dislocations density, Figure 127. TEM studies of material in this condition revealed two types of precipitation behavior. In fully recrystallized grains, a homogeneous and dense dispersion of very thin, small precipitates (about 50Å) are observed, Figure 128a. These precipitates are apparently coherent with the austenitic matrix as evidenced by the elastic strain contrast and absence of diffraction effects. In the partially recrystallized grains, which contain dislocation substructure, the precipitates are equiaxed in shape with considerably larger particle size and are less dense, Figure 128b. Preliminary electron diffraction analysis shows that the larger precipitates have a bcc structure and are enriched in refractory metals. However, confirming evidence has not been obtained using X-ray diffractometry as shown in Table 51. To coarsen the precipitates for easier phase structure identification, alloy 140 was heat treated at a higher temperature (No. 2 in Table 51). Additional structures were observed after this treatment including a bcc phase and the presence of a small quantity of a phase tentatively identified as a hexagonal MoC. TEM of the material reveals, in addition to the equiaxed particles, the formation of thin plates, Figure 129, which may correspond to the MoC phase identified by X-ray. The plates are enriched in Al and Ni. Interestingly, the dense population of the thin, coherent precipitates could no longer be observed after the higher temperature heat treatment.

TABLE 51. RESULTS OF PHASE IDENTIFICATION BY X-RAY FROM FILINGS OF ALLOY 140 CRK α RADIATION

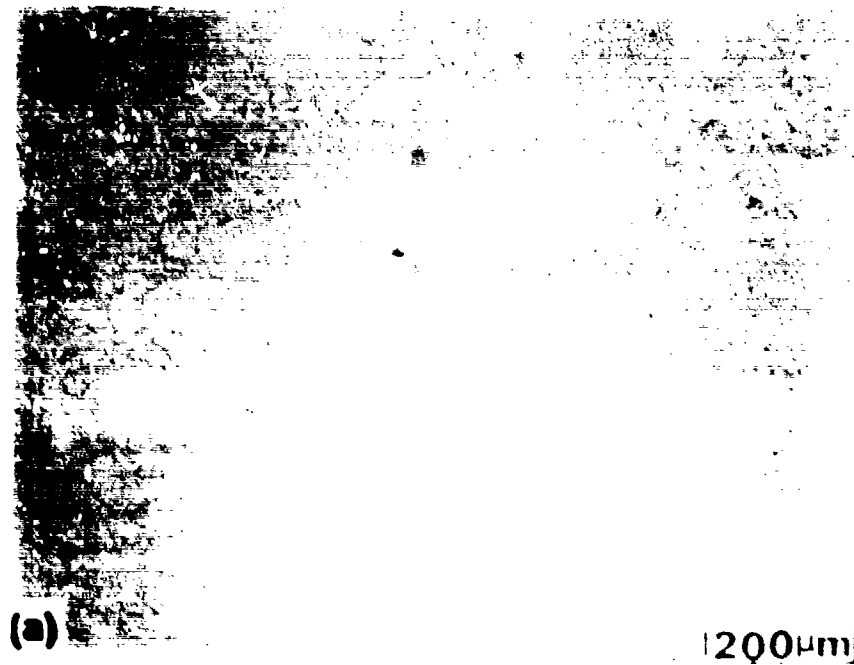
1. 1900°F/1h/oQ+1200°F/16h/AC	Single phase disordered fcc ($a_0 \approx 3.6596\text{\AA}$)
2. 2050°F/1h/OQ+1300°F/100h/AC	$\approx 95-90$ v/o disordered fcc ($a_0 \approx 3.653\text{\AA}$) $\approx 5-10$ v/o bcc* ($a_0 \approx 2.993\text{\AA}$) $\approx \leq 1$ v/o unidentified phase, possibly hexagonal MoC

* Due to the weakness of the fundamental reflections, no atomic ordering information was obtained

7480C

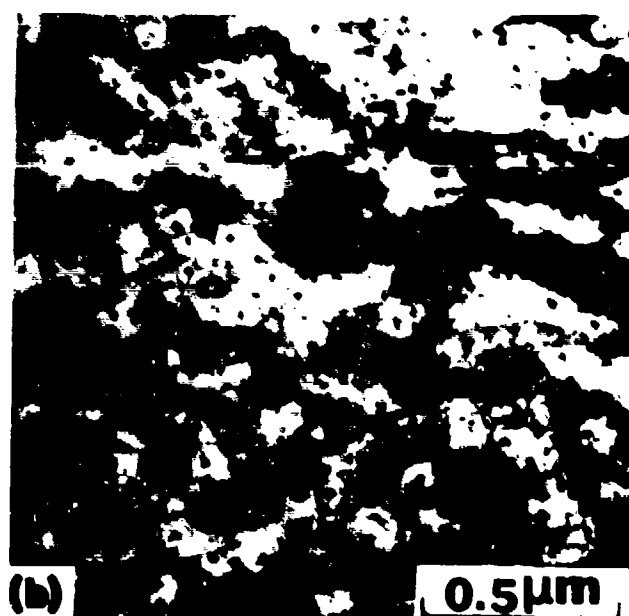
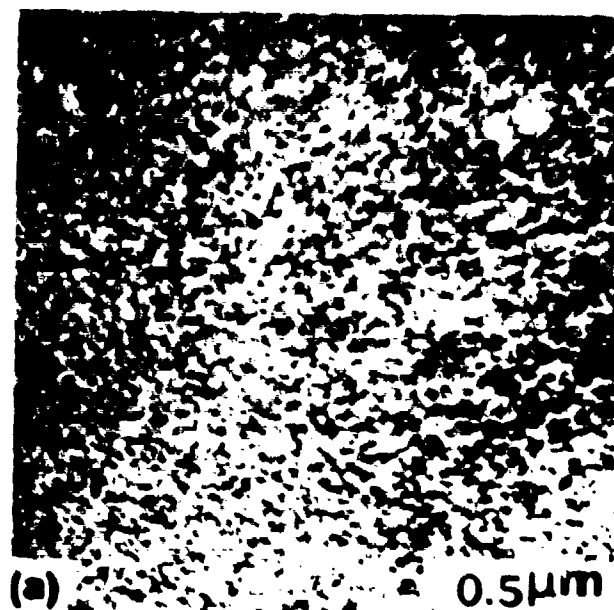
Similar changes are observed after aging at lower temperatures 1200°F (650°C) and 1250°F (675°C) for long times (about 300 hours). It appears that the coherent precipitates may well be

the precursor of the more stable equiaxed particles. As will be shown later, there is an apparent correlation of creep resistance in alloy 140 with the presence of the coherent precipitate.



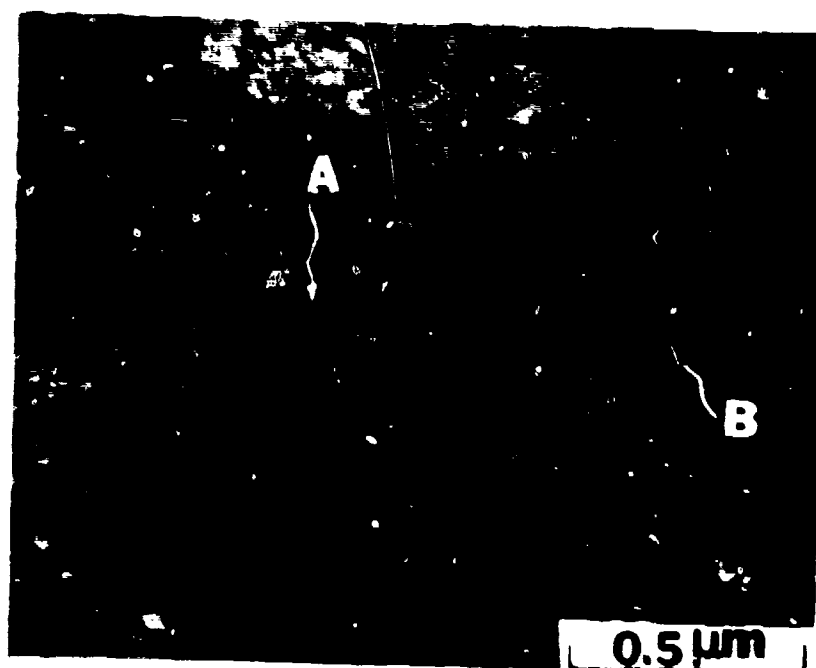
FD 318384

Figure 127. Microstructure of Alloy 140 After Heat Treatments of 1040°C/1h/OQ and 650°C/16h/AC. Note the Inhomogeneous Grain Structure in This Material



FD 318385

Figure 128. *Detailed Microstructures of Alloy 140 With Heat Treatments Described in the Preceding Figure Illustrating (a) Densely Populated Fine Coherent Precipitate in Recrystallized Grains (b) Coarser Particles in Grains Undergoing Recovery and Recrystallization*



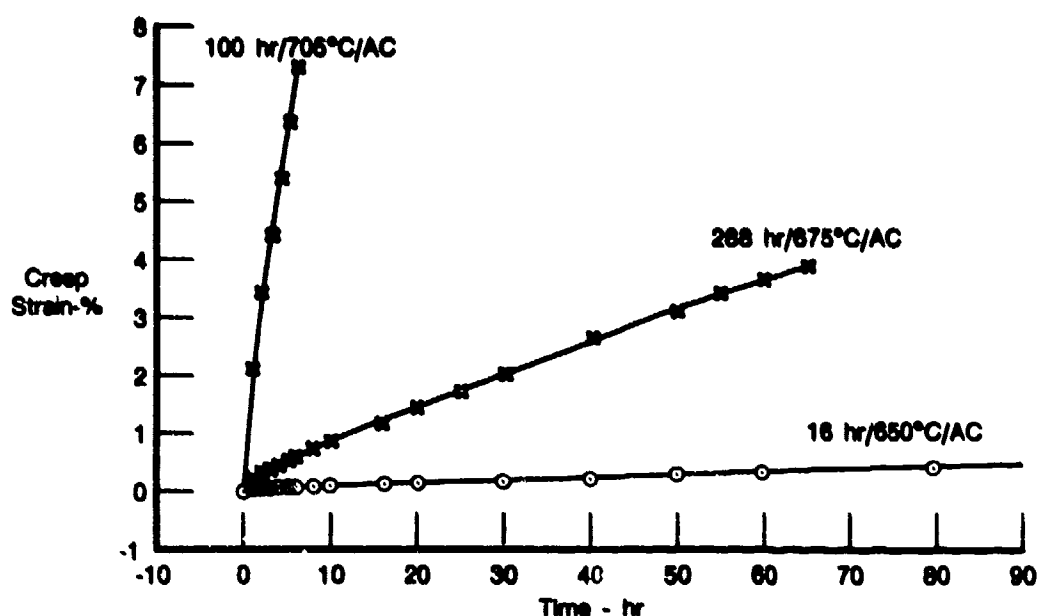
FD 316386

Figure 129. Microstructure of Alloy 140 After Aging at 705°C for 75 Hours Illustrating the Presence of a New Phase, A. With a Plate Morphology and Equiaxed Particles, B. The Latter Are Present Also at a Lower Aging Temperature. The Fine Coherent Precipitate Which Forms at a Lower Aging Temperature Can No Longer be Observed (See Figure 128)

Creep Behavior

Compressive creep tests on alloys 67 and 68 were performed at 1200°F (650°C) and a stress of 425 ksi (293 MPa). The minimum creep rates of these alloys are $2.57 \times 10^{-2} \text{h}^{-1}$ and $3.82 \times 10^{-2} \text{h}^{-1}$, respectively which are considerably higher than those observed in some of the Fe-Mn-Al alloys studied in a previous P&W program. The factors which contribute to the poor creep resistance in these two powder alloys were considered to be the fine grain structure, and the presence of a substantial amount of bcc phase. Based on the creep results, further study of these two alloys will not be continued.

The microstructural studies on alloy 140 indicated formation of at least three different precipitate phases in this alloy after different heat treatments. To determine the effects of these phases on the creep behavior of alloy 140, creep testing was conducted on a series of specimens which had been given aging treatments of 1200°F (650°C) for 16 hours, 1250°F (675°C) for 290 hours and 1300°F (705°C) for 100 hours, respectively. Results, given in Figure 130, show the highest creep resistance to be associated with the formation of the coherent precipitate in the 1200°F (650°C)/16 hours aging treatment. The creep resistance decreases drastically when the coherent precipitates are replaced by the thin plate phase after prolonged aging/exposure at 1200°F (650°C) and above.



FDA 318387

Figure 130. Creep Behavior of Alloy 140 at 650°C and 293 MPa After Various Aging Heat Treatments Indicated. Solution Heat Treatment 1040°C/1h/OQ

Fe-Mn-Al-C Alloys — First Series

The analyzed compositions of alloys 97, 101, and 102 are given in Table 52. All three alloy compositions have been predicted by recent Japanese work (Reference 3) to result in a single phase with an ordered fcc $L1_2$ -type structure under rapid solidification conditions, as previously shown in Figure 109. Alloy 97 was produced using the RSR powder process, and alloys 101 and 102 were vacuum atomized at Homogeneous Metals, Inc. (HMI).

TABLE 52. ANALYZED COMPOSITIONS OF POWDER ALLOYS

Alloy	Fe	Mn	Al	C	Cr	Ni	Si	Mo	Nb	Ti	V	B
97												
Ingot	Bal.	23.4	9.2	1.94	—	—	—	—	—	—	—	—
97	Bal.	24.1	9.4	1.92	—	—	—	—	—	—	—	—
101	Bal.	39.8	5.1	1.81	5.0	—	—	—	—	—	—	—
102	Bal.	19.6	4.8	1.74	4.9	20.6	—	—	—	—	—	—

7448C

Microstructure of Alloy 97

Alloy 97 was studied in ingot form, as-received powder, and consolidated powder. The ingot microstructure was characterized to provide structural information on the material after a slow solidification sequence. In this case, a sample was taken from the core region of the ingot subsequently remelted to make powder.

An optical micrograph of an alloy 97 ingot sample, Figure 131, shows coarse grains within which a very fine "basket weave" microstructure can be observed. The details of the ingot microstructure, illustrated by the transmission electron micrograph in Figure 132, shows a somewhat irregular rectangular blocky phase distribution similar to that observed by the Japanese workers in the material rapidly quenched from the melt. Further, the rectangular pattern is oriented in $\langle 100 \rangle$ directions, a feature also reported by the Japanese workers. The origin of the rectangular pattern will be discussed later. Electron diffraction patterns with zone axes of $[001]$, $[110]$, $[211]$, and $[301]$ are given in Figure 133. Indexing of these patterns is consistent with the phase being an ordered fcc with $L1_2$ -type structure. Definitive evidence of ordering in the Alloy 97 ingot sample was also obtained from X-ray powder diffraction data on filings (annealed at 1900°F (1040°C) for 4 hours in a vacuum). The X-ray data in Table 53 show the presence of two fcc phases with lattice parameters of 3.672°\AA and 3.781°\AA . The phase with the larger lattice constant is ordered and constitutes 30 to 40 volume percent in the ingot sample.



FD 318386

Figure 131. Grain Structure in Alloy 97 Ingot

The presence of the ordered phase in the ingot samples was a major surprise as Inoue et al., had described the ordered $L1_2$ -type phase as a nonequilibrium phase with its occurrence restricted to conditions of rapid solidification. It seems clear from the present work that the $L1_2$ -type phase also occurs as an equilibrium phase, which has important implications for the stability of these alloys and their creep resistance. Since neither Fe nor Mn forms an $L1_2$ -type compound with Al, it is logical to assume that the observed $L1_2$ -type phase in alloy 97 is a ternary compound involving carbon. A ternary compound, which bears a close relationship to the ordered phases of the $L1_2$ -type, is characterized by the general formula T_3BC_x ($x = 0.3$ to 1). About 40 of these compounds have been identified by Stadelmaier (Reference 13). Compounds of present interest consist of Fe, Mn, and Ni as the T (transition) elements, and Al as the B element. An ideal structure of the ternary compound in which $x = 1$ is shown in Figure 134. In this ideal (perovskite) structure, the Al atoms occupy the unit cell corners, the transition element atoms occupy the face centers, and the C atoms occupy the octahedral positions in the centers of the cells. One of the ternary compounds which exhibits the ideal structure is Mn_3AlC .



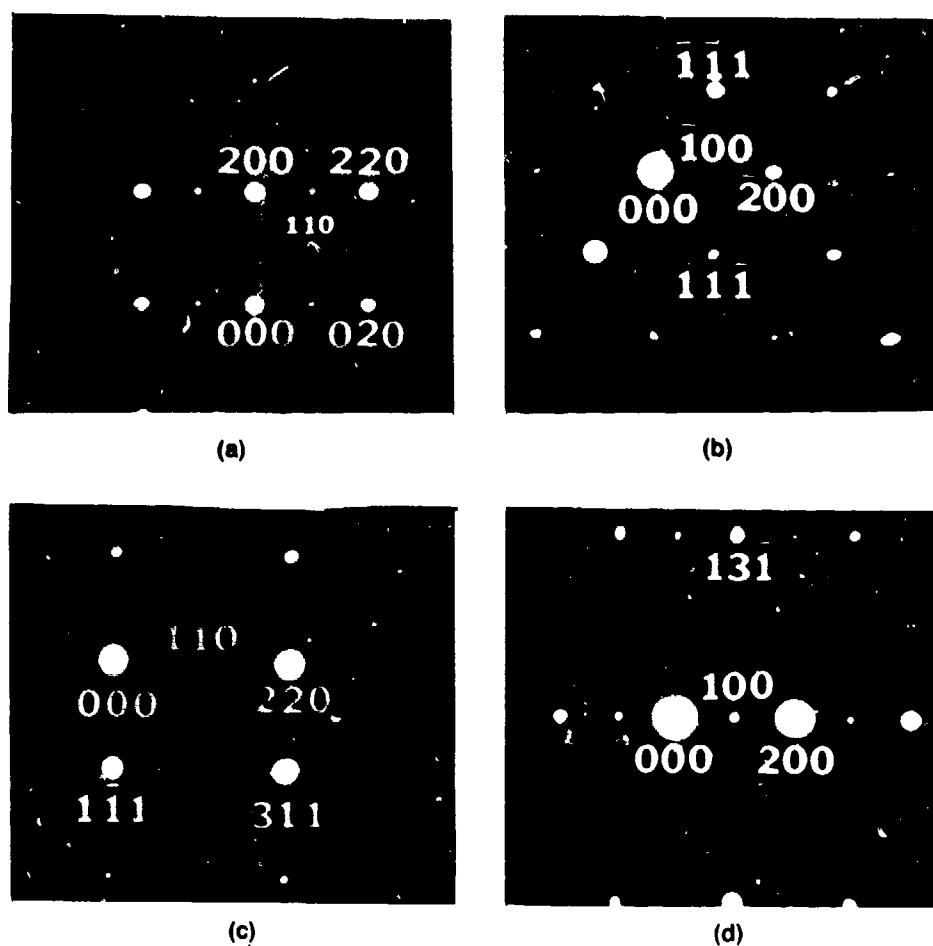
FD 318369

Figure 132. Transmission Electron Micrograph of Alloy 97 Ingot Showing the Ordered fcc Phase. The White Rectangular Pattern Was Believed To Be the Boundaries of Ordered Domains (Ref. 3)

The phase fields of the ternary compounds of present interest have been summarized from the work of Stadelmaier by Rosen and Sprange (Reference 14), and are given in Figure 135 which may have an important implication on the stability of mixed transition element ternary compounds. If one can assume continuous phase fields for such compounds, then replacing Fe with Mn requires a decrease of Al and an increase of C, whereas replacing Fe with Ni requires an increase of Al and a decrease in C for stability.

The formation of the ordered $L1_2$ -type phase as an equilibrium phase can be expected from the Fe-Al-C ternary, shown in Figure 136. The position of a ternary alloy, which has the same Al and C contents as alloy 97, is indicated by point 1 in Figure 136 in the three-phase field consisting of ferrite (α), austenite (γ) and perovskite (ϵ). If the substitution of Fe by Mn can be assumed to have a similar effect as increasing the carbon content with the resulting elimination of the ferrite phase, the formation of phases with the disordered fcc and $L1_2$ -type structure in alloy 97 can be understood. Similarly, the observation in alloy 103, indicated by point 2 in Figure 136, of the $L1_2$ -type ordered phase in the austenitic matrix can be rationalized on the same basis. These observations obviously have important implications for formulating Fe-Mn-Al austenitic alloys containing $L1_2$ -type precipitate.

Turning now to the characterization of the materials in the powder form, an optical micrograph of alloy 97 F5R powder in the as-received condition, Figure 137a, shows the usual dendritic structure. X-ray diffraction analysis of the powder indicated a single austenitic phase with lattice constant of 3.708 \AA . Transmission electron micrographs obtained from the powder particle, Figure 137b, reveal a single phase with no discernible rectangular pattern observed in the relatively slowly solidified ingot material. The structure of the powder particles was determined by electron diffraction to be a weakly ordered fcc with $L1_2$ -type lattice. Note that the linear features in Figure 137b are probably slip bands resulting from deformation of the powder particles during the thin foil preparation process.



FD 243828

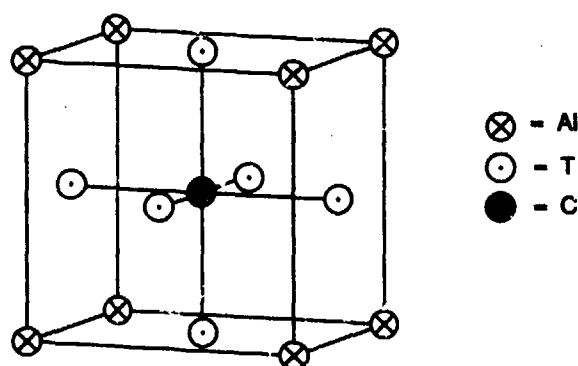
Figure 133. Selected Area Diffraction Patterns of Alloy 97 Ingot With Zone Axes (a) [001], (b) [011], (c) [112], and (d) [013]

TABLE 53. X-RAY DIFFRACTION DATA OF ALLOY 97 INGOT SAMPLE
ANNEALED AT 1040°C
FOR 4 HOURS

<i>d</i> Spacing nm	(hkl)	<i>a</i> nm	<i>I</i> / <i>I</i> ₀ *	Structure
0.3778	100	0.3778	0.121	Ordered fcc
0.2675	110	0.3783	0.021	Ordered fcc
0.2183	111	0.3781	1.000	Ordered fcc
0.2120	111	0.3672	1.000	fcc
0.1891	200	0.3782	0.395	Ordered fcc
0.1835	200	0.3670	0.284	fcc
0.1691	210	0.3781	0.026	Ordered fcc
0.1337	220	0.3782	0.316	Ordered fcc
0.1297	220	0.3668	0.209	fcc

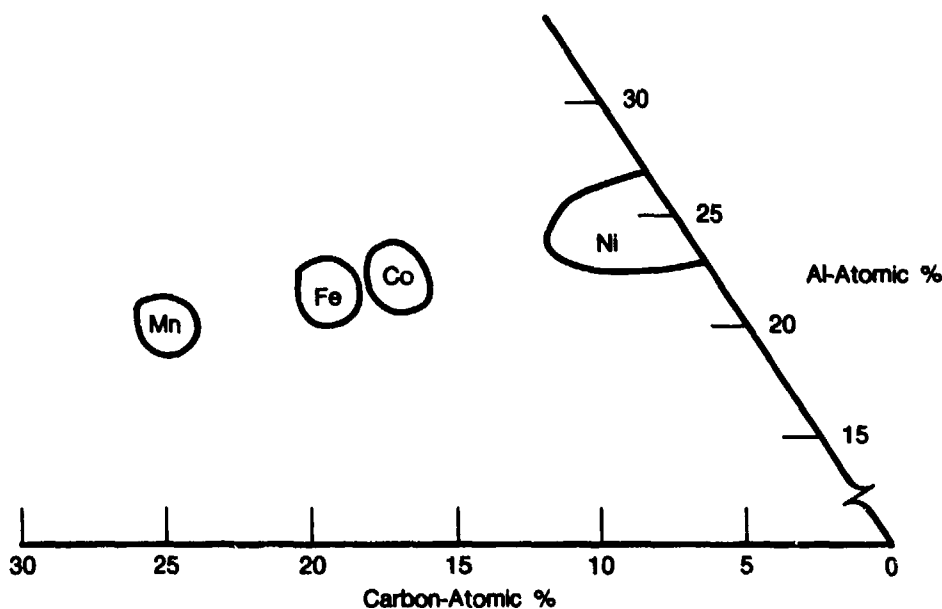
* Intensities are based on peak heights not on integrated intensities.

7450C



FD 318391

Figure 134. Unit Cell of T_3BC

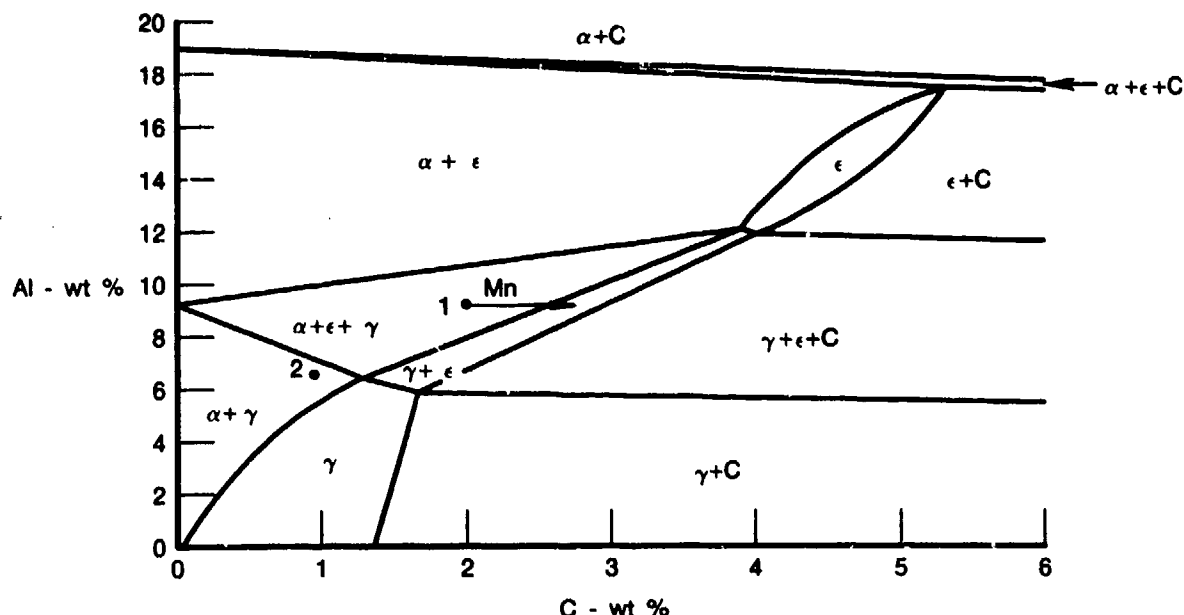


FD 318392

Figure 135. Phase Fields of Some Ternary T_3AlC_x Compounds

Alloy 97 powder was consolidated by hot isostatic pressing at 1900°F (1040°C) and 15 ksi (100 MPa). The powder compact appeared metallographically to be fully dense. However, cracks were observed in the powder compact in the as-consolidated condition. The origin of cracks was considered to be due to the poor inter-particulate bonding. Similar situations have been observed in other iron-aluminide studies (Reference 15), and were rectified by consolidating the powder by extrusion. The optical micrograph, Figure 138, shows the fine-grained structure in the powder compact. Phase structures of the compacted material, determined by X-ray analysis, consist of about 70 volume % austenite with a lattice parameter of 3.678 Å and the remainder an ordered $L1_2$ -type phase with a lattice parameter of 3.764 Å. These results are virtually identical with those determined from the ingot sample. The distribution of the phases was studied by TEM techniques and the results, illustrated in Figure 139a, show an elongated phase in a matrix consisting of very fine rectangular patterns. The structure of the elongated phase was determined to be a $L1_2$ -type phase by selected area diffraction technique. Detailed examination of the matrix, shown in Figure 139b, revealed a modulating phase structure with a wavelength of about 360 Å.

The $L1_2$ -type diffraction patterns were also obtained from the matrix, indicating the presence of either isomorphous-ordered fcc phases or coherent-ordered and disordered fcc phases in a modulated structure. However, only the latter is consistent with the X-ray data. The composition of the elongated phase determined by EDS analysis is 50.6Fe, 28.2Mn, and 21.2Al in at.%, which is close to the stoichiometric composition $(\text{Fe, Mn})_3\text{Al}$; carbon is not detectable by the EDS technique used. The elongated phase is, therefore, considered a perovskite carbide.

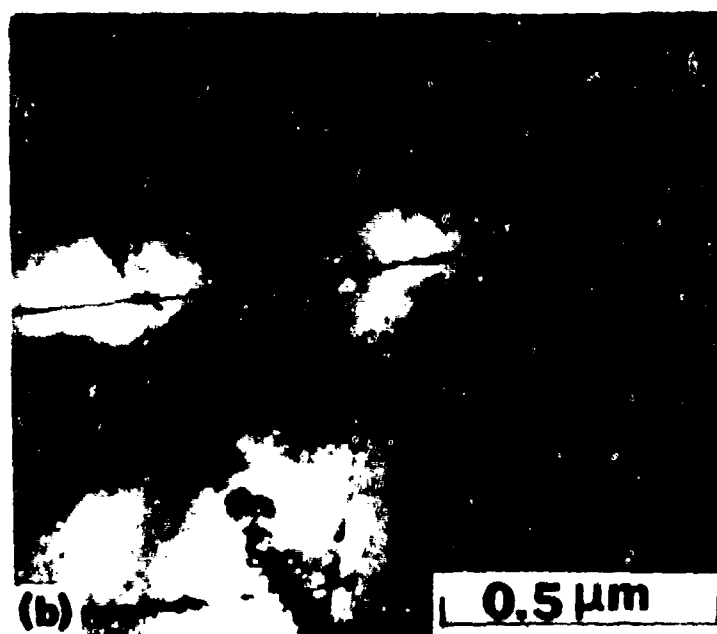


FDA 318393

Figure 136. Isothermal Section Through the Fe-Al-C Phase Diagram at 1000°C. After Morral, 1934***. The Positions of Alloys Which Have the Same Al and C Contents as Alloys 97 and 103 Are Indicated by the Filled Circles 1 and 2, Respectively. α Ferrite, γ Austenite, ϵ = Perovskite

The Japanese workers explained the formation of the modulating structure in terms of ordered domain boundaries. In view of the observations made in the present studies, a different explanation is offered. It is proposed that the modulating structure was produced by spinodal decomposition of an initially homogeneous solid solution into ordered and disordered fcc phases. An approximation to the homogeneous solid solution has, in fact, been observed in the RSR powder particles, shown in Figure 137b. Since spinodal decomposition cannot be completely suppressed, irrespective of the quenching rate, clusters of ordered regions must have been present in the RSR powder particles resulting in the very weak superlattice reflections observed in the electron diffraction patterns. Heat treatment of a spinodal alloy above the spinodal temperature results in classical nucleation and growth of the precipitate phase. This apparently occurred in alloy 97 during consolidation at 1900°F (1040°C) resulting in formation of the elongated perovskite carbide, Figure 139a. Spinodal decomposition occurred subsequently during cooling of the powder compact and resulted in the modulated phase structure. Other microstructural features observed in alloy 97 favoring the spinodal origin of the modulated structure include similarity in structures of the matrix and precipitate phases and the $\langle 001 \rangle$ directions of the modulation which is an elastically soft direction in fcc structure.

*** F. R. Morral: Iron and Steel Inst. J., 1934, Vol. 130, p. 419.



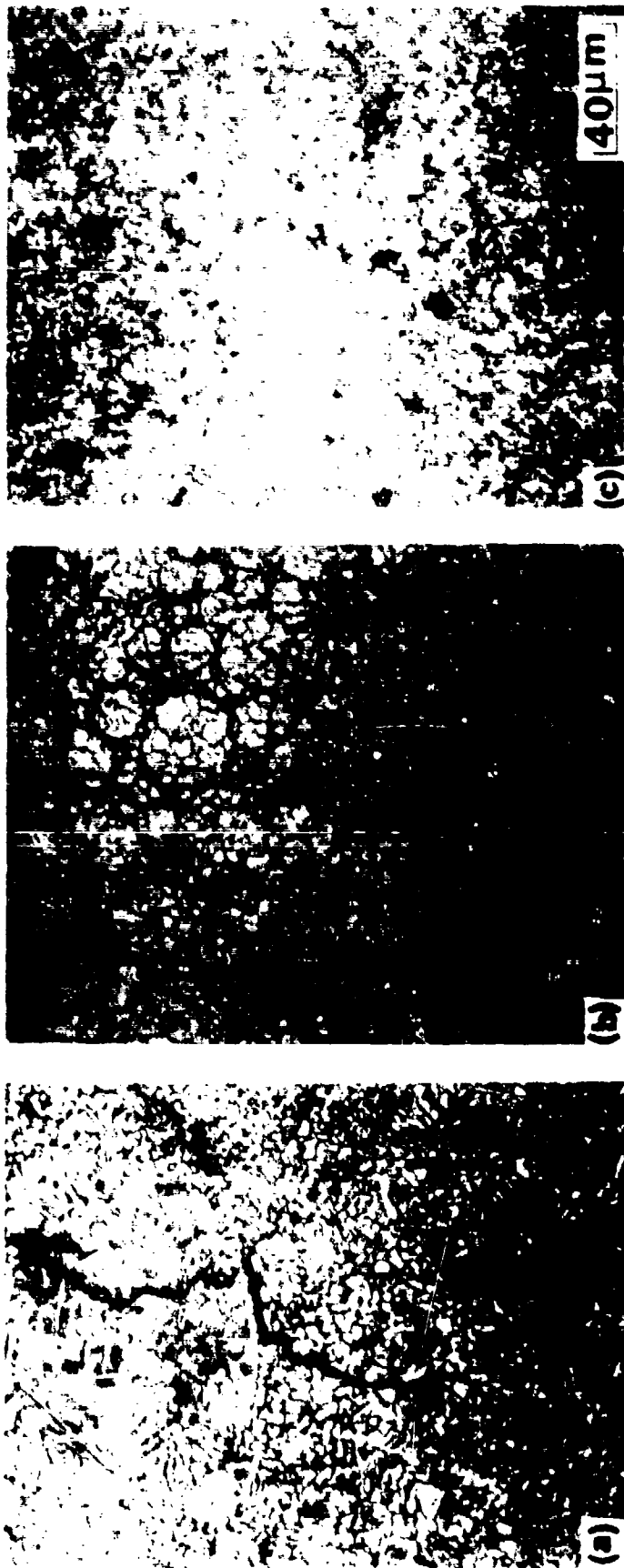
FD 318394

Figure 137. Microstructure of Alloy 97 RSR Powder (a) Optical Micrograph Showing the Usual Dendritic Structure, (b) Transmission Electron Micrograph Illustrating That the RSR Powder Particle Is Essentially a Single Phase Solid Solution



FD 315260

Figure 138. Microstructures of (a) Alloy 97 (b) Alloy 101 and (c) Alloy 102 After Hot Isostatic Consolidation at 1040°C and 100 MPa. Cracks Are Present in All the Powder Compacts in the As-Consolidated Condition



FD 318386

Figure 139. Transmission Electron Micrographs of Consolidated Powder Alloy 97 (a) Elongated $L1_2$ -Type Ordered Precipitates in a Matrix With Modulating Contrast, (b) Modulating Structure Shown in a High Magnification, (c) Modulating Structure Imaged Using a Superlattice Reflection

Microstructure of Alloys 101 and 102

The microstructure of the powder alloys 101 and 102 after HIP at 1900°F (1040°C) for three hours is shown in Figures 138b and 138c. As in the case of alloy 97, cracks have also been observed in these alloys in the as-consolidated conditions. The interparticulate nature of the crack can be clearly observed in alloy 101. The structural data, obtained by X-ray analysis, are summarized in Table 54. Note that both alloys have nominally the same compositions; the only difference is that half of the Mn is substituted by Ni in alloy 102. The effect of Ni in promoting formation of the ordered bcc phase with a CsCl-type structure is evident by comparing the phase structures of the as-received powder and the compacted powder between these two alloys. The structure of the as-received powder in alloy 101 is a single-phase austenite while an ordered bcc phase was present in small quantities in the as-received powder and in much larger amounts in the consolidated powder of alloy 102. The $M_{23}C_6$ -type carbide was the only precipitate observed in the consolidated powder of alloy 101.

TABLE 54. STRUCTURAL DATA OF ALLOYS 101 AND 102 OBTAINED BY X-RAY DIFFRACTION ANALYSIS

Alloy	Form	Structure and Phase
101 Fe-40Mn-5Al -5Cr-2C	-325 Mesh Powder	Single phase austenite, $a_0 \approx 3.695\text{\AA}$; no evidence of ordering
	Consolidated Powder*	$\approx 90-95$ v/o austenite, $a_0 \approx 3.674\text{\AA}$. $\approx 10-5$ v/o fcc $M_{23}C_6$.
102 Fe-19.7Mn-21.1Ni -4.9Al-4.9Cr-2C	-325 Mesh Powder	$\approx 93-97$ v/o austenite, $a_0 \approx 3.661\text{\AA}$; no evidence of ordering.
		$\approx 7-3$ v/o bcc.
	Consolidated Powder*	$\approx 80-85$ v/o austenite, $a_0 \approx 3.624\text{\AA}$ $\approx 15-10$ v/o bcc, $a_0 = 2.892\text{\AA}$ ≤ 5 v/o possible Cr_7C_3 (hexagonal)

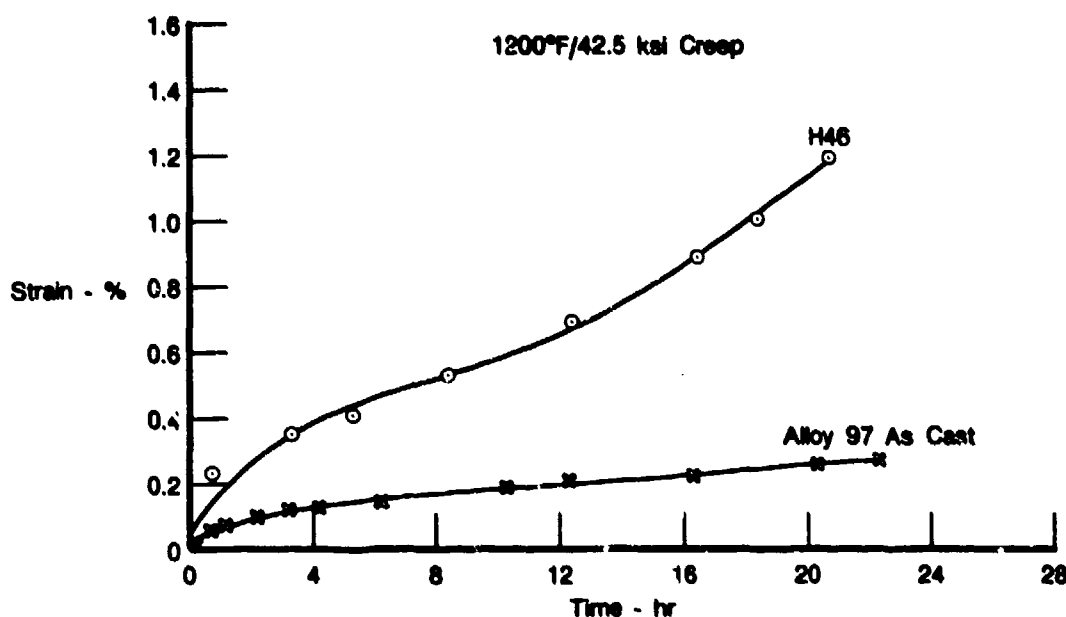
* Hot isostatic pressing at 1040°C under 100 MPa for 3 hours.

7449C

The above microstructural observations indicate that an ordered bcc phase with B2 structure and/or $M_{23}C_6$, Cr_7C_3 -type carbides were formed in preference to the perovskite phase when Cr and Ni were added to the base composition (alloy 97), a trend consistent with that of the cast and wrought Fe-Mn-Al alloys described in the microstructure subsection. As previously discussed in the Fe-Mn-Al alloy creep behavior subsection, the ordered bcc precipitate resulted in low creep resistance. Thus, alloys 101 and 102 would not be studied further.

Creep

The cracking problems in the powder compacts of alloys 97, 101, and 102 precluded the evaluation of these alloys in powder form. Alloy 97 was therefore tested in ingot form in the as-cast condition and after a heat treatment for 4 hours at 1900°F (1040°C), which is a thermal cycle used for powder consolidation. The creep tests were conducted at 1200°F (650°C) and a stress of 42.5 ksi (290 MPa). The creep behavior of the alloy in these two conditions was determined to be practically the same. Creep curve for the as-cast material, shown in Figure 140, shows that the creep resistance of alloy 97 is considerably better than H46 steel. The good creep resistance of alloy 97 was attributed to the formation of uniform fine-scale coherent perovskite precipitate.



FDA 318307

Figure 140. Creep Behavior of Alloy 97 in As-Cast Condition at 650°C and 290 MPa

Fe-Mn-Al-C Alloys — Second Series

Interest to further develop the austenite-perovskite alloys stemmed from several key observations derived primarily from alloy 97.

- A ternary compound $(\text{FeMn})_3\text{AlC}_x$ with the perovskite (CaTiO_3) structure can be produced in the austenitic matrix of Fe-Mn-Al-C alloys under equilibrium conditions. The perovskite carbide is an ordered fcc compound structurally similar to the gamma prime phase in Ni-base superalloys. Because of these similarities, it was anticipated that the austenite-perovskite alloys would also possess the desirable characteristics of the superalloys. In fact, the austenite-perovskite alloy studied (No. 97) exhibited the highest creep resistance of all the Fe-Mn-Al-C-X alloys tested during the first year of this program.
- The precipitation behavior of the perovskite carbide in alloy 97 exhibited several features characteristic of spinodal decomposition, including a modulated structure with phase aligned along $\langle 001 \rangle$ directions. Spinodal alloys can result in fine-scale coherent precipitates with considerable stability to coarsening.

The scope for formulation of a second alloy series was found to be constrained by the observation that an ordered bcc phase with FeAl-type structure was formed in preference to the perovskite carbide when Cr, Si, Ni were added (2-5 wt%) to the base composition. The ordered bcc compound resulted in lower creep resistance. These alloying additions also resulted in the formation of M_{23}C_6 -type carbides. To circumvent the stabilization of ferrite and MC-type carbide, additions of elements such as Ti, V, Mo, etc., were, in general, excluded from the present alloy series. This consideration severely limited the choice of alloying elements. Thus, the

primary goal of the alloy series, Table 55, evaluated in the second year of the program was to optimize the base composition with respect to the Mn and Al contents, using creep resistance as the major criterion.

TABLE 55. AUSTENITE — PEROVSKITE ALLOYS NOMINAL COMPOSITION (Wt%)

Alloy	Fe	Mn	Al	C	Other	Comment
97	Bal.	23.1	9.1	2.0	—	Base composition
141	Bal.	18.0	9.0	2.0	5% Co	Co substituted for Mn to reduce perovskite lattice parameter.
145	Bal.	0.0	7.5	2.0	—	Mn content increases systematically.
142	Bal.	13.0	9.0	2.0	—	
154	Bal.	30.0	9.0	2.0	—	
143	Bal.	40.0	9.0	2.0	—	Low Al content
144	Bal.	23.0	8.0	2.0	—	
146	Bal.	20.0	10.5	3.0	—	High Al and C content.
155	Bal.	30.0	9.0	2.0	1% Mo, 0.5% W	Alloy 154 + Mo and W

7448C

In alloys 145, 142, 154, and 143 the Mn content was systematically increased from 0% to a maximum of 40 wt%. In Alloy 146 the Al content was increased to 10.5 wt%, and to offset the ferrite forming tendency of Al, the C content was simultaneously increased to 3.0 wt%. To control the number of compositional variables in other alloys, the carbon content was kept constant at 2 wt%. This carbon level would theoretically produce a maximum of 35% perovskite carbide assuming all the carbon atoms reside in the carbide phase.

Cobalt was added (alloy 141) as it could be beneficial in promoting coherency between the perovskite structure and the austenite matrix by changing the lattice parameter. Substitution of Fe or Mn should reduce the parameter of the ordered phase and, therefore, result in better lattice registry with the matrix.

The analyzed compositions of the alloys in this series are given in Table 56, which show that most of the values are close to the aim chemistries. However, relatively large deviations can be observed for several alloys in the austenite-perovskite series. Alloys 141 and 145 are about 0.5% Al deficient, and alloys 97 and 154, 0.6% C deficient relative to aim. The most serious deviations can be noted in alloy 143. These deviations will again be noted in subsequent sections.

TABLE 56. ANALYZED COMPOSITIONS OF ALLOYS Wt% Austenite-Perovskite Series

Alloy	Fe	Mn	Al	C	Other
97	Bal.	22.6	9.2	1.35	—
141	Bal.	18.2	8.4	1.93	5.2 Co
145	Bal.	—	7.0	2.12	—
142	Bal.	13.2	8.8	2.08	—
154	Bal.	29.9	9.1	1.45	—
143	Bal.	19.8	11.3	3.10	—
144	Bal.	22.6	7.7	2.04	—
146	Bal.	19.4	10.2	3.00	—
155	Bal.	30.0	9.2	2.04	1.0 Mo, 0.7 W

7450C

Workability

With the exception of alloys 143 and 155, all the alloys in the austenite-perovskite series were successfully rolled to 60% reduction at 2100°F (1150°C). Alloy 143 appeared to be extremely

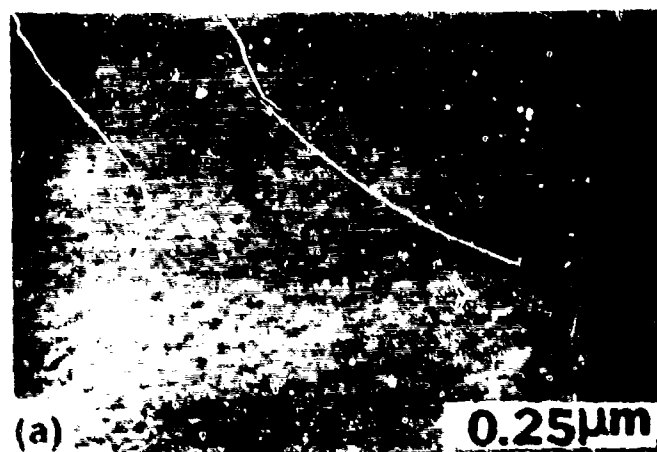
brittle as the ingot cracked during removal from the mold and again during heating prior to rolling. The basic causes for the poor workability of alloys 143 and 155 are unknown but the compositional factors can be observed from Table 55. By comparing alloy 143 with alloy 146, and alloy 155 with alloy 154 and with alloy 140, it is seen that the brittleness in alloy 143 can be attributed to an increase of Al content from 10.2 to 11.3%. In the case of alloy 155 the poor workability was probably attributable jointly to the high Al and C content and the refractory metal additions.

Microstructure

Because of its interesting microstructural characteristics and good creep resistance, the alloys in this series, Tables 55 and 56, were studied in more detail than alloys in other series. X-ray diffraction analyses revealed that, with the exception of alloy 145, the phases present in alloys of this series were predominantly austenite and perovskite carbide. The phases present in alloy 145 were determined to be ferrite and perovskite carbide. The formation of ferrite may not be unexpected in the absence of Mn, although the Fe-Al-C ternary phase diagram places this alloy composition within the austenite plus perovskite phase field at 1830°F (1000°C). This observation clearly shows that the equilibrium phases present in Fe-Mn-Al-C alloys include austenite, ferrite and perovskite carbide. Increasing the Mn content and/or higher temperatures favor formation of austenite over ferrite. Because of the poor creep resistance associated with formation of bcc structures, interest for high temperature applications centers on alloys containing higher Mn levels, typically over 20%.

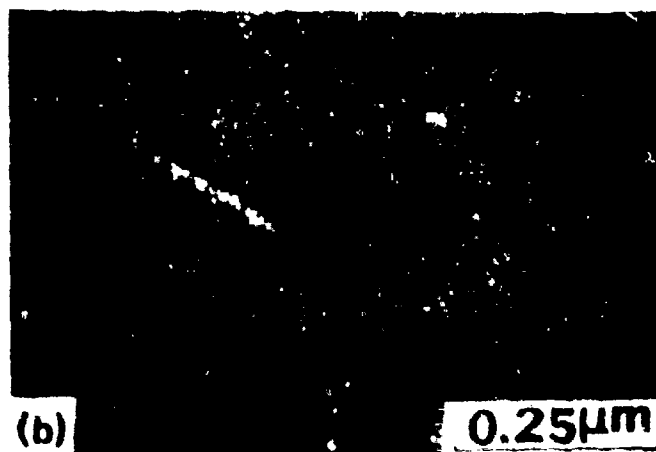
Although the phase structures of alloys in this series, with the exception of alloy 145 noted previously, are similar, the morphology and distribution of the perovskite carbides are rather different depending on the Mn content. The microstructures of high Mn alloys are typified by alloys 97, 154, and 155, and those for the low Mn alloys by alloy 142. In the following paragraphs the microstructures of these alloys will be described in detail.

Alloy 97, the baseline composition, was analyzed carefully with the objectives of elucidating the precipitation mechanism and optimizing heat treatment with respect to creep resistance. Figure 141 shows transmission electron micrographs of alloy 97 after a solution treatment of 2100°F (1150°C) for 5 minutes followed by quenching in oil. The alloy appears to be a single phase in the bright field micrograph, Figure 141a, but does exhibit superlattice reflections, Figure 141c, from an $L1_2$ -type lattice. Dark field imaging with a superlattice reflection (Figure 141b) clearly shows the presence of very fine ordered particles. Similar microstructural features were observed when alloy 97 was quenched from 1900°F (1040°C). These observations indicate that precipitation occurred during the quench, and at temperatures below 1900°F (1040°C). After solution and isothermal aging treatments at 1200°F (650°C) and 1400°F (760°C), a prominent microstructural feature of alloy 97, shown in Figure 142, is a discontinuous phase reaction occurring preferentially at grain boundary regions. The cellular colonies are shown in greater detail in Figure 142c. Microelectron diffraction analysis revealed that the structures of the constituent phases, Figure 143, comprising the colonies are disordered bcc (ferrite) and $L1_2$ -type (perovskite carbide). The precipitate within the grains in isothermally-aged materials are distributed homogeneously, and are crystallographically aligned, producing various tweed patterns shown by the secondary electron micrographs in Figure 144. Considerably more coarsening of the precipitate occurred at 1400°F (760°C), Figure 144b, than at 1200°F (650°C), Figure 144a. The morphology of the precipitate particles in the 1200°F (650°C) aged material, shown by the secondary electron micrograph and the dark field transmission electron micrograph in Figures 145a and 145b, respectively, appear to be rectangular and tend to coalesce preferentially along certain crystallographic directions which have been determined to be $\langle 001 \rangle$. Electron diffraction analysis showed that the particles are the perovskite carbide phase which precipitated coherently in the austenitic matrix. The cause for the poor contrast in Figure 145b is considered to be the coherency strain resulting from a large lattice mismatch between the austenite and the perovskite carbide phases (about 3%).



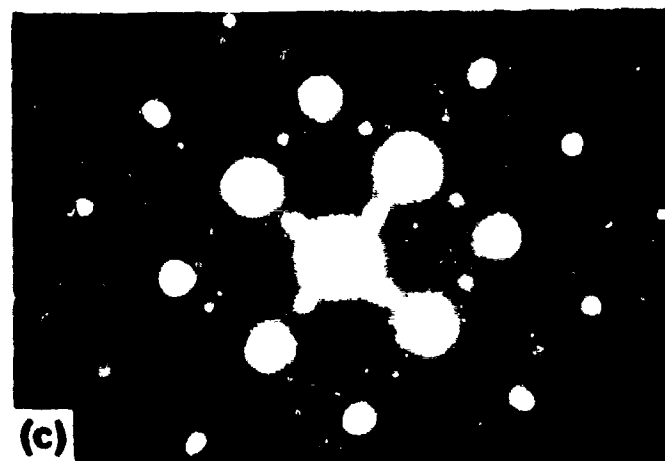
(a)

0.25μm



(b)

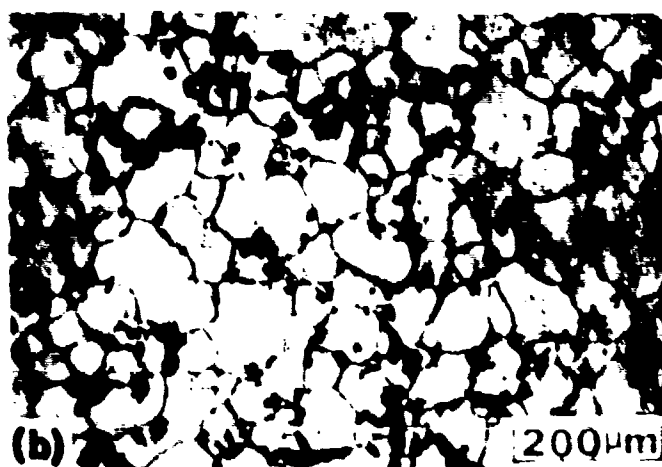
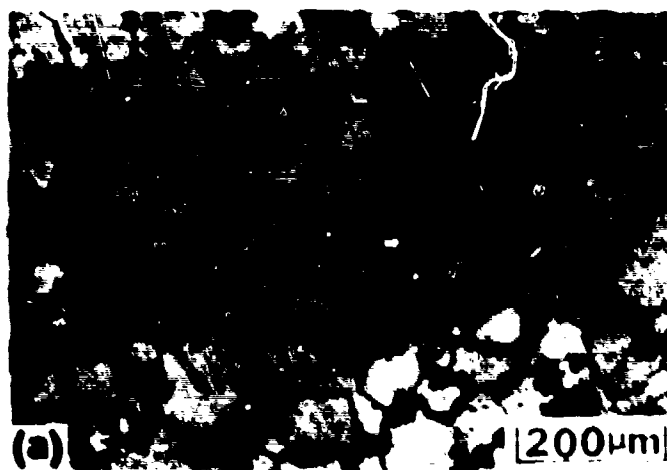
0.25μm



(c)

FD 318398

Figure 141. Electron Micrographs of Alloys 97 After a Solution Treatment at 1150°C (2100°F) for 5 Minutes Followed by Quenching in Oil. (a) Bright Field (b) Dark Field Using a Superlattice Reflection (c) Selected Area Diffraction Pattern, <001> Zone Axis



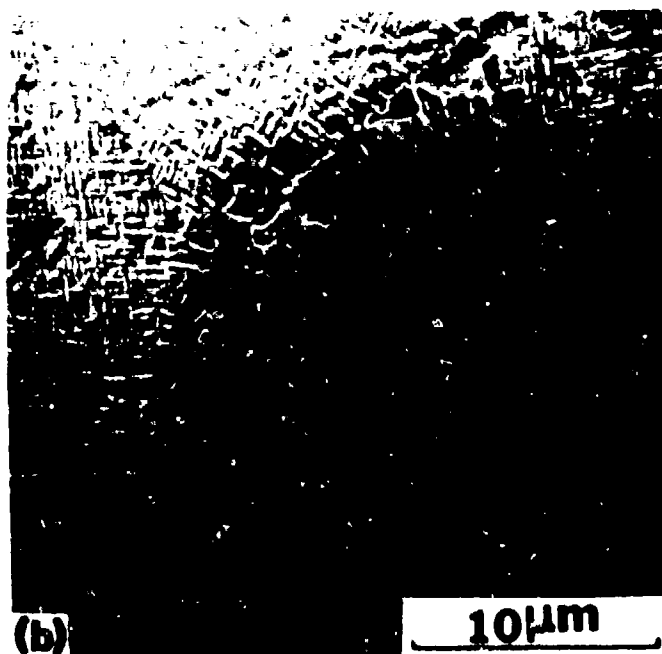
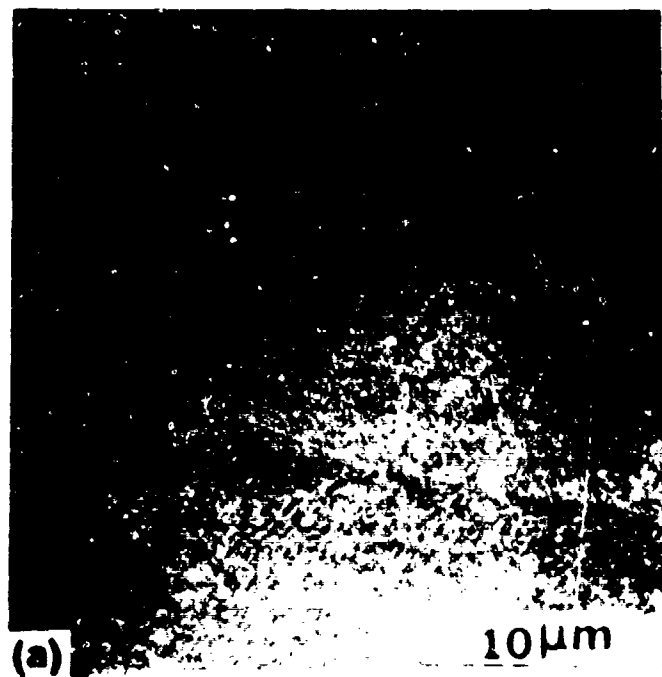
FD 318390

Figure 142. *Optical Micrographs of Alloy 97 After a Solution Treatment at 1150°C (2100°F) for 5 Minutes Followed by Quenching in Oil and Aging at (a) 650°C for 24 Hours (b) 760°C for 8 Hours (c) Illustrates the Grain Boundary Microstructure Resulting from Heat Treatments in (a) and (b)*



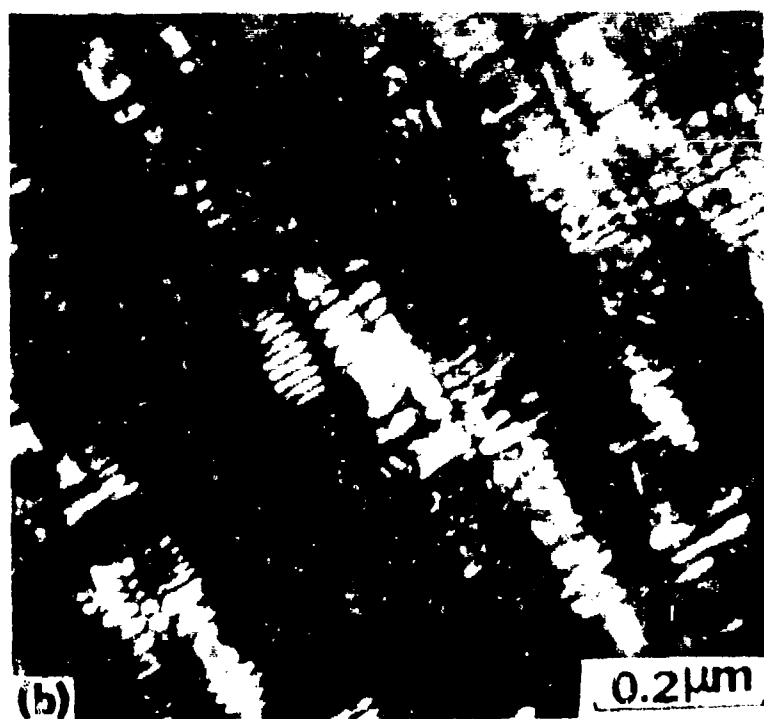
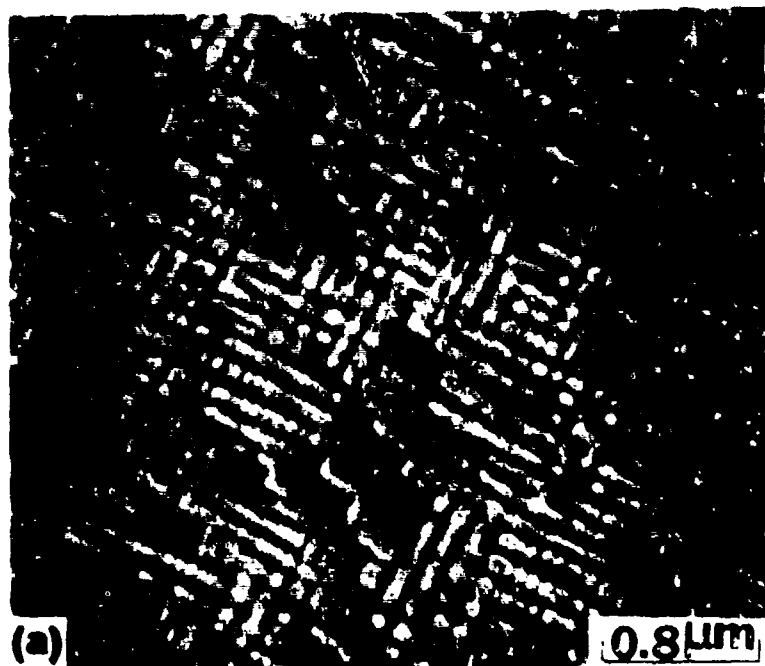
FD 318400

Figure 143. Electron Micrograph of the Lamellar Structure at Grain Boundary Regions in Alloy 97. The Dark and Light Phases Were Identified, Using Microelectron Diffraction Techniques, as Perovskite Carbide and Ferrite, Respectively



FD 318401

Figure 144. Secondary Electron Micrographs of Alloy 97 Illustrating the Modulated Phase Structures Resulting from Isothermal Aging Treatments at (a) 650°C for 24 Hours (b) 760°C for 8 Hours



FD 318402

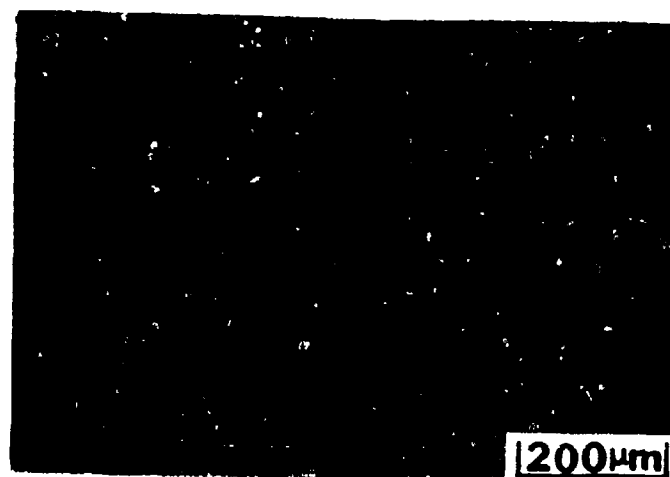
Figure 145. Micrographs of Alloy 97 After the 650°C/24 Hour Aging Treatment Illustrating the Modulated Phase Structure in Greater Detail (a) Secondary Electron Image Showing Square and Rectangular Cross Sections of the Perovskite Particles (b) Dark Field Transmission Electron Micrography Imaged With a Superlattice Reflection. The Perovskite Carbide Particles Are Aligned Along $\langle 001 \rangle$ Directions

The microstructural features and precipitation behavior described above and the structural similarity of the austenite and perovskite phases strongly suggest that the precipitation in alloy 97 is by spinodal decomposition. Further supporting evidence was reported most recently by Korean workers (Reference 16) who studied, using X-ray diffraction techniques, early stages of precipitation in Fe-Mn-Al-C alloys similar in composition to alloy 97. A sidebanding phenomenon characteristic of initial phase separation in spinodal systems was reported by these workers. It is therefore considered established that alloy 97 precipitates by a spinodal decomposition mechanism. From the limited heat treatment studies performed, the spinodal temperature of alloy 97 is estimated to be about 1850°F (1010°C).

The observation of discontinuous phase coarsening reaction in spinodal systems is not new. It has been reported in systems such as Cu-Ni-Fe (Reference 17) and Cu-Ni-Sn (Reference 18). The formation of a different phase mixture by the cellular transformation is not so common. However, the discontinuous precipitation behavior in spinodal systems appears to have a common origin, initially involving a loss of coherency with the matrix because of a large difference in lattice mismatch and/or composition. It is considered that controlling the wavelength of the phase separation will be important in achieving a large difference in composition without a loss of coherency and possibly suppressing the grain boundary reaction (Reference 17). DeFontain (Reference 19) and Ditchek (Reference 20) have developed a criterion for the loss of coherency in modulated structures. It requires that as the misfit between two adjacent phases increases, the spinodal wavelength necessary to maintain coherency decreases. Thus, it is predicted that short wavelengths allow the two phases to be coherent with a large difference in composition. To achieve this desired condition, one obvious method is simply to age the solution treated spinodal material at a low temperature for a long period of time. This method is usually impractical because an excessively long aging time is involved. As an alternative, a step-aging heat treatment was proposed by Kubarych et al. (Reference 17) which involves initially aging at a relatively high temperature for a short time sufficient for phase separation to be complete without coarsening of the spinodal microstructure. This aging procedure is repeated for successively lower temperatures. The proper aging time for each selected temperature in the aging sequence is determined, in separate experiments, by noting the age hardening response of the spinodal material. The step-aging treatment takes advantage of the fast diffusivities at high temperatures and drastically reduces the time to achieve a given phase separation compared with isothermal aging at a low temperature. A variation of the step-aging treatment, which is simpler in practice, is continuous cooling in a furnace with a reduced power level.

Based on the above considerations, alloy 97 was given a slow cool heat treatment consisting of a solution treatment at 1900°F (1040°C) for 10 minutes followed by cooling in the furnace to 1500°F (815°C) at an average rate of about 2.5°C per minute and air cooling from 1500°F (815°C) to room temperature. The furnace-cooled microstructure of alloy 97, illustrated by optical micrograph in Figure 146, appears to be a single-phase material because the modulated structure was too fine to be resolved. Such structures will be shown in detail later in derivative alloys 154 and 155. An important difference is the absence of discontinuous phase reaction in the furnace cooled material in strong contrast to the isothermally aged material (Figure 142). Although cellular microstructure was not present in alloy 97 after the furnace cool heat treatment, creep testing of the treated material at 1200°F (650°C) resulted in gradual formation of this microstructure, shown in Figure 147, during the test and led to deterioration of creep resistance. It was clear that heat treatment alone could not stabilize the spinodal microstructure in alloy 97 against the grain boundary cellular reaction. Since the grain boundary heterogeneity in alloy 97 involves an austenite-to-ferrite transformation, the creation of a more stable austenite could be considered beneficial. This was the reason for the selection of alloys 154 and 155 which contain a higher Mn content. Figure 148 shows the microstructures of alloy 154 after a solution treatment at 1900°F (1040°C) and after the furnace cool heat treatment. In the solution heat treated condition, the microstructure, Figure 148a, appears to be a single phase. Precipitation and

coarsening of particles at grain boundaries and within the grains are evident after the furnace cool heat treatment, Figure 148b. These particles, identified as perovskite carbide by electron diffraction, are shown in greater detail in the secondary electron image given in Figure 148c. The matrix of the furnace cool material consists of a very fine modulated austenite-perovskite structure illustrated by transmission electron micrograph shown in Figure 149a. Some coarsening of the modulated structure occurred heterogeneously during the furnace cooling and resulted in patches of $\langle 100 \rangle$ aligned arrays of cuboidal particles, Figure 149. To determine the stability of this higher Mn alloy against the grain boundary cellular reaction, the furnace cooled material was exposed at 650°C for 100 hours. The microstructure, illustrated in Figure 146, shows an apparent discontinuous precipitation reaction at grain boundary regions which is in fact coarsening of perovskite carbide particles. The blocky perovskite particles at grain boundaries and patches of coarsened modulated structure within the grains are shown in detail in Figure 150c. As will be shown later, the improved phase stability in alloy 154 leads to higher creep resistance.

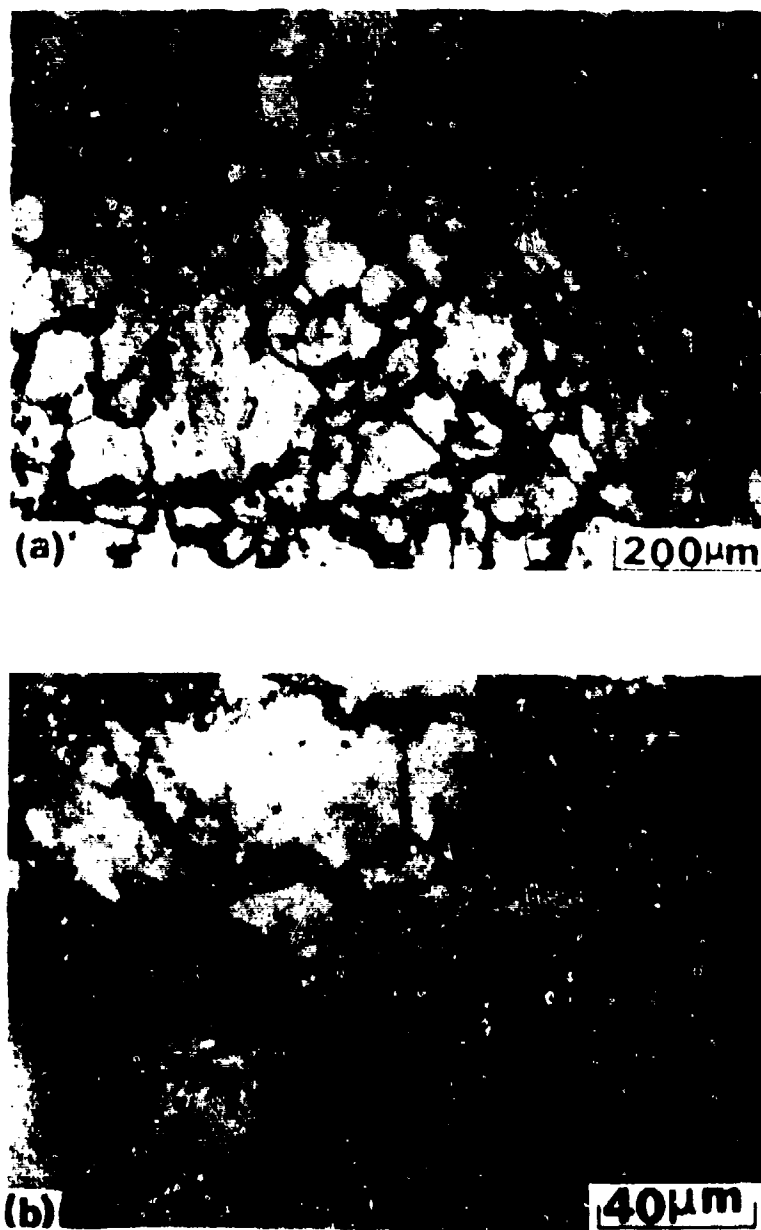


FD 318403

Figure 146. Optical Micrograph of Alloy 97 After a Furnace-Cool Heat Treatment from 1040°C to 815°C at an Average Rate of 2.5°C per Minute

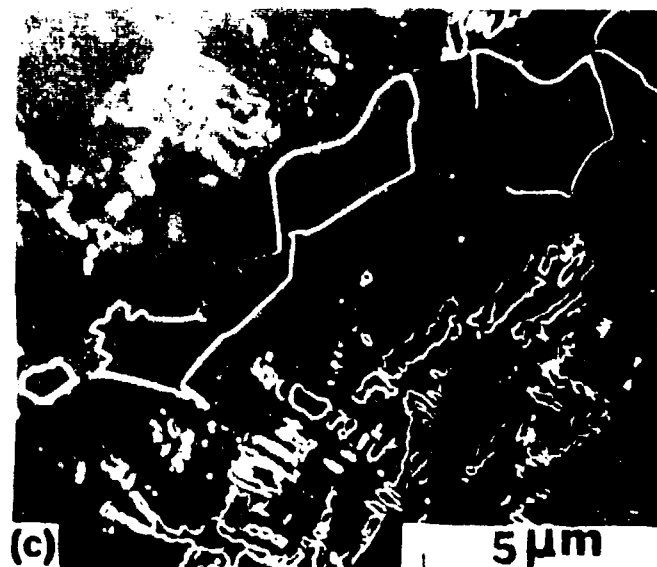
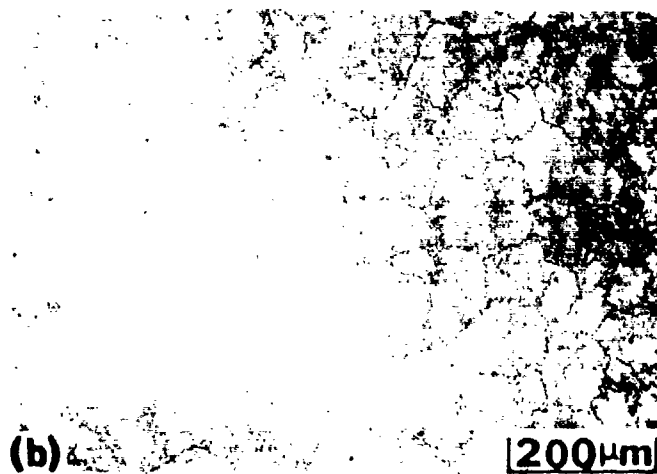
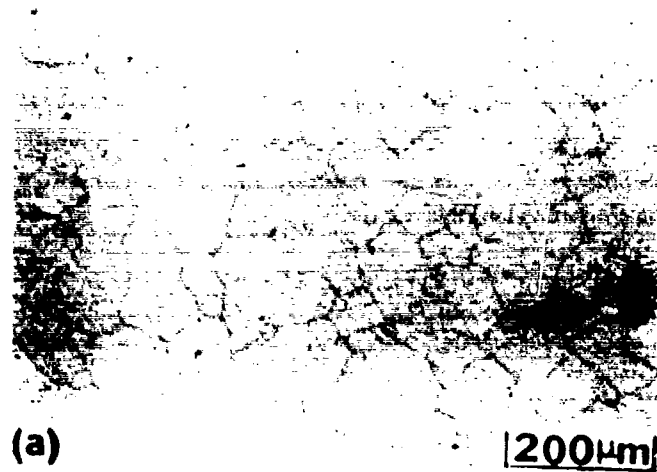
Alloy 155 has similar Mn content as alloy 154 but contains, in addition, small amounts of Mo and W. It was observed that the small refractory metal additions produced a significant increase in the spinodal temperature. This is evident from the microstructure of this alloy after the similar solution treatment as that for alloys 97 and 154. Instead of a single phase microstructure, a "basket weave" precipitate pattern shown in Figure 151a was observed probably as a result of coarsening of preexisting spinodal structure during the solution treatment. Solution treatment at 2000°F (1095°C), followed by oil quenching, showed a single phase structure Figure 151b. From the limited heat treatment studies conducted on this alloy, the spinodal temperature is estimated to be about 1950°F (1060°C), 125°F (50°C) higher than alloys 97 and 154. Consequently a higher solution temperature 2000°F (1095°C) was used for alloy 155, and the material was furnace cooled from this temperature to about 1500°F (815°C). The furnace-cooled microstructure is shown in Figures 152 and 153. A prominent "basket weave" microstructure is again observed which must have developed by coarsening of the spinodal structure during the furnace cooling. The various stages of coarsening of the modulated structure and coalescence of the coarsened particles to form $\langle 001 \rangle$ aligned arrays are shown in Figure 153. The rapid coarsening of the modulated structure in alloy 155 compared with alloy 97 and 154 is simply due to the higher temperatures, thus, faster diffusivities, involved during the furnace cooling. The amount of intragranular coarsening can be reduced, if deemed desirable, by

furnace cooling at a temperature lower than that for the solution treatment. The higher spinodal temperature in alloy 155 results in improved stability of the modulated structure at low temperatures and elimination of the cellular reaction. As will be shown, alloy 155 has the best creep resistance of all Fe-Mn-Al alloys tested.



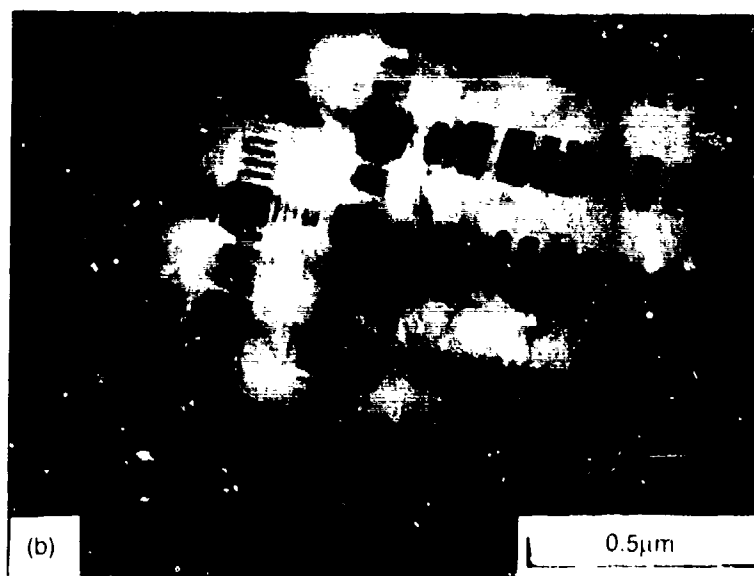
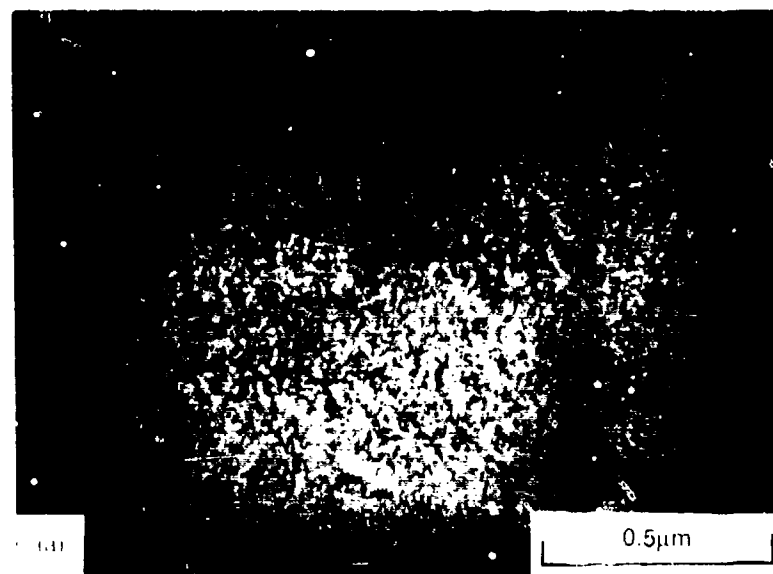
FD 318404

Figure 147. Optical Micrographs of Alloy 97 After the Furnace-Cool Treatment Described in the Preceding Figure with Additional Exposure at 650°C for 50 Hours. Note the Presence of Lamellar Colonies at Grain Boundary Regions Which Were Produced During the 650°C Exposure



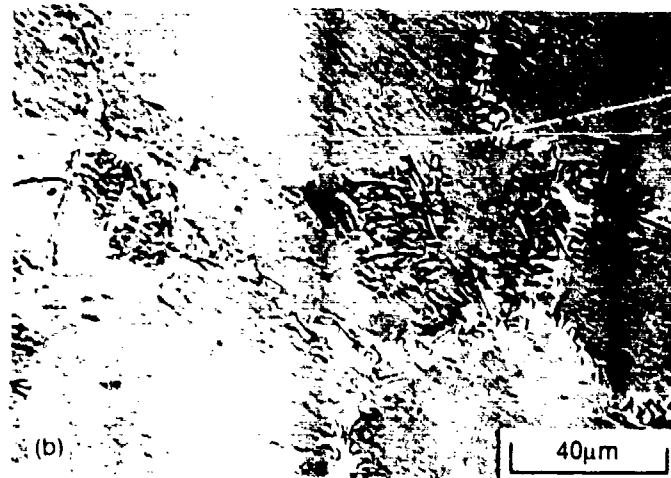
FD 318405

Figure 148. *Microstructures of Alloy 154 After Solution Treatment of 1040°C/1h/OQ (a), Reheated to 1040°C and Furnace Cooled to 815°C at an Average Rate of 2.5C per Minute (b) (c) Detailed Microstructure Resulting from Heat Treatment (b) Illustrating the Blocky Perovskite Carbide at Grain Boundary Regions and Coarsening of the Modulated Structure in Certain Regions Within the Grains*



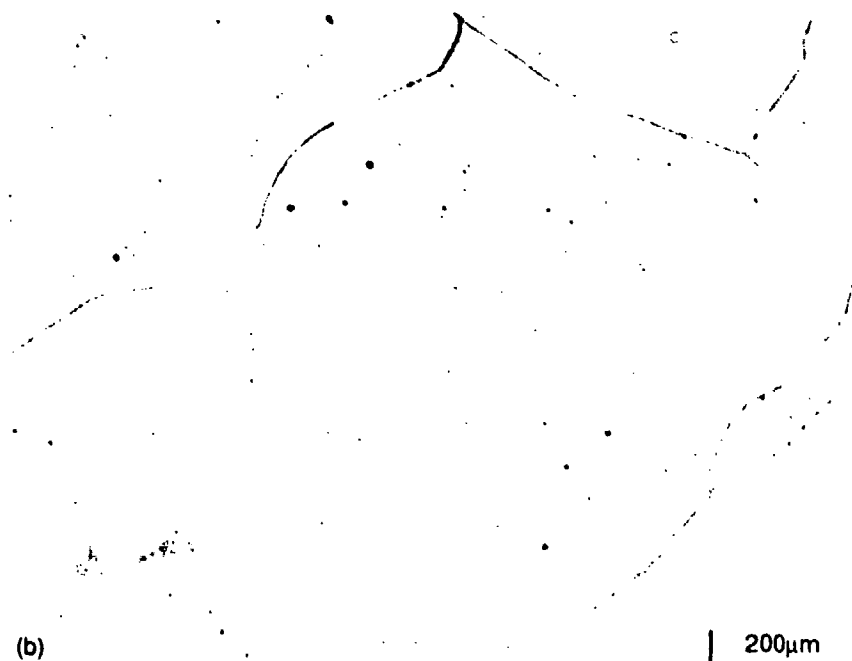
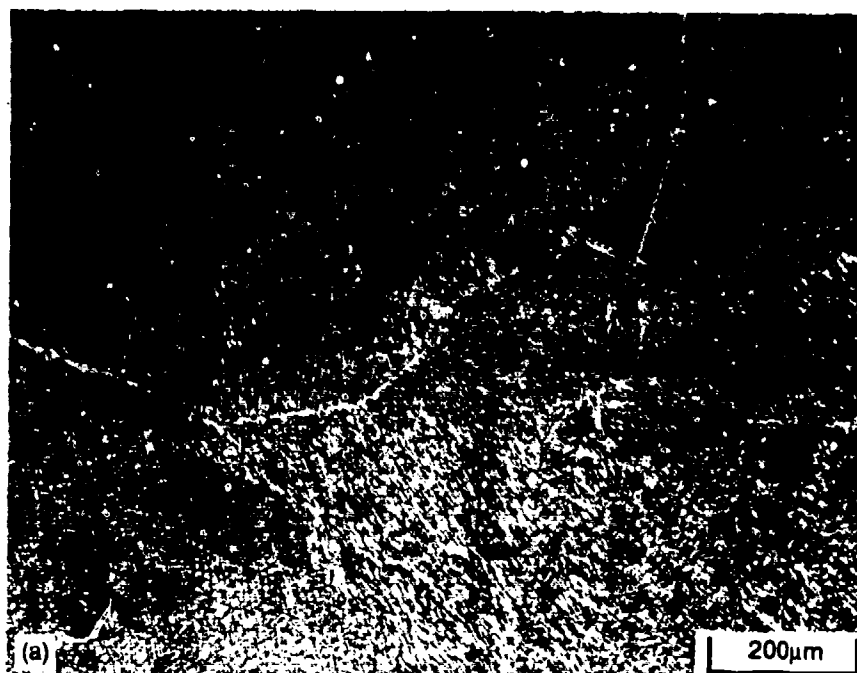
FD 318406

Figure 149. *Transmission Electron Micrographs of Alloy 154 After the Furnace Cool-Heat Treatment Described in the Preceding Figure Illustrating (a) the Very Fine Modulated Structure Produced in the Grains (b) Coarsened Modulated Structure in Certain Regions of the Grains Shown in the Preceding Figure*



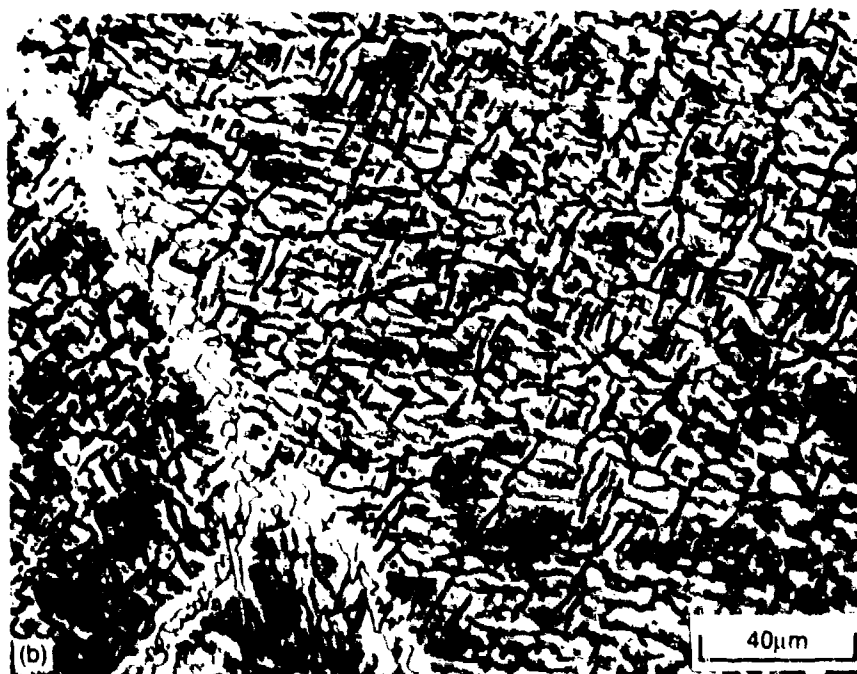
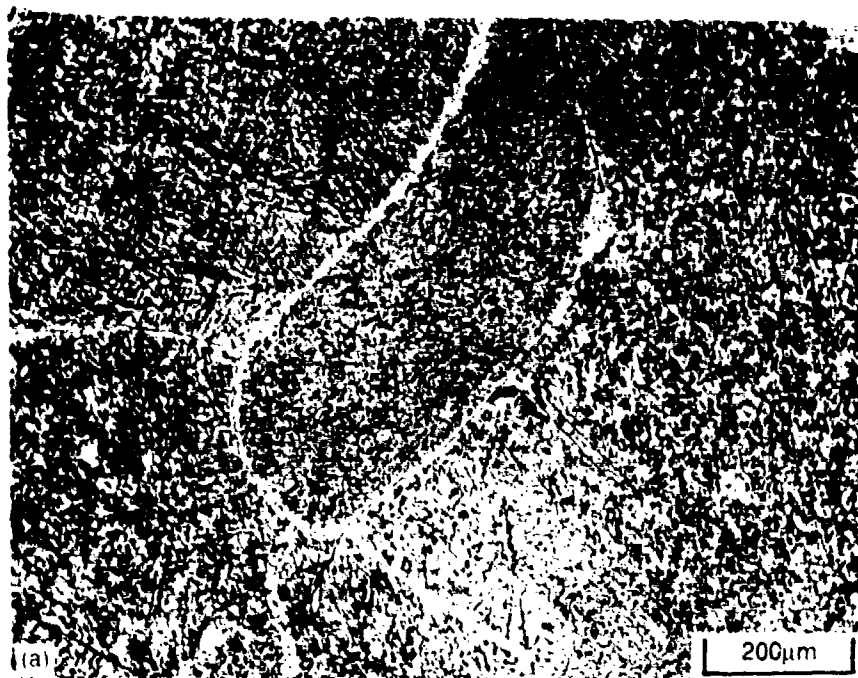
FD 318407

Figure 150. *Microstructure of the Furnace-Cooled Alloy 154 After Additional Exposure at 650°C for 100 Hours. The Apparent Discontinuous Precipitation at Grain Boundary Regions Shown in (a) and (b) Is in Fact Coarsening of Perovskite Carbide Particles. (c) Illustrates the Blocky Perovskite Carbide at Grain Boundaries and Extensive Coarsening of the Modulated Structure*



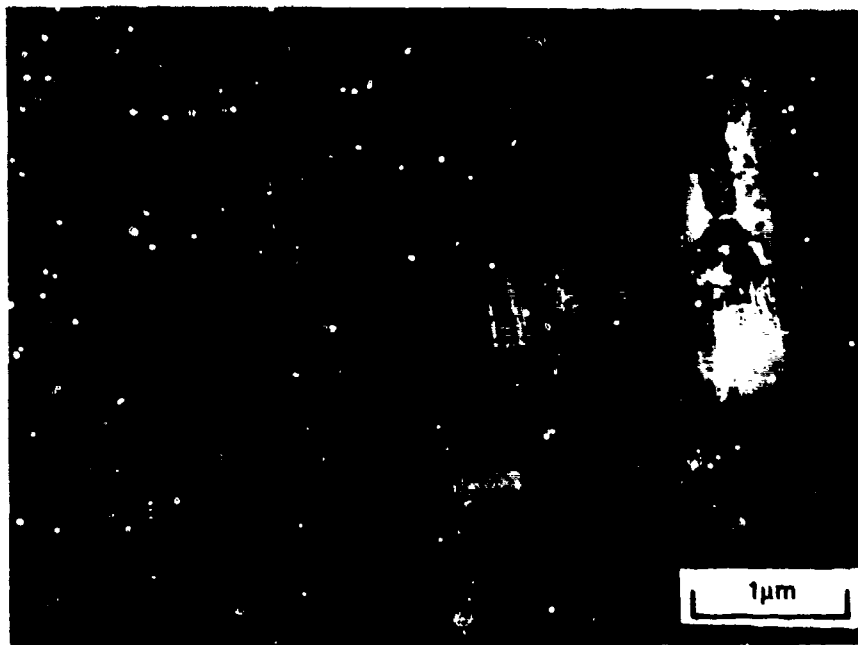
FD 318408

Figure 151. *Microstructures of Alloy 155 After (a) "Solution" Treatment of 1040°C/1h/OQ
(b) Solution Treatment of 1095°C/1h/OQ*



FD 318409

Figure 152. *Microstructure of Alloy 155 After Heat Treatment at 1095°C for 1 Hour Followed by Cooling to 815°C at an Average Rate of About 2.5°C Per Minute. Note the Rapid Coarsening of the Modulated Structure During the Slow Cooling from 1095°C*



FD 318410

Figure 153. *Transmission Electron Micrograph Illustrating the Modulated Structure in Alloy 155 After the Slow-Cool Heat Treatment Described in the Preceding Figure*

At the other end of the microstructural spectrum in the austenite-perovskite series is the highly uniform microduplex structure exhibited by alloy 142 after the furnace cool heat treatment (Figure 154). The perovskite particles have an equiaxed shape and are located preferentially at the austenite grain boundaries. The particle/grain diameter is about 10 microns. The reasons for the formation of a microduplex structure in alloy 142 are not completely clear. Similar microstructure has been observed in a Cu-Ni-Fe spinodal material which was rolled and annealed, in which the formation of the microduplex structure was attributed to: (1) coarsening and coagulation of Ni-rich phases, and (2) subsequent recrystallization in areas depleted of Ni which are free of the modulated structure (Reference 21). A lower spinodal temperature in alloy 142 due to the lower Mn content may have contributed to the formation of this structure.

Mechanical Properties

A heat treatment study was conducted on selected alloys in the austenite-perovskite family to maximize the creep resistance. The selected heat treatment was then used throughout in the subsequent study of compositional effects. Two types of heat treatment were conducted: (1) solution treatment and quenching followed by an isothermal age, or (2) slow cooling from the solutioning temperature. It was considered that the latter heat treatment would promote coherency of the spinodal structure at large phase separation. The first type of heat treatments studied included a solution treatment at either 2100°F (1150°C) for 5 minutes or 1900°F (1040°C) for 1 hour followed by quenching in oil and aging isothermally at temperatures ranging from 1200 to 1700°F (650°C to 925°C). For the second type of heat treatment, material was cooled slowly from 1900°F to 1500°F (1040 to 815°C) at an average rate of 2.5°C per minute. The influence of heat treatment on creep properties is shown in Figure 155 for alloy 9/ and Figure 156 for alloy 141. For both alloys, the creep resistance increases with increasing aging temperature, but the best properties are found after the slow cool treatment. Similar results were obtained for alloys

144 and 146. The poorer creep resistance of the materials after isothermal age, especially at 1200 to 1500°F (650 to 815°C), may well be associated with the presence of ferrite produced during aging as a result of discontinuous precipitation reaction at grain boundary regions, Figure 142. The kinetics of such reaction in solution treated alloy 97 was determined to be most rapid at these temperatures. Likewise, the onset of tertiary creep in the furnace-cooled or solution-treated materials may also be traced to formation of a critical amount of ferrite at grain boundary regions during the creep test at 1200°F (650°C). It is also of interest to compare the creep behavior of alloy 97, shown in Figure 155, in the solution treated and quenched condition with that of the furnace-cooled material. The initial slow creep rates of materials in either condition are attributed to austenite-perovskite structures; the creep rates accelerate as a critical amount of ferrite is produced at grain boundaries. The better phase stability of the furnace-cooled material, as evidenced by the prolonged secondary creep stage, may be attributed to a larger amount of phase separation which had occurred during the furnace-cooling heat treatment, reducing the propensity for the discontinuous precipitation.

Using the slow-cool aging treatment defined above, the effects of Mn, Al and C contents on creep resistance of the austenite-perovskite alloys were evaluated. The effect of Mn on creep behavior can be observed readily by comparing the results from alloys 145 (0 wt% Mn), 142 (13 wt% Mn), 146 (19 wt% Mn), 97 (22 wt% Mn); and 154 (30 wt% Mn) shown in Figure 157. Although there are differences in the Al and C contents among the alloys being compared, there is no doubt that creep resistance clearly increases with increasing Mn content. Some of the beneficial effect of the Mn may be simply attributed to its austenite stabilizing tendency as indicated in the preceding section. Another effect of Mn is on the grain structure, morphology and distribution of the perovskite phase. Low Mn alloys tend to exhibit fine grains and equiaxed perovskite carbide distributed at austenite grain boundaries, Figure 154. In contrast, the high Mn alloys have considerably coarser grains and the perovskite carbide particles are distributed homogeneously in the grains, Figure 150; both of these microstructural features contribute to creep resistance. The Al or C effect cannot be evaluated independently from the present set of alloy compositions. However, it is interesting to compare for a given Mn content the creep behavior of alloy 144 (7.7 wt% Al, 2 wt% C) with alloy 97 (9.2 Al, 1.4C) shown in Figure 158. It can be observed that the high Al-low C combination imparts better creep resistance than low Al-high C combination.

The effects of alloying with Co, Mo, and W on creep behavior can be observed by comparing results of alloy 141 (5% Co) with those of alloys 144 and 155 (1% Mo + 0.7% W) with alloy 154 as shown in Figure 159. It appears that the additions of both the Co and the refractory metals have a beneficial effect on creep resistance, if the effects arising from variations in Al and C contents could be considered secondary in making these comparisons. The creep resistance and stability of alloy 155 is especially remarkable.

Strength and ductility in the austenite-perovskite alloys were explored using compressive yield tests over a range of temperatures and bend tests at room temperature as a measure of low-temperature ductility. An alloy is considered ductile if it can be bent through 180 degrees without fracture. Alloys selected for evaluation were given the same heat treatments as those for the microstructural studies. Results shown in Figure 160 indicate that the base alloy 97 is ductile in as-solution heat treated condition and after the slow cool or the 1400°F (760°C) isothermal aging treatment. However, the alloy fractured with only limited ductility when aged at 1200°F (650°C) which also resulted in the highest hardness. As shown in Figure 161, the fracture occurred intergranularly. Alloy 154 was tested in bending in two aging conditions: (1) slow cool, and (2) slow cool plus additional aging at 1200°F (650°C) for 100 hours. The ductility was observed to be limited under both conditions, and the fracture mode is intergranular in the case of the slow-cool aging, Figure 162a, and transgranular with the additional isothermal aging, Figure 162b. A

possible reason for the change in fracture mode can be deduced from Figure 162a, which also shows some cracking of the large perovskite particles at grain boundaries indicating the brittle nature of the perovskite carbide phase. Since the additional isothermal aging resulted in considerable coarsening of the perovskite carbide throughout the microstructure (and hence the transgranular fracture), these observations suggest that ductility in an alloy 154-type microstructure may be achieved by: (1) minimizing the amount of coarse perovskite particles at grain boundaries, (2) stabilizing the perovskite phase against coarsening, and (3) modifying thermal processing. Alloy 142, treated in the slow-cool aging condition only, shows a rather different mode of fracture consisting of ductile failure in the austenite grains and cleavage fracture in the perovskite particles, Figure 163. These fracture features resulted from a microduplex phase distribution in this alloy shown in Figure 154. The yield strengths of alloys 142, 154, and 155 at various temperatures are shown in Figure 164 along with A286 for comparison. The yield strength of alloy 142 is highest at room temperature 1610 MPa (234 ksi), but decreases rather rapidly with increasing temperature to 415 MPa (60 ksi) at 1200°F (650°C). The yield strengths of alloys 154 and 155 are higher than A286 for temperatures up to about 1200°F (650°C) and the temperature dependence appears to be similar in these three alloys which is considerably lower than that in alloy 142. The rapid decrease in strength with increasing temperature in the case of alloy 142 may be attributed to its fine grain size (~10 microns).

Fe-Mn-Al-C Alloys — Third Series

The studies conducted on the second alloy series have led to several advances as described in the preceding section. Significant strength and creep resistance improvements have been achieved in this type of alloy by microstructural control through a slow-cool heat treatment which allows large phase separation in the modulated structure without loss of coherency. This minimizes the discontinuous grain boundary cellular reaction which was shown to be detrimental to creep resistance. The use of high manganese levels to stabilize the austenite against transformation to ferrite has also been found to increase creep capability. The addition of small quantities of refractory metals, 1 Mo+0.5W (wt%) which increase the spinodal temperature thereby improving the thermal stability at low temperatures, is also an effective approach. The latter observation suggested that further creep performance improvement of this type of alloy may be achieved by more extensive alloying additions. For this purpose, a series of alloys, shown in Table 57 has been formulated for studies. The base alloy 168, contains 33 wt% Mn, 8 wt% Al, and 2 wt% C. The level of alloying additions that could be studied was restricted, since it was observed during the first year of this program that an ordered bcc phase with B2-type structure was formed in preference to the perovskite carbide when Cr, Si, Ni were added in moderate amounts (2 to 5 wt%). This ordered bcc compound reduced the creep resistance dramatically. To reduce the risk of more radical perturbations of the system, carbide formers are added in small quantities, 0.5 wt% and singly so that individual effects could be identified. The austenite stabilizers were also added singly, but in larger quantities, 1.5 wt%.

The alloys were produced as castings which were sectioned and one piece of each alloy was heated to 1150°C (2100°F) and, where possible, rolled on 130 mm diameter unheated rolls to about 60% reduction in thickness. Intermediate reheating after each 7% reduction was employed to facilitate processing.

The analyzed compositions of this series of alloys, given in Table 58, show no major deviations from the nominal compositions except for alloy 166, in which the Si content is 46% lower than aim. Hot rolling of the cast ingots proved to be difficult as most fractured during rolling at 2100°F (1150°C). (Most recent work has shown that this type of alloy can be extruded successfully in stainless steel containers coupled with a carefully controlled process cycle.) Consequently, only cast material was evaluated. Prior to testing, the castings were given a homogenization heat treatment of 2100°F (1150°C) for 72 hours under a partial pressure of

argon. The homogenized materials were then reheated to 2000°F (1095°C) for 15 minutes, furnace cooled to 1500°F (815°C) followed by cooling in air. The slow cooling promotes large phase separation which has been shown to produce superior creep resistance among the various heat treatment cycles evaluated previously.

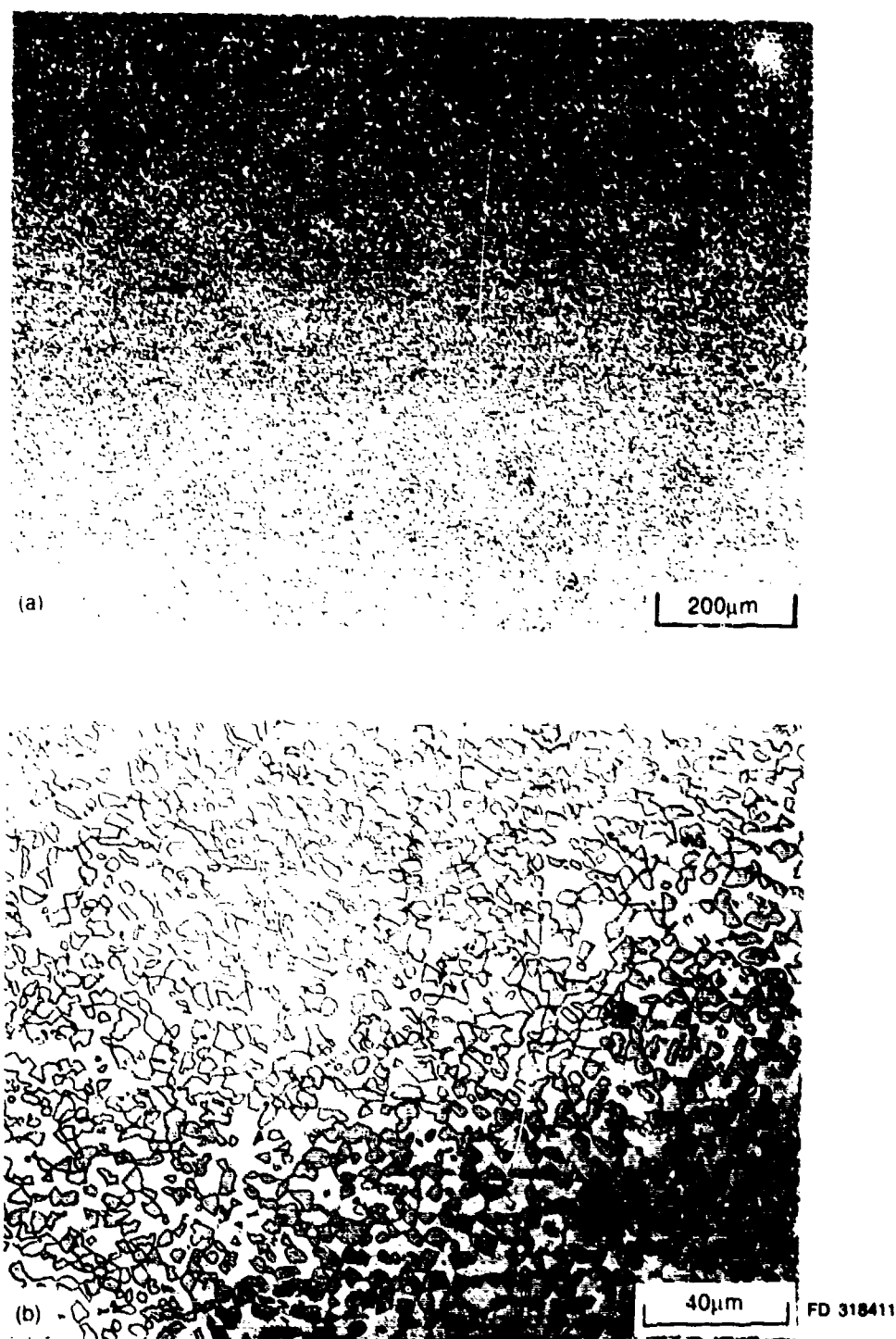
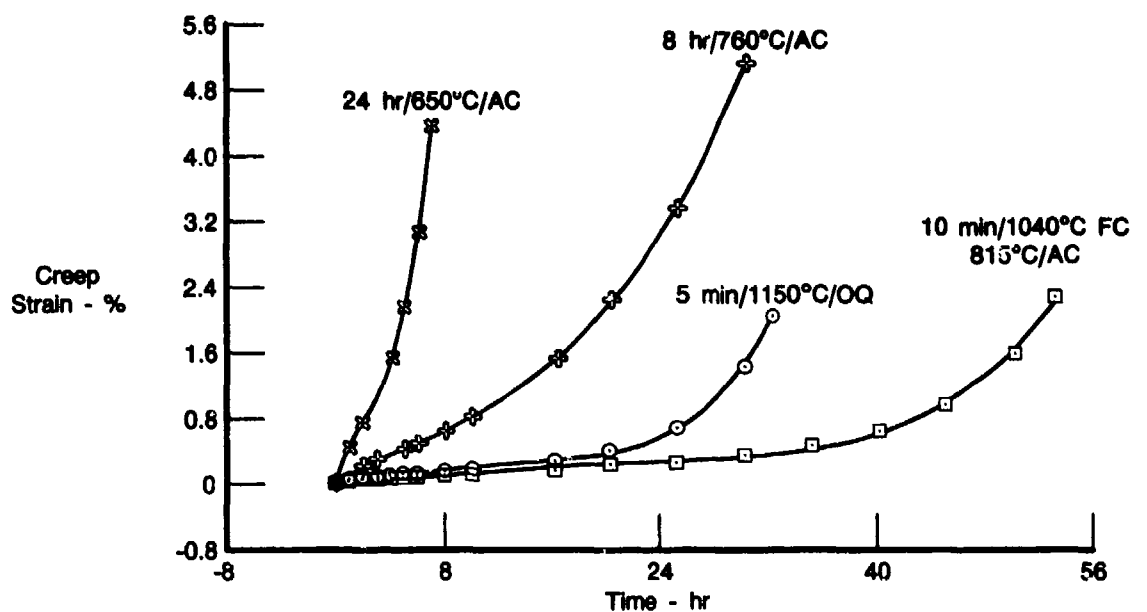
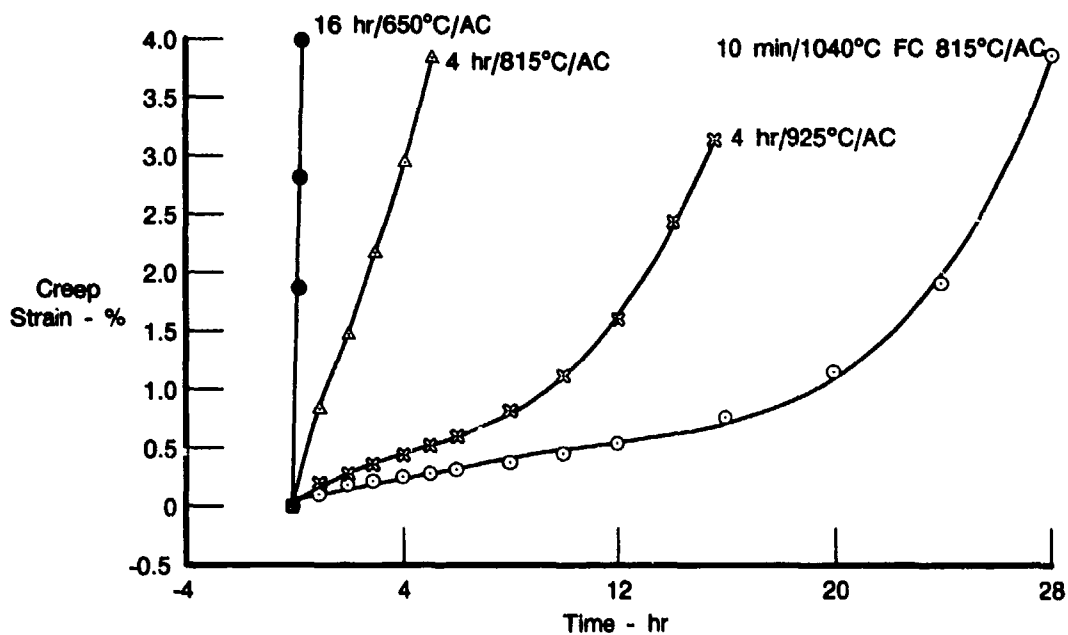


Figure 154. Microduplex Structure Consisting of Perovskite Particles and Austenite Grains Observed in Alloy 142 After Heat Treatment at 1040°C for 10 Minutes Followed by Cooling to 815°C at an Average Rate of 2.5°C Per Minute



FDA 318412

Figure 155. Creep Behavior of Alloy 97 at 650°C and 293 MPa After Various Aging Heat Treatments Indicated. Solution Heat Treatment 1150°C/5 min/OQ



FDA 318413

Figure 156. Creep Behavior of Alloy 141 at 650°C and 293 MPa After Various Aging Heat Treatments Indicated. Solution Heat Treatment 1040°C/1h/OQ

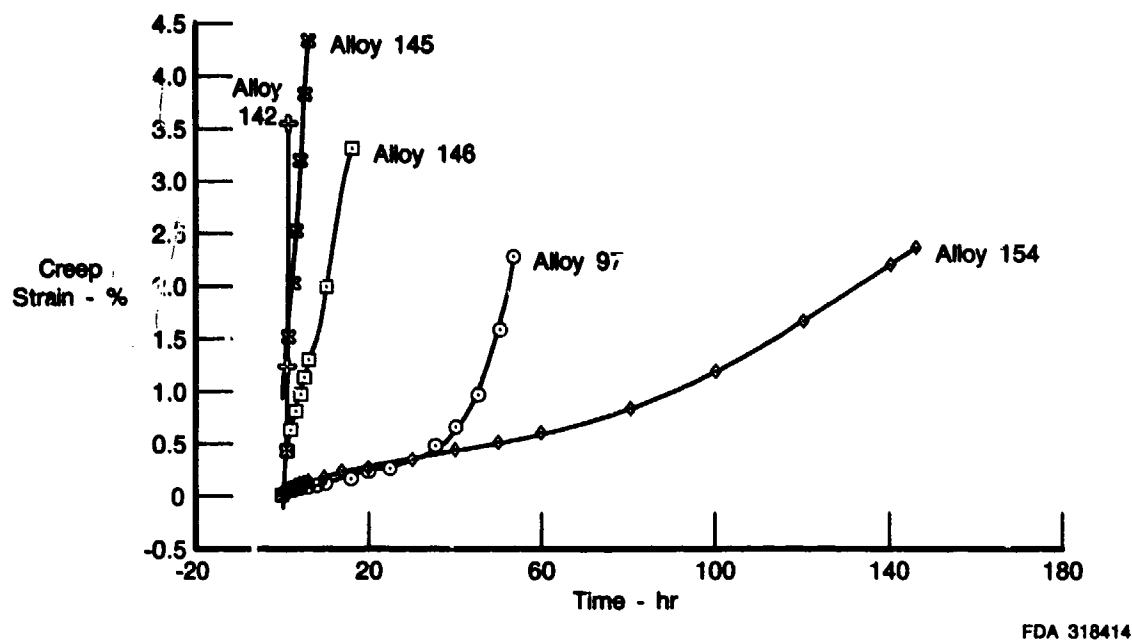


Figure 157. Creep Curves of Alloys 97, 142, 145, 146 and 154 at 650°C and 293 MPa Illustrating the Effect of Mn on Creep Resistance

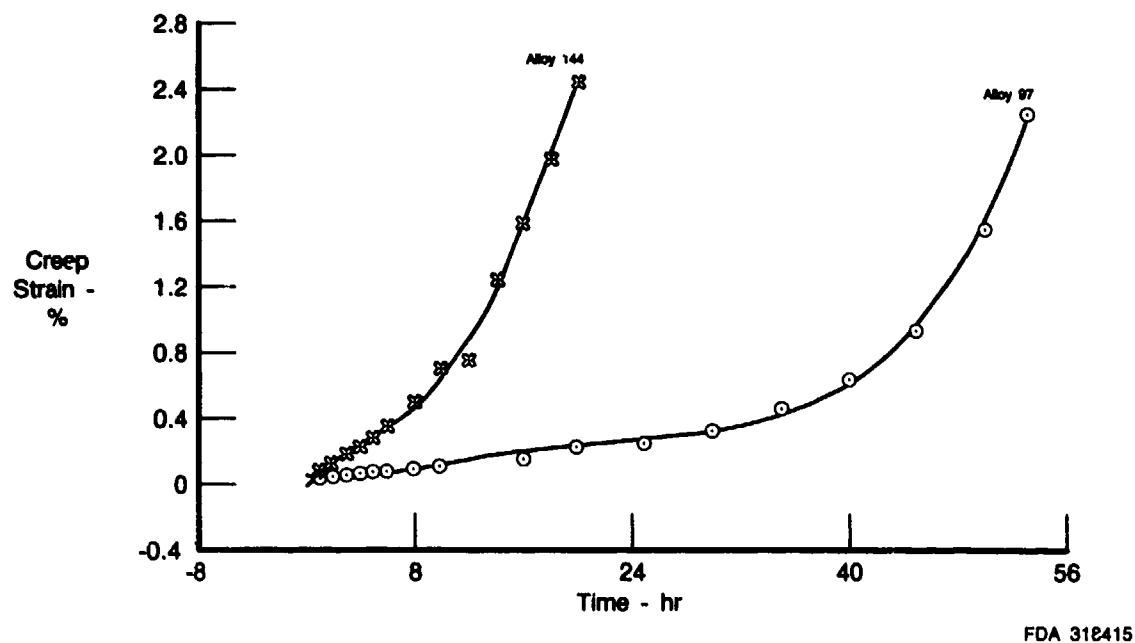
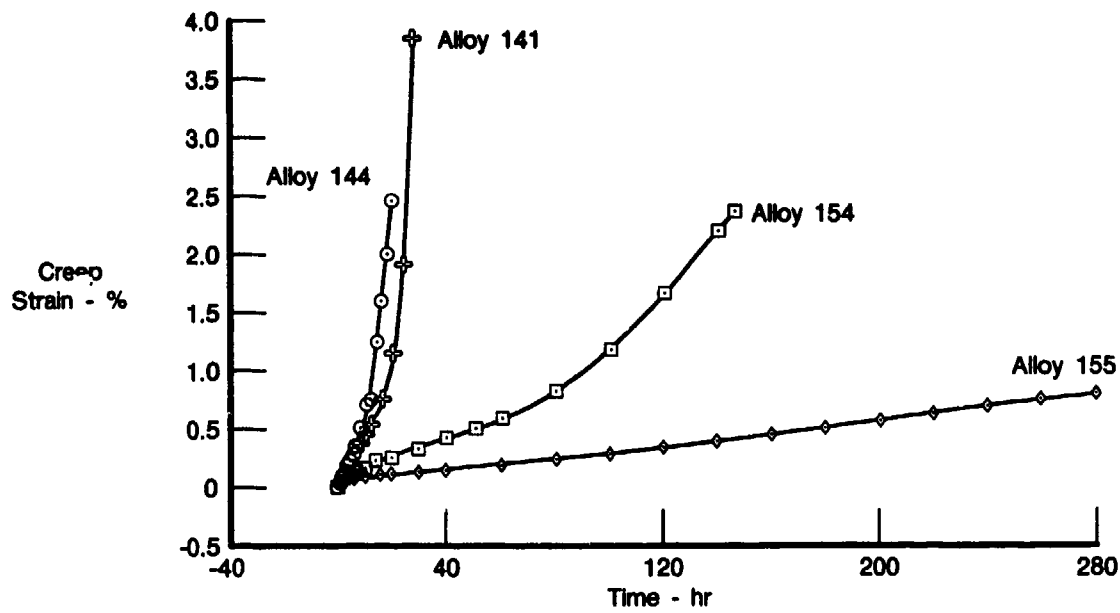
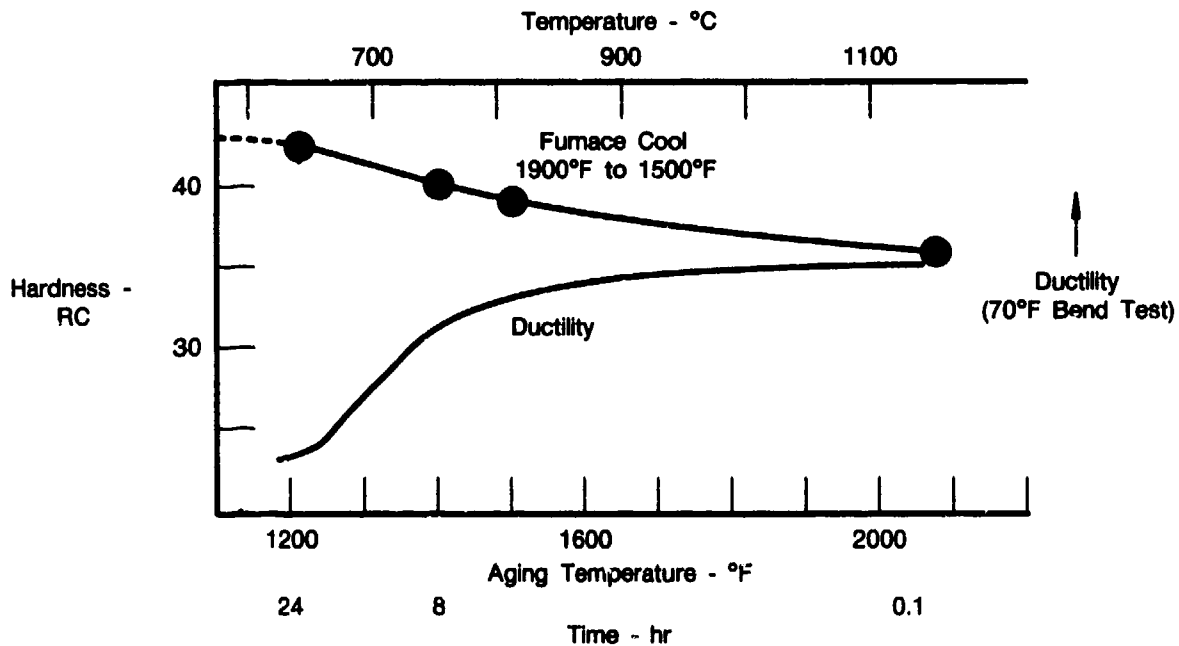


Figure 158. Creep Curves of Alloys 97 and 144 at 650°C and 293 MPa Illustrating the Effect of Two Different Combinations of Al and C Contents on Creep Resistance



FDA 318416

Figure 159. Creep Curves of Alloys 141, 144, 154 and 155 at 650°C and 293 MPa Illustrating the Affects of Co and Refractory Metals Additions on Creep Resistance



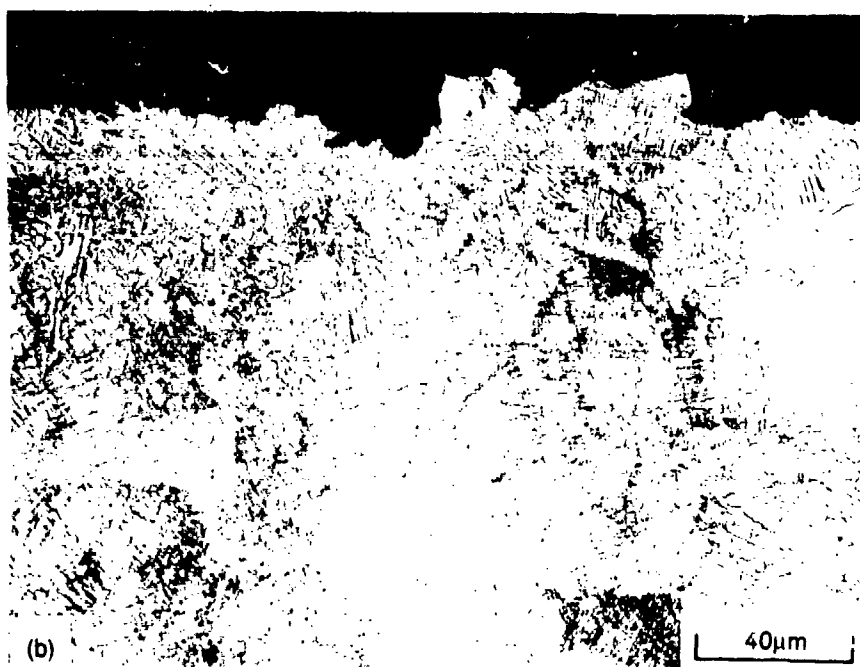
FDA 318417

Figure 160. Hardness and Room Temperature Bend Ductility of Alloy 97 After Various Heat Treatments



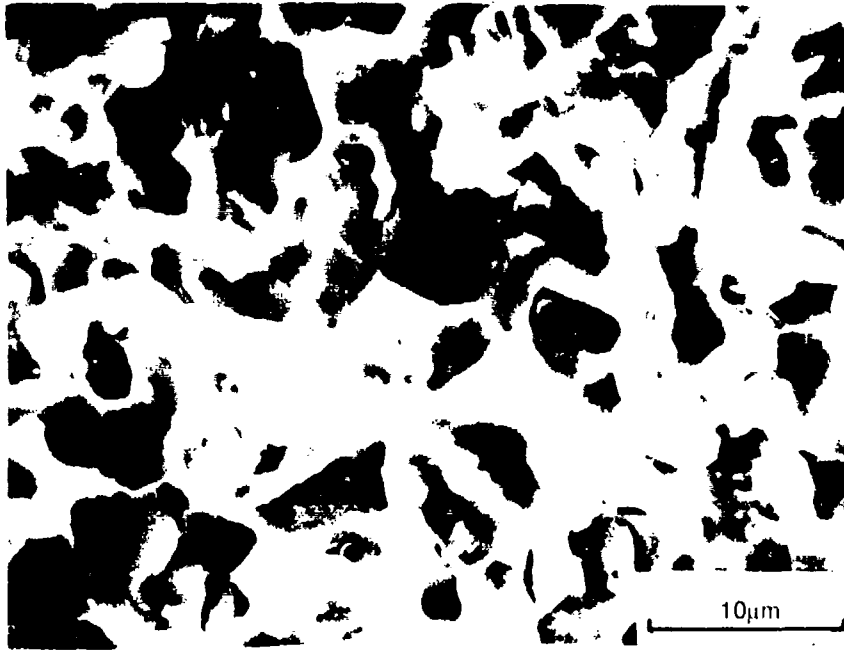
FD 318418

Figure 161. Fracture Features of Alloy 97 in a Room Temperature Bend Test. Heat Treatment: 1150°C/5 min/OQ+ 650°C/24h/AC



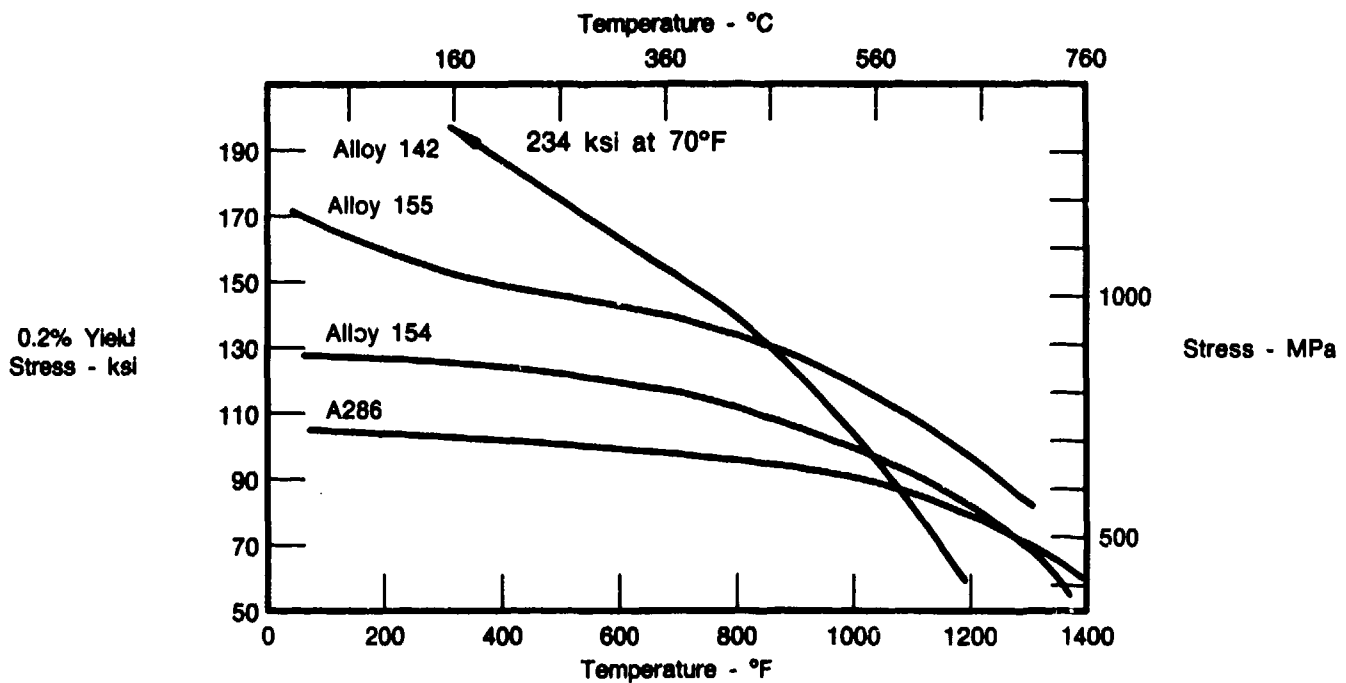
FD 318419

Figure 162. *Fracture Features of Alloy 154 in a Room Temperature Bend Test. Heat Treatment: (a) 1040°C/10 min/Cooled to 815°C at a Rate of 2.5°C/min Followed by Cooling to Room Temperature in Air (b) Heat Treatment as in (a) Plus Isothermal Aging at 650°C for 100 Hours*



FD 318420

Figure 163. Fracture Surface Features of Alloy 142 in a Room Temperature Bend Test. Heat Treatment: 1040°C/10 min/Cooled to 815°C at a Rate of 2.5°C/min Followed by Cooling to Room Temperature in Air



FDA 318421

Figure 164. 0.2% Yield Strengths of Alloys 142, 154, and 155 and the Iron-Base Superalloy A286

TABLE 57. NOMINAL COMPOSITIONS OF Fe-Mn-Al-C ALLOYS, Wt%

<i>Alloy</i>	<i>Fe</i>	<i>Mn</i>	<i>Al</i>	<i>C</i>	<i>Other</i>
156	Bal	33	8	2	0.5Ti
157	Bal	33	8	2	0.5Zr
158	Bal	33	8	2	0.5Hf
159	Bal	33	8	2	0.5V
160	Bal	33	8	2	0.5Cr
161	Bal	33	8	2	0.5Mo
162	Bal	33	8	2	0.1W
163	Bal	33	8	2	0.1Co
164	Bal	33	8	2	0.5Ni
165	Bal	33	8	2	0.5Cu
166	Bal	33	8	2	0.5Si
167	Bal	33	8	2	0.5Mo + 0.020B
168	Bal	33	8	2	—

7480C

TABLE 58. ANALYZED COMPOSITIONS OF Fe-Mn-Al-C ALLOYS, Wt%

<i>Alloy</i>	<i>Fe</i>	<i>Mn</i>	<i>Al</i>	<i>C</i>	<i>Other</i>
156	Bal	33.5	7.8	2	0.62Ti
157	Bal	33.8	8.2	2	0.41Zr
158	Bal	33.1	8.2	2	0.45Hf
159	Bal	33.9	7.8	2	0.58V
160	Bal	33.2	8.2	2	0.67Cr
161	Bal	34.4	7.7	2	0.55Mo
162	Bal	34.2	7.6	2	0.76W
163	Bal	34.4	7.6	2	1.60Co
164	Bal	33.8	8.2	2	1.59Ni
165	Bal	32.5	8.3	2	1.58Cu
166	Bal	33.8	8.2	2	0.27Si
167	Bal	33.5	8.2	2	0.041B + 0.54Mo
168	Bal	34.0	7.7	2	—

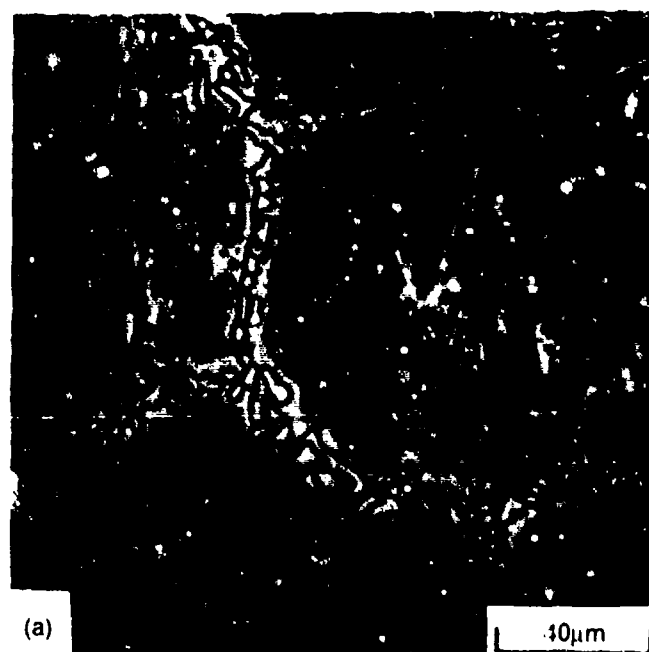
7480C

Microstructure (Alloys 156-168)

Important microstructural features of this type of alloy have been established in preceding sections. Basically the microstructure of the Fe-Mn-Al-C alloys of interest consists of uniformly distributed perovskite carbide particles precipitated in the austenitic matrix. The size of these perovskite carbide particles depends on heat treatment. In particular, with the selected slow-cool heat treatment at 2000°F (1095°C) which is below the carbide solvus, coarsening of the primary carbide particles and precipitation of fine particles occur simultaneously during the slow cooling. The cooling perovskite carbide particles are submicron in size and coherent with the matrix. Particle coarsening occurs by growth and coalescence mechanisms. The coarsened particles tend to be rectangular in shape with sides aligned along <001> directions. Coarsening of the perovskite carbide is accompanied by a gradual loss of lattice coherency with the matrix.

The microstructure of the base alloy 168 is presented in Figure 165a, and those with alloying addition in Figures 165b to 165m. The phase structures of some of these alloys were determined using X-ray powder diffraction technique. Results, given in Table 59, show that the major phases present are austenite and perovskite carbide, confirming the expectation that small alloying additions would not change the phase balance in the base composition. The microstructure of the base alloy, Figure 165a, consists of coarsened primary perovskite carbide particles distributed intragranularly and at grain boundary regions. The intragranular particles appear to be rod-like with some preferred alignment, and those at the grain boundary

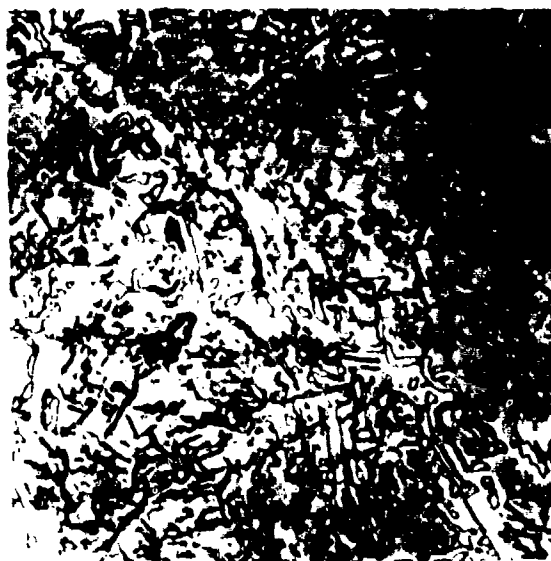
region are block-type. These microstructural characteristics, with minor variations, prevail in all the modified alloys with the exception of the vanadium modified alloy 159. In this case, spheroidized perovskite carbide particles were observed. Figure 165b. Further, the dimensions of the particles are considerably smaller than those in other alloys of this series. These observations suggest that V has a major effect on the perovskite carbide coarsening kinetics, and could be used to control the size and morphology of the perovskite carbide particles. The microstructure of the V-modified alloy was studied in greater detail using thin-foil electron microscopy techniques. The transmission electron micrograph, shown in Figure 166, shows the coarsened equiaxed-shaped perovskite carbide particles, labeled b, and the mottled appearance of the matrix due to the formation of a very fine modulated structure. Figure 166 also shows large strain contrast around the coarsened particles. Examination of the particle/matrix interface revealed some fringes and a low density of isolated dislocations indicating that the coarsened particles may be semi-coherent with the matrix. A small number of V-rich particles, labeled c in Figure 166, probably vanadium carbide, were also observed in this alloy.



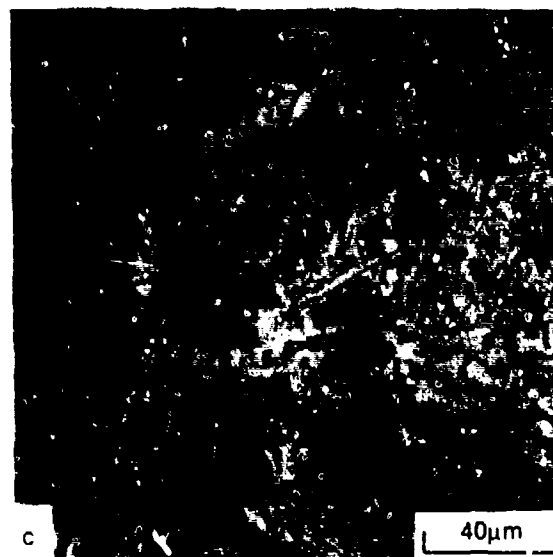
Base

FD 270172

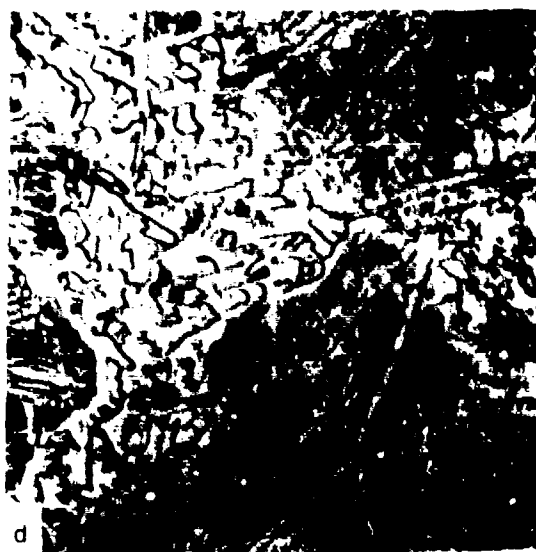
Figure 165(a). Optical Micrographs of Alloys in the Third Series After a Solution Treatment of 750°C for 30 min Followed by Furnace Cooling to 815°C at a Rate of 10°C/min. (Alloy 168)



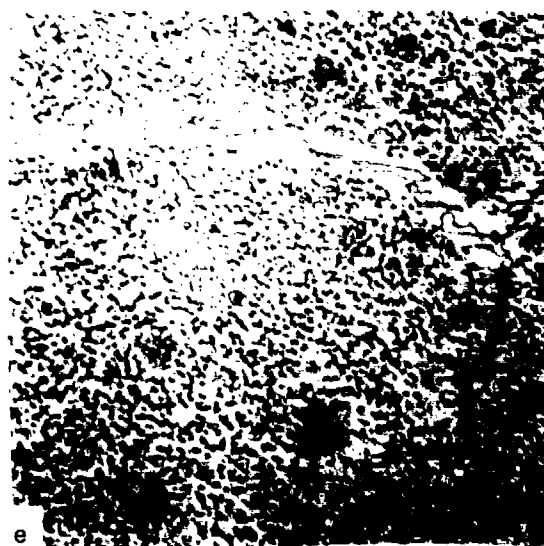
0.5 Ti



0.5 Zr



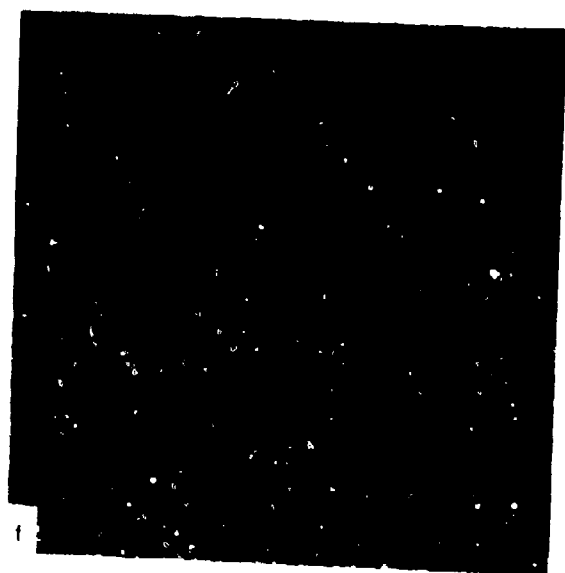
0.5 Hf



0.5 V

FD 270173

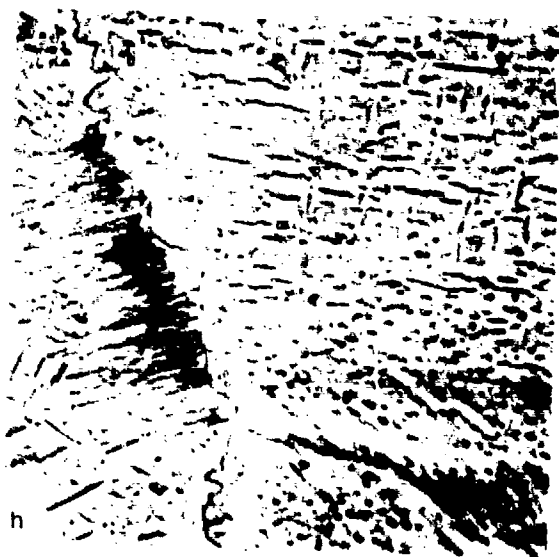
Figure 165(b). Optical Micrographs of Alloys in the Third Series After a Solution Treatment of 1095°C for 30 min Followed by Furnace Cooling to 815°C, b. Base + 0.5 wt% Ti (Alloy 156) c. Base + 0.5 wt% Zr (Alloy 157) d. Base + 0.5 wt% Hf (Alloy 158) e. Base + 0.5 wt% V (Alloy 159)



0.5 Cr



0.5 Mo



0.5 W



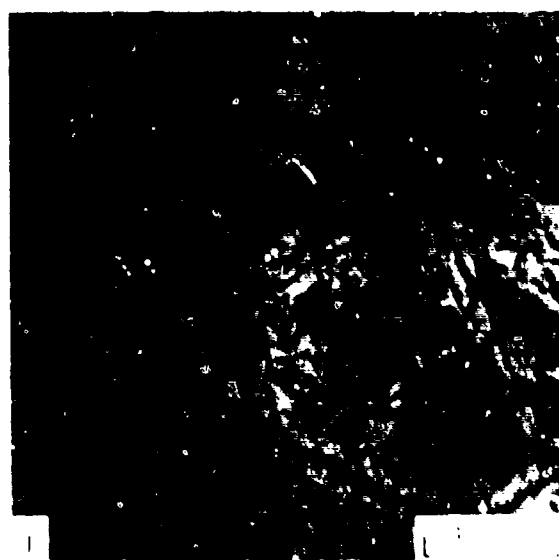
1.5 Co

FD 270174

Figure 165(c). Optical Micrographs of Alloys in the First Series After a Solution Treatment of 1095°C for 30 min Followed by Furnace Cooling to 815°C f. Base + 0.5 wt% Cr (Alloy 160) g. Base + 0.5 wt% Mo (Alloy 161) h. Base + 0.5 wt% W (Alloy 162) i. Base + 1.5 wt% Co (Alloy 163)



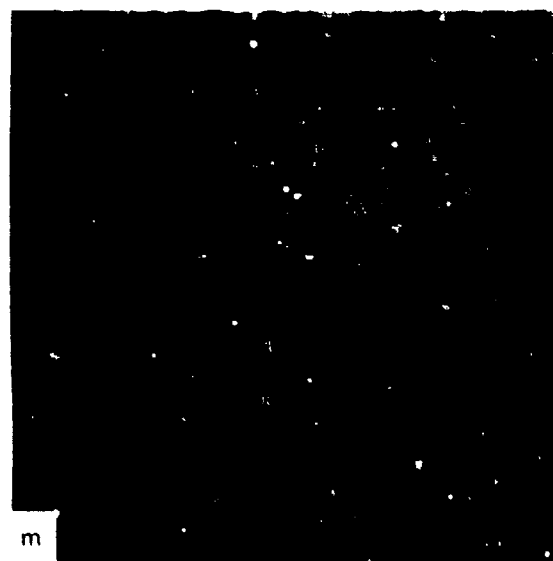
1.5 Ni



1.5 Cu



0.5 Si



0.5 Mo + 0.02 B

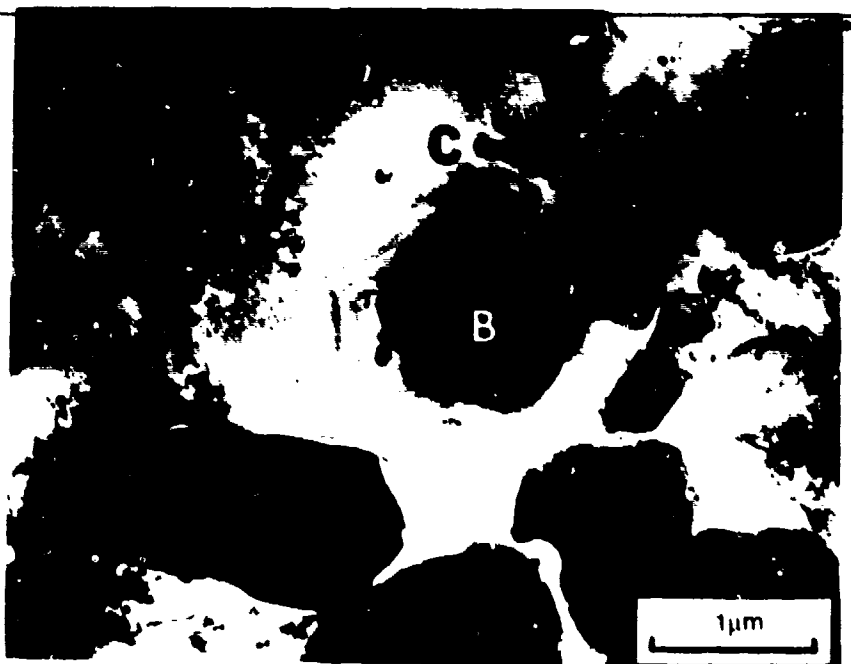
FD 270175

Figure 165(d). *Optical Micrographs of Alloys in the First Series After a Solution Treatment of 1095°C for 30 min Followed by Furnace Cooling to 815°C j. Base + 1.5 wt% Ni (Alloy 164) k. Base + 1.5 wt% Cu (Alloy 165) l. Base + 0.5 wt% Si (Alloy 166) m. Base + 0.5 wt% Mo + 0.02 wt% β (Alloy 167)*

TABLE 59. X-RAY ANALYSIS FROM FILINGS

*Structures of Phases and Estimated Amounts
in Fe-33Mn-8Al-2C-X (wt%) Alloys
HT:2000°F/1 min/Furnace Cooled to 1500°F
CrK α Radiation*

Alloy	Wt%X	
168	—	80-85 v/o disordered fcc Fe Solid Solution ($a_0 \approx 3.6786$) 15-20 v/o ordered fcc AlFe ₃ C Structure ($a_0 \approx 3.7960$)
156	0.5 Ti	85-90 v/o disordered fcc Fe Solid Solution ($a_0 \approx 3.6835$) 10-15 v/o ordered fcc AlFe ₃ C Structure ($a_0 \approx 3.7969$)
159	0.5V	~90-95 v/o disordered fcc Fe Solid Solution ($a_0 \approx 3.6835$) ~5-10 v/o ordered fcc AlFe ₃ C Structure ($a_0 \approx 3.8006$)
161	0.5 Mo	70-75 v/o disordered fcc Fe Solid Solution ($a_0 \approx 3.6810$) 25-30 v/o ordered fcc AlFe ₃ C Structure ($a_0 \approx 3.7973$)
162	0.5 W	70-75 v/o disordered fcc Fe Solid Solution ($a_0 \approx 3.6860$) 25-30 v/o ordered fcc AlFe ₃ C Structure ($a_0 \approx 3.7969$)
163	1.5 Co	75 v/o disordered fcc Fe Solid Solution ($a_0 \approx 3.6736$) 25 v/o ordered fcc AlFe ₃ C Structure ($a_0 \approx 3.7952$)



FD 270176

Figure 166. Transmission Electron Micrograph of Alloy 159 After the Furnace Cool Heat Treatment Described in the Preceding Figure Illustrating the Precipitation of Very Fine Perovskite Carbide Particles in the Matrix (a), the Equiaxed Shaped Primary Perovskite Carbide Particles (b), and the Vanadium-Rich Particles (c)

It is also of interest to examine the effect of alloying on precipitate/matrix lattice mismatch using the lattice parameters of austenite and perovskite carbide shown previously in Table 59. The calculated mismatch values, shown in Table 60, are slightly over 3% for all the alloys studied.

TABLE 60. EFFECT OF ALLOYING ON AUSTENITE AND PEROVSKITE CARBIDE LATTICED PARAMETERS

Alloy	Wt%X	Atomic Radius of X	Δa_a^x %	Δa_p^x %	Δa_{a-p} %
168	Fe, Mn	1.26Å	0	0	3.191
156	0.5 Ti	1.47Å	0.133	0.0237	3.079
159	0.5 V	1.34Å	0.133	0.1211	3.179
161	0.5 Mo	1.39Å	0.065	0.0474	3.173
162	0.5 W	1.39Å	0.201	0.0237	3.009
163	0.5 Co	1.25Å	-0.136	-0.0211	3.310

Δa_a^x = Change in austenite lattice parameter by alloying element x
 $= (a_a^x - a_a)/a_a \times 100$

Δa_p^x = Change in perovskite lattice parameter by alloying element x
 $= (a_p^x - a_p)/a_p \times 100$

Δa_{a-p} lattice mismatch between austenite and perovskite
 $= (a_p^x - a_a^x)/a_a^x \times 100$

Where a_a and a_p are the lattice parameters of the austenite and perovskite, respectively in the base alloy 168.

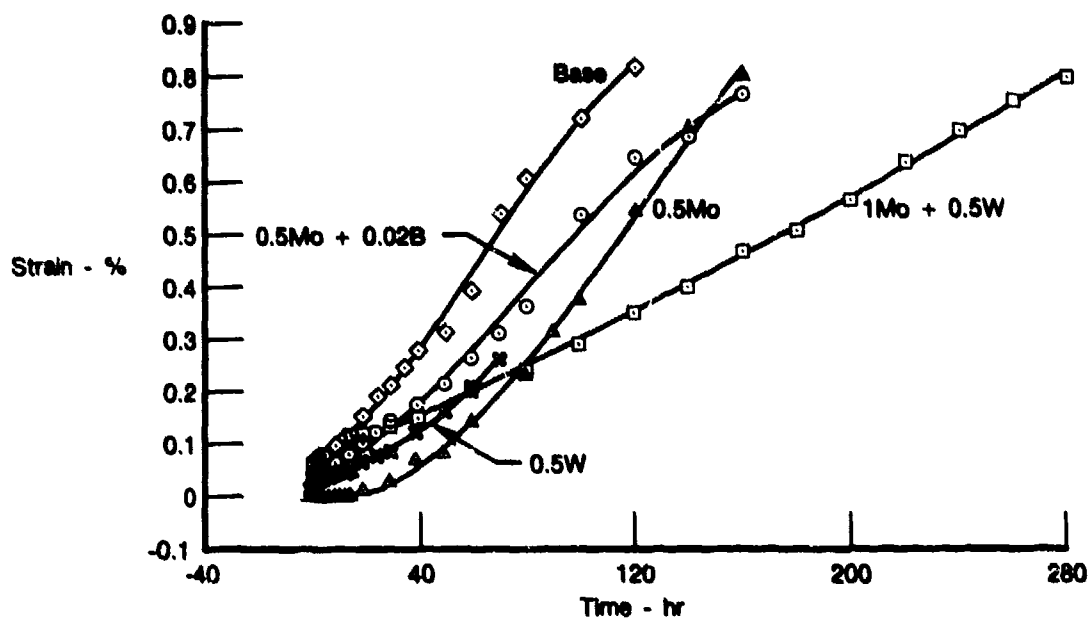
7440C

Creep Behavior

The creep results for this alloy series are presented in three groups. The group with the highest creep resistance consists of alloys with additions of Mo (alloys 161, 167), W (alloy 162), Mo+W (alloy 155), and V (alloy 159). The results, presented in Figure 167 show there are no important differences between these alloying additions. The best resistance in this group was observed in alloy 155 which contains a 1 wt% Mo+0.5 wt% W. The second group consists of alloys modified with an austenite stabilizer Co (alloy 163), Ni (alloy 164), and Cu (alloy 165). Results, given in Figure 168, again indicate only minor differences between these alloys which exhibit lower creep resistance compared with alloys in the first group. The third group comprises the remaining alloys in this series, including primarily those with additions of carbide-forming elements. Results, illustrated in Figure 169, show that creep resistance increases in the order Zr, Si, Ti, Cr=Hf, V.

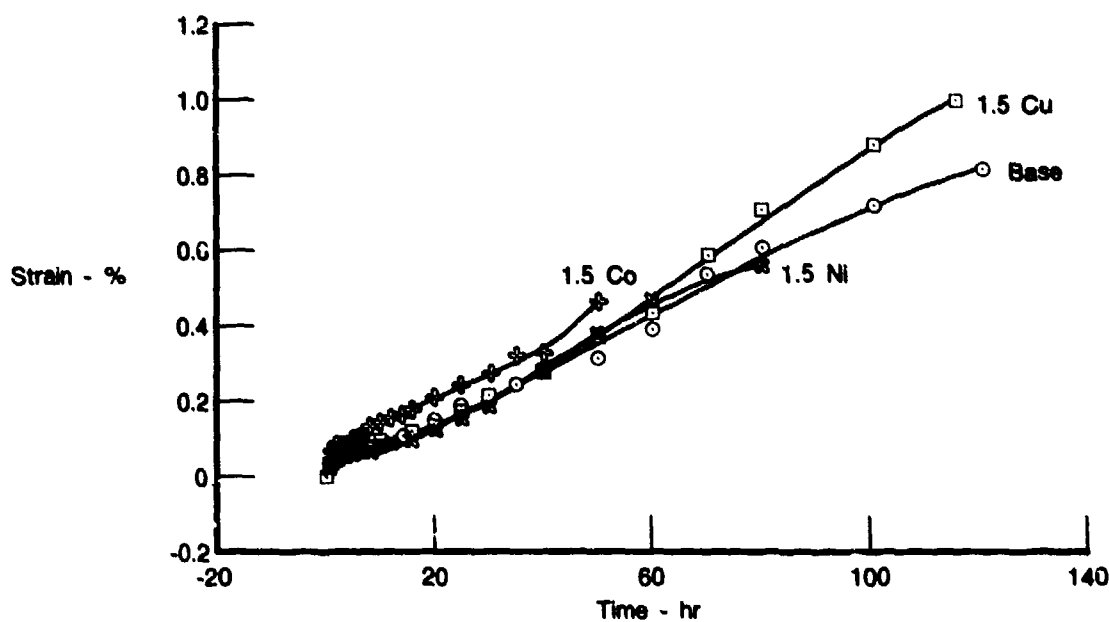
Fe-Ni/Mn-Al/Ti Alloys

The analyzed compositions of the Fe-Ni/Mn-Al and Fe-Ni/Mn-Ti alloys, given in Tables 61 and 62, respectively, show no major deviations from the aim compositions. The Fe-Ni/Mn-Ti alloys were studied in the cast form after a solution treatment of 1900°F (1040°C) for 1 hour followed by quenching in oil and then aging at 1200°F (650°C) for 16 hours. In the case of the Fe-Ni/Mn-Al alloys, a section of each casting was heated to 2100°F (1150°C), and then rolled between 130 mm diameter unheated rolls (with reheating after each 7% reduction) to an approximately 60% reduction in thickness. It was observed that the high-Ni, alloys 147, 148, and 149, cracked during rolling. The remaining alloys (150 through 153) were successfully rolled to about 60%.



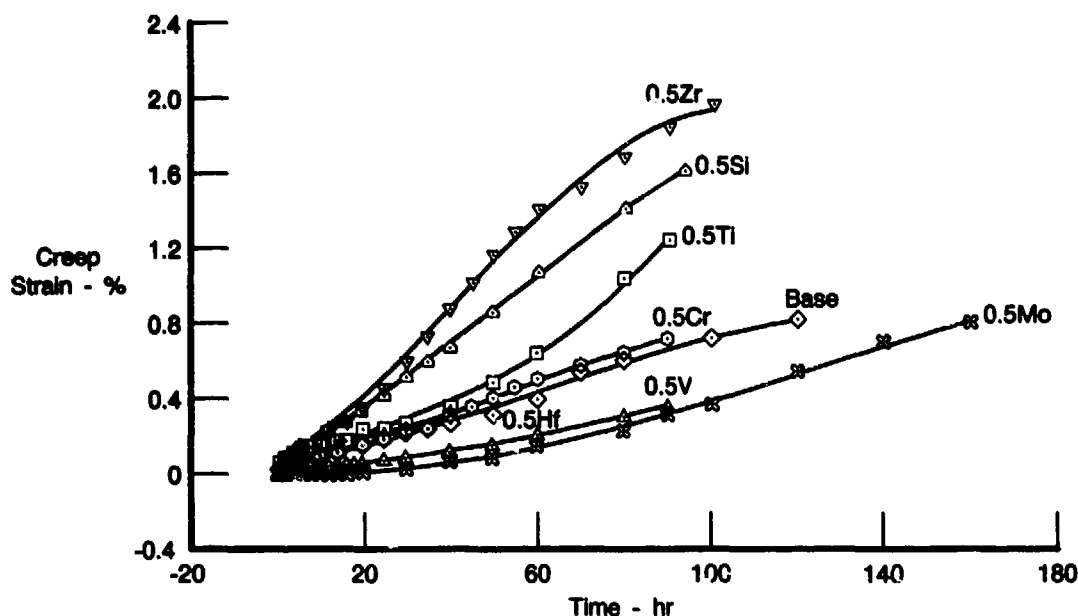
FDA 318422

Figure 167. Creep Curves of Alloys 155 (1 wt% Mo + 0.5 wt% W), 161 (0.5 wt% Mo), 162 (0.5 wt% W), 167 (0.5 wt% + 0.2 wt% β) and 168 (Base) at 650°C and 293 MPa



FDA 318423

Figure 168. Creep Curves of Alloys 156 (1.5 wt% Co), 164 (1.5 wt% Ni) 165 (1.5 wt% Cu) and 168 (Base) at 650°C and 293 MPa



FDA 318424

Figure 169. Creep Curves of Alloys 156 (0.5 wt% Ti), 157 (0.5 wt% Zr), 158 (0.5 wt% Hf), 159 (0.5 wt% V), 160 (0.5 wt% Cr), 161 (0.5 wt% Mo), and 166 (0.5 wt% Si and 168 (Base)) at 650°C and 293 MPa

TABLE 61. ANALYZED COMPOSITIONS OF Fe-Ni/Mn-Al ALLOYS, Wt%

	Fe	Mn	Ni	Al	Other
147	Bal	37.8	25.8	5.1	—
148	Bal	37.3	25.5	2.3	4.0 Ti
149	Bal	34.8	26.4	5.1	0.86 C
150	Bal	52.3	11.7	6.6	—
151	Bal	50.6	12.2	6.8	1.05 C
152	Bal	24.8	—	2.4	—
153	Bal	33.8	—	2.4	4.8 Ti

7450C

TABLE 62. ANALYZED COMPOSITIONS OF Fe-Ni/Mn-Ti ALLOYS, Wt%

Alloy	Fe	Mn	Ni	Ti	Mo	Al	Other
169	Bal	35.2	25.1	1.6	—	—	—
243	Bal	—	30.8	3.4	0.95	0.11	—
244	Bal	17.9	12.3	3.2	0.92	0.10	—
245	Bal	21.5	7.8	3.2	0.97	0.11	—
246	Bal	—	46.6	3.3	0.96	0.11	—
247	Bal	26.9	18.3	3.4	0.97	0.10	—
248	Bal	33.4	11.8	3.2	0.98	0.10	—
170	Bal	35.9	24.6	3.3	—	—	—
249	Bal	36.5	23.9	3.3	0.98	0.16	—
250	Bal	13.9	11.8	3.2	0.94	0.10	2.29Cu
251	Bal	23.4	7.6	3.2	0.94	0.10	2.27Cu

7450C

Microstructure of Fe-Ni/Mn-Al Alloys

The structures of alloys 147-153, as determined by X-ray analysis, are summarized in Table 63. With the exception of alloy 152, major constituents in these alloys are austenite and a CsCl-type ordered bcc phase. Based on projections from some of the results from the first year of this program and the literature, an ordered fcc phase with $L1_2$ type structure was anticipated instead of the ordered bcc phase. These structural results coupled with the poor creep performance of alloys in this series, as will be described in a following section, indicate the difficulty of this particular alloying approach.

TABLE 63. RESULTS OF PHASE IDENTIFICATION BY X-RAY FROM FILINGS OF ALLOYS 147-153, CRK α RADIATION

Alloy ⁺	$\approx 60-65$ v/o disordered f.c.c. ($a_0 \approx 3.628\text{\AA}$) and
147 ⁺	$\approx 40-35$ v/o ordered b.c.c. ($a_0 \approx 2.914\text{\AA}$)
148 ⁺	$\approx 75-70$ v/o disordered f.c.c. ($a_0 \approx 3.629\text{\AA}$), $\approx 25-30$ v/o ordered b.c.c. ($a_0 \approx 2.934\text{\AA}$) and $\approx <1$ v/o possibly MnO (f.c.c.) single peak
149 ⁺	≈ 55 v/o disordered f.c.c. ($a_0 \approx 3.628\text{\AA}$) ≈ 40 v/o ordered b.c.c. ($a_0 \approx 2.916\text{\AA}$) and ≈ 5 v/o tetragonal $\text{Fe}_{0.4}\text{Mn}_{3.6}\text{C}$ ($a_0 \approx 6.722\text{\AA}$ and $c_0 \approx 9.427\text{\AA}$)
150 ⁺	$\approx 60-55$ v/o primitive cubic, FeMn_4 ($a_0 \approx 6.293\text{\AA}$) and $\approx 40-45$ v/o ordered b.c.c. ($a_0 \approx 2.896\text{\AA}$)
151 ⁺	$\approx 55-50$ v/o disordered f.c.c. ($a_0 \approx 3.662\text{\AA}$), $\approx 35-30$ v/o ordered b.c.c. ($a_0 \approx 2.888\text{\AA}$), ≈ 10 v/o primitive cubic, FeMn_4 ($a_0 \approx 6.291\text{\AA}$) and $\approx 5-10$ v/o tetragonal $\text{Fe}_{0.4}\text{Mn}_{3.6}\text{C}$ ($a_0 \approx 6.774\text{\AA}$ and $c_0 \approx 9.426\text{\AA}$)
152 ⁺	Single phase, disordered f.c.c. ($a_0 \approx 3.614\text{\AA}$)
153 ⁺	≈ 75 v/o-80 v/o disordered f.c.c. ($a_0 \approx 3.628\text{\AA}$) and ≈ 25 v/o-20 v/o disordered b.c.c. $\alpha\text{-Mn}$ ($a_0 \approx 8.894\text{\AA}$)

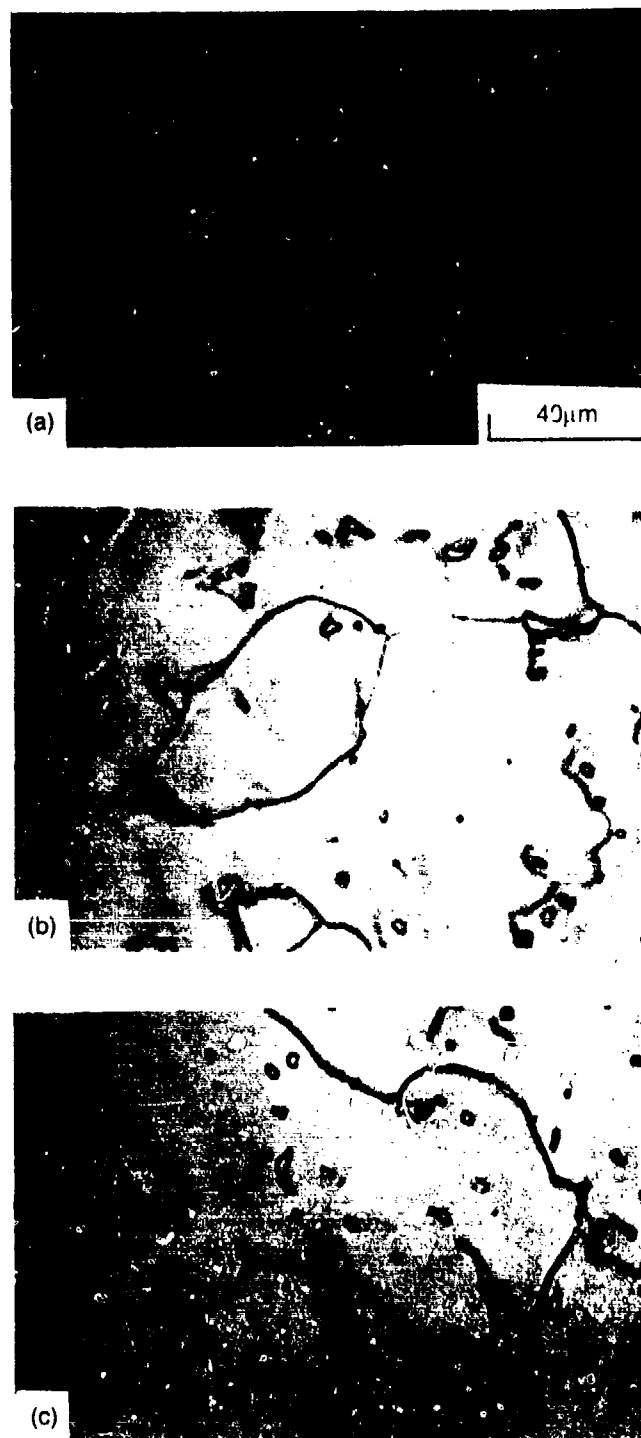
* Alloys were solution heat treated at 1040°C/1h/OQ and aged at 650°C/16h/AC

+ Alloy fractured during hot rolling. Castings were homogenized at 1150°C/50h prior to the solution and age heat treatments described above

7448C

Microstructure of Fe-Ni/Mn-Ti Alloys

Microstructures of alloys with increasing Mn/Ni ratio are shown in Figure 170. With high-Ni content, alloys 243, 246, and 170 appear to be essentially single phase, Figure 170a. However, detailed electron micrographs (Figure 171) show the precipitation of fine particles in these alloys about 50Å in diameter which exhibit $L1_2$ -type structure, and are coherent with the austenitic matrix. The presence of a more massive second phase became noticeable when the Ni content was lower than about 12 a/o, Figure 170b, and became increasingly evident as the Mn content increased at the expense of Ni, Figure 170c. The more massive phase is distributed throughout the microstructure with some preference for grain boundaries. The composition and structure of this phase were determined using electron microscopy techniques. Results, given in Figures 172 and 173, show that the second phase is enriched in Ti (21 a/o) and exhibits a hexagonal structure with $a = 4.56\text{\AA}$ and $c = 40\text{\AA}$. These parameters correlate with the Laves phases Fe_2Ti and Mn_2Ti with hexagonal MgZn_2 -type structure (C14) although with lattice parameters slightly larger than those measured in the present studies. The substitution of Mn and Fe with the smaller Ni atoms may account for the smaller lattice parameters.



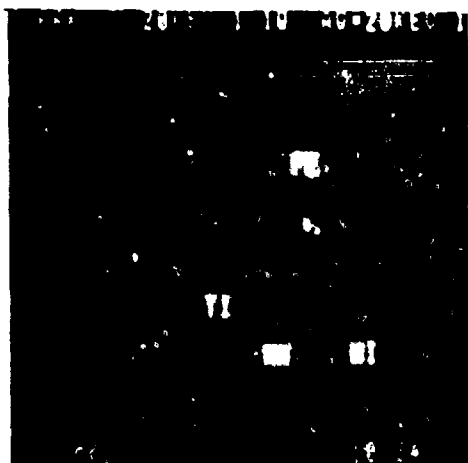
FD 270180

Figure 170. *Optical Micrographs of Selected Alloys in the Fe-Ni/Mn-Ti Alloy Series Illustrating Microstructure Changes When an Increasing Amount of Ni Was Replaced With Mn Alloys Were a Solution Heat Treated at 1040°C for 1 hr Followed by Quenching in Oil and Then Aging at 650°C for 16 hr. a. Alloy 243 (30 a/o Ni) b. Alloy 244 (18.5 a/o Mn+11.5 a/o Ni) c. Alloy 245 (22.5 a/o Mn + 7.5 a/o Ni)*

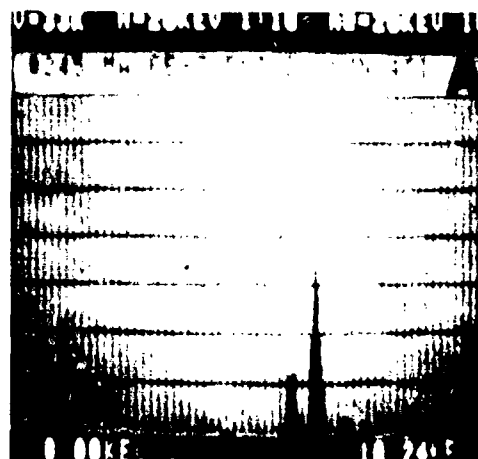


FD 270181

Figure 171. Transmission Electron Micrographs of Alloy 243 After the Heat Treatment Described in the Preceding Figure. These Figures Illustrate the Precipitation of Very Fine $L1_2$ -Type Particles (A) Bright Field (B) Dark Field Illuminated by a Superlattice Reflection



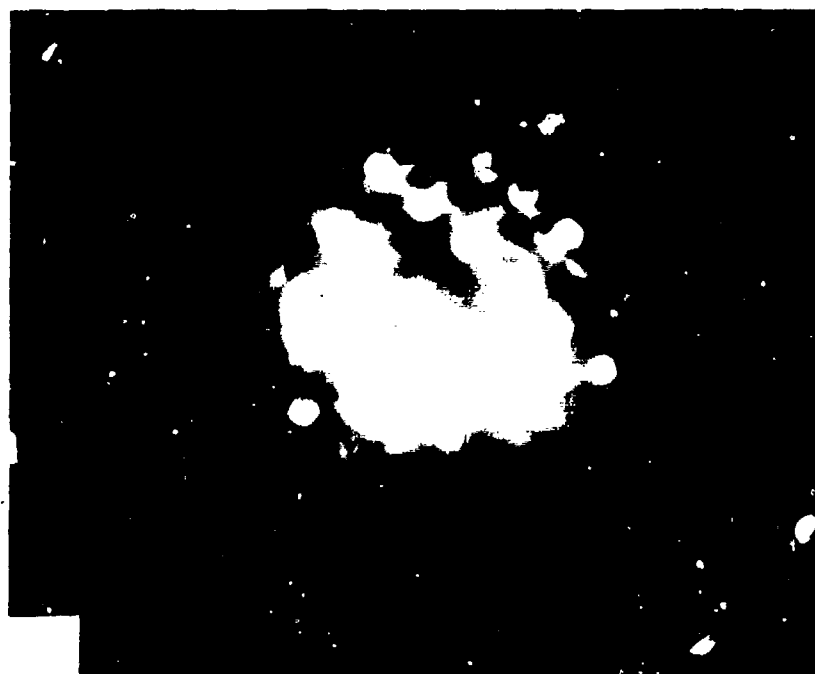
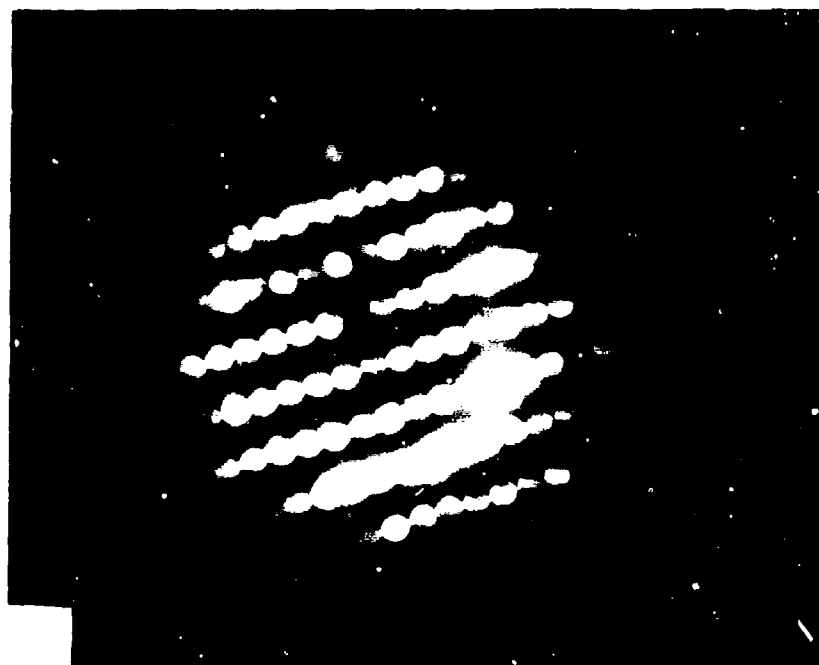
Fe - 59.9 wt%, 58.1 at%
 Ni - 6.6 wt%, 6.1 at%
 Mn - 14.5 wt%, 14.3 at%
 Ti - 19.1 wt%, 21.6 at%



Fe - 70.1 wt%, 69.7 at%
 Ni - 6.4 wt%, 6.1 at%
 Mn - 20.9 wt%, 21.1 at%
 Ti - 2.7 wt%, 3.1 at%

FD 270182

Figure 172. Electron Micrograph of Alloy 245 Illustrating the Absence of $L1_2$ Type Particles in the Matrix and the Formation of More Massive Ti-Rich Particles Distributed Throughout the Alloy

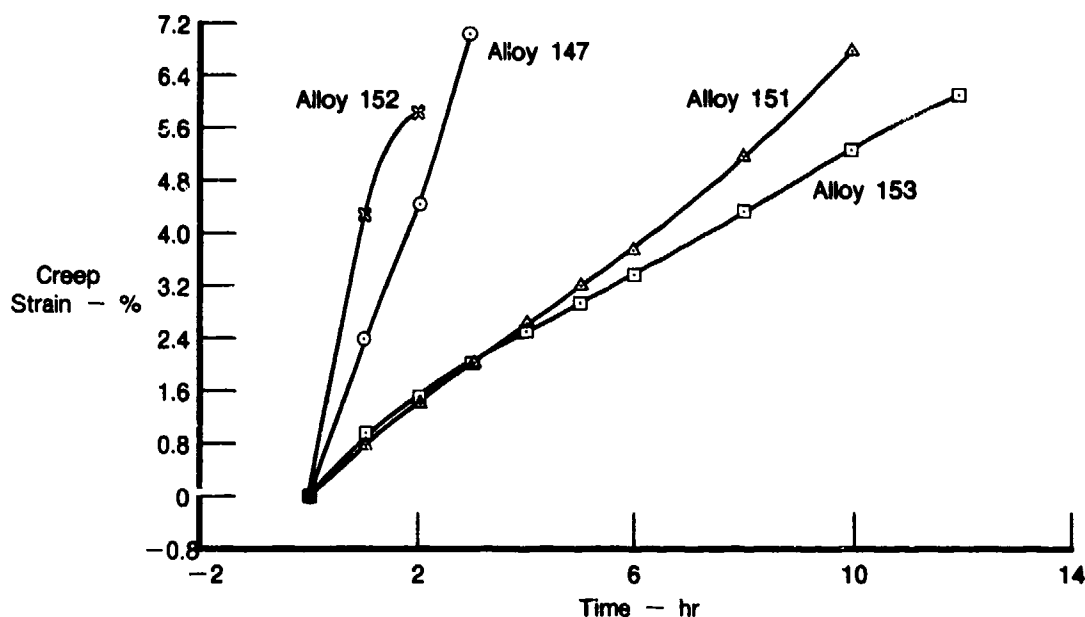


FD 270183

Figure 173. Micro-micro Electron Diffraction Patterns from the Ti-rich Particles Shown in the Preceding Figure. These and Other Diffraction Patterns Could be Indexed as hcp With Lattice Parameters of $a = 4.56\text{\AA}$, $c = 7.40\text{\AA}$, (a)(100), (b)(231)

Creep Behavior of Fe-Ni/Mn-Al Alloys

Creep results of selected alloys in this series, illustrated in Figure 174, show that the creep resistance of the alloys in this series is generally much lower than that of the austenite-perovskite series. Alloys 148 and 149, which cracked during hot rolling, were given a homogenizing heat treatment at 2100°F (1150°C) for 50 hours. Alloy 148 showed incipient melting at grain boundary regions after this heat treatment, and therefore was not tested. Difficulty was encountered in machining specimens from alloy 150 as the specimen cracked readily at room temperature, and therefore no test was conducted. Because of the poor performance of the alloys in this series, further evaluations do not appear to be worthwhile.



FDA 318425

Figure 174. Creep Curves of Alloys 147, 151, 152, and 153 at 650°C and 293 MPa

The effect of Ti level on creep resistance can be observed in Figure 175, which shows the creep behavior of alloys 169 and 170 with 1.7 and 3.4 wt% Ti, respectively. It is evident from these results that for good creep resistance a Ti level larger than 2 wt% is required (for comparison, iron base superalloy A286 contains about 2.15 wt% Ti).

Alloys with different Ni levels (243, 246, and 170) and situated in the $\gamma + (\text{Fe,Ni})_2\text{Ti}$ or γ phase field of the Fe-Ni-Ti ternary diagram, see Figure 111, can be used to assess the effect of Ni level on creep behavior. The creep behavior of these alloys is illustrated in Figure 176, which appears to show that alloys in the $\gamma + (\text{Fe,Ni})_2\text{Ti}$ phase field exhibit better creep resistance than alloys in the γ phase field.

The effect of replacing Ni with Mn can be observed from the creep results of two groups of alloys: (1) alloys 243, 244, and 245 with $(\text{Mn} + \text{Ni}) = 30$ a/o, and (2) alloys 246, 247, and 248 with $(\text{Mn} + \text{Ni}) = 45$ a/o, given in Figures 177 and 178 respectively. Figure 177 shows that the creep resistance of alloy 243 was reduced drastically when the Ni content was reduced to less than 12 a/o. The poor creep resistance in alloys 244 and 245 can be correlated with the formation of the Laves phase in these alloys. Similar relationships between resistance and microstructure can also

be seen in the results of the second group of alloys, alloys 246, 247, and 248. It is interesting to note the similarity in the creep resistance of alloys 246 and 247 even though the Ni contents differ significantly, i.e., 45 a/o and 17 a/o, respectively. This observation, coupled with those from the first group of alloys, Figure 177, indicates the minimum Ni content required to stabilize the L_{12} structure in the Fe-Mn/Ni-Ti alloys is in the range of 12 to 17 a/o. However, ternary Fe-Ni-Ti alloys with these Ni contents lie in the ferrite + austenite + Laves 3-phase field, Figure 111. The absence of ferrite in the present alloys can be directly attributed to the austenite stabilizing effect of Mn. It may therefore be concluded that although Mn does not appear to promote the formation of the L_{12} phase, it does exhibit a beneficial effect by suppressing the formation of the ferrite phase, thus allowing creep resistance to be retained to a lower Ni level.

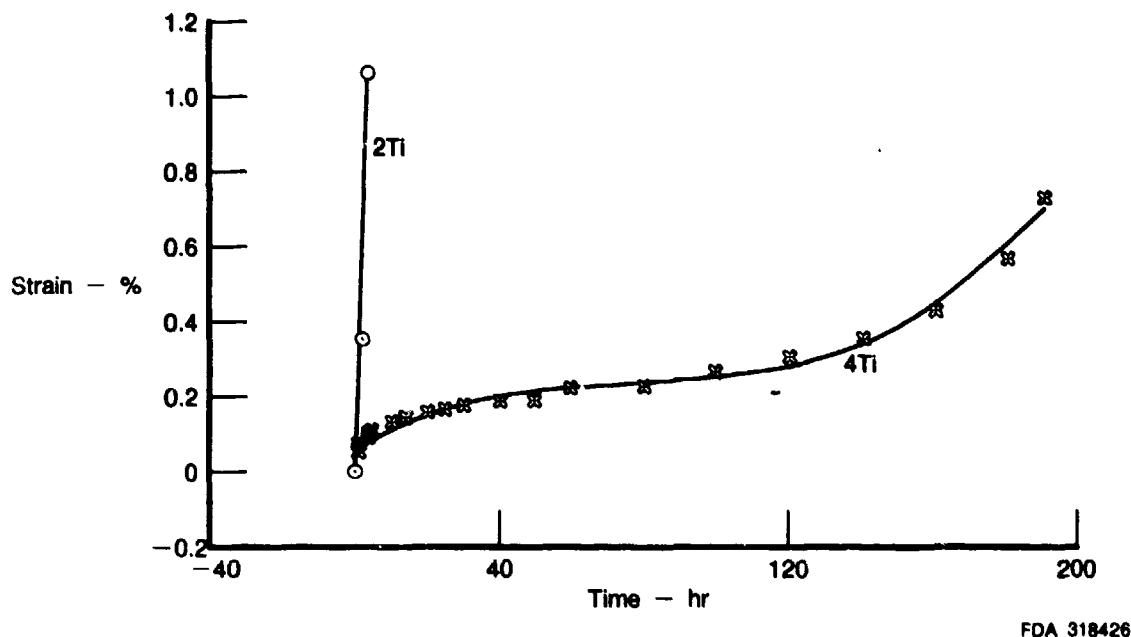


Figure 175. Creep Curves of Alloys 169 (2 a/o Ti) and 170 (4 a/o Ni), at 650°C and 293 MPa

The effect on creep resistance of alloying with Cu can be observed from the creep behavior of alloys 244 and 250 illustrated in Figure 179 which shows that Cu does not have a beneficial effect on resistance of this type of alloy.

Corrosion Studies

Cyclic oxidation between 68 and 1400°F (20 and 760°C) was studied in alloys 74, 75, 76, A286, and H46. The changes in weight as a function of exposure time are shown in Figure 180. The appearance of the specimens after 250 hours (125 thermal cycles) is shown in Figure 180b. Results show that all the Fe-Mn-Al alloys have a better oxidation resistance than the stainless steels A286 and H46. There are no significant differences between the individual Fe-Mn-Al alloys, but alloy 76, which has the higher aluminum content, appears to be slightly better than alloys 74 and 75. The weight change data for the latter two alloys fall almost on the same curve, indicating that a 2 wt% difference in Cr content has no effect on oxidation.

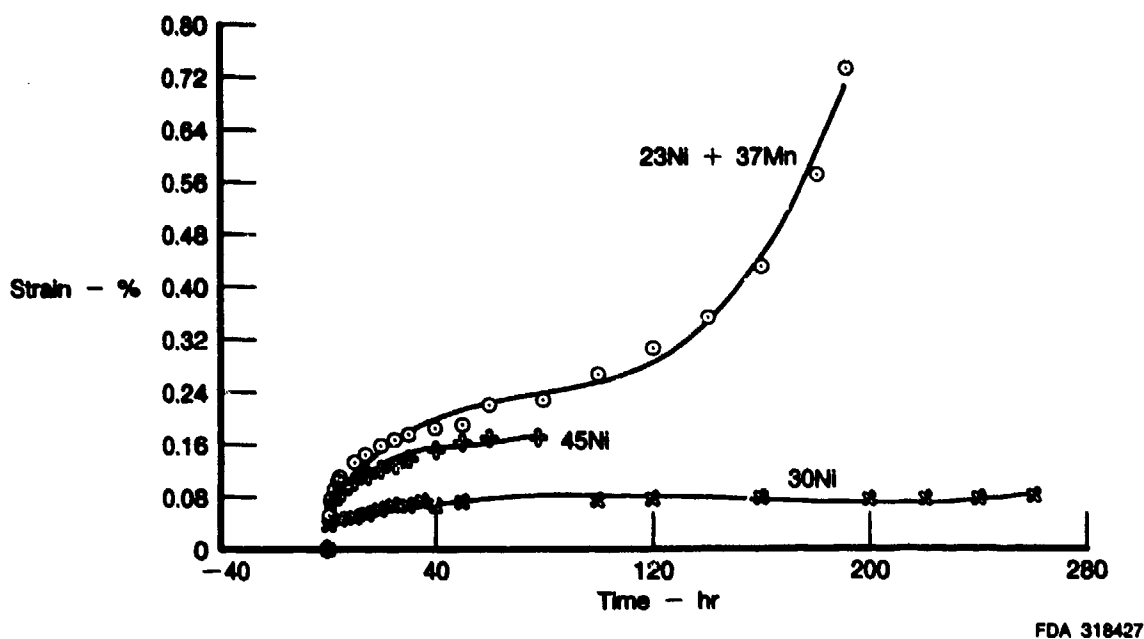


Figure 176. Creep Curves of Alloys 243 (30 a/o Ni), 246 (45 a/o Ni), and 170 (23 a/o Ni + 37 a/o Mn) at 650°C and 293 MPa

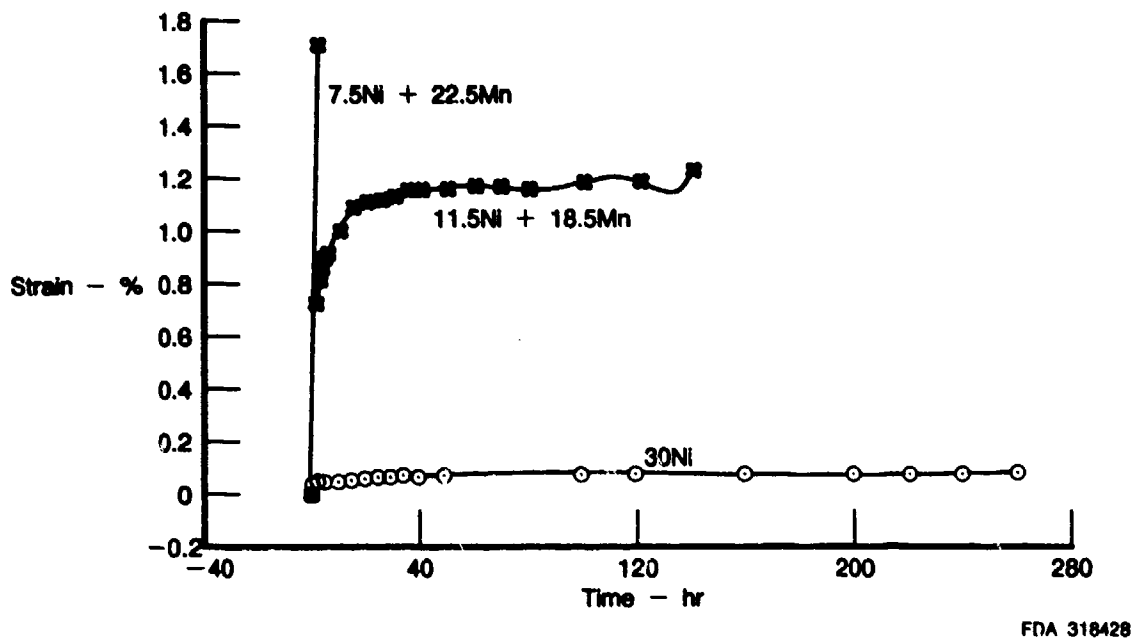
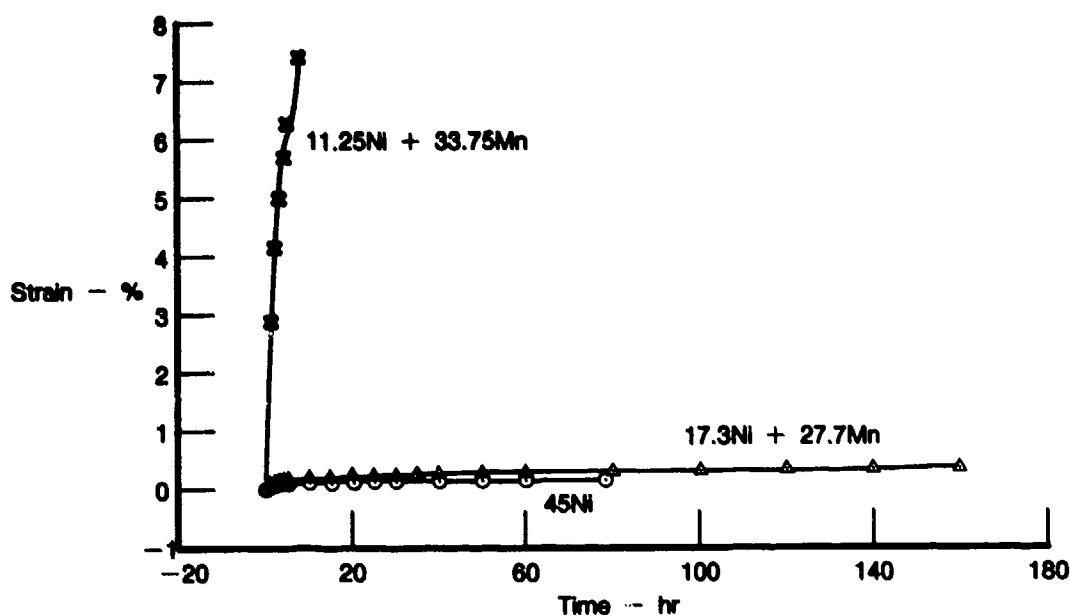
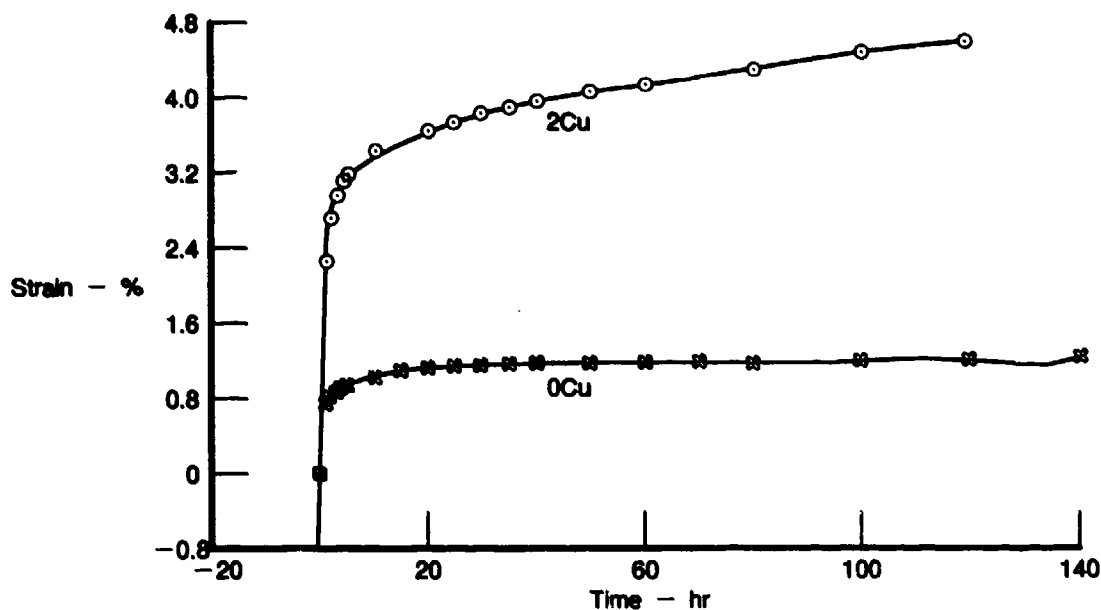


Figure 177. Creep Curves of Alloys 243 (30 a/o Ni), 244 (11.5 a/o Ni + 18.5 a/o Mn) and 245 (7.5 a/o Ni + 22.5 a/o Mn) at 650°C and 293 MPa



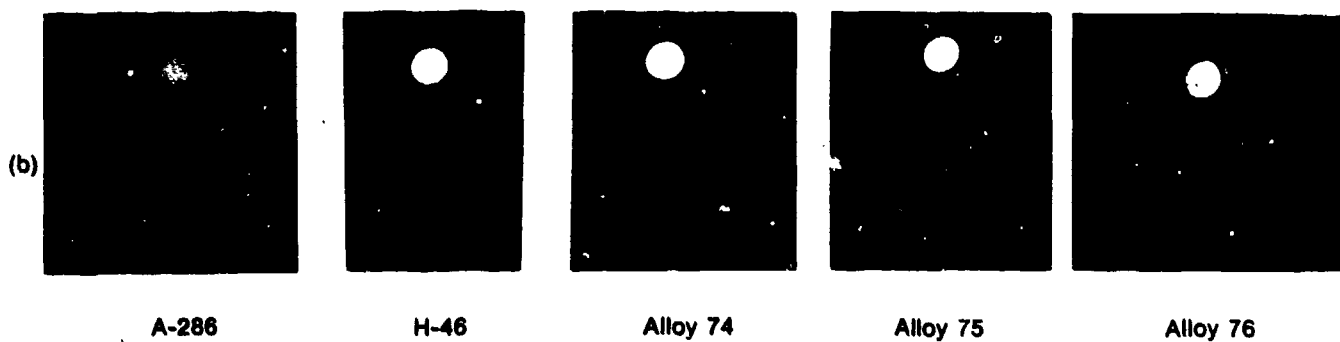
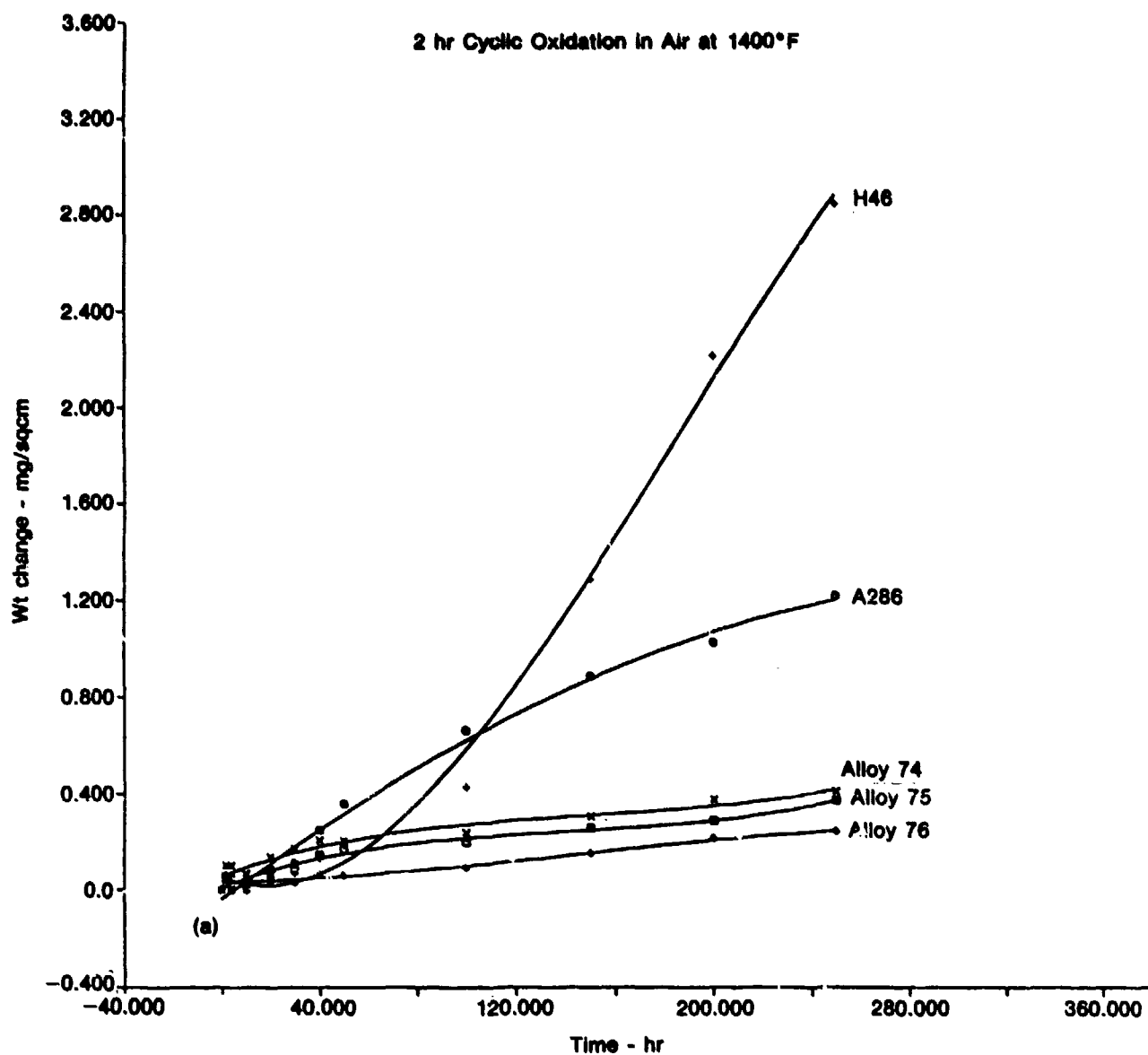
FDA 318429

Figure 178. Creep Curves of Alloys 246 (45 a/o Ni), 247 (17.3 a/o Ni + 27.7 a/o Mn) and 248 (11.25 a/o Ni + 33.75 a/o Mn) at 650°C and 293 MPa



FDA 318433

Figure 179. Creep Curves of Alloys 244 (0 Cu) and 250 (2 Cu) at 650°C and 293 MPa



FD 243632

Figure 180. (A) Weight Change Versus Exposure Time in Cyclic Oxidation Between 20 and 760°C in 2-Hour Cycle. (B) Appearance of the Specimens After 250 Hours

Corrosion (sulfidation) of the uncoated alloys in a mixture of Na_2SO_4 and NaCl at 1200°F (650°C) in static air was studied at two NaCl concentration levels, 50 and 25% by weight. The weight change data and the surface appearance of specimens after 250 hours using these two mixtures of salts are shown in Figures 181 and 182, respectively. Although the data show some differences among the alloys, the test results were judged to be nondiscriminating because of the severity of the sulfidation attack as evidenced by the surface appearance after the 250-hour exposure. With the less severe corroding media (25% NaCl mixture), alloy 76 appears to be less severely attacked than the other alloys studied. Among the Fe-Mn-Al alloys, the Cr-free alloy (alloy 50) appears to be inferior to the Cr-containing ones. In general, the sulfidation results of the uncoated alloys taken collectively seem to suggest that the sulfidation resistance of the Fe-Mn-Al alloys under the conditions studied is about the same as A286 and H46.

The results of the corrosion tests on the specimens protected with aluminized coatings and chromized coatings are presented in Figures 183 and 184. As can be seen from Figure 183 the aluminized coating (PWA 73) provided excellent sulfidation protection for A286 and to a lesser extent H46 also. However, such coating was ineffective for the Fe-Mn-Al alloys which show severe pitting and spalling. In contrast, chromized coating (PWA 70) provides considerably better sulfidation protection to all the alloys (Figure 184). We may also note that alloy 75, which contains the highest Cr content (5%) among the Fe-Mn-Al alloys, compares favorably with A286 and H46.

DETAILED EVALUATIONS OF SELECTED ALLOYS

The goal for the final stage of this program task was to select promising alloys for detailed evaluations. Alloys based on the austenite-perovskite phase structure were selected because of their interesting microstructure and good creep resistance. The nominal compositions of the selected alloys, designated No. 252 and 253 are (in wt%):

<u>Alloy</u>	<u>Fe</u>	<u>Mn</u>	<u>Al</u>	<u>C</u>	<u>Others</u>
252	Bal	30	9.0	2.0	1Mo, 0.5W
253	Bal	33	9.0	1.5	1Mo, 0.5W

The alloys based on the Fe-Ni/Mn-Ti system exhibited equally desirable microstructure and excellent creep resistance, but were not as cost effective because of a moderate amount of Ni needed for stabilization of the L1_2 precipitate phase. Further, the environmental resistance of Fe-Ni/Mn-Ti alloys is probably inferior to the Fe-Mn-Al-C alloys at elevated temperatures.

Experimental

Alloy Preparation

Vacuum induction melted ingots of alloys 252 and 253 were procured from Homogeneous Metals Incorporated (HMI). To eliminate the casting pores, the ingots were enclosed in stainless steel cans and then hot isostatically pressed at 2200°F (1205°C) for 8 hours under 15 ksi (103 MPa). After machining into extrusion preforms 2.95 inches (7.5 cm) in diameter and 7 inches (17.8 cm) long, the HIP ingots were equilibrated in a furnace preheated to 1000°F (540°C) followed by a slow rate of temperature increase until the extrusion temperature was reached. The ingots, still in HIP containers, were extruded at 2150°F (1175°C) using an extrusion ratio of 9. The extrusion was conducted at the Air Force Materials Processing Laboratory.

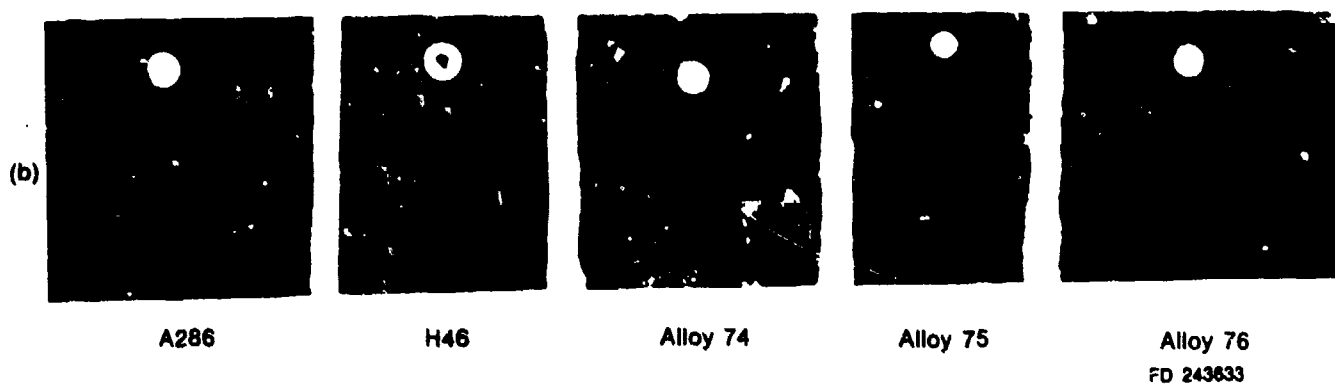
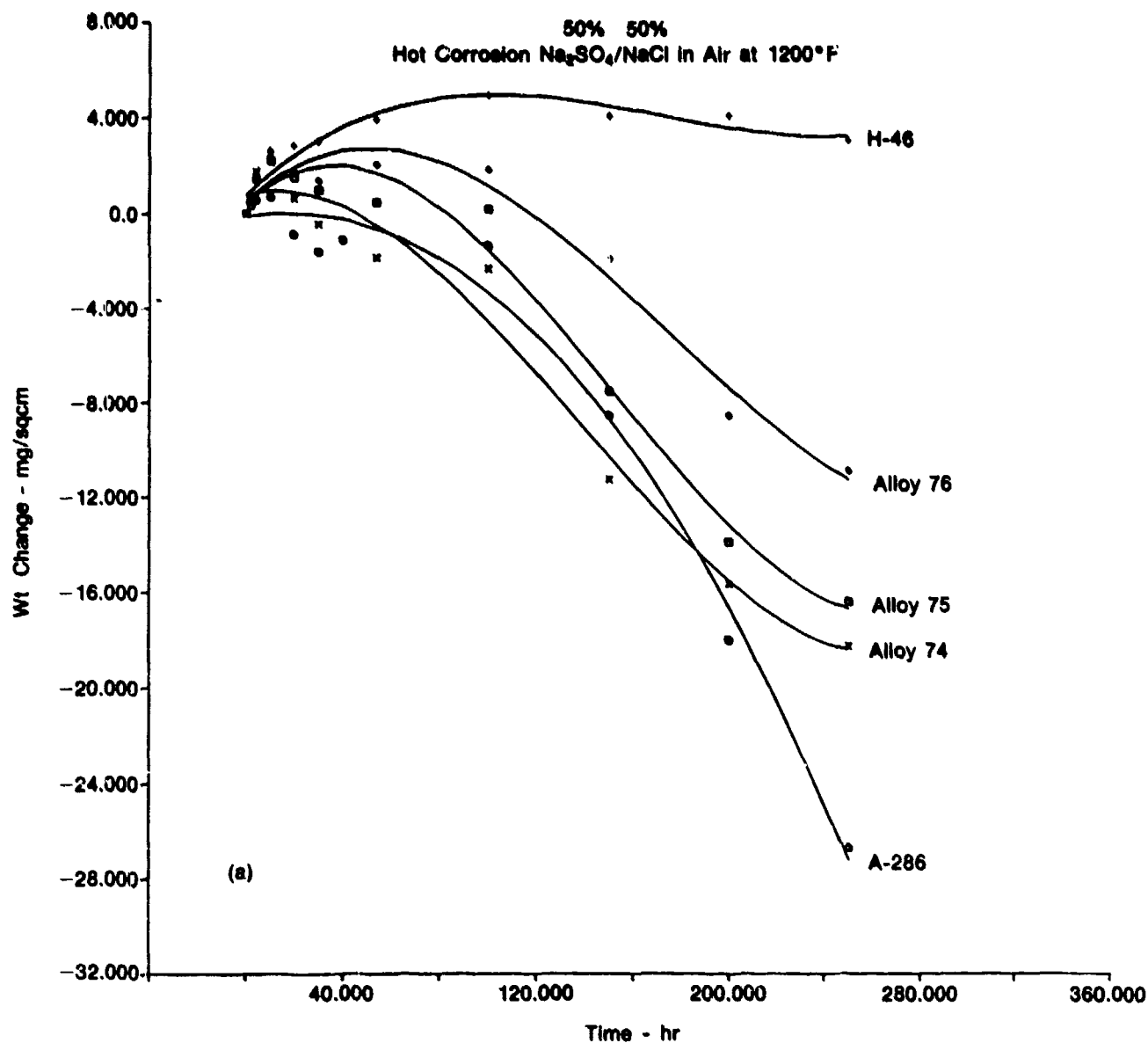


Figure 181. (A) Weight Change Versus Exposure Time in 650°C Sulfidation Tests With a Mixture of 50 Wt% Na_2SO_4 and 50 Wt% NaCl . (B) Appearance of the Specimens After 250 Hours

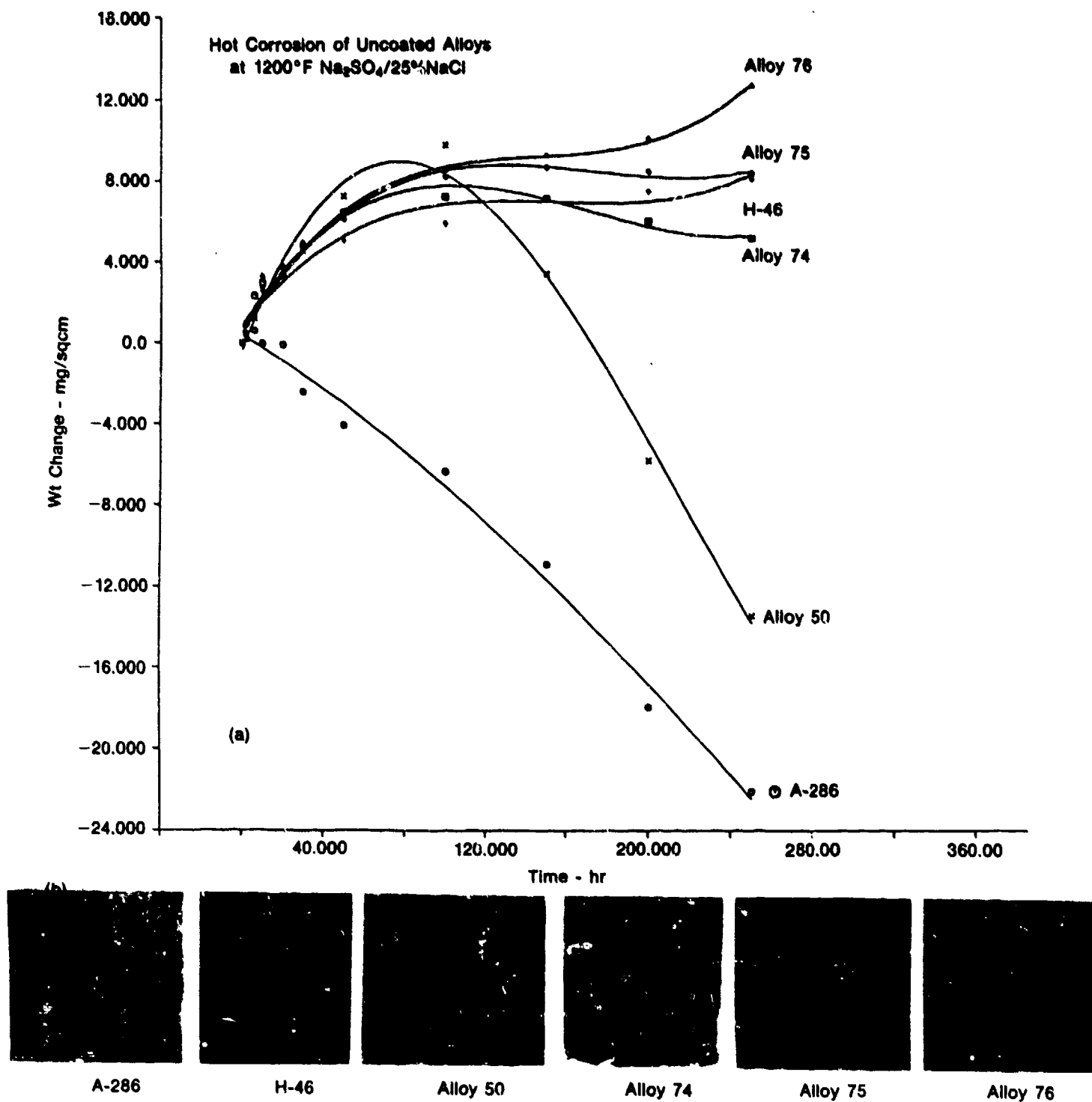


Figure 182. (A) Weight Change Versus Exposure Time in 650°C Sulfidation Tests With a Mixture of 75 Wt% Na_2SO_4 and 25 Wt% NaCl. (B) Appearance of the Specimens After 250 Hours

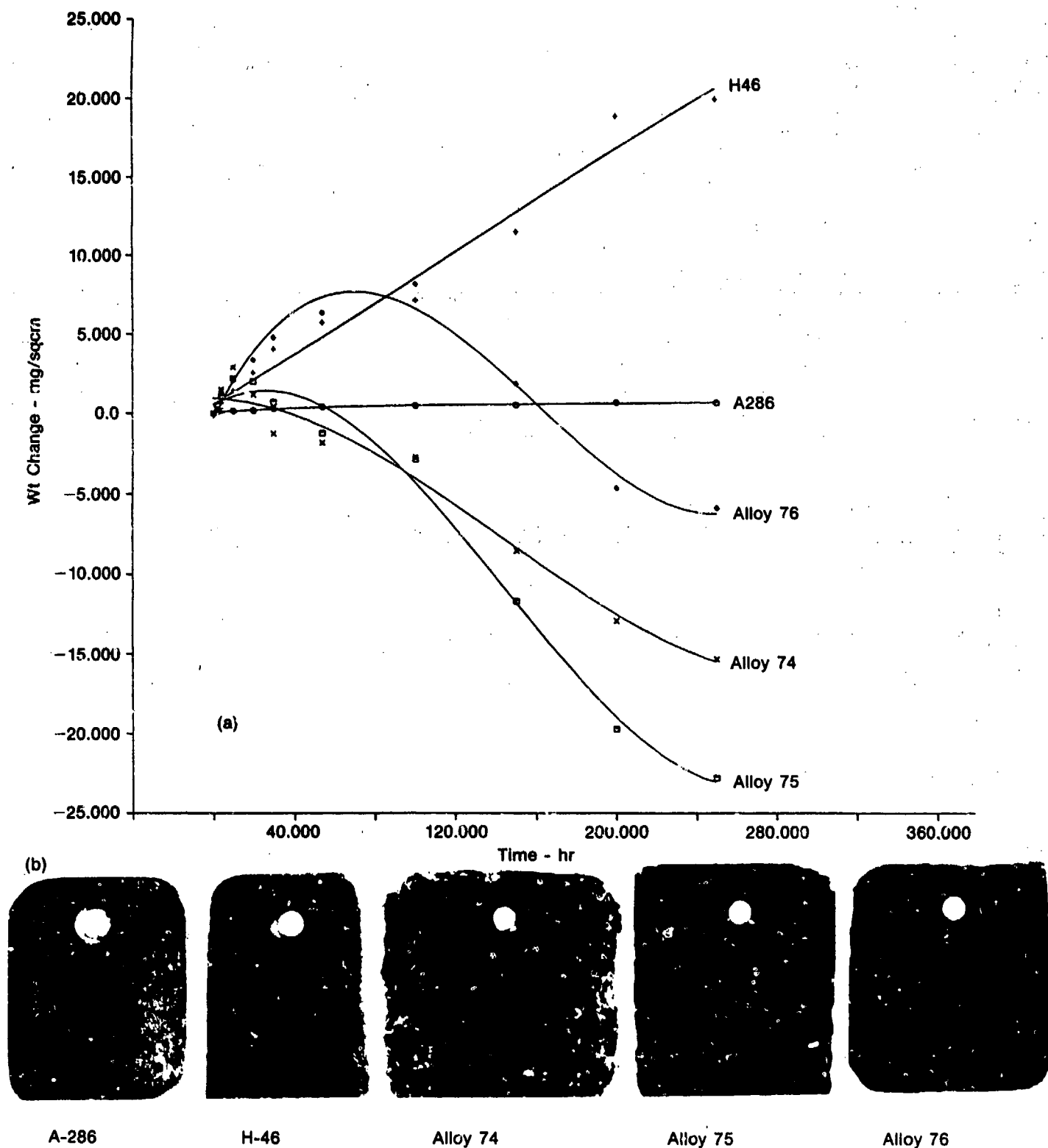
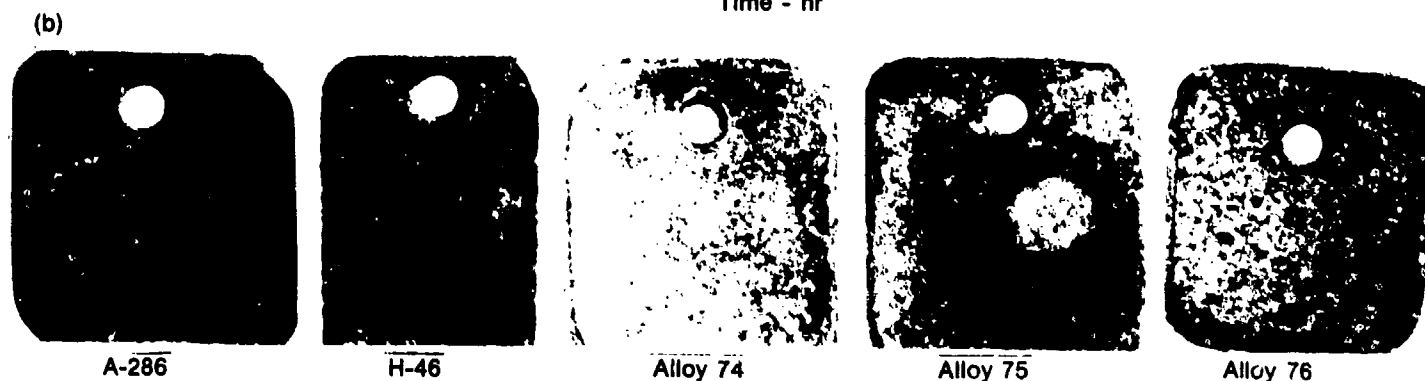
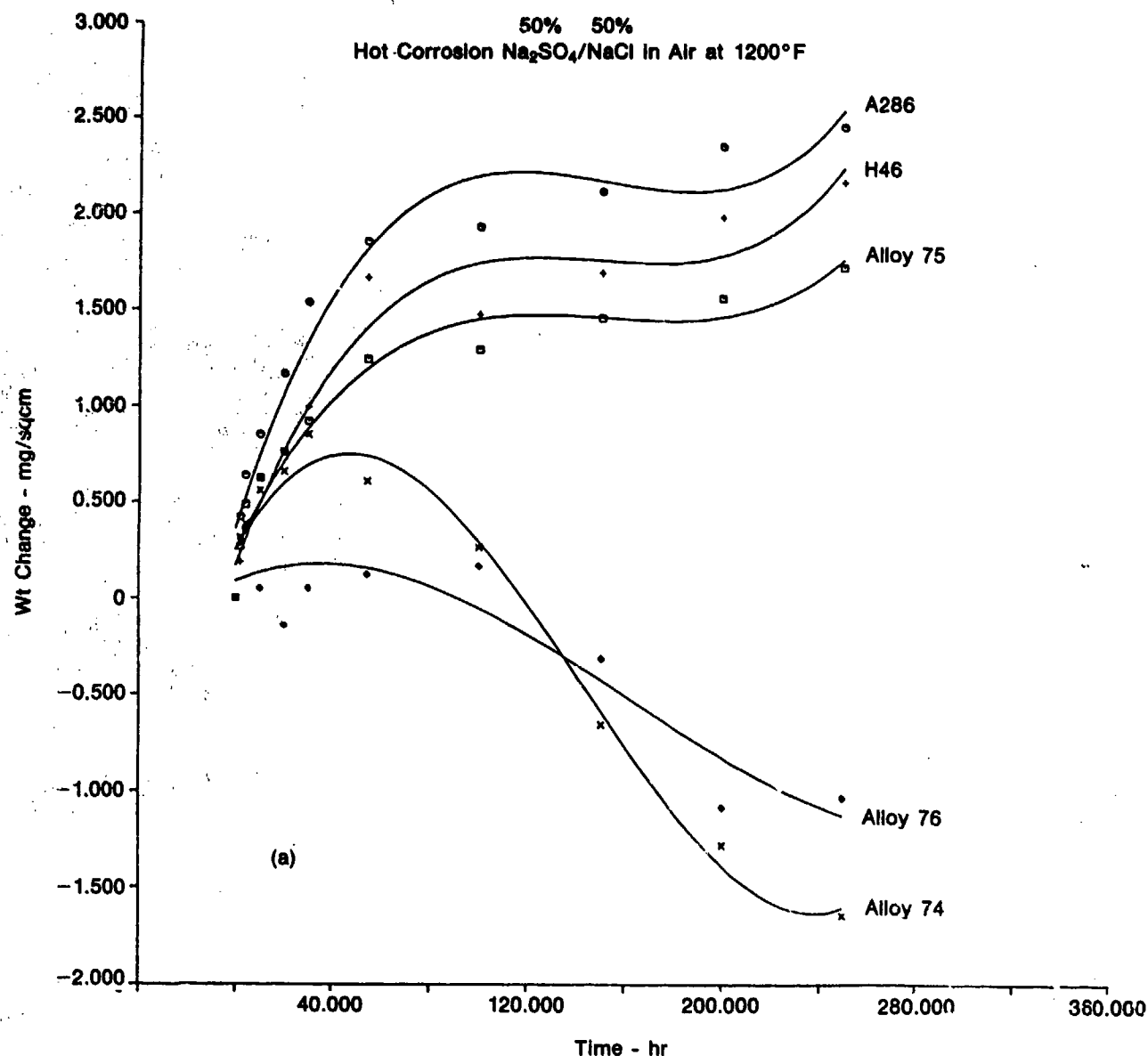


Figure 183. (A) Weight Change Versus Exposure Time in 650°C Sulfidation Tests With a Mixture of 50 Wt% Na_2SO_4 50 Wt% NaCl . Specimens Protected With Aluminized Coatings. (B) Appearance of the Specimens After 250 Hours



FD 243636

Figure 184. (A) Weight Change Versus Exposure Time in 650°C Sulfidation Tests With a Mixture of 50 Wt% Na_2SO_4 and 50 Wt% NaCl . Specimens Protected With Chromized Coatings. (B) Appearance of the Specimens After 250 Hours

Mechanical Evaluations

Prior to mechanical evaluations, the extruded alloys 252 and 253 were given a heat treatment cycle (identified in the alloying screening studies) which consisted of a solution treatment at 2050°F (1120°C) followed by furnace cooling to 1500°F (815°C) at an average rate of 3.5°F (2°C) per minute, and removal from the furnace for air cooling to room temperature. Mechanical properties evaluated include tensile, creep rupture, fracture toughness, fatigue, and elastic stiffness. Standard specimen configurations, given in Figure 185, were machined with the specimen axis parallel to the extrusion direction. Except for the elastic stiffness, all testing was conducted following the respective ASTM-prescribed procedures. The elastic properties were measured at Southern Research Institute, Birmingham, Alabama using a resonance technique. Specimens machined to the configuration, shown in Figure 186, were used for the measurement of dynamic elastic moduli. The technique involved exciting the specimen by electrostatic means, detecting and measuring the resonant frequency of the specimen by similar means. Figure 187 is a block diagram of the equipment used. Support of the specimen was accomplished at the middle of its length which coincides with a vibration node, and therefore has no effect on the resonant frequency. The following relationship was used to calculate the dynamic modulus.

Where:

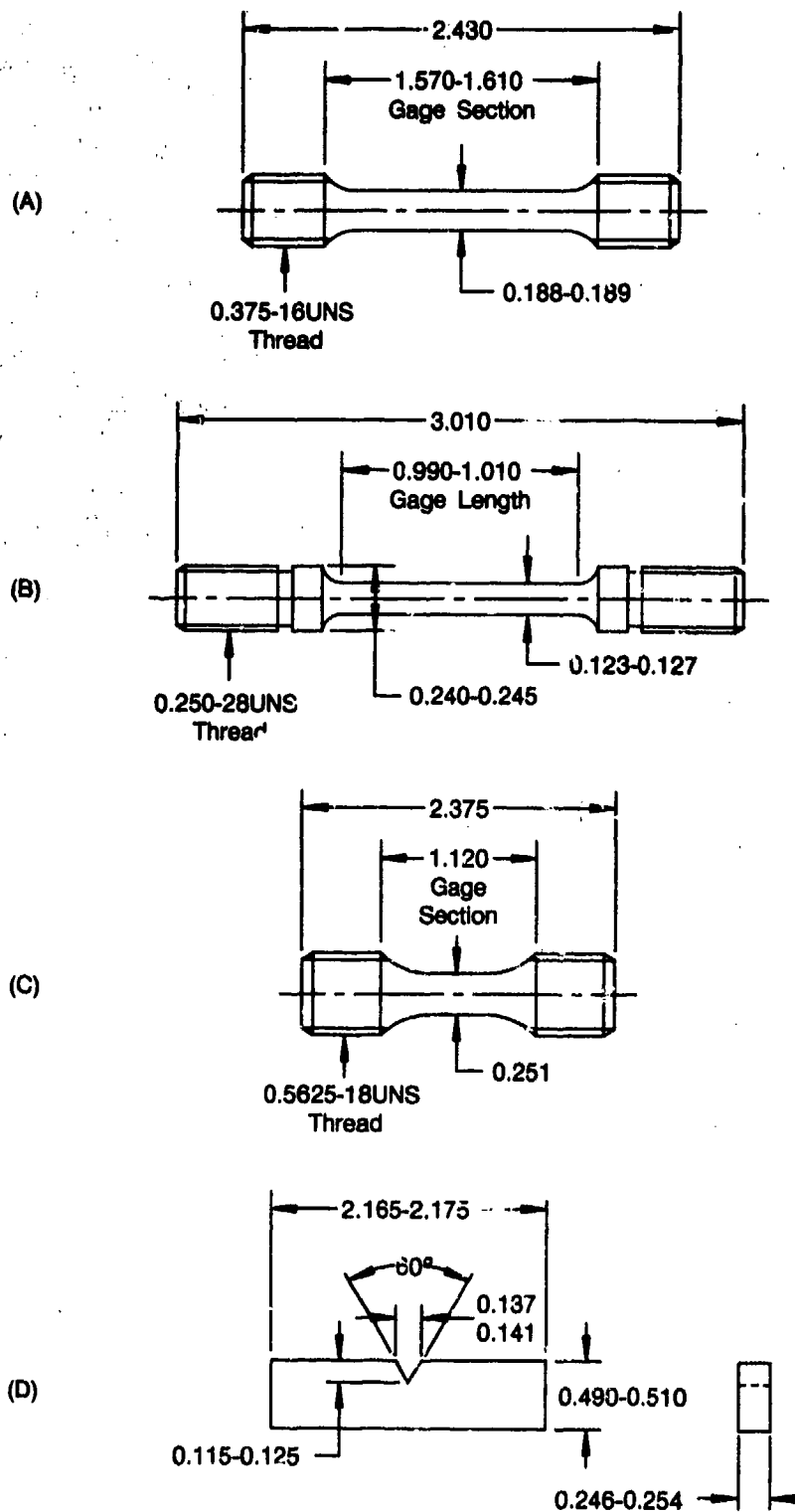
- $E = 4\rho L^2f$
- E = Young's dynamic modulus
- ρ = Density
- L = length, in.
- f = resonant frequency, Hz.

Physical Evaluations

The physical properties measured on alloys 252 and 283 include density and thermal expansivity. Density was determined from a cylindrical specimen shown in Figure 187 by accurately weighing and measuring the specimen dimensions. To determine the thermal expansivity, a dilatometer with a platinum standard was used to measure dimensional changes in a cylindrical specimen 2 inches long and 0.128 inch diameter (5.1 cm long, 0.3 cm diameter) as a function of temperature.

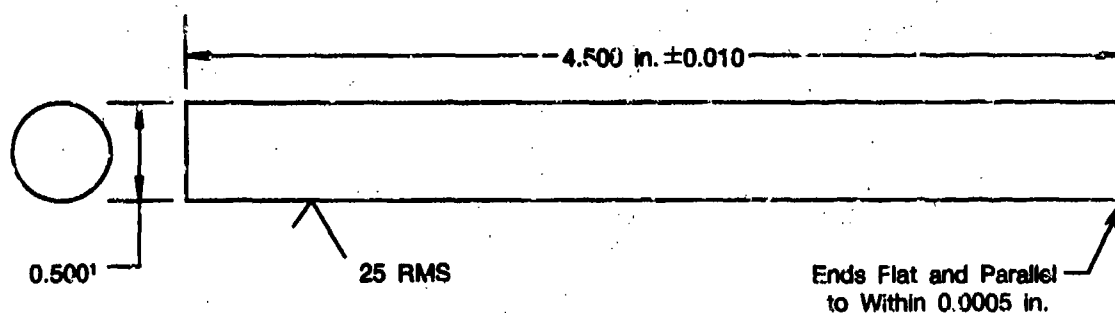
Results and Discussion

Cracking problems were encountered during the initial extrusion of alloys 252 and 253. It was found that by eliminating the ingot casting defects and severe temperature gradient in the ingot during the extrusion cycle, the present alloys could be extruded successfully at 2150°F (1175°C) without difficulties. Figure 188 shows the relative dimensions and appearance of the preform and the extruded bar. The chemical analysis of the alloys, given in Table 64 shows no major deviations from the aims. The microstructure of the alloys in the as-extruded condition are given in Figures 189 and 190. The higher carbon content in alloy 252 is reflected in the microstructure in terms of larger and more numerous perovskite carbide particles. Another remarkable microstructural feature is a continuous decoration of grain boundaries with carbide particles in alloy 253. The microstructures of alloys 252 and 253 after the furnace cooling heat treatment appear to be essentially similar to the respective microstructures in the as-extruded condition.



FCA 318431

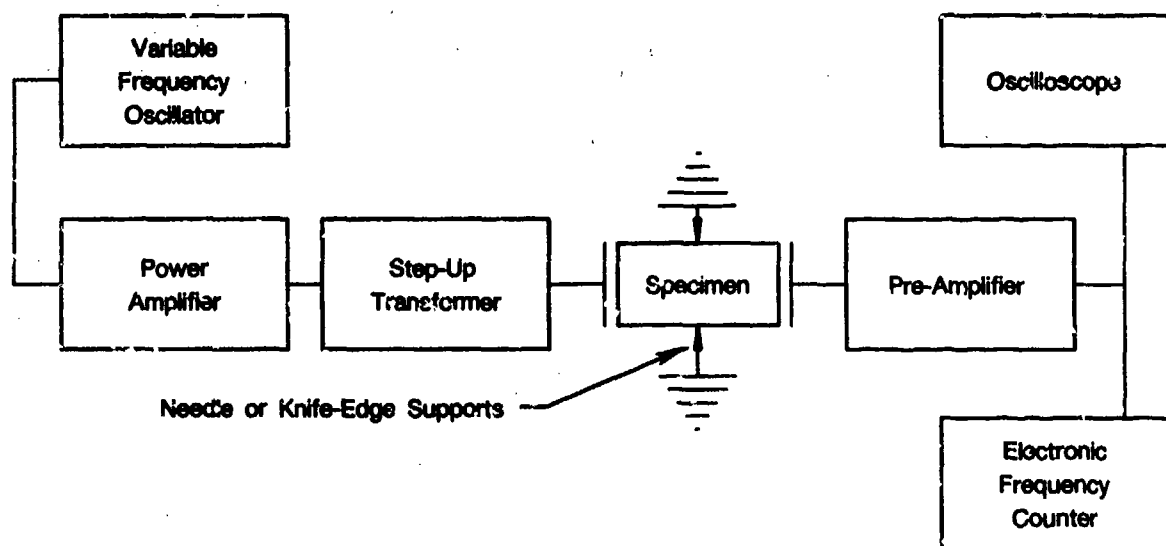
Figure 185. Standard Specimen Configurations



Note 1: Diameter should not vary more than 0.0005 in. along the entire specimen length.

FDA 318432

Figure 186. Specimen Configuration for Dynamic Modulus Determinations by the Longitudinal Vibration Method



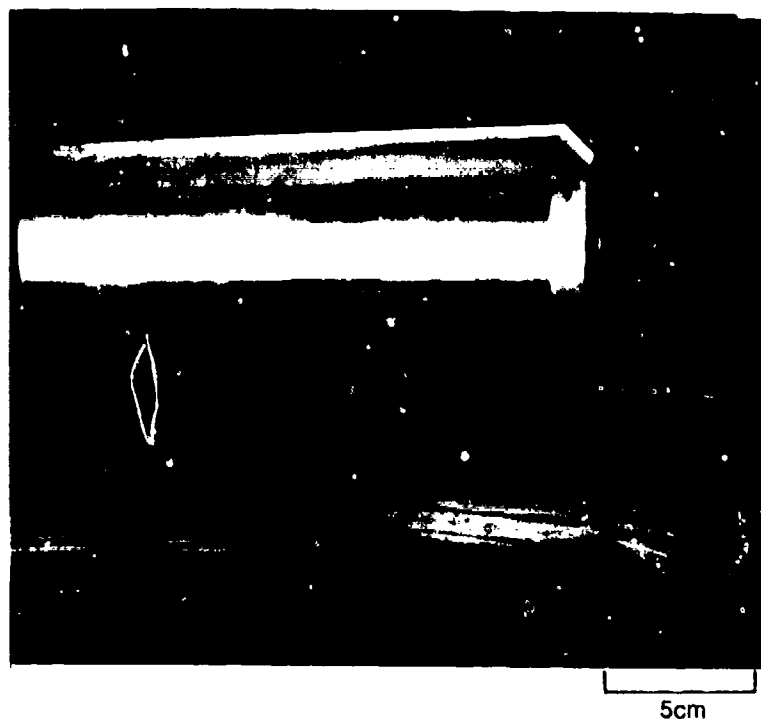
FDA 318433

Figure 187. Schematic of the Dynamic Modulus Apparatus

Tensile Properties

The tensile properties of alloys 252 and 253, given in Table 65, show similar characteristics. Both alloys exhibit high yield strength to intermediate temperatures and poor ductility at low temperatures. The yield strength of both alloys compares favorably with A286, but the ultimate tensile strength is considerably lower due to a lower degree of work hardening, Figure 191, in these alloys. As shown in Figure 192, the low temperature brittleness of the present alloys can be attributed to the cracking of the large perovskite carbide particles at grain boundaries and linking of the microcracks to produce intergranular fracture. At temperatures over 400°F (205°C) both alloys show good tensile ductility, and less cracking of intergranular carbide particles was observed. The tensile fracture mode at intermediate temperatures tends to be a mix of

intergranular and transgranular (Figure 193). The ductility changes can apparently be correlated with changes in deformation behavior at various temperatures. Figures 194 and 195 show that the low temperature brittleness of alloy 252 is associated with the formation of slip bands and that microtwinning becomes the predominant mode of deformation at temperatures above 400°F (205°C).



FD 318434

Figure 188. The Relative Dimensions and Appearance of the Extrusion Preform and the Extruded Bar of Alloy 252

TABLE 64. ANALYZED COMPOSITIONS OF PHASE III ALLOYS, WT%

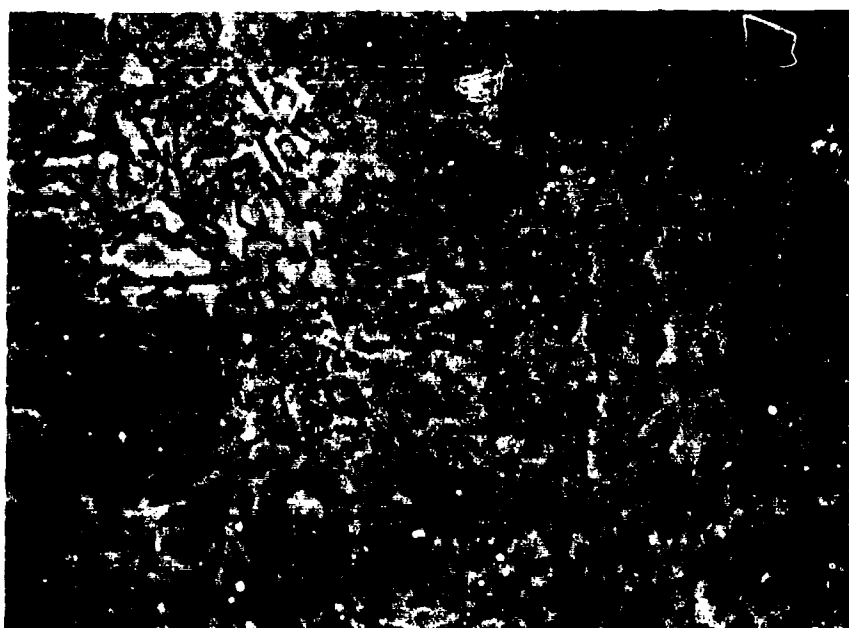
<i>Alloy</i>	<i>Fe</i>	<i>Mn</i>	<i>Al</i>	<i>C</i>	<i>Others</i>
252	Bal	30.6	8.6	2.0	1.14Mo, 0.39W
2C	Bal	32.2	9.5	1.2	1.16Mo, 0.45W

7450C



(a)

200μm

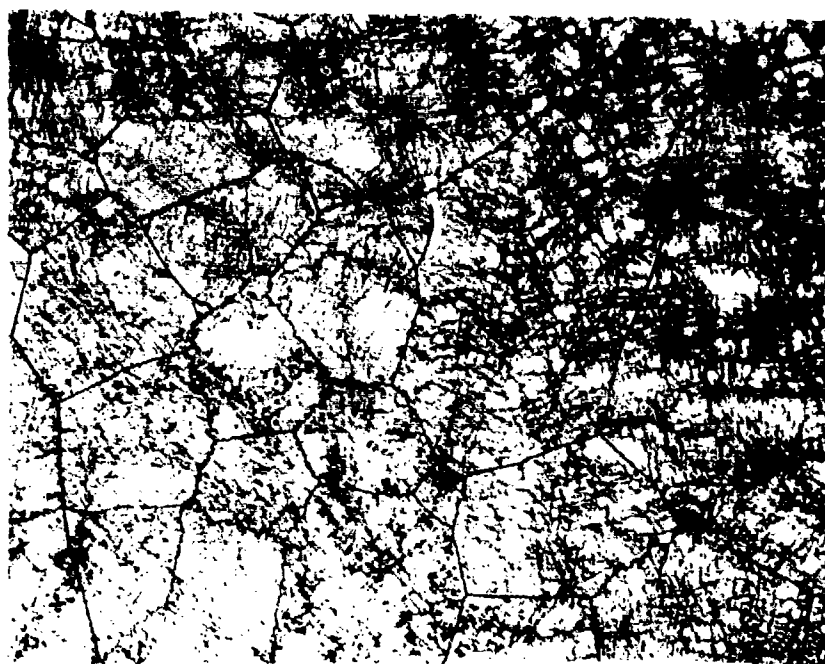


(b)

40μm

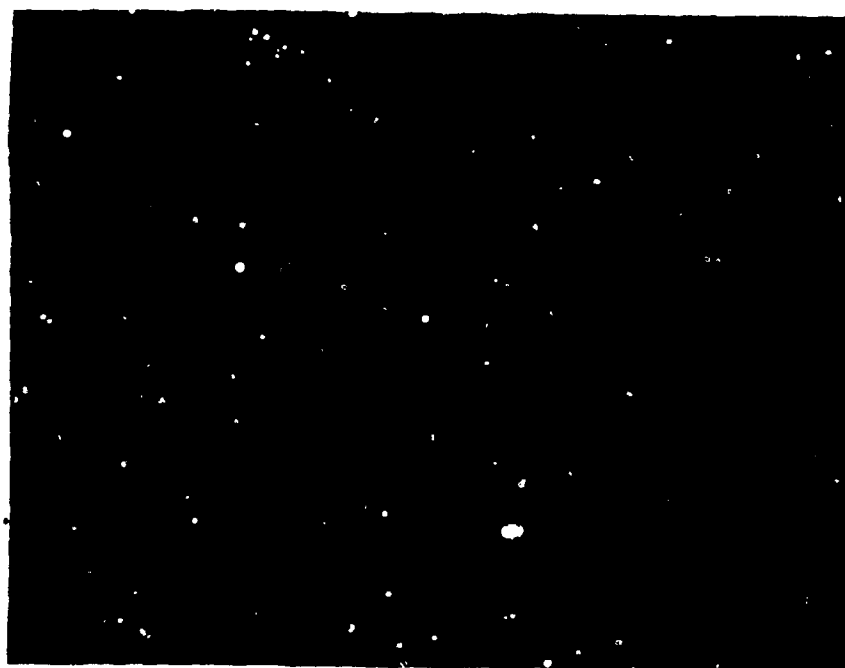
FD 318435

Figure 189. Microstructure of Alloy 252 in the As-extruded Condition



(a)

200μm



(b)

40μm

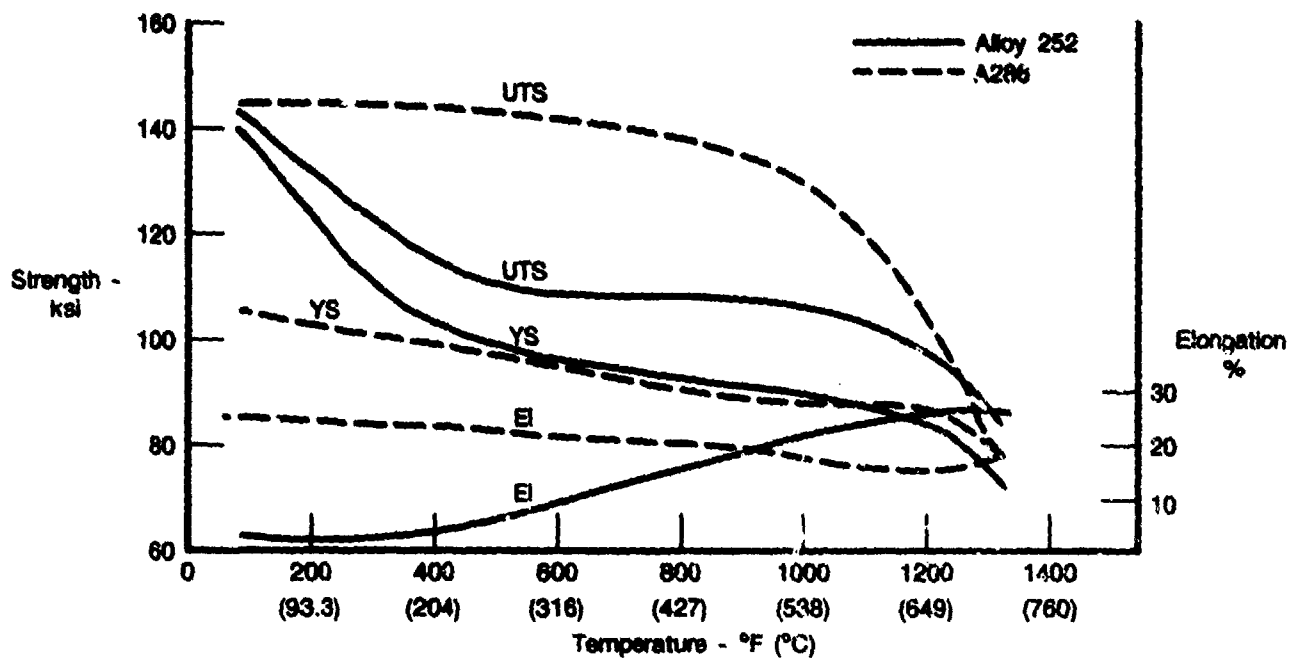
FD 318435

Figure 190. Microstructure of Alloy 253 in the As-extruded Condition

TABLE 65. TENSILE PROPERTIES OF PHASE III ALLOYS

Temp °F	0.2% YS ksi	UTS ksi	E1 %	RA %
Alloy 252				
70	136.7	144.8	0.7	—
70	132.9	137.5	0.6	0.5
400	96.9	111.3	2.7	2.8
400	100.2	115.3	2.1	2.6
800	92.1	125.6	15.0	13.9
800	90.7	124.3	13.2	10.8
1200	83.6	103.5	23.2	28.0
1200	81.6	98.3	31.7	39.1
1300	74.3	88.8	26.0	28.9
1500	73.9	88.5	27.4	28.0
Alloy 253				
70	*	*	*	*
70	*	*	*	*
400	99.2	111.0	13.1	12.2
400	102.5	112.6	10.5	10.4
800	95.5	109.6	23.6	48.6
800	95.3	109.2	36.2	45.3
1200	82.4	95.7	12.0	29.7
1200	87.5	96.2	10.1	31.1
1300	78.2	83.9	21.6	26.2
1300	76.9	85.8	23.8	26.0
* Specimen fractured without yielding				

7448C



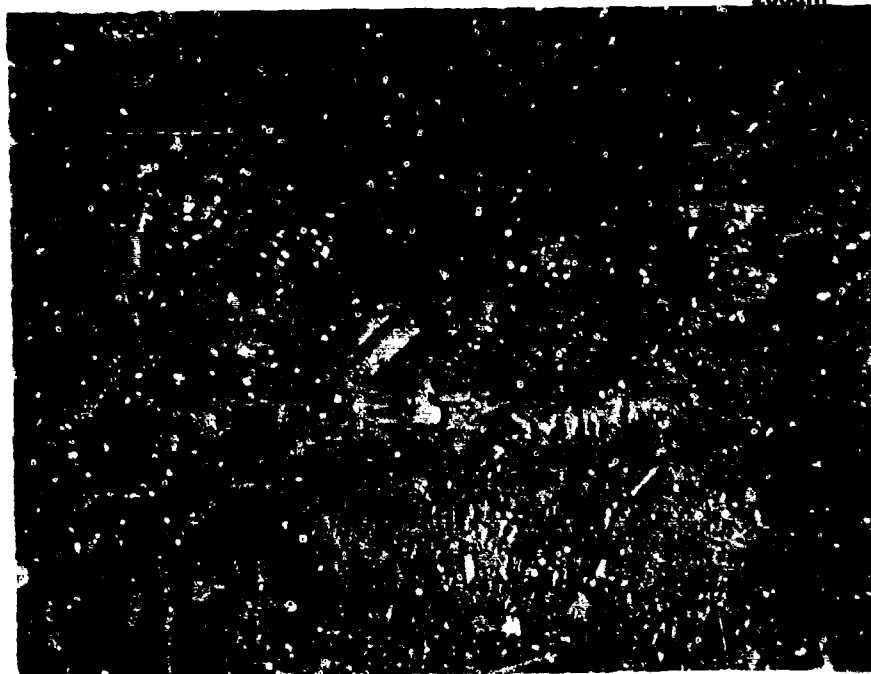
FDA 318437

Figure 191. Yield Strength and Ultimate Tensile Strength of Alloy 252 and A286



(a)

200μm

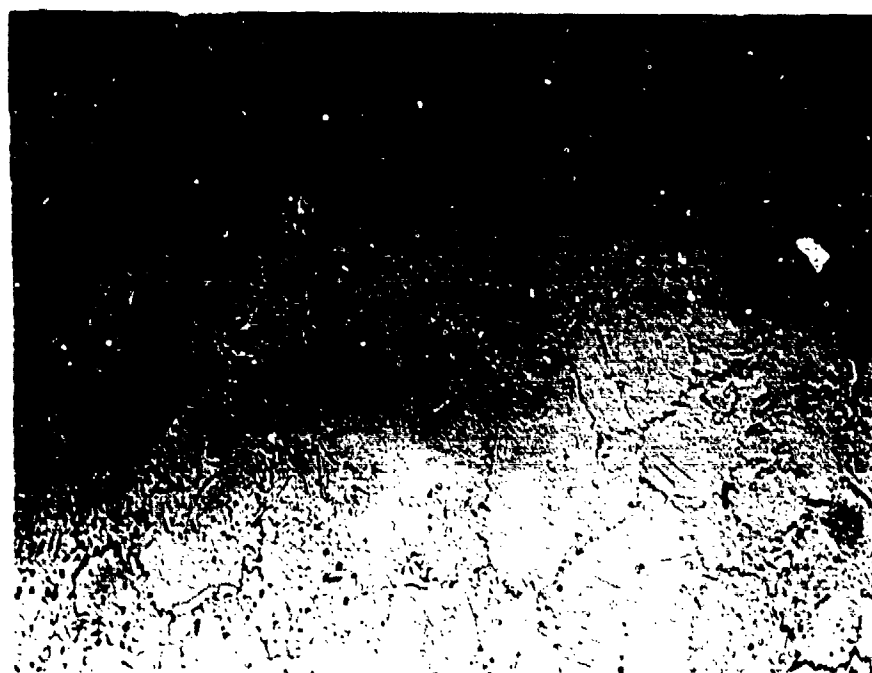


(b)

40μm

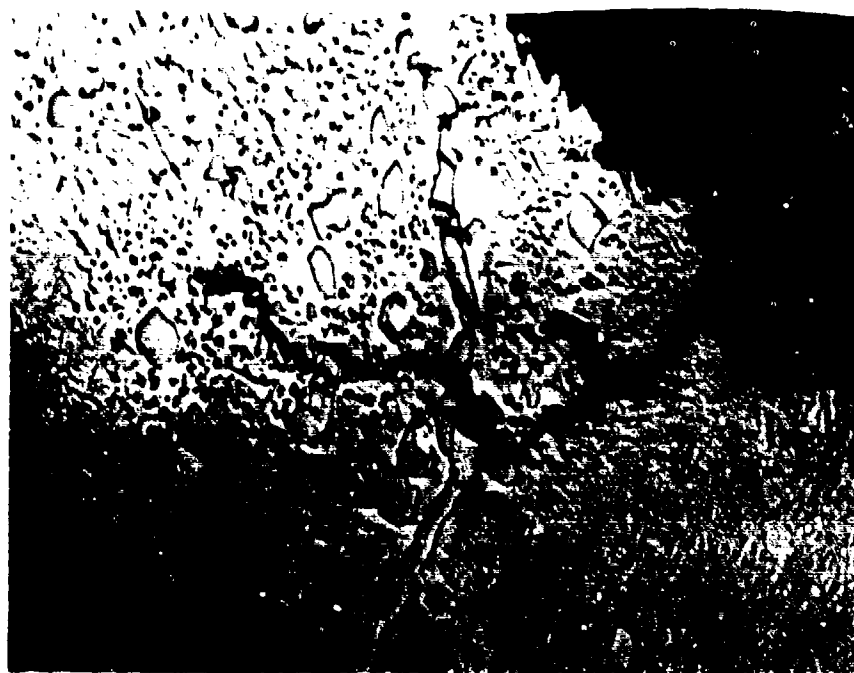
FD 318438

Figure 192. Tensile Fracture of Alloy 252 at 400°F (204°C)



(a)

200μm



(b)

40μm

FD 318439

Figure 193. Tensile Fracture of Alloy 252 at 1300°F (704°C)



1 μ m

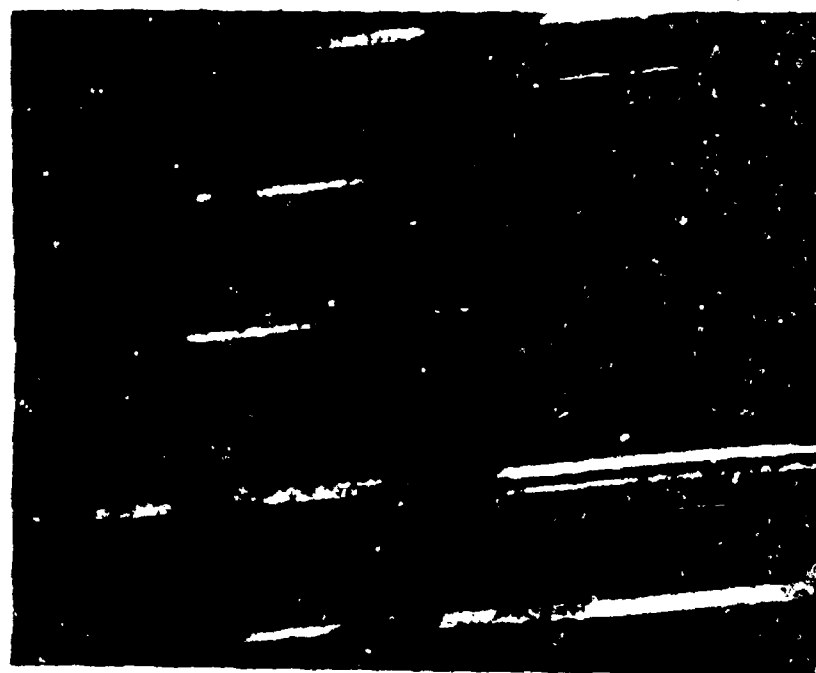
FD 319440

Figure 194. Dislocation Structure in Alloy 252 Resulting from Tensile Deformation at Temperatures Below the Brittle-Ductile Transition



(a)

1 μm



(b)

1 μm

FD 318441

Figure 195. Dislocation Structure in Alloy 252 Resulting from Tensile Deformation at Temperatures Above the Brittle-Ductile Transition (a) Bright Field Micrograph (b) Dark Field Showing Microtwins in the Same Area as (a)

Creep Rupture Properties

Creep rupture data of alloys 252 and 253, given in Table 66 show that, in contrast to tensile properties, alloy composition has an important effect on rupture life. The rupture life of alloy 252, which contains 2 wt% carbon, is two to three times longer than that of alloy 253 with 1.2 wt% carbon. It is also remarkable that alloy 252 showed considerably higher creep rupture ductility than alloy 253. Table 67 shows a comparison of the 100-hour creep rupture strength of the present alloys with A286. It can be seen that the creep rupture strength of alloy 252 is equivalent to A286 at 1200°F (650°C), but is slightly lower at 1300°F (704°C). As may be expected, creep fracture in both alloys 252 and 253 was found to be caused by intergranular separation.

TABLE 66. CREEP RUPTURE PROPERTIES OF PHASE III ALLOYS

Temperature °F	Stress ksi (MPa)	Fracture Time hr	El %	RA %
Alloy 252				
1200	40	343	32	50
	40 (276)	467	27	42
	50	398	18	21
	50 (345)	310	20	25
	60	102	16	13
	60 (413)	108	13	14
1300	35	169	21	16
	35 (241)	202	23	18
	40	75	23	15
	40 (276)	82	25	20
	50	15	22	38
	50 (345)	24	18	20
Alloy 253				
1200	40	94	7	4
	40 (276)	110	4	3
	50	80	8	5
	50 (345)	78	5	4
	60	51	7	5
	60 (413)	38	4	4
1300	30	57	7	8
	35	40	13	11
	35 (241)	35	11	7
	40	29	8	5
	40 (276)	35	7	6

7460C

TABLE 67. ONE-HUNDRED-HOUR RUPTURE STRENGTH
ksi (MPa)

	<i>Alloy 252</i>	<i>253</i>	<i>A286</i>
1200°F (650°C)	60 (413)	40 (276)	61 (420)
1300°F (704°C)	38 (262)	25 (172)	44 (303)

7450C

Transmission electron microscopy was performed on alloy 252 after creep testing at 1200°F (650°C) for 100 hours. Figure 196a shows that considerable coarsening of the perovskite carbide had occurred during the test. Further, the fine perovskite carbide: matrix interface is no longer coherent which is apparent from the formation of the interfacial dislocations as shown in Figure 196b. The interfacial dislocations were determined to be of pure edge type with spacing of about 80Å. Analysis of dislocations in the austenitic matrix was unsuccessful because of the small spacing between the fine perovskite carbide particles. However, analysis was conducted on dislocations observed in the large perovskite particles, Figure 197. The dislocation systems were determined to be $\{ \bar{1}11L <011>$ with a mixed character. Evidence of dislocation pairing (shown by an arrow in Figure 197) was also observed.

Fracture Toughness

The fracture toughness of alloys 252 and 253 was determined at room temperature using the slow bending technique, and results are given in Table 68. As may be expected from the brittleness of these two alloys at low temperatures, the plane strain fracture toughness was found to be relatively low, two to three times lower than superalloys.

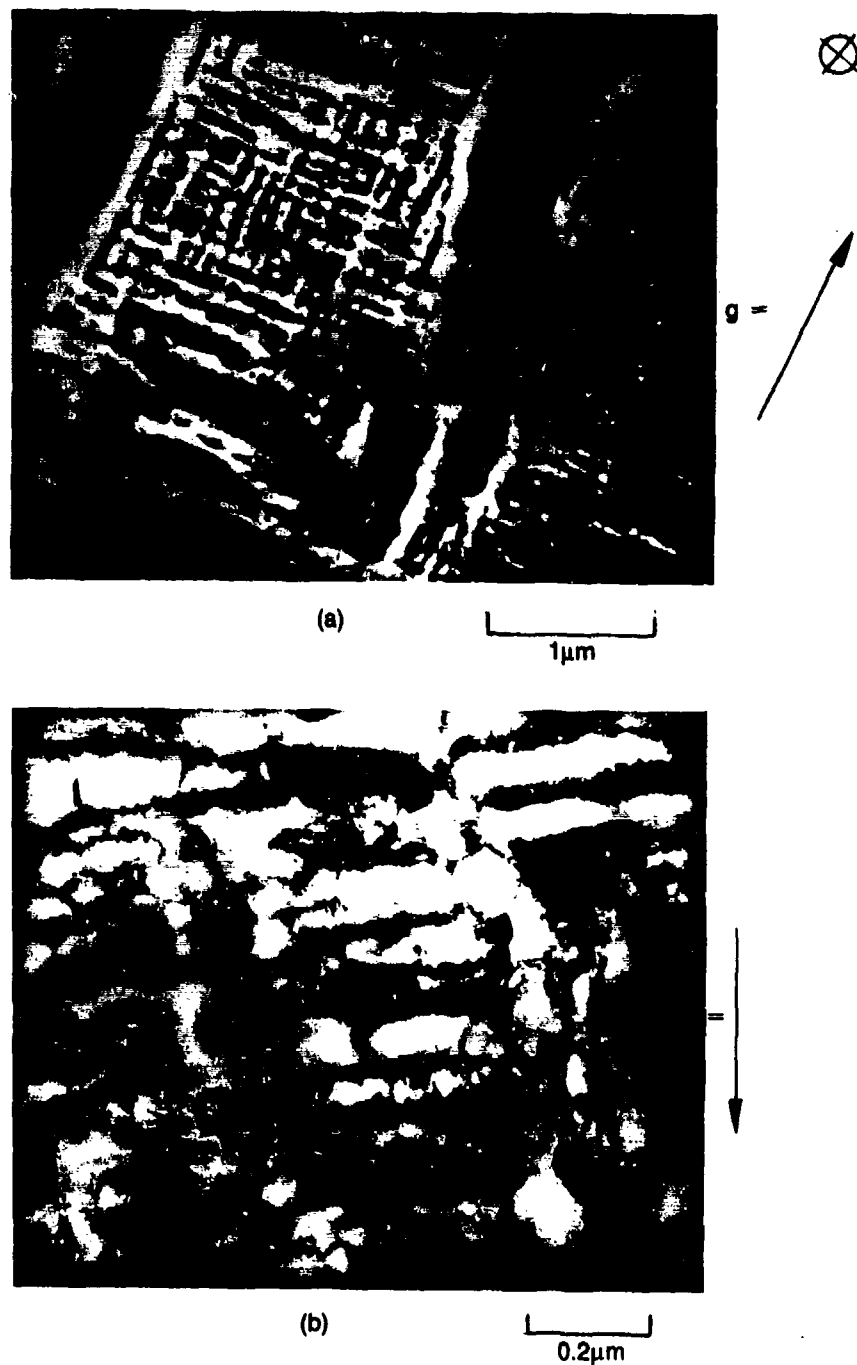
Fatigue Properties

Fatigue tests were conducted on alloys 252 and 253 at room temperature using cylindrical specimens with smooth gage sections and at a stress ratio R (minimum stress: maximum stress) of 0.1 and a frequency of 1 cycle per second. Results, given in Figure 198, show that the fatigue properties of the present alloys are comparable to the austenitic stainless steel of type 304 (fatigue data of A286 at similar test conditions were not available for comparison). The fatigue fracture of alloys 252 and 253 was found to be rather similar to tensile fracture at low temperatures which occurred intergranular, Figures 199 and 200. The relatively low fatigue strength of these two alloys could be related to the ease of grain boundary cracking at low temperatures.

The fatigue crack growth behavior of alloys 252 and 253 at room temperature, $R=0.1$ and 1 Hz, is shown in Figure 201. Relative to A286, the present alloys showed poor crack growth characteristics.

Dynamic Elastic Modulus and Density

The physical data used for calculating the dynamic elastic moduli and density are given in Table 69. The measured densities for the alloys are generally lower than iron-base superalloys, by 15% when compared with A286. The dynamic moduli calculated from the resonance frequency measurements are tabulated in Table 70. The dynamic moduli for alloy 252 were found to be considerably higher than those of alloy 253. In general, the elastic moduli for both alloys are lower than those of iron-base superalloys by 10 to 20% in the temperature range studied.



FD 318442

Figure 196. (a) General Microstructure of Alloy 252 After Creep Testing at 1200°F (650°C) for 110 hours $g = [020]$. (b) Detailed Appearance of the Fine Perovskite Carbide Particles Showing Presence of Interfacial Dislocations, $g = [020]$



$g =$

0.2 μ m

FD 318443

Figure 197. Dislocations in the Large Perovskite Carbide Particles of Alloy 252 After Creep Testing at 1200°F (650°C) for 110 hours. Arrow Indicates Paired Dislocations, $g = [200]$

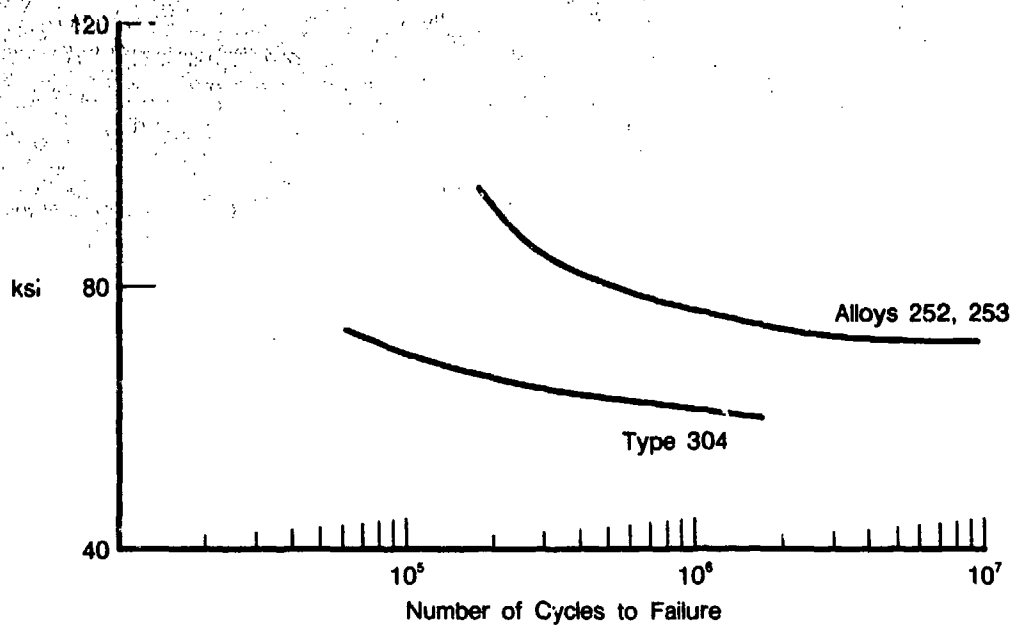
TABLE 68. FRACTURE TOUGHNESS OF AUSTENITE-PEROVSKITE ALLOYS AT ROOM TEMPERATURE

Alloy	K_{Ic} , ksi $\sqrt{in.}$ (MPa \sqrt{m})
252	19.5, 21.7, 26.3, 29.6 (21.4, 23.8, 28.9, 32.5)
253	12.4, 15.5, 17.9, 19.1 (13.6, 17.0, 19.7, 21.0)

7448C

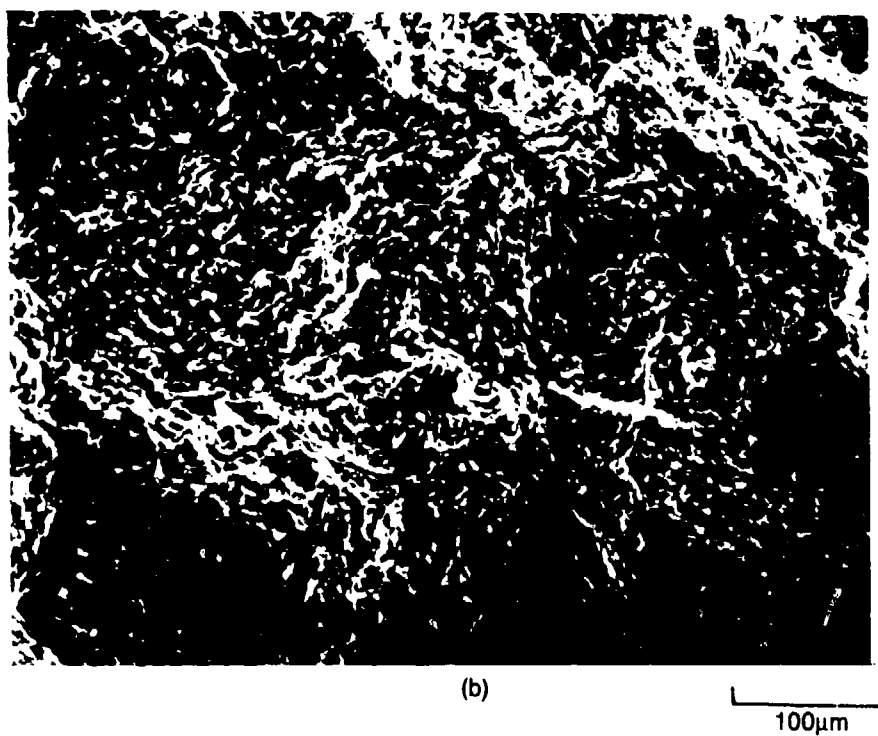
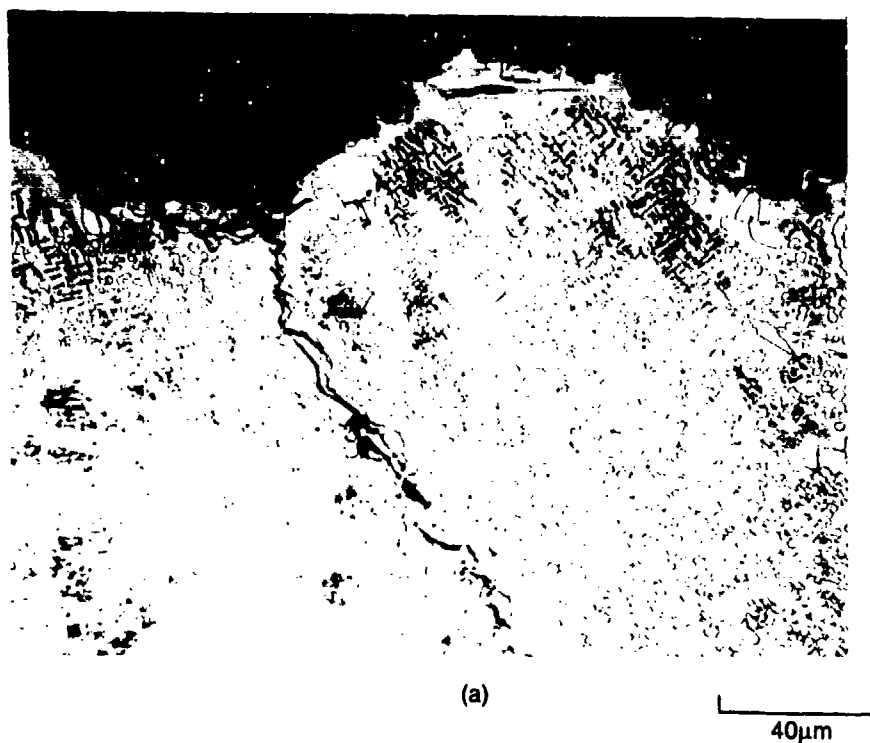
Thermal Properties

The mean thermal expansion of alloys 252 and 253 as a function of temperature are given in Table 71, and shown plotted in Figure 202. The dimensional changes with temperature in alloys 252 and 253 were found to be larger relative to both austenitic stainless steels and the iron-base superalloy A286, Figure 202.



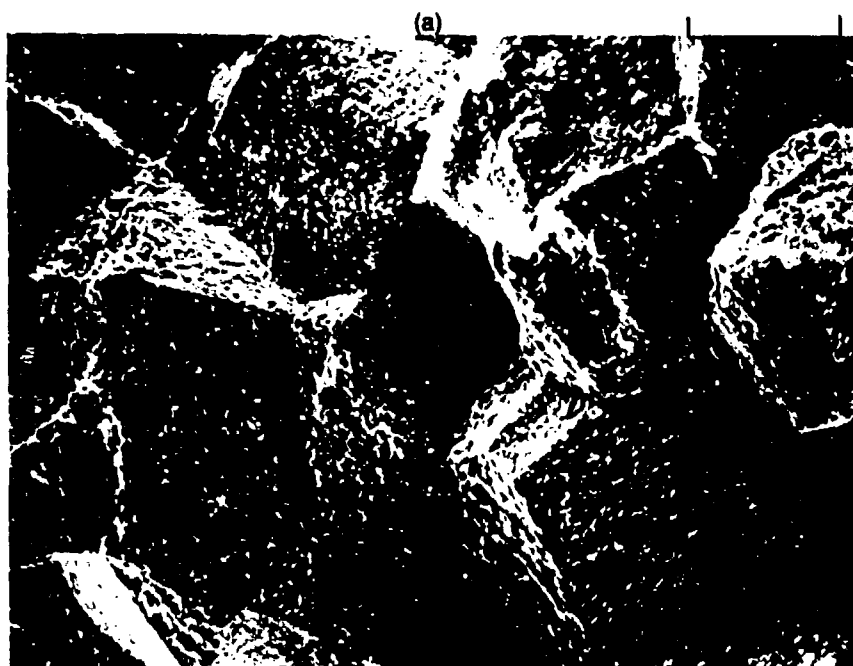
FDA 318444

Figure 198. Stress vs Number of Cycles to Failure for Alloys 252 and 253 Fatigue Tested at Room Temperature, $R=0.1$ and 1 Hz. Corresponding Data for an Austenitic Stainless Steel Type 301 Are Also Included for Comparison



FD 318445

Figure 199. Fatigue Fracture of Alloy 252 of 70F (20C). (a) Sectional View Showing Formation of Cracks in Large Perovskite Carbide Particles at Grain Boundary (b) Appearance of Fracture Surface

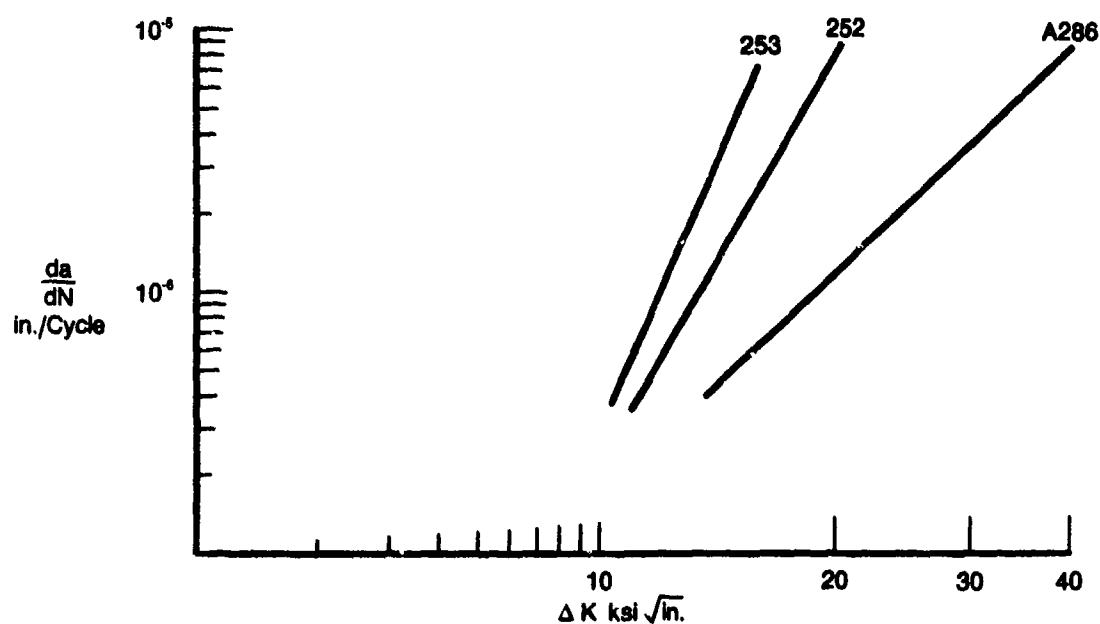


(b)

100μm

FD 318448

Figure 200. Fatigue Fracture of Alloy 253 at 70F (20C) (a) Sectional View Showing Intergranular Fracture (b) Appearance of Fracture Surface



FDA 318447

Figure 201. Fatigue Crack Growth Rates of Alloys 252 and 253 at Room Temperature, Stress Ratio of 0.1 and Frequency of 1 Hz. Corresponding Data for A286 Are Also Shown for Comparison

TABLE 69. PHYSICAL DATA FOR CALCULATION OF DENSITIES AND ELASTIC MODULI OF ALLOYS 252 AND 253

Alloy	Diameter in.	Length in.	Weight gm	Specific Weight lb/in. ³
252	0.5002	4.3224	93.7086	0.2432
253	0.5001	4.6446	99.5387	0.2405

7480C

TABLE 70. DYNAMIC MODULUS DATA AT ROOM AND ELEVATED TEMPERATURES FOR ALLOYS 252 AND 253

Temperature °F	Alloy 252 (10 ⁶ psi)	253 (10 ⁶ psi)
70	25.58	23.00
70	25.57	23.02
70	25.58	23.01
	Avg. 25.58	23.01
400	24.18	21.67
400	24.18	21.67
400	24.18	21.67
	Avg. 24.18	21.67
800	22.08	19.82
800	22.08	19.82
800	22.08	19.82
	Avg. 22.08	19.82
1200	19.90	17.94
1200	19.93	17.98
1200	19.90	17.95
	Avg. 19.91	17.96
1300	19.27	17.41
1300	19.26	17.43
1300	19.28	17.43
	Avg. 19.27	17.42

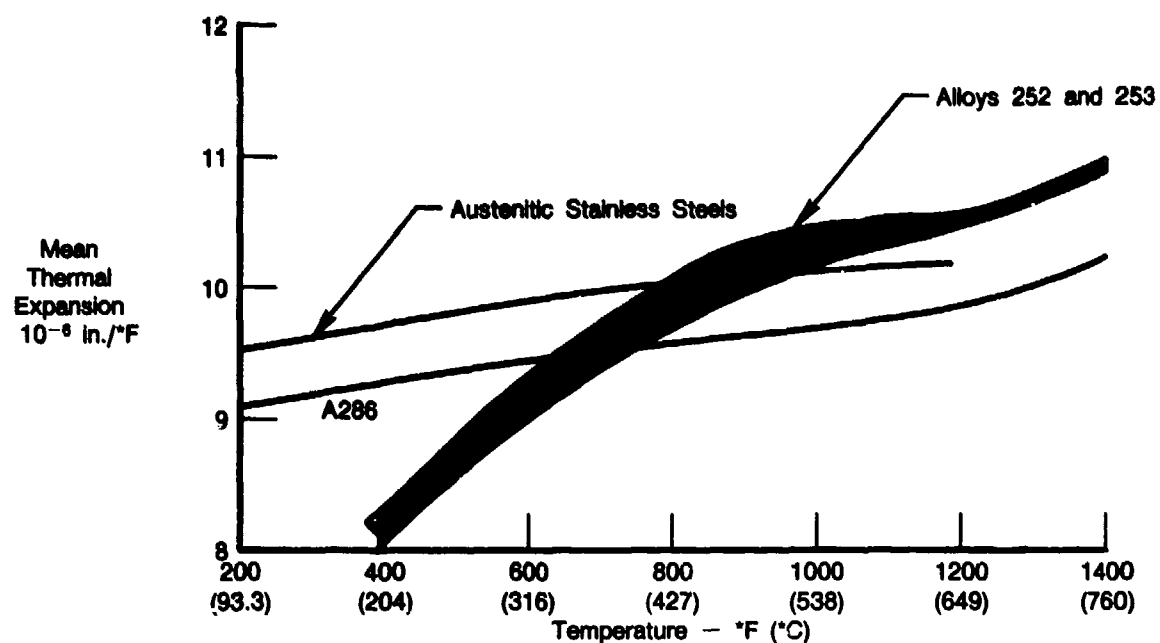
7480C

TABLE 71. MEAN COEFFICIENT OF THERMAL EXPANSION (70° TO TEMP.) × 10⁻⁶/°F

Temperature	Alloys		
	252	253	A286*
400	8.34	8.07	9.35
600	9.41	9.04	9.47
800	10.06	9.68	9.64
1000	10.52	10.21	9.78
1200	10.84	10.63	9.88
1400	11.10	10.94	10.32
1600	11.35	11.25	—
1800	11.55	11.59	—
2000	11.79	11.89	—
2100	—	12.01	—

* Nickel Base Alloys INCO Data Book, 1964

7480C



FDA 318448

Figure 202. Thermal Expansion Characteristics of Alloys 252 and 253. Corresponding Data for Austenitic Stainless Steels and A286 Are Included for Comparison

CONCLUSIONS — TASK III

1. A new class of precipitation hardened alloys based on the Fe-Mn-Al-C system was identified. These alloys consist of an austenitic matrix with an ordered and semi-coherent perovskite carbide precipitate $(\text{Fe, Mn})_3 \text{AlC}_x$.
2. It was shown that the microstructure and mechanical properties of the austenite-perovskite alloys could be significantly changed by heat treatment and alloying modification. Alloys with tensile and creep strengths equivalent to iron-base superalloys were identified.
3. The current austenite : perovskite alloys have mechanical property deficiencies at ambient temperatures including ductility, fracture toughness, and fatigue cracking characteristics.
4. Future work should concentrate on defining compositions for optimum properties.